수의학박사학위논문

포도당 결핍에 따른 종양조직 구성세포들의 표현형 및 분자생물학적 특성 변화

Glucose deficiency-induced changes in tumor tissues: Phenotypic and molecular aspects

2021 년 8 월

서울대학교 대학원

수의학과 수의병인생물학 및 예방수의학 전공

황 성 현

Glucose deficiency-induced changes in tumor tissues: Phenotypic and molecular aspects

By

Sung-Hyun Hwang

A dissertation submitted to the faculty of the Graduate School of Seoul National University in partial fulfillment of the requirements for the degree of Doctor of Philosophy in Veterinary Pathobiology and Preventative Medicine

Supervised by

Professor Yongbaek Kim, D.V.M., Ph.D.

August 2021

Department of Veterinary Medicine

The Graduate School

Seoul National University

포도당 결핍에 따른 종양조직 구성세포들의 표현형 및 분자생물학적 특성 변화

지도교수 김 용 백

이 논문을 수의학 박사 학위논문으로 제출함

2021 년 06 월

서울대학교 대학원

수의학과 수의병인생물학 및 예방수의학 전공

황 성 현

황성현의 박사 학위 논문을 인준함

2021 년 8 월

위 원 장 김 대 용

부 위 원 장 김 용 백

위 원 백 승 준

위 원 류 덕 영

위 원 박 준 원

ABSTRACT

Glucose deficiency-induced changes in tumor tissues: Phenotypic and molecular aspects

(Supervisor: Yongbaek Kim, D.V.M., Ph.D.)

Sung-Hyun Hwang

Department of Veterinary Medicine
Graduate School of Veterinary Medicine
Seoul National University

Within a hostile tumor microenvironment, irregular vasculature and aerobic glycolysis induce a glucose deficiency. Tumor mass is constituted with cancerous and non-cancerous cells such as cancer-associated fibroblasts (CAFs) and tumor-infiltrating lymphocytes (TILs). Compared to normal counterparts, those cells are acquired different phenotypes and metabolism, and their crosstalk enforces the tumor progression. However, the comprehensive impact of glucose deficiency in cancer cells, CAFs and TILs have not been elucidated. In this study, we investigated that glucose deficiency renders metabolic reprogramming in cancer cells, CAFs and TILs compared to complete condition and promote tumor progression.

The effect of glucose deficiency on phenotype of human malignant mesothelioma (HMM) cells remains unclear. Our data demonstrated that survived HMM cells by glucose deficiency enhanced the resistance to metformin treatment with upregulation of multidrug resistance protein 1 (MDR1) expression in mitochondria. Adapted HMM cells to glucose deficiency showed an irregular mitochondrial metabolic status with elongated morphology and dysfunction including mitochondrial membrane potential (MMP) hyperpolarization. Intriguingly, increased MDR1 expression in the cells was suppressed by treatment of carbonyl cyanide m-chlorophenyl hydrazine (CCCP), an inducer for MMP depolarization. In MDR1-knockout (KO) cells, sensitivity to metformin was dramatically augmented compared to parental cells with upregulation of apoptosis and autophagy.

CAFs are major components in non-cancerous stromal cells in tumor microenvironment and protecting cancer cells. However, compared to normal fibroblasts (NFs), distinctive characteristics of CAFs under glucose-deficient conditions are rarely studied. Irregular vasculature induces the heterogeneous response in tumor mass. To determine the heterogeneous response in CAFs, we dissected a tumor mass as 6 pieces and isolated CAFs from each piece. The ATP production and proliferation were enhanced in CAFs under glucose-deficient condition, but not in NFs. Moreover, their patterns were consistent in whole CAFs, but the degree was heterogeneous. In contrast to NFs, transforming growth factor-β (TGF-β) signaling and mitochondrial

calcium uniporter (MCU) expression was higher in CAFs and more enhanced under glucose-deficient condition, but these phenotypes were suppressed by inhibition of TGF-β signaling. Intriguingly, treatment of Ru360, a selective MCU inhibitor also mitigated the TGF-β signaling in CAFs. The influx of calcium into mitochondria enhanced the ATP production in CAFs by activation of ATP synthase. However, treatment of ATP synthase inhibitor enhanced the apoptosis by excessive calcium influx into mitochondria via inactivation of mitochondrial permeability transition pore.

CAFs reinforces the cancer cell malignancy via direct- and soluble-factor mediated communication. Here, we demonstrated that CAFs-derived lipids especially oleic acid (OA) were transition into H460 cells via lipid transporter and enhanced stearoyl-CoA desaturase (SCD) expression under glucose-deficient conditions. Expression of SCD augmented autophagic response in CAF-supernatant treated H460 cells under glucose-deficient condition and promoted stemness, but their phenotypes were suppressed by treatment of CAY10566, a selective SCD inhibitor. SCD-overexpressing cells exhibited enhancement of stemness with nuclear localization of YAP through actin-polymerization compared to parental and SCD-KO cells. Furthermore, a larger size of tumor was observed in SCD-overexpressing cells injected mice than parental cells, whereas SCD-KO cells resulted in smaller tumors. Additionally, SCD was correlated with poor prognosis in patients with lung adenocarcinoma.

CAFs-derived OA was also transferred in $CD4^+$ tumor-infiltrating lymphocytes (TILs) and augmented SCD expression under glucose-deficient condition. In $CD4^+$ TILs, SCD enhanced the phenotype of Th1 cell including IL-2, tumor necrosis factor-α, T-bet and interferon-ɣ expression, whereas regulatory T cell (Treg) phenotype including CD25, Foxp3 and TGF-β were suppressed. However, it was reversed by treatment of CAY10566. SCD biosynthesized unsaturated fatty acid from saturated fatty acids. Amounts of OA, unsaturated fatty acids, was increased in SCD overexpressed T cells and upregulated the phenotype of Th1 cell. However, enrichment of palmitic acid (PA) among saturated fatty acids in SCD-KO cells enhanced Treg cell phenotype. Moreover, a robust secretion of C-X-C motif chemokine 11 (CXCL11) from SCD-upregulated $CD4^+$ T cells activated CXC-chemokine receptor 3 (CXCR3) signaling in $CD8^+$ T cells, improving cancer-killing effect in 4T1 mouse model.

Collectively, the present study demonstrated that glucose deficiency is impacted on the cancer cell malignancy and induces metabolic reprogramming in CAFs and TIL. For a better understanding of the effects of glucose deficiency, our data provide a detailed mechanism and phenotypes in cancer cells, CAFs and TIL. These features aimed approach could enhance anticancer therapeutics.

Keywords: Tumor microenvironment, Glucose-deficient condition, Cancer cell, Cancer-associated fibroblasts, Tumor-infiltrating lymphocyte, Lipid metabolism, Anticancer.

Student Number: 2016-21772

CONTENTS

ABBREVIATIONS

HMM: Human malignant mesothelioma

H460: NCI-H460

ROS: Reactive oxygen species

EMT: Epithelial to mesenchymal transition

MDR1: Multi drug resistance protein 1

ABCG2: ATP-binding cassette super-family G member 2

CSCs: Cancer stem cells

TGF-β: Transforming growth factor beta

OCT4: Octamer-binding transcription factor 4

YAP: Yes-associated protein

CAF: Cancer-associated fibroblast

MCU: Mitochondrial-calcium uniporter

SCD: Stearoyl-CoA desaturase

SREBP: Sterol regulatory element binding protein

TIL: Tumor-infiltrating lymphocyte

CXCL11: C-X-C chemokine ligand 11

CXCR3: C-X-C chemokine receptor 3

IFN-ɣ: Interferon-ɣ

TNF-α: Tumor necrosis factor-α

RT-PCR: Reverse transcription polymerase chain reaction

qPCR: Quantitative polymerase chain reaction

Glut-1: Glucose transporter 1

HIF-1α: Hypoxia-inducible factor-1α

GAPDH: Glyceraldehyde 3-phosphate dehydrogenase

MMP: Mitochondrial membrane potential

mPTP: Mitochondrial permeability transition pore

mtROS: mitochondrial reactive oxygen species

OXPHOS: Oxidative phosphorylation

MTT: 3-(4,5-dimethylthiazol-2-yl)-2,5-diphenyl tetrazolium bromide

JC-1: 5,5',6,6'-tetrachloro-1,1',3,3' -tetraethyl-benzimidazolylcarbocyanine chloride

CCCP: Carbonyl cyanide m-chlorophenyl hydrazone

LITERATURE REVIEW

Glucose deficiency in tumor microenvironment

Compared to normal cells, the glycolysis pathway is different in cancer cells. In normal cells, glucose is metabolized to produce pyruvate for activation of TCA cycle and lactate is occasionally biosynthesized from pyruvate upon environmental stress conditions such as hypoxia (Hu et al. 2017). On the other hand, cancer cells generally produce lactate from glucose and activate aerobic glycolysis to generate ATP more than glycolysis. To meet the energy demand of cancer cells for rapid proliferation, generated ATP by aerobic glycolysis is quickly wasted and leads to glucose-deficient condition in tumor hostile microenvironment (Liberti 2016) (Fig. 1). Indeed, the concentration of glucose is lower in tumor interstitial fluid than normal plasma in the mice model (Sullivan et al. 2019). The concentration of glucose is lower in colon and stomach tumor (123 ± 43, 424 ± 131 nmol/g) than in normal counter parts (1220 ± 150, 1290 ± 168 nmol/g) (Hirayama et al. 2009). Moreover, angiogenesis is advanced in tumor mass to supply the energy and oxygen for growth. As closer to the vasculature, tumor cells acquire more glucose and nutrient more than the distal region, resulting in a glucose-deficient condition in the region (Jeong and Deasy 2014) (Fig. 2). Thus, glucose deficiency encounters not only cancer cells but also non-cancerous cells including cancer-associated fibroblasts (CAFs), endothelial and immune cells (Lin et al. 2020).

Glucose deficiency induces the metabolic reprogramming rather than glycolytic pathway, leading to physiological and pathological change in cancer cells (Lin et al. 2019). In cancer cells, alternative metabolisms using glutamine and lipid are activated to compensate for the energy in the absence of glucose. Glutamine-mediated TCA cycle is activated in cancer cells by the loss of protein kinase C to produce energy under glucose-deficient condition (Ma et al. 2013). The aerobic glycolysis induces lipid metabolic reprogramming rather than canonical glycolysis such as pentose phosphate and hexosamine pathway (Vander Heiden et al. 2009, Hay 2016). Indeed, glucose level and glycolysis are significantly mitigated in fasted mice compared to fed mice, but lipid and cholesterol metabolisms are substantially activated dependent on sirtuin1 expression (Rodgers and Puigserver 2007). Under glucose-deficient conditions, lipid metabolism is reprogrammed to provide the energy (Snaebjornsson et al. 2020). Mechanically, increased 3-oxoacid CoA-transferase 1 (OXCT1) by phosphorylation of Akt activates the lipid metabolism under glucose-deficient condition and induces the acetyl-CoA synthesis for activation of TCA cycle (Huang et al. 2016). Additionally, under glucose-deficient condition, stored lipids are digested by autophagic response and generate fatty acids to provide lipid metabolism and energy source (Singh et al. 2009, Roa-Mansergas et al. 2018). However, impairment of autophagy by deletion of Atg 5 and 7 genes suppresses the lipid metabolism through impairment of PPARα expression (Saito et al. 2019).

Additionally, glucose deficiency augments autophagic response through upregulation of AMP-activated protein kinase (AMPK) (Liu et al. 2020). Mechanistically, AMPK induces the phosphorylation of tuberous sclerosis complex 2 and suppresses the mammalian target of rapamycin (mTOR) signaling, leading to activation of autophagy (Inoki et al. 2003). The mTOR is constituted with mTORC1 and mTORC2 and plays a sensor for nutrient and growth factors. Insulin, glucose, and amino acids activate the Akt/PI3K and MAP4K3 signaling to generate energy for cell survival by mTOR activity. Moreover, activated mTOR by nutrients and growth factor phosphorylates the ULK1, 2, and Atg family, but inhibition of mTOR induces the dephosphorylation of ULK1, 2 and Atg 13 and activates the autophagy in cancer cells (Jung et al. 2010). Autophagy, a double-edged sword could kill the xenobiotics and infected cells and protect cells from oxidative stress (Shintani and Klionsky 2004). In the process of autophagy, the lysosome is fused with autophagosome which surrounding the harmful damaged and genetically unstable residues, preventing the tumor progression (Mizushima 2007). Loss of Beclin-1, an essential regulator for autophagy enhances the necrosis with inflammation rather than apoptosis, resulting in poor prognosis (Degenhardt et al. 2006). On the other hand, under glucose-deficient conditions, activated autophagy produces energy by recycling the degraded cellular organelles and provides energy for survival of cancer cells (Mathew et al. 2007). Autophagy provides the energy in cancer cells to restoration of nutrients that gradually induces tumorigenesis with

upregulation of the cancer stem cell population (Nazio et al. 2019). And autophagy protects the cancer cells from significant DNA damage and genomic instability and leads to dramatical tumor growth (Karantza-Wadsworth et al. 2007).

Glucose deficiency enhances the apoptosis of cancer cells with reduction of ATP and increased reactive oxygen species (Liu et al. 2003). However, adapted cancer cells to media with low glucose enhance the resistance against anticancer drugs including 5-FU and carboplatin dependent on PI3K pathway compared to those cells cultured in complete media (Bhattacharya et al. 2014). Moreover, glucose deficiency augments the tumor malignancy by enhancement of oxidative stress and oncogenic transcription factors including c-Myc, c-Fos, and c-Jun (Spitz et al. 2000). Increased nuclear factor E2-related factor 2 in cancer cells under glucose-deficient condition binds to the promoter region of matrix metalloproteinase (MMP-9) and enhances the invasiveness and metastasis (Endo et al. 2018). Glycolysis is frequently activated in mitochondria to produce energy in normal cells. However, adapted cancer cells to glucose-deficient conditions show enhancement of resistance to anticancer drug with mitochondrial dysfunction including morphological elongation, mitochondrial-membrane potential (MMP) hyperpolarization and aberrant ATP production (Hwang et al. 2019). Under glucose-deficient conditions, resistance to temozolomide and carboplatin is enhanced in glioblastoma cells with activation of autophagy, but chemoresistance and quiescence are attenuated by

treatment of bafilomycin A1, a selective autophagy inhibitor (Wang et al. 2018). Analogously, glucose deficiency also protects the colorectal cancer cells from oxaliplatin and 5-fluorouracil by elevated ATF4-signaling. However, knockdown of ATF4 expression alleviates the resistance (Hu et al. 2016). Additionally, metabolic reprogramming by glucose deficiency upregulates the epithelial-mesenchymal transition (EMT) with expressions of N-cadherin and snail, whereas proliferation-related protein (PCNA) is suppressed (Jo et al. 2020).

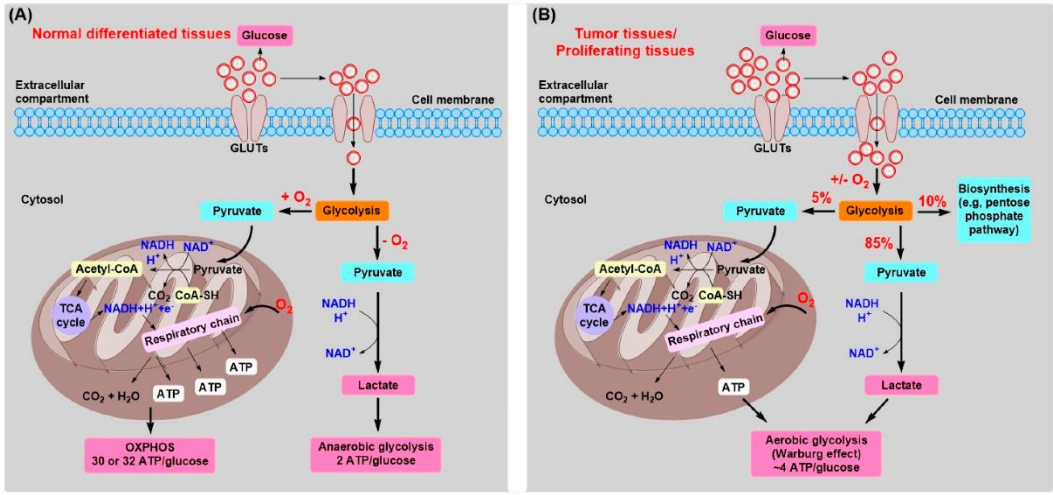

Figure 1. The schematic diagram for massive glycolysis in tumor microenvironment by aerobic glycolysis (Fan et al. 2019).

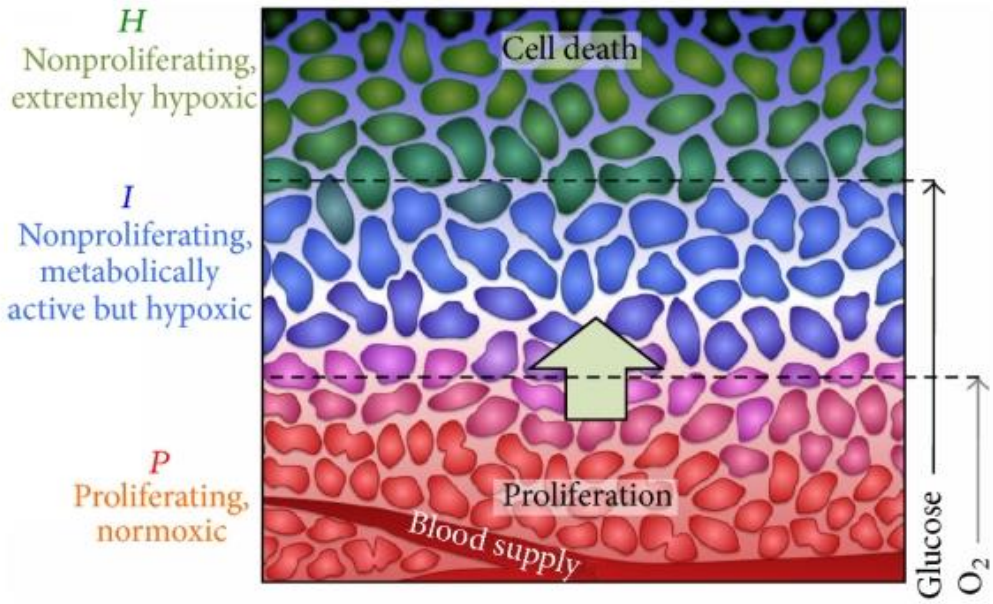

Figure 2. Glucose is restricted in the distal region from vasculature in tumor microenvironment (Jeong and Deasy 2014).

The role of CAFs in tumor microenvironment

Tumor mass is constituted of cancerous cells and non-cancerous cells. Non-cancerous cells are important to assist cancer cell growth by cell-cell communication and indirect way. Cancer-associated fibroblasts (CAFs) are the main components of the non-cancerous stromal cells and similar to myofibroblasts which mediate the wound-healing and inflammation (Östman 2009). It is noteworthy that CAFs promote cancer cell malignancy by interaction with the physical structure and soluble factors such as cytokines and metabolites (Santi et al. 2018). CAFs disrupt the basement membrane of surrounding normal tissue by degradation of the extracellular matrix via protease- and force- remodeling (Gaggioli et al. 2007). In parallel, epithelial-mesenchymal transition by CAF promotes the migration of cancer cells toward near-normal tissues for invasiveness and metastasis (Labernadie et al. 2017).

Within the tumor microenvironment, cancer cells produce various cytokines to stimulate themselves and neighboring stromal cells, leading to malignant transformation from inactive-quiescence state of normal fibroblast. Malignant transformation of the fibroblasts induces wound-healing in tumor mass for significant growth and invasiveness (Eyden et al. 2009). Particularly, transforming growth factor-β (TGF-β) that is secreted from colorectal cancer cells transforms normal fibroblasts toward CAFs with activation of STAT3 signaling and interacts with cancer cells for metastasis (Calon et al. 2012). Additionally, secretion of platelet-derived

growth factor (PDGF) from cancer cells is conjugated with PDGF-receptor on fibroblasts and differentiates to malignant form. To conjugate with PDGF from cancer cells, fibroblasts are migrated to cancer cells and reinforces the angiogenesis and tumor growth by osteopontin (Anderberg et al. 2009). Malignant transformation of normal fibroblasts by bladder cancer cells-derived insulin growth factor 1 (IGF-1) activates estrogen receptor β (ERβ)-signaling in the fibroblasts and protects the cancer cells by reduction of sensitivity to cisplatin in *in vitro* and *in vivo* model (Long et al. 2019).

Furthermore, CAFs also produce numerous cytokines and stimulate not only themselves but also cancer cells to acquire aggressiveness (Fig. 3). In contrast to control, higher levels of TGF-β and stromal cell-derived factor-1 (SDF-1) are secreted from well-differentiated CAFs and stimulate the C-X-C chemokine receptor 4 (CXCR4)-pathway in cancer cells, leading to significant tumor growth (Kojima et al. 2010). Moreover, CAFs-derived IL-6 activates the CXCR7-mediated STAT3 signaling in cancer cells and enhances the resistance to cisplatin and 5-fluorouracil in a mouse model (Qiao et al. 2018). As a shelter for cancer cells, CAFs protect the cancer cells from anticancer therapy. Docetaxel treatment enhances the WNT16B expression in CAFs and is transferred to neighboring prostate cancer cells. It activates the canonical-Wnt and NF-kB signaling in cancer cells, leading to the enhancement of chemoresistance (Sun et al. 2012). Additionally, the expression of versican is augmented in ovarian cancer cells by CAFs-derived TGF-β and promotes the invasion and motility of cancer cells

through activation of NF-kB signaling pathway and cancer stemness (Yeung et al. 2013).

Additionally, cancer cell-induced aerobic glycolysis changes the metabolism in CAFs. Enrichment of metabolites from cancer cells are stored in CAFs and they are utilized in nutrient-deficient conditions (Lin et al. 2020). Catabolism in CAFs by aerobic glycolysis substantially produces metabolites and molecules including pyruvate, lactate, and acetyl-CoA. They transfer to neighboring cells in the tumor microenvironment and lead the metabolic reprogramming which is called as 'Reverse Warburg effect' (Pavlides et al. 2009, Fu et al. 2017). Notably, CAFs provide lactate and fatty acids to feed the neighboring cancer cells and enhance mitochondrial biogenesis (Whitaker-Menezes et al. 2011). Lactates and fatty acids secreted from CAFs by upregulation of MCT4 are transferred to cancer cells and used as fuel to activate oxidative phosphorylation and fatty acid metabolism. Thus, MCT4 expression in CAFs is negatively correlated with the survival rate in breast cancer patients (Witkiewicz et al. 2012).

Furthermore, crosstalk of CAFs-induced metabolites and cytokines with immune cells also play a central role in the tumor immune microenvironment. CAFs-derived cytokines and metabolites also affect the activation of immune cells (Liu et al. 2019). Indeed, CXCL12 from CAFs promotes tumorigenesis and inhibits the infiltration of effector T cells in xenografted tumors. However, depletion of CAFs by diphtheria toxin injection elevates the effector T cell infiltration and suppresses the tumor growth compared

to non-injected ones (Feig et al. 2013). CAFs produce the IL-8 and CCL2 and activates the pro-inflammatory response of neutrophils through activation of STAT3-pathway in hepatocellular carcinoma. Dominant pro-inflammation by neutrophils mitigates the activity of effector T cells with downregulation of interferon-γ (IFN-γ) (Cheng et al. 2018). Moreover, IL-8 and SDF-1 that are secreted from CAFs recruit the tumor-associated macrophages and promote M2 polarization, resulting in poor prognosis (Zhang et al. 2019). However, various metabolites from CAFs indirectly increase the cytotoxic effect of $CD8^+$ T cells with upregulation of IL-21 and suppress the tumor growth in mouse model (Fu et al. 2017, Hermans et al. 2020).

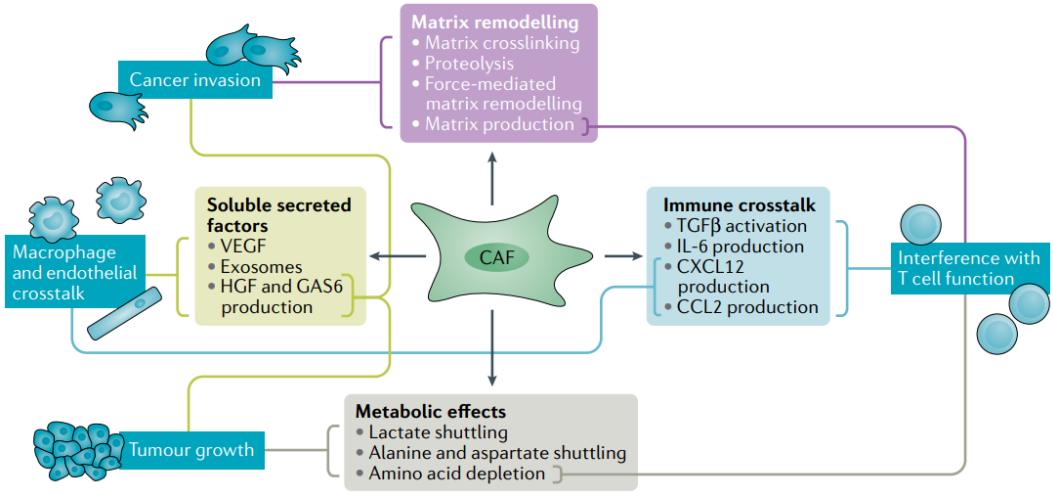

Figure 3. The effect of cytokines and metabolites from CAFs on cancerous and noncancerous cells (Sahai et al. 2020).

Lipid metabolism in tumor malignancy

Cancer cell-induced aerobic glycolysis and glucose restriction by irregular vasculature induce the glucose-deficient condition in tumor hostile microenvironment. Cancerous and non-cancerous cells are adapted to glucose-deficient condition and activate the lipid metabolism to compensate energy demand for proliferation and generate the pro-inflammatory cytokines including IL-1 and TNF-α (Van Cutsem and Arends 2005). Glucose deficiency activates the de novo lipid synthesis to rewire the lipid metabolism for the survival and growth of cancer cells. Among lipid components, the synthesis of cholesterol by long-chain acyl-CoA synthase 3 induces irregular mitochondrial function and is associated with poor prognosis in patients with prostate cancer (Migita et al. 2017). Additionally, hostile tumor microenvironment such as nutrient deficiency and hypoxia enhances the expression of CD36, lipid transporter. Its expression permits the entrance of lipids from extracellular into the cancer cells, and aggravates the tumor growth in patients with melanoma or breast cancer (Mwaikambo et al. 2009, Pascual et al. 2017). The main enzymes in lipid metabolism including fatty acid synthase (FASN), stearoyl-CoA desaturase (SCD), and sterol regulatory element-binding protein (SREBP) are activated in cancer cells by glucose deficiency, but not in complete medium (Munir et al. 2019). Under glucose-deficient conditions, SCD expression is significantly upregulated and induces the biosynthesis of fatty acids to

produce the energy, but not in complete medium (Holder et al. 2013, Peck et al. 2016).

These enzymes not only activate the lipid metabolism but also augment the tumor progression. By glucose deficiency and hypoxia, expressions of ATP-citrate lyase (ACLY), FASN, SCD, SREBP and fatty acid-binding proteins (FABPs) are dramatically increased in cancer cells and induce the lipogenesis and chemoresistance (Lewis et al. 2015). SREBP is a transcription factor regulating synthesis of fatty acid and cholesterol and is highly stained in malignant tumor tissues than normal ones (Furuta et al. 2008). However, loss of SREBP suppresses the size of spheroids and resistance to doxorubicin treatment (Lewis et al. 2015). SCD is an enzyme to convert unsaturated fatty acid to saturated fatty acid and augments the tumor progression (Li et al. 2017). Especially, biosynthesized unsaturated fatty acid by SCD promotes the proliferation, chemoresistance, and stemness of cancer cells through enhancement of Wnt, Hippo signaling (Flowers and Ntambi 2008, Noto et al. 2017). SCD expression activates the canonical Wnt/β-catenin pathway and is correlated with the stage of lung cancer patients (Noto et al. 2017). In bladder cancer, SCD expression is higher in CSC with stemness markers including Nanog, CD133, Oct4, and ALDH1 than parental one. Its expression enhances the resistance to pirarubicin and proliferation, but it is reversed by inhibition of the expression (Piao et al. 2019). However, inhibition of SCD suppresses the tumor growth and improves the sensitivity to anticancer therapies (Roongta

et al. 2011, Von Roemeling et al. 2013). Additionally, FASN, an oncogenic factor enhances the phosphorylation of Akt-signaling and cell cycles, leading to invasiveness in breast cancer (Menendez et al. 2004).

Lipid metabolism also promotes cancer stemness by activation of oncogenic factors (Yi et al. 2018). The number of cancer stem cells (CSC) is very small, but the cells are self-renewal, tumor initiation and resistance to anticancer therapies by advanced ATP-binding cassette (ABC) transporters (Begicevic and Falasca 2017). In contrast to non- stem cancer cells, higher expression of Nanog which the main regulator for cancer stem cell (CSC) initiates tumorigenesis by metabolic reprogramming from oxidative phosphorylation (OXPHOS) to fatty acid metabolism. Mechanistically, Nanog is conjugated with the promoter of PPAR and ACADVL and activates the lipid metabolism rather than OXPHOS in the mice model (Chen et al. 2016). Activation of lipid metabolism is beneficial in CSC by enhancement of fluidity and self-renewal growth compared to glycolysis (Corominas-Faja et al. 2014). However, inhibition of fatty acid oxidation suppresses the tumorigenesis in CSC (Wang et al. 2018). Compared to non-CSC, higher lipid amounts in CSC directly augment the Wnt pathway and population of CD133 positive cells and suppress the harmful lipid peroxidation (Bailey et al. 2015, Tirinato et al. 2015). Lipid desaturation is also essential in CSC to enhance the cell membrane and fluidity by NF-kB signaling and ALDH1, leading to division, metastasis, and signal transduction (Taraboletti et al. 1989, Li et al. 2017). Additionally, fatty acid oxidation is

strongly activated in CSC and enhances the pluripotency maintenance and PPAR activity by mitophagy, whereas the production of ROS is suppressed (Yi et al. 2018). However, inhibition of lipid metabolism in CSC by treatment of inhibitor for FASN, SCD, CD36 is promising anticancer therapy through suppression of CSC proliferation.

Furthermore, reprogrammed lipid metabolism critically affects the phenotype of immune cells in the tumor microenvironment. Activated lipid metabolism in M2 macrophages increases the secretion of IL-1β and encourages the enhancement of invasion and migration of cancer cells, but it is reversed by treatment of inhibitor for fatty acid oxidation (Zhang et al. 2018). Compared to normal macrophages, amounts of lipid are higher in tumor-associated macrophages (TAMs) by significant lipids transition through CD36, leading to activation of fatty acid oxidation. Treatment of Etomoxir, an inhibitor for fatty acid oxidation suppresses the phenotype of M2 TAM and tumor growth in the mice model (Su et al. 2020). Additionally, upregulation of AMPK by activation of lipid metabolism enhances the proliferation of Treg cells and Foxp3 expression (Michalek et al. 2011). Lipid metabolism enhances the population of IFN-ɣ$^{+}$ CD4^{+}T cells by c-Maf expression (Perucha et al. 2019). Differentiation from naïve T cells to IFN-ɣ$^{+}$CD4^{+} T cells is augmented according to activation of lipid metabolism (Haghikia et al. 2015). In B-cell lymphoma, activation of lipid metabolism partially enhances the function of natural killer (NK) cells such as IFN-ɣ production and mitochondrial membrane potential (Kobayashi et al. 2020).

Escape of immunosurveillance in tumor immune microenvironment

Within the tumor microenvironment, cancer cells escape the immunosurveillance by binding with inhibitory receptors in $CD8^+$ T cells such as programmed death-1 (PD-1) (Facciabene et al. 2012). Especially, regulatory T (Treg) cells inhibit the activity of antigen-presenting cells (APCs) and effector T cells including Th1 and $CD8^+$ T cells by cytotoxic T lymphocyte-associated antigen 4 (CTLA-4) and TGF-β (Li et al. 2020). Abundant IL-35, TGF-β in tumor microenvironment enhances the differentiation of Treg cells from naïve $CD4^+$ T cells, rather than other conventional ones (Turnis et al. 2016, Togashi et al. 2019). In general, $CD4^+CD25^+$ Treg cell prevents the autoimmune disease by attenuation of excessive immune self-tolerance (Sakaguchi et al. 2010). However, in tumor microenvironment, Treg cells assist the escape of cancer cells from immunosurveillance, resulting in enhancement of chemoresistance and tumor growth. On the surface of Treg cells, developed CD25, an IL-2 receptor is high affinity with IL-2 and impedes the availability of IL-2-mediated stimulation in conventional $CD4^+$ T cells, $CD8^+$ T cells and antigen-presenting cells (APCs) (Takahashi et al. 1998). Moreover, compared to control, deletion of TGF-β in Treg cells substantially augments the expression of IFN-ɣ, T-bet, GATA3, and IL-17 that are an indicator for effector T cells including Th1, Th2, and Th17 cells (Konkel et al. 2017). Additionally, cytotoxic T lymphocyte antigen 4 (CTLA-4) is highly expressed on the surface of Treg cells and mitigates the priming and

activation of effector T cells and APC function by conjugated with CD86 and CD80 (Perez et al. 1997). However, CTLA4-KO mice exhibit that populations of IFN-ɣ, IL-4 and IL-17 positive cells are higher than wild-type mice. Moreover, tumor growth is halted in CTLA4-KO mice within 3 weeks, but wild-type mice show significant growth (Wing et al. 2008).

In tumor mass, Th1 cells are positive to IFN-ɣ and produce cytokines including IL-2, IL-10, IFN-ɣ, and TNF-α for stimulation of $CD8^+$ T cells and M1 polarization (Cavalcanti et al. 2012). The secretion of IFN-ɣ from Th1 cells promotes C-X-C motif chemokine 9 (CXCL9), -10, and -11 in macrophage, leading to recruitment of $CD8^+$ T cells for cancer eradication. Additionally, the macrophages release the IL-6 and IL-1β that activate the function of Th1 cells (Haabeth et al. 2011). Th1 cells augment the anticancer immunity, thus, stimulation of the cells could improve the cancer-killing effect of $CD8^+$ T cells and NK cells. Notably, treatment of lenalidomide enhances the population of Th1 cells with upregulation of IFN-ɣ and T-bet expression that recruits the $CD8^+$ T cells in leukemia patients compared to non-treated ones (Aue et al. 2018).

In contrast to Th1 cells, pro-inflammation by Th2 cells increases the tumor growth. Thymic stromal lymphopoietin that is secreted from CAFs and DCs induces the differentiation from naïve T cells to Th2 cells. Subsequently, $GATA\text{-}3^+$ Th2 cells secret the IL-5 and IL-13 that activate the M2 polarization of TAM, resulting in tumor growth (Protti and De Monte 2012). Indeed, a poor prognosis is observed in patients with pancreatic cancer

according to a decrease of GATA-3/T-bet expression (De Monte et al. 2011). Moreover, enrichment of Th17 cells in tumor mass by immature myeloid cell-induced CCL17, CCL20, CCL22, and RANTES upregulates the tumor growth (Chen et al. 2012). Similar to Treg cells, TGF-β is also necessary to differentiate Th17 cells, but IL-6 and IL-21 are additionally required, unlike Treg cells. Naïve T cells are differentiated to RAR-related orphan receptor-ɣ$^{+}$ (Rorɣ) Th17 cells by IL-17, IL-21, and IL-23, and that increases the pro-inflammatory response (Najafi and Mirshafiey 2019). Bacteroides fragilis (ETBF) initiates the colon carcinogenesis in mouse model with upregulation of Th17 cells (Wu et al. 2009). In patients with hepatocellular carcinoma, the population of tumor-infiltrating Th17 cells is positively correlated with poor survival rate. CCR4 and CCR6 are highly expressed from Th17 cells and mediate the migration of those cells toward cancer cells for tumor progression (Zhang et al. 2009). However, published studies suggest that the high plasticity of Th17 cells could transdifferentiate to Th1 cells and assist in good prognosis in ovarian, prostate, lung cancer patients, but it is controversial (Wilke et al. 2011). In general, CD8^{+} T cells is killing the xenobiotic and mutated one by specific recognition of peptide (Jiang et al. 2015). However, cancer cells selectively express the inhibitory receptors including programmed death 1 (PD-1), TIM-3, and LAG3 that are binding with CD8^{+} T cells, leading to exhaustion and self-tolerance (Anderson et al. 2016). Thus, their targeted therapies such as neutralization antibodies and vaccination enhance the survival rate in cancer patients

(Maimela et al. 2019). Although anti-inhibitory receptors are good therapeutics, optimization of the appropriate dose and injection time in all age warrants further study. Additionally, the efficiency of anti-inhibitory receptor-aimed therapy is compelling in lymphoma and myeloid leukemia, but it is limited in solid tumors (Park 2017).

In addition, the polarization of M0 macrophages to M1 or M2 is determined according to the tumor microenvironment. The characterization of M1 and M2 is different. They are differentiated from M0 to M1 and M2 by treatment of granulocyte-macrophage colony-stimulating factor and macrophage colony-stimulating factor, respectively (Jaguin et al. 2013). M1 polarization inhibits the pro-inflammatory response and tumor growth with the secretion of cytokines including IL-12, TNF-α, CXCL-10, and IFN-ɣ, whereas M2 polarization produces the cytokines such as IL-10, IL-13, and IL-4 for immunosuppression, resulting in tumor progression (Lin et al. 2019). In contrast to M1 polarization, secretion of CCL2 is higher in M2 polarization and conjugates with CCR2 itself for production of IGF1, FOLR2, HTR2B, and SLC40A1, but a loss of CCR2 enhances the M1-related cytokines (Sierra-Filardi et al. 2014). Crosstalk between M2 macrophages and cancer cells augments the tumor invasion, survival, and extracellular matrix degradation by increased vascular endothelial growth factor (VEGF), matrix metalloproteinases (MMP), and epithelial-mesenchymal transition (EMT) (Lin et al. 2019). Cytokines from M2 polarization increase the expressions of snail and NF-kB signaling in breast cancer cells, leading to tumor growth

and metastasis (Wu et al. 2009). Thus, the agents to suppress the M2 polarization could be a good approach for anticancer therapy. For example, zoledronic acid (ZA) treatment induces the repolarization from M2 to M1 with downregulation of VEGF, CD31, and CD11b in TAM (Coscia et al. 2010). In 1803 breast and colorectal cancer patients, administration of ZA enhances the therapeutics of anastrozole and tamoxifen that substantially increases the survival rate and disease-free survival (Gnant et al. 2011).

Summary

Within a hostile tumor microenvironment, glucose deficiency induces the lipid metabolic reprogramming and promotion of tumor malignancy. Under the glucose-deficient conditions, cancer cells augment the stemness and resistance to anticancer therapies. Moreover, compared to counterparts, the activity of lipid metabolism is higher in CAFs and TILs. However, the effect of glucose deficiency on metabolic reprogramming in cancer cells, CAFs, and TILs have not been delineated. We investigated that how glucose deficiency-induced metabolic alteration affects the phenotypes of cancer cells, CAFs, and TILs. Particularly, we focused on lipid metabolic reprogramming which was activated by glucose-deficient condition.

CHAPTER I.

Glucose deficiency enhanced the drug resistance by upregulation of mitochondrial MDR1

Abstract

Chapter I elucidated the enhancement of resistance for metformin in cancer cells under glucose-deficient conditions with underlying mechanisms.

Within a hostile tumor microenvironment, cancer cells are hijacking the glucose amounts, resulting in glucose-deficient conditions. It augments the malignancy such as stemness, drug resistance and epithelial-mesenchymal transition (EMT). However, the effect of glucose deficiency in human malignant mesothelioma (HMM) cells had not been investigated. Moreover, Metformin is a type 2 diabetes drug and is treated in patients with numerous types of cancer, but it is not affected on HMM patients.

In this chapter, we demonstrated that glucose starvation-induced drug resistance in cancer cells with upregulation of multi-drug resistance protein 1 (MDR1). Compared to normal cells, cancer cells were survived and adapted in glucose-deficient conditions. In both cancer cells, glucose-deficient condition induces the resistance to metformin with upregulation of mitochondrial multidrug resistance protein 1 (MDR1) in cancer cells. These cells showed aberrant mitochondrial function including ATP synthesis, morphological elongation, and hyperpolarization of mitochondrial membrane potential (MMP). Increased MDR1 was abolished by treatment with carbonyl cyanide m-chlorophenyl hydrazine (CCCP) which is MMP depolarization inducer. Under glucose-deficient conditions, apoptosis and autophagy were significantly enhanced in MDR1 knockout (KO) cells by treatment with metformin. Collectively, our study demonstrated MDR1-targeting could improve the therapeutic efficacy of metformin.

Introduction.

The tumor microenvironment, which includes glucose starvation, hypoxia, and acidic conditions, is a distinctive feature of tumor masses and is generated by the abnormal tumor vasculature causing malignancy (Tredan et al. 2007, Wang and Youle 2009, Yeom et al. 2012, Hu et al. 2016). Adapted cancer cells to the tumor microenvironment show metabolism alteration that leads to their survival and enhances chemoresistance, which is the main obstacle to cancer therapy (Liu et al. 2003, Sun et al. 2012, Lee 2014, Nishimoto et al. 2014, Visioli et al. 2014, De Palma et al. 2017). Several mechanisms have been suggested for chemoresistance, such as protection against DNA damage, anti-apoptosis, the overexpression of drug transporters, and the existence of cancer stem cells (van Dijk et al. 2012, Lee 2014). Particularly, multidrug resistance protein 1 (MDR1), an ATP-binding cassette (ABC) transporter, effluxes xenobiotics from cells and is highly expressed in cancer cells that are resistant to chemotherapy (Abolhoda et al. 1999, Vasiliou et al. 2009). The regulation of MDR1 expression level is an important strategy for decreasing the cancer cells' resistance to anticancer drugs. The effects and mechanism of glucose starvation in the context of chemoresistance of cancer cells are largely unknown.

Glucose is metabolized mainly in mitochondria, which is essential for generating energy for cell proliferation. Glucose starvation disturbs mitochondria function and changes the cellular phenotype (Liu et al. 2003,

Mammucari and Rizzuto 2010, Masgras et al. 2012, Wappler et al. 2013). Under glucose deficient conditions, autophagy provides energy to sustain cellular metabolism and is considered a hindrance to cancer therapy that disturbs cellular physiology (Degenhardt et al. 2006, Yang et al. 2011). In contrast that excessive autophagy contributes to cell death, which is considered to be a target for effective cancer therapy (Kroemer and Levine 2008).

Human malignant mesothelioma (HMM) is an aggressive tumor that is closely associated with exposure to asbestos fibers approximately 20-40 years prior to tumorigenesis. HMM patients present poor therapeutic due to traditional anticancer drug resistance such as cisplatin and pemetrexed (Robinson et al. 2005). Metformin, which is commonly used for the management of type II diabetes mellitus, has been suggested as an alternative anticancer drug (Eikawa et al. 2015, Shimazu et al. 2017). Recent studies have shown a potential therapeutic value of metformin in HMM cells, which is exerted through the inhibition of mTOR and cell cycle arrest (Shimazu et al. 2017). However, metformin treatment causes resistance in human breast cancer cells, although the precise mechanism was not elucidated (Qu et al. 2014). Expanding our understanding of the mechanism of drug resistance is urgently needed to improve poor prognosis in cancer patients and to develop effective therapeutic strategies.

The present study was performed to determine the impact of glucose deficiency on the development of resistance to metformin and the

underlying mechanism in HMM cells. The results of the present study suggest that glucose starvation enhances drug resistance in HMM cells via mitochondrial MDR1 elevation. The identification of the mechanism associated with enhanced resistance to metformin will be valuable for improving therapeutic efficacy in cancer patients.

Materials and Methods

Cell lines and culture conditions

The HMM cell lines MS1 and NIH-513 (H513) were kindly provided by Dr. Jablons (University of California San Francisco, San Francisco, CA, USA) and Dr. R. Kratzke (University of Minnesota, Minnesota, MN, USA), respectively. Met-5A benign transformed mesothelial cells were purchased from the ATCC (Manassas, VA, USA). These mesothelial cell lines were cultured as described previously (Kim et al. 2018), and various concentrations of glucose (0, 1, 5, and 10 mmol/L) were added to the medium.

Cell proliferation and viability assay

Cell viability was evaluated by using an MTT assay (Sigma-Aldrich, St. Louis, MO, USA). Briefly, MTT solution (MTT dissolved in PBS, 5 mg/mL) was added to each well and incubated for 1 hour at 37°C. Subsequently, each well was treated with 100 mL of a solution that contained DMSO (Sigma-Aldrich) and 2-propanol (Millipore, Billerica, MA, USA) at a 9:1 ratio and absorbance was measured at a wavelength of 570 nm using a microplate reader (BioTek Epoch, Izasa, Barcelona, Spain). For the cell proliferation assay, 5 × 104 cells were seeded in 6-well plates and incubated in conditioned medium with glucose concentrations ranging from 0 to 10 mmol/L for 3 days. The surviving cells on each day were counted manually

under a light microscope.

Apoptosis assay

The apoptosis assay was performed using an EzWay Annexin V-FITC Apoptosis Detection Kit (Koma Biotech, Seoul, Korea). Annexin V reagent was added to harvested cells and incubated for 15 minutes in the dark. After washing, the cells were incubated in 1× binding buffer containing propidium iodide (PI). The stained cells were immediately analyzed by flow cytometry (Becton Dickinson, Mountain View, CA, USA). Total apoptosis included late (positive for Annexin and PI) and early (positive for Annexin and negative for PI) apoptotic cells.

Western blotting assay

The cells were lysed using EzRIPA buffer (ATTO, Tokyo, Japan). The lysate protein concentration was quantified by a Bradford assay (BioRad, Hercules, CA, USA) and measured using a BioTek Epoch Microplate Reader. Twenty micrograms of protein were subjected to 10%-15% sodium dodecyl sulfate-polyacrylamide gel electrophoresis and transferred to a nitrocellulose membrane (Amersham, GE Healthcare, Barcelona, Spain) using the electrophoretic method. The membrane was blocked by a PBS-T solution which contained 5% skim milk for 60 minutes at room temperature. The primary antibodies, PINK1 (Novus Biologicals, Littleton, CO USA), phosphorylated AMPK (Cell-Signaling Technology, Boston, MA, USA), MDR1 (Santa Cruz Biotechnology, CA, USA), and β-actin (Cell-Signaling Technology) were diluted 1:1000 in blocking solution (PBS-T with 4% BSA)

and incubated overnight at 4°C. The secondary HRP-conjugated anti-rabbit (Santa Cruz Biotechnology) and anti-mouse (Santa Cruz Biotechnology) antibodies were used at a dilution of 1:1000 in blocking solution for 2 hours. Protein expression was detected by a chemiluminescence imaging system (ATTO) after spreading the Luminata Forte Western HRP Substrate (Millipore).

Subcellular fractionation assay

Subcellular fractionation of the cytoplasm, mitochondria and nucleus was achieved using a fractionation kit (Abcam, Burlingame, CA, USA) according to the manufacturer's recommendations. Alpha-tubulin (Santa Cruz Biotechnology), COX IV (Abcam) and Lamin A/C (Santa Cruz Biotechnology) were used as endogenous control markers for the cytoplasm, mitochondria and nucleus, respectively.

Quantitative real-time PCR

Total RNA was extracted using TRIzol LS Reagent (Ambion, Austin, TX, USA) and quantitation was performed using a BioTek Epoch Microplate Spectrophotometer (Izasa, Barcelona, Spain). A total of 1000 ng of RNA was subjected to cDNA synthesis using a QuantiTect Reverse Transcription Kit (Enzynomics, Seoul, South Korea). An SYBR Green RT-PCR Kit (Enzynomics) was used for gene expression analysis. The primer sequences are presented in Table 1. The relative changes in gene expression levels were normalized to 18S rRNA and calculated using the ΔΔC t method (Rao et al.

2013).

Autophagy detection

The autophagy activity was assessed using a Cyto-ID Autophagy detection kit (Enzo Life Sciences, Farmingdale, NY, USA). Briefly, the Cyto-ID Autophagy Detection Reagent was added to the cell pellet, and incubated for 30 minutes at 37°C protected from light and analyzed using flow cytometry (Becton Dickinson).

Immunofluorescence assay

Human malignant mesothelioma cells were seeded in 8-well chamber slides (SPL Life Sciences, Pocheon, Korea) and incubated with MitoTracker Deep Red (Molecular Probes, Eugene, OR, USA) for 30 minutes in the dark. Fixation, permeabilization and blocking were carried out using 4% paraformaldehyde (Millipore), 0.1% Triton X-100 (Amresco, Solon, OH, USA) and blocking solution (BSA 3% in PBS with 0.1% Tween-20 [PBST]) for 15, 10 and 30 minutes, respectively. After washing with PBS, Mdr1 antibody was added in blocking solution and incubated overnight at 4°C. Subsequently, the Alexa Fluor 488-conjugated anti-mouse secondary antibody (Molecular Probes) was added in blocking solution and incubated for 2 hours in the dark. In addition, nuclear was stained using DAPI (Molecular Probes). Fluorescence images were captured using an LSM710 confocal laser scanning microscope (CLSM; Carl Zeiss, Göttingen, Germany) and analyzed

using LAS AF Lite software (Leica, Wetzlar, Germany).

Transmission electron microscopy

Cell pellets were immersed in Karnovsky's solution (2% glutaraldehyde, 0.05 mol/L cacodylate, 2% paraformaldehyde and distilled water) and incubated overnight (Morris 1965). After washing with 0.05 mol/L sodium cacodylate buffer, the cells were subjected to post-fixation using 2% osmium tetroxide for 2 hours, followed by washing in distilled water. For fixation, 0.5% uranyl acetate was added, and the cells were then washed with ethanol. Propylene oxide was added to the pellet for transition. For infiltration, the cells were incubated in propylene oxide and Spurr's resin mixed at a 1:1 ratio for 2 hours at room temperature. For solidification, the solution was replaced with fresh Spurr's resin and incubated at 70°C overnight. After thin sectioning using an ultramicrotome (MT-X; RMC, Tucson, AZ, USA), the intracellular organelles morphology was examined using a JEM 1010 transmission electron microscope (JEOL, Tokyo, Japan).

Assessment of mitochondrial function

The cellular level of ATP was measured using the ATP Colorimetric/Fluorometric Assay Kit (BioVision, Milpitas, CA, USA), according to the manufacturer's recommendations. Briefly, a mixture of ATP assay buffer, probe, converter and developer was added to the cell lysate obtained from 1×10^6 cells. In addition, the resulting absorbance was measured at a wavelength of 570 nm using a microplate reader (BioTek

Epoch) and calculated using a standard curve.

Mitochondrial membrane potential was evaluated using 5,5′,6,6′-tetrachloro-1,1′, 3,3′-tetraethylbenzimidazolylcarbocyanine iodide; JC-1, Molecular Probes). HMM cells were treated with 2.5 μmol/L JC-1 solution and incubated at 37°C for 30 minutes in the dark. Subsequently, MMP was analyzed by flow cytometry (Becton Dickinson), and compartmentalized as green and red in a dot plot. As depolarization control, 50 μmol/L carbonyl cyanide m-chlorophenyl hydrazone (CCCP) was added to the cells prior to JC-1 treatment. Using the depolarization baseline with red/green ratio decreased by CCCP treatment, the MMP data were normalized.

Production of knockout cells using the clustered regulated interspaced short palindromic repeats/Cas9 technique

Human malignant mesothelioma cells were transfected with 2 μg of MDR1 CRISPR/Cas9 KO plasmids containing a GFP-coding region and either control or MDR1 (Table 1; Santa Cruz Biotechnology) using the HiPerFect Transfection Reagent (Qiagen, Hilden, Germany) following the manufacturer's recommendations. GFP-positive cells were selectively collected by using a BD Aria III cell sorter (BD Biosciences Clontech, Palo Alto, CA, USA) 3 days post–transfection. The knockout efficiency for the target gene was verified by real-time RT-PCR for MDR1.

Statistical analysis

The experiments described above were performed independently at least 3 times. Data were expressed as the mean ± SD. GraphPad Prism Software

(GraphPad Software) was used for all graphs and statistical analysis. Tukey's pairwise comparison and one-way ANOVA were applied for comparisons between groups. Statistical significance was accepted at $P < 0.05$.

Table 1. Primer sequence, PINK1, MDR1, ABCG2 and GAPDH for quantitative of Real time RT-PCR. CRISPR/Cas9 MDR1 sgRNA sequence

Name		Sequence
PINK1	Forward	5'-TAC CAG TGC ACC AGG AGA AG -3'
	Reverse	5'-GCT TGG GAC CTC TCT TGG AT -3'
MDR1	Forward	5'-GCC TGG CAG CTG GAA GAC AAA TAC -3'
	Reverse	5'-AGA CAG CAG CTG ACA GTC CAA-3'
ABCG2	Forward	5'- GGG TTC TCT TCT TCT GAC GAC C-3'
	Reverse	5'-TGG TTG TGA GAT TGA CCA ACA GAC C-3'
18S rRNA	Forward	5'-GGC CCT GTA ATT GGA ATG AGT C-3'
	Reverse	5'-CCA AGA TCC AAC TAC GAG CTT-3
MDR1	sgRNA	GAA GCT AAC CCT TGT GAT TT

Results

Survived human malignant mesothelioma cells under glucose-starved conditions desensitized against to metformin treatment

To assess the impact of glucose concentration on cell proliferation, the MS1, H513 and Met-5A cell lines were cultured in conditioned medium containing 0, 1, 5 and 10 mmol/L glucose. The proliferation of human malignant mesothelioma (HMM) cells was decreased in medium with 0 and 1 mmol/L glucose (Fig. 1 A), while the number of cells increased in medium with 5 and 10 mmol/L glucose. Met-5A cells cultured under glucose-deficient conditions did not survive after 3 days. In contrast, the HMM cell lines, MS1 and H513, survived under glucose-deficient conditions. These results demonstrated that glucose is essential for cell proliferation and that HMM cells have a distinct capacity for survival under glucose starved conditions compared to benign mesothelial cells. Human malignant mesothelioma cells were precultured in medium with 0, 1, 5 and 10 mmol/L glucose for 2 days, followed by treatment with 5 mmol/L metformin for 1 day. The viability of HMM cells cultured with 5 and 10 mmol/L glucose was significantly decreased by metformin treatment, but this feature was minimally affected in HMM cells precultured under glucose-deficient conditions (Fig. 1 B, C). To determine glucose starvation-enhanced metformin resistance, HMM cells were precultured in medium containing different concentrations of glucose for 2 days, replated with identical numbers of cells and treated with metformin for 1 day. HMM cells precultured in medium with 5 or 10 mmol/L

glucose exhibited a significant reduction of cell viability compared to 0 or 1 mmol/L glucose (Fig. 1 D, E). These data revealed that adapted HMM cells to glucose-deficient conditions acquired greater resistance to metformin than did cells cultured under glucose abundant conditions.

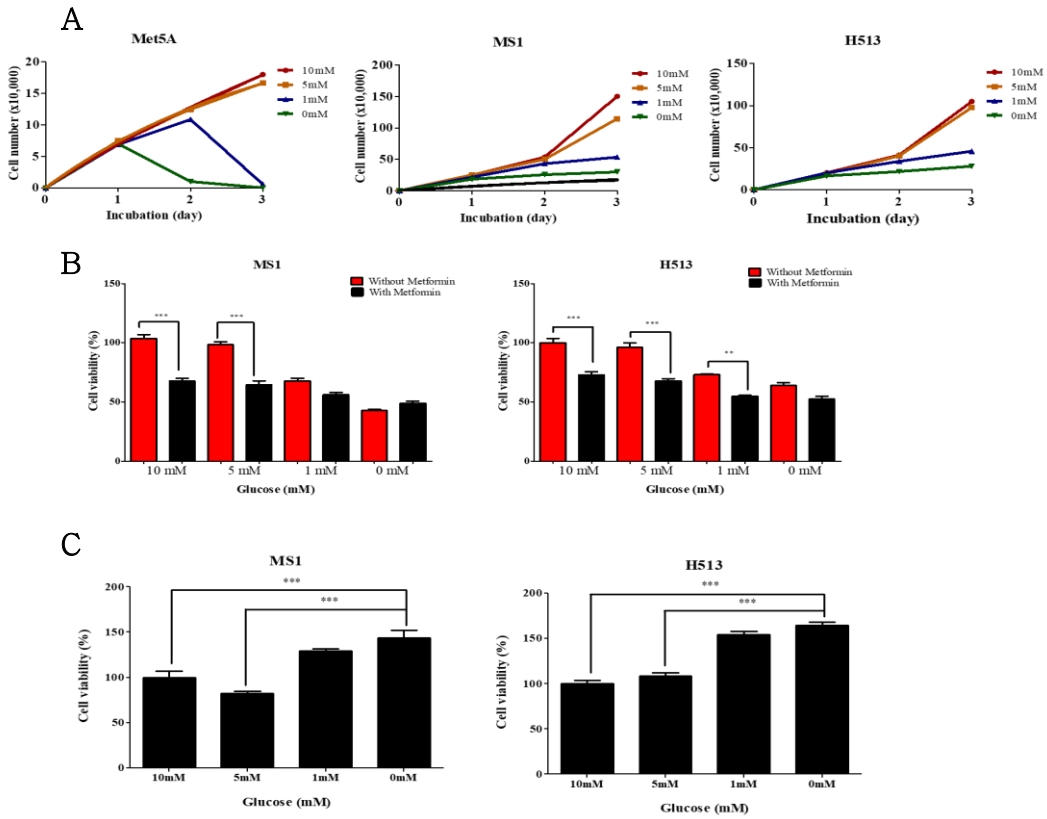

Figure 1. Assessment of glucose concentration effect in cell proliferation and metformin resistance

(A) Proliferation of human malignant mesothelioma cells under each glucose concentration contained medium was measured for 3 d by macroscopic analysis. (B, C) MS1 and H513 cells were cultured in medium containing the various concentrations of glucose for 2 d and subsequently treated with 5 mmol/L of metformin for 1 d. Red column: metformin nontreatment. Black column: 5 mmol/L metformin treatment. (D, E) MS1 and H513 cells incubated in the various concentrations of glucose for 2 d were replated same number and treated 5 mmol/L metformin for 1 d. All error bars indicate the SEM with n = 8. Significant differences are indicated by $^{**}P < 0.01$, and $^{***}P < 0.001$.

Treatment of human malignant mesothelioma cells cultured under glucose starvation with metformin suppressed apoptosis and autophagy

Total apoptosis was suppressed by metformin treatment in HMM cells cultured under glucose-deficient conditions. In contrast, glucose starvation or metformin treatment increased the total apoptosis ratio (Fig. 2 A). Furthermore, either metformin treatment or glucose starvation increased the expression of cleaved Parp-1 (Fig. 2 B). However, the treatment of glucose-starved HMM cells with metformin significantly reduced the expression of cleaved Parp-1 compared to those cells cultured in complete medium. In line with that, autophagic activity was increased by glucose starvation or metformin treatment (Fig. 2 C). In contrast, the treatment of glucose-starved HMM cells with metformin significantly suppressed autophagic activity compared to those cells cultured in complete medium. The expression of LC3B, p-AMPK and AMPK was increased by either glucose starvation or metformin treatment in HMM cells (Fig. 2 D). However, that was decreased in the treatment of glucose-starved HMM cells with metformin. In addition, mTOR expression was decreased by either glucose starvation or metformin treatment in MS1.

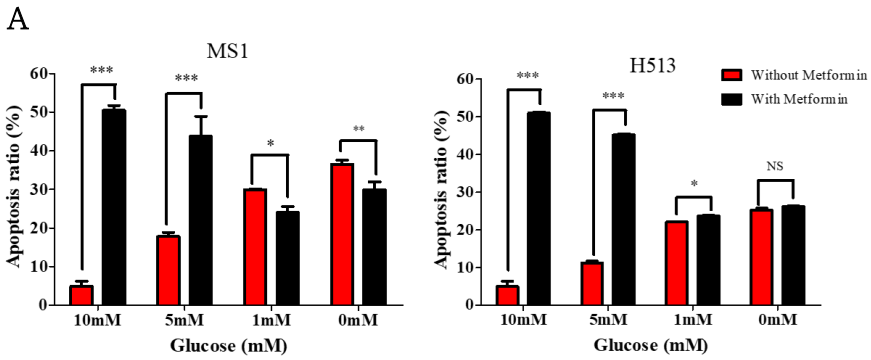
A
MS1
H513
Without Metformin
With Metformin
Apoptosis ratio (%)
Glucose (mM)
10mM
5mM
1mM
0mM
***
**
*
NS

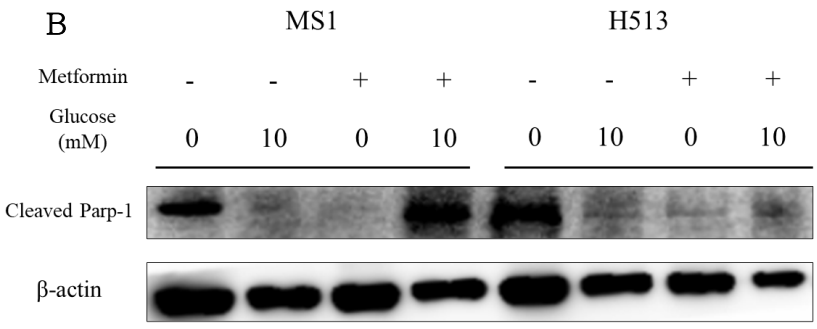
B
MS1
H513
Metformin
Glucose (mM)
Cleaved Parp-1
β-actin

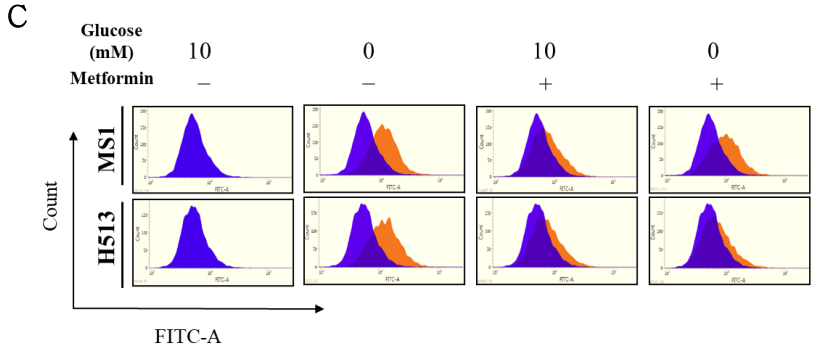
C
Glucose (mM)
Metformin
MS1
H513
Count
FITC-A

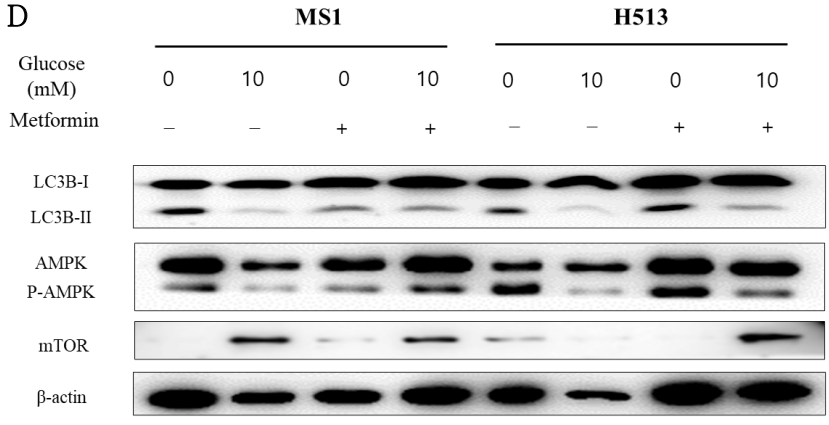
D
MS1
H513
Glucose (mM)
Metformin
LC3B-I
LC3B-II
AMPK
P-AMPK
mTOR
β-actin

Figure 2. Glucose starvation and/or metformin treatment regulated apoptosis and autophagy

(A) Total apoptosis in human malignant mesothelioma cells cultured under each glucose concentration containing medium and/or 5 mmol/L metformin treatment are presented. All error bars represent SEM with n = 3. Significant differences are indicated by $^{*}P < 0.05$, $^{**}P < 0.01$, and $^{***}P < 0.001$. (B) Western blot analyses of the expression of cleaved Parp-1 and β-actin. (C) Autophagy activity was assessed by flow cytometry. Blue: 10 mmol/L glucose. Orange: each glucose concentration and/or 5 mmol/L metformin treatment. (D) Autophagy indicated molecules, LC3B, AMPK, p-AMPK, mTOR and β-actin; expression was confirmed by western blot assay

MDR1 is significantly elevated in mitochondria of glucose-starved HMM cells by treatment with metformin

The treatment of glucose-starved HMM cells with metformin increased the mRNA expression of MDR1 and ABCG2 (Fig. 3 A, B). In particular, MDR1 mRNA expression in glucose-starved cells with metformin treatment was approximately 10-fold higher than those cells cultured in complete medium. To determine Mdr1 expression in subcellular fractions, the cytoplasm, nucleus and mitochondria were isolated. The expression level of membrane Mdr1 was not significantly altered by glucose content or metformin treatment (Fig. 4 A). In MS1 cells, the majority of Mdr1 expression was found in the mitochondria and minimal expression was found in the nuclear and cytoplasmic fractions. In addition, mitochondrial Mdr1 expression was significantly increased in the treatment of glucose-starved conditions with metformin (Fig. 3 C, D). These results suggested that the treatment of glucose-starved HMM cells with metformin elevated Mdr1 expression exclusively in fractionated mitochondria. In H513 cells, however, Mdr1 was found in all subcellular fractions, although substantial enrichment in the mitochondrial and nuclear fractions was observed under glucose-starved conditions. Previous research reported that MDR1 is increased in hepatocellular carcinoma cells with mitochondrial defects (Ling et al. 2010). Moreover, dependent on glucose content decreasing and metformin treatment, the mRNA expression of MDR1 and PINK1 showed positive correlation (Fig. 4 B). The Mdr1 fluorescence in glucose-starved MS1 cells

with metformin treatment was significantly increased and exhibited co-localization with MitoTracker (Fig. 3 E). However, the Mdr1 expression in HMM cells cultured in complete medium was unchanged by metformin treatment. In addition, mitotracker expression increasing which was a mitochondria damage indicator was detected in HMM cells cultured under glucose starvation and metformin treatment compared to those HMM cells cultured in complete medium (Fig. 4 C).

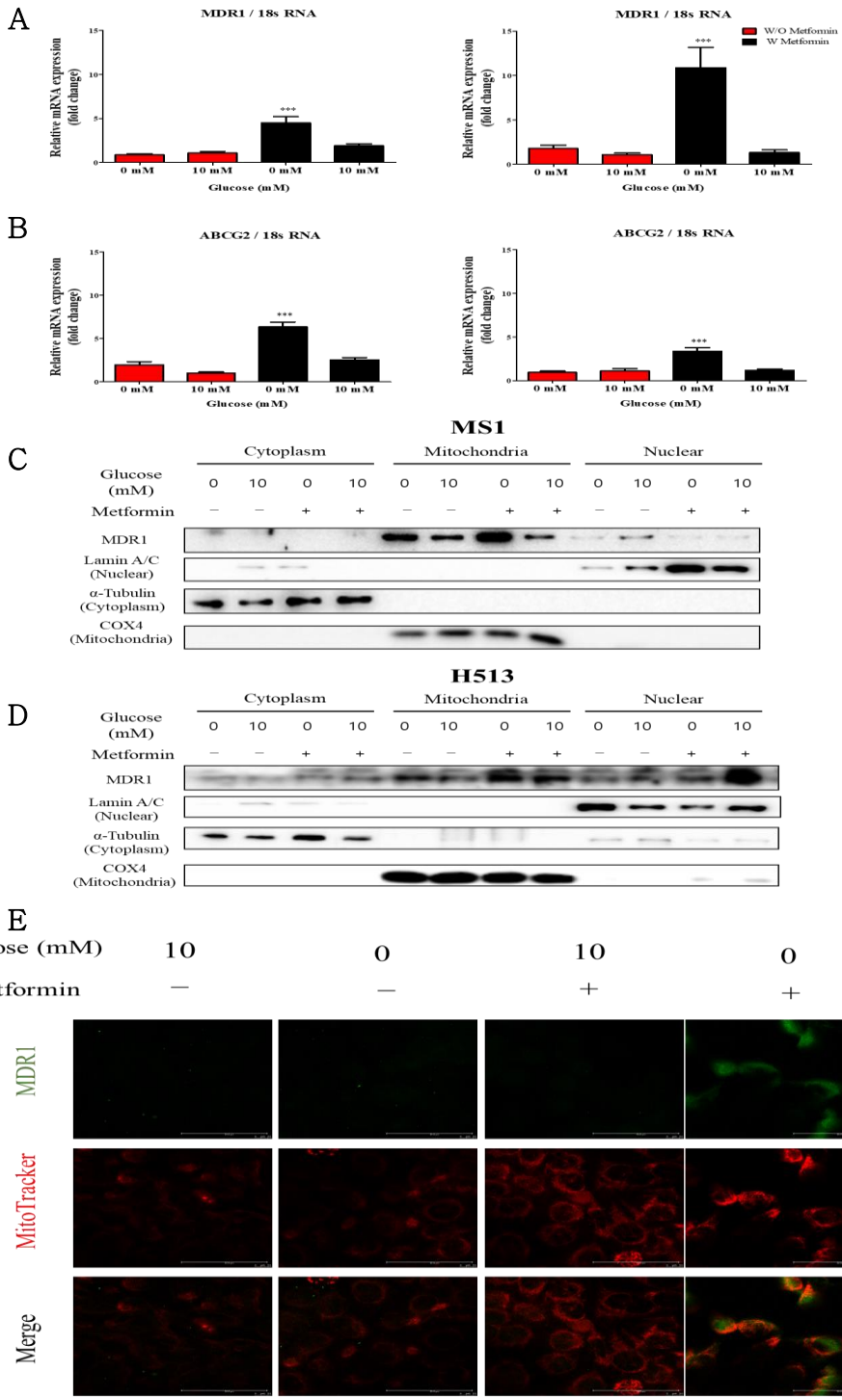
A
MDR1 / 18s RNA
Relative mRNA expression (fold change)
Glucose (mM)
0 mM
10 mM
0 mM
10 mM
***
W/O Metformin
W Metformin
B
ABCG2 / 18s RNA
C
MS1
Cytoplasm
Mitochondria
Nuclear
Glucose (mM)
Metformin
MDR1
Lamin A/C (Nuclear)
α-Tubulin (Cytoplasm)
COX4 (Mitochondria)
D
H513
E
Glucose (mM)
Metformin
MDR1
MitoTracker
Merge

Figure 3. Regulation of drug-related molecule expression by glucose concentration and/or metformin treatment

(A, B) The mRNA expression of multidrug resistance protein 1 (MDR1) and ATP-binding cassette sub-family G member 2 expression was measured in MS1 and H513 cells. Significance: $^{*}P < 0.05$, $^{**}P < 0.01$, and $^{***}P < 0.001$. Each data represents the mean ± SEM (n = 4). (C, D) Western blot analysis of Mdr1 expression from mitochondria, cytoplasmic and nuclear fractions. The α-tubulin, COXIV and Lamin A/C were used for normalization of cytoplasmic, mitochondria and nuclear fractions. (E) Immunofluorescence of MDR1 and mitotracker in MS1 was exhibited by confocal laser scanning microscope. The Mdr1 and mitotracker expressed green and red fluorescence.

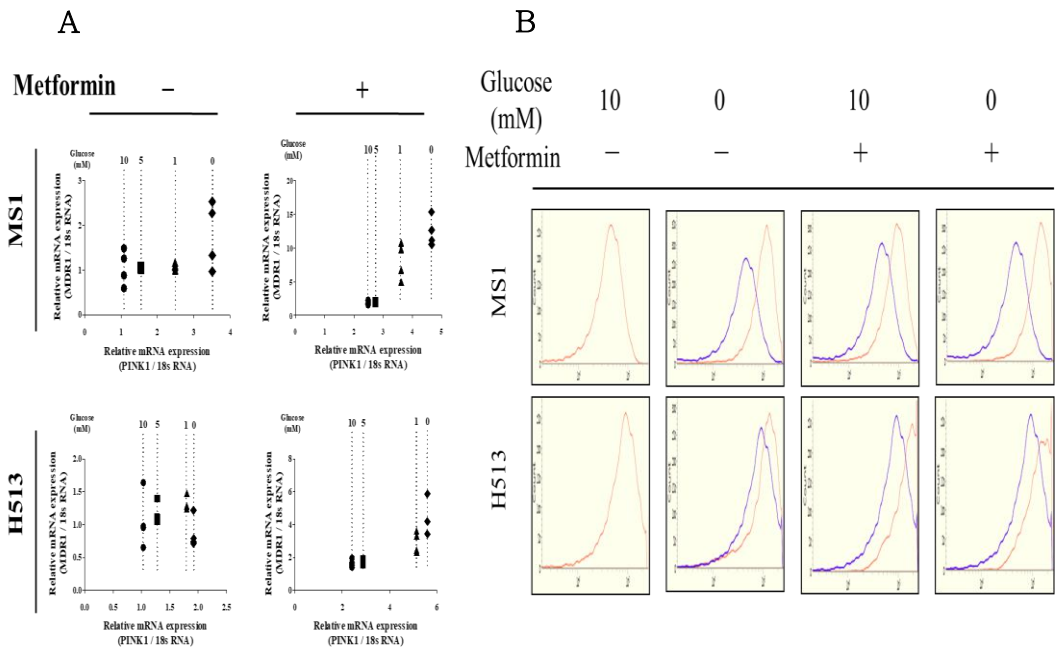

Figure 4. Identification of the relationship between mitochondrial damage and MDR1 expression

(A) The fold changes in mRNA expression of MDR1 and PINK1 in HMM cells cultured under each glucose concentration and/or metformin treatment was presented. The X-axis indicates PINK1 expression normalized to 18S rRNA, and the Y-axis shows MDR1 expression normalized to 18S rRNA. (B) The MitoTracker intensity was measured in HMM cells by glucose concentration and/or 5 mM metformin treatment. Blue: 10 mM glucose-containing medium, Orange: each glucose concentration and/or metformin treatment.

Dysfunctional mitochondria induced by glucose starvation and/or metformin treatment

To further examine the mitochondria integrity, the expression of Pink1, a mitochondrial damage marker, was measured. The expression of Pink1 was increased by glucose starvation and/or metformin treatment (Fig. 5 A). Moreover, ATP synthesis was assessed in HMM cells cultured under glucose starvation and/or metformin treatment. The ATP level was decreased by either glucose starvation or metformin treatment in HMM cells (Fig. 5 B). The ATP level in the treatment of glucose-starved HMM cells with metformin was lower than 4-fold compared to those HMM cells cultured in complete medium. To evaluate the mitochondrial ultrastructure, TEM was performed. Intriguingly, elongated mitochondria with condensed cristae were observed in glucose-starved HMM cells with metformin treatment (Fig 5 C). In the mPTP assay, the FITC intensity was significantly increased in HMM cells cultured under glucose-starved conditions or metformin treatment, but not in glucose-starved HMM cells with metformin treatment (Fig. 5 D). Metformin treatment induced the depolarization of the MMP, but glucose starvation alone did not affect the MMP. In contrast, the treatment of glucose-starved HMM cells with metformin induced MMP hyperpolarization, especially in MS1 cells (Fig. 5 E, F). Mitochondrial membrane potential regulated protein import in mitochondria (Jin et al. 2010). Therefore, to determine the MMP hyperpolarization in the treatment of glucose-starved HMM cells with metformin-regulated mitochondrial Mdr1

expression, 5 μmol/L CCCP was treated for 3 days. CCCP treatment suppressed the increased MMP and Mdr1 expression in mitochondria of HMM cells cultured under glucose starvation with metformin (Fig. 5 G).

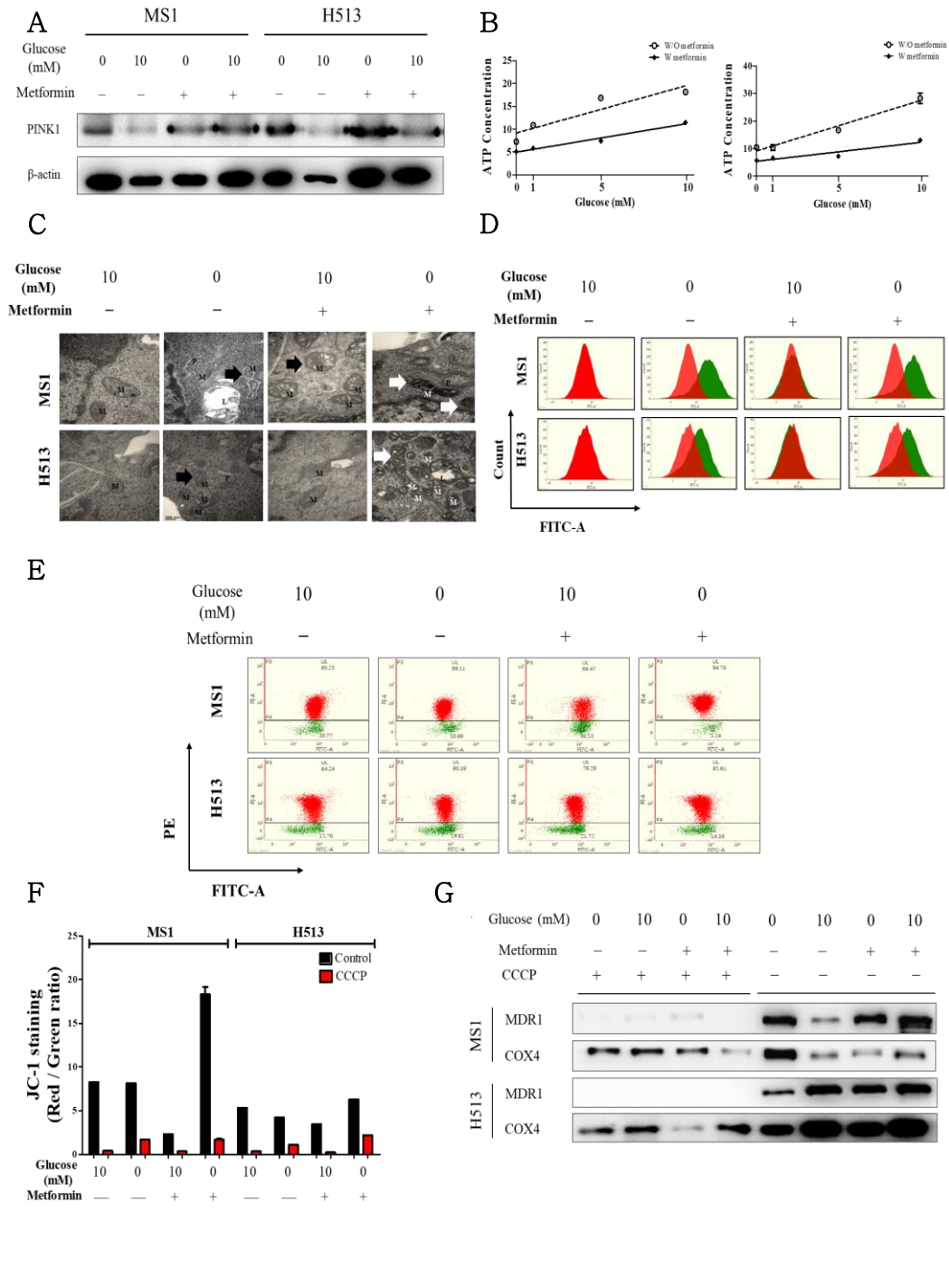
A
MS1
H513
Glucose (mM)
0 10 0 10 0 10 0 10
Metformin
– – + + – – + +
PINK1
β-actin
B
W/O metformin
W metformin
ATP Concentration
Glucose (mM)
C
Glucose (mM)
10 0 10 0
Metformin
– – + +
MS1
H513
D
Glucose (mM)
10 0 10 0
Metformin
– – + +
MS1
H513
Count
FITC-A
E
Glucose (mM)
10 0 10 0
Metformin
– – + +
MS1
H513
PE
FITC-A
F
MS1
H513
Control
CCCP
JC-1 staining (Red / Green ratio)
Glucose (mM)
10 0 10 0 10 0 10 0
Metformin
— — + + — — + +
G
Glucose (mM)
0 10 0 10 0 10 0 10
Metformin
– – + + – – + +
CCCP
+ + + + – – – –
MS1
MDR1
COX4
H513
MDR1
COX4

Figure 5. Mitochondrial dysfunction and morphological alteration in glucose-starved HMM cells in cases treated or not treated with metformin

(A) The expression of Pink1 and β-actin expression was assessed by western blot assay. (B) Adenosine triphosphate (ATP) generation was measured in MS1 and H513 cells. (C) Cellular morphological alteration was detected by transmission electron microscopy assay which is usually performed to classify the intracellular organelle morphology. L, lysosome; M, mitochondria; N, nuclear; P, phagophore. (D) The mitochondrial permeability transition pore assay was performed in HMM cells cultured under glucose-starved condition and/or 5 mmol/L metformin treatment by flow cytometry. Red: 10 mmol/L glucose. Green: each glucose concentration contained medium and/or 5 mmol/L metformin treatment. (E) Analysis of the mitochondrial membrane potential (MMP) by flow cytometry in HMM cells cultured under glucose starvation and/or 5 mmol/L metformin treatment. Data were normalized with the red/green ratio result of MMP depolarization induced by 50-μm carbonyl cyanide m-chlorophenyl hydrazine (CCCP) treatment used as positive control. The green part increasing compared to the red portion indicates hyperpolarization. (F) The ratio of red to green is presented. The red and black columns show incubation with or without 5 mmol/L CCCP for 3 d. All error bars represent SEM with (n = 3). (G) The expression of Mdr1 in mitochondria with or without 5 mmol/L CCCP was measured by a western blotting assay in HMM cells cultured with glucose starvation and/or 5 mmol/L metformin treatment.

MDR1 regulates chemoresistance under glucose-starved conditions

To evaluate whether MDR1 is directly mediated metformin resistance in glucose-starved HMM cells, MDR1 was knocked out using the CRISPR/CAS9 system. The MDR1 gene was significantly decreased close to zero in MDR1 knockout (KO) HMM cells compared with control cells (Fig. 6 A). The viability of the MDR1 KO HMM cells was similar to those of the parental cells. In contrast to the parental HMM cells, the treatment of glucose-starved MDR1 KO HMM cells with metformin induced a significant reduction of viability (Fig. 6 B). Apoptosis and autophagy assays were performed to assess cell death pathways that were regulated by MDR1. Compared to those of the control, increased apoptosis was found in the glucose-starved MDR1 KO HMM cells by metformin treatment (Fig. 6 C). The autophagic response was increased in metformin treatment against glucose-starved MDR1 KO cells, while this response was decreased in the control cells (Fig. 6 D). However, a consistent level of autophagy was exhibited in MDR1 KO HMM cells cultured under glucose starvation or metformin treatment compared to those of the parental cells.

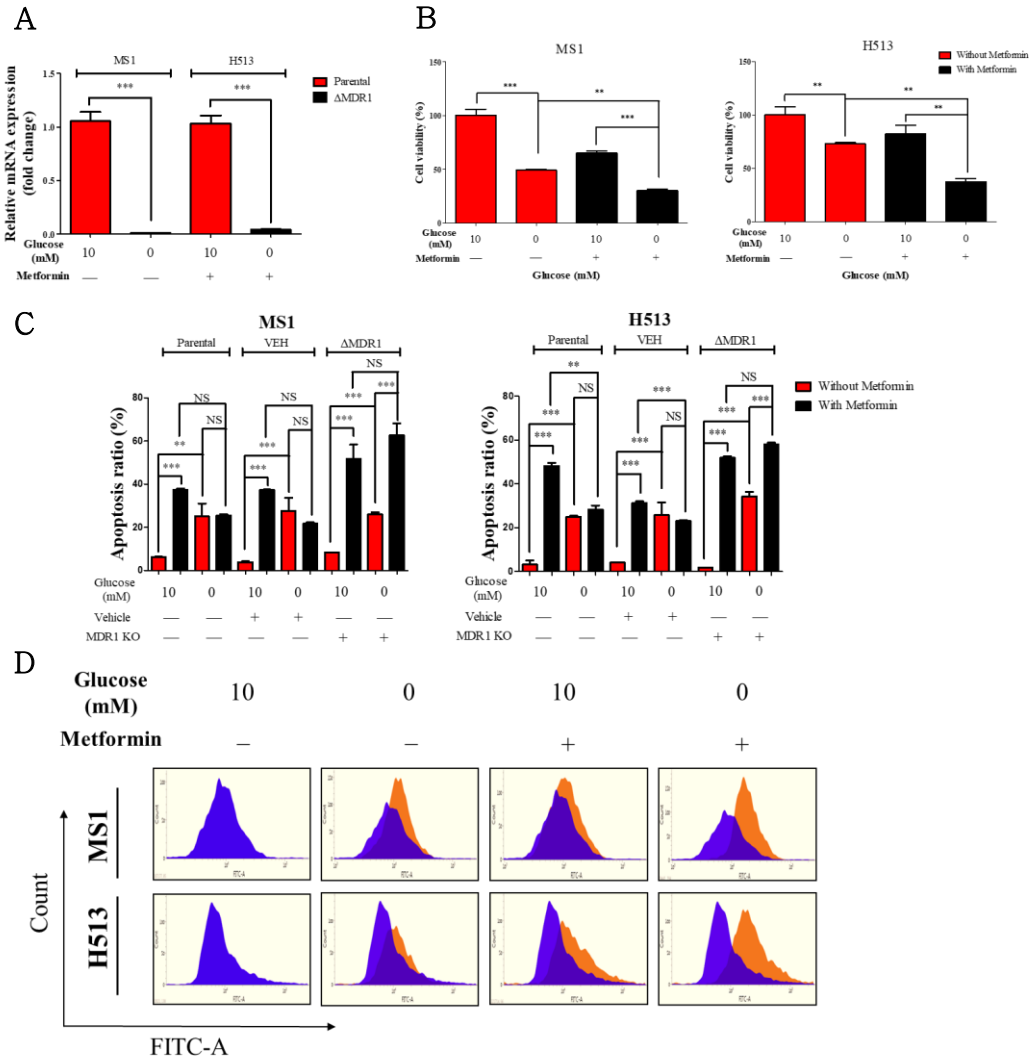
A
MS1
H513
Parental
ΔMDR1
Relative mRNA expression (fold change)
Glucose (mM)
Metformin
B
MS1
H513
Without Metformin
With Metformin
Cell viability (%)
Glucose (mM)
Metformin
C
MS1
H513
Parental
VEH
ΔMDR1
Without Metformin
With Metformin
Apoptosis ratio (%)
Glucose (mM)
Vehicle
MDR1 KO
D
Glucose (mM)
Metformin
MS1
H513
Count
FITC-A

Figure 6. Survival of glucose-starved human malignant mesothelioma (HMM) cells subjected to metformin treatment was controlled by multidrug resistance protein 1 (MDR1)

(A) The mRNA expression of MDR1 was measured in control and Mdr1-CRISPR/Cas9 plasmid-transfected HMM cells. ΔMDR1: MDR1-CRISPR/Cas9 plasmid-transfected HMM cells. Control: cells transfected with a noncoding CRISPR/Cas9 plasmid. The error bars represent the SEM (n = 4). Significant differences are indicated by $^{**}P < 0.01$ and $^{***}P < 0.001$. (B) The Mdr1 expression in the parental HMM cells and MDR1 KO HMM cells by western blot assay. MDR1 KO: MDR1-CRISPR/Cas9 plasmid-transfected HMM cells. Control cells were HMM cells transfected with a noncoding CRISPR/Cas9 plasmid. (C) The viability of ΔMDR1 HMM cells with glucose starvation and/or metformin treatment. All error bars represent the SEM (n = 8). Significant differences are indicated by $^{**}P < 0.01$ and $^{***}P < 0.001$. (D) Analysis of apoptosis in parental cells, control cells and ΔMDR1 cells. (E) Activated autophagy in ΔMDR1 HMM cells cultured under glucose starvation and/or metformin treatment was investigated by flow cytometry (purple: control; red: experimental condition). CRISPR, clustered regulated interspaced short palindromic repeats; KO, knockout

Discussion

Despite efforts in anticancer drug development, cancer mortality remains high due to the therapeutic resistance of cancer cells. During progression to the malignant stage, cancer cells survive in an adverse microenvironment and develop drug resistance (Sun et al. 2012, Lee 2014, Visioli et al. 2014). This study was performed to elucidate the mechanism of enhanced metformin resistance in glucose-starved HMM cells. HMM cells used a distinct metabolism to generate energy compared to normal mesothelial cells and glucose starvation promoted more severe metabolic alterations (Kroemer and Pouyssegur 2008, Justus et al. 2015). Therefore, energy-deficient cancer cells survived through PKA over activated metabolism alteration (Palorini et al. 2016). Surviving HMM cells under glucose starvation exhibited metformin resistance. The viability of HMM cells cultured under glucose starvation with metformin was unchanged and apoptosis was decreased compared to those of cells cultured in complete medium. Excessively activated autophagy induces cell death during cancer therapy (Yang et al. 2011). However, the treatment of glucose-starved HMM cells with metformin decreased autophagy activation compared to that of untreated cells. Therefore, during glucose starvation, metabolism-altered HMM cells survived for 3 days and exhibited enhanced resistance to metformin.

Glucose-starved HMM cells were survived by metformin treatment more than those cells cultured in complete medium, although mitochondrial

integrity, including ATP generation, morphology, MMP and mPTP, was compromised. The treatment of glucose-starved HMM cells with metformin resulted in a significant ATP synthesis reduction; a major function of mitochondria that supported mitochondrial function was disrupted and could not active mitochondrial-mediated cell death. Moreover, elongated mitochondria and thick cristae were detected in the treatment of glucose-starved HMM cells with metformin. That phenotype was observed during mitochondrial fusion, with inhibited cytochrome C release, leading to anti-apoptotic effects (Cribbs and Strack 2007, Suen et al. 2008, Park et al. 2015). The de-phosphorylation of Ser 656 on dynamin-related protein 1, a mitochondrial fission marker, induced mitochondrial elongation and prompted an anti-apoptotic response (Reddy 2014). The mPTP penetrated through the mitochondrial inner and outer membranes, which maintain the calcium homeostasis. Excessive calcium was accumulated in damaged mitochondria through mPTP inactivation, which disturbs homeostasis and leads to cell death (Karch et al. 2013). In line with this, glucose starvation or metformin treatment induced mPTP inactivation and mitochondrial swelling. However, the treatment of glucose-starved HMM cells with metformin exhibited a similar level of mPTP activation compared to HMM cells cultured under complete medium. Cyclophilin D, which is a component of the mPTP inhibition by cyclosporine A treatment, protects calcium-mediated cell death in cardio myocytes (Rasola and Bernardi 2011). Furthermore, the treatment of glucose-starved HMM cells with metformin

increased MMP. MMP hyperpolarization permitted the hyperaccumulation of anions in the inner membrane, leading to protein import to the intermembrane space (Neupert and Herrmann 2007, Nunnari and Suomalainen 2012, Forkink et al. 2014). Moreover, MMP hyperpolarization is simultaneously observed with mitochondrial p-glycoprotein overexpression under stressful conditions (Marchenko et al. 2000). A comparatively low amount of hyperpolarization was present in H513 cells compared to MS1 cells. The translocation of p53 to the mitochondria alters the MMP; however, H513 cells, which are p53-mutated HMM cells, exhibit disturbances in MMP changes that leading relatively lower mitochondrial Mdr1 expression compared to MS1 cells (Kathawala et al. 2015). Therefore, we proposed that significantly increased MMP in the treatment of glucose-starved HMM cells with metformin protected mitochondrial integrity and promoted cell survival through overexpressed Mdr1 in mitochondria. In contrast, mitochondrial Mdr1 expression was not changed in the treatment of glucose-starved HMM cells with metformin and CCCP. Therefore, MMP hyperpolarization in the treatment of glucose-starved HMM cells with metformin promotes Mdr1 overexpression in compromised mitochondria.

Metformin combined with serum in medium obtains a hydrophobic feature that could be a substrate of MDR1 (Neupert and Herrmann 2007, Nunnari and Suomalainen 2012, Forkink et al. 2014). Multidrug resistance has been attributed to ABC transporters that encode p-glycoprotein, which regulates drug resistance via the efflux of hydrophobic substrates from the

intracellular membrane (de Kant et al. 1996). Furthermore, MDR1 interacts with the membrane as a fluid mosaic model located in lipid bilayer membranes and activate binding with ATP, which contributes to the efflux of the accumulated drug and small molecules to the extracellular space (Daniel et al. 2013). The MDR1 is expressed not only in the plasma membrane, but also in mitochondria and nucleus (Daniel et al. 2013). Moreover, p-glycoprotein is highly expressed to protect attenuated mitochondria and promotes ion and chemical homeostasis (Ling et al. 2012, Ho et al. 2018). Mitochondrial Mdr1 has a distinct role as a unidirectional pump that sequesters drug infiltrated mitochondria and is subsequently degraded by lysosome to prevent drug distribution (de Kant et al. 1996). Overexpressed Mdr1 of mitochondria in glucose-starved HMM cells spill out the accumulated metformin for survival. In contrast to MS1 cells, H513 cells exhibited nonspecific Mdr1 expression in mitochondria. The p53 mutant form induced a high level of Mdr1 expression in colorectal cancer metastases (de Kant et al. 1996). The role of MDR1 was verified by knockout using the CRISPR/Cas9 system. In contrast to the parental cells, apoptosis and autophagy were increased and viability was decreased in the treatment of glucose-starved MDR1 KO HMM cells with metformin. ATP is required for autophagy activation. However, the ATP amount was insufficient in glucose-starved HMM cells with metformin because that energy was wasted in MDR1 overexpression. Therefore, an inadequate ATP amount could not facilitate autophagy. However, further research is

necessary on the relationship between autophagy and MDR1. In addition, the expression level of ABCG2 mRNA was increased in glucose-starved HMM cells with metformin treatment. However, the extent of ABCG2 upregulation was less dramatic than that of MDR1 in our study. The role of ABCG2 in metformin resistance and the underlying mechanism warrants further study.

The present study demonstrated that overexpressed Mdr1 in defected mitochondria rescued glucose-starved HMM cells from metformin treatment. Although MDR1 is important in chemoresistance, the mechanism of its expression and localization are not yet clear in HMM cells. Therefore, tumor recurrence and chemoresistance in malignant mesothelioma patients could be suppressed by Mdr1 repression through MMP reduction, which promote the anticancer efficacy.

CHAPTER II.

Cancer-associated fibroblasts survived under glucose-deficient conditions with excessive calcium influx into mitochondria

Abstract

Compared to normal fibroblasts (NFs), discriminative nature was observed in CAFs under glucose-deficient conditions. Within tumor microenvironment, CAFs surrounding cancer cells promotes the invasion, metastasis and drug resistance for progression of tumor. Under glucose-deficient condition, CAFs showed significant increase of viability, ATP production by upregulation of mitochondrial calcium via mitochondrial calcium uniporter (MCU), but it was reversed when those cells treated with Ru360, an selective MCU inhibitor. Notably, activated transforming (TGF-β) signaling augmented MCU-mediated calcium influx in CAFs under glucose-deficient conditions. Additionally, oligomycin treatment in CAFs significantly reduced the viability and ATP synthesis, whereas excessive mitochondrial calcium was observed under increase under glucose-deficient conditions. Intriguingly, treatment of glucose starved CAFs with oligomycin enhanced cell death with aberrant calcium homeostasis via inactivation of mitochondrial permeability transition pore (mPTP). This study demonstrated that the discriminative calcium influx into mitochondria through MCU coordinated cell growth and apoptosis in glucose-starved CAFs but not in NFs.

For this study, isolation of fibroblasts was required from the xenografted tumors. Thus, xenograft model was established using H460 cells which an epithelial cells, not HMM cells.

Introduction

Glucose starvation is a common feature of the tumor microenvironment. Metabolic reprogramming of the cell components in tumor mass is essential for their survival in glucose-limited conditions that are caused by abnormal angiogenesis (Buono and Longo 2018, Sullivan et al. 2019). Glucose deficiency not only affects cancer cell survival via mitochondrial machinery and endoplasmic reticulum stress but also induces drug resistance and metastasis through matrix metalloprotein-9 and AMPK signaling (Li et al. 2017, Endo et al. 2018, Hwang et al. 2019). Because diffusion of nutrients in a tumor mass is area-dependent, heterogeneity of cancer cells in metabolic and phenotypic features is detected (Kim et al. 2015).

Among the cellular components of tumor tissue, CAFs are a representative noncancerous cells that influences cancer cell behaviors via various signaling molecules (Shiga et al. 2015, Ciardiello et al. 2016, Wang et al. 2017, Chen and Song 2019). In human breast and ovarian cancers, CAFs exacerbate cancer cell malignancy through secreted chemokines, such as interleukin-6 (IL-6), cyclooxygenase (COX) and CXCL2 (Erez et al. 2013). Also, transforming growth factor-β (TGF-β) released from CAFs recruits neighboring cancer cells to promotes invasion by extracellular matrix (ECM) degradation and the epithelial to mesenchymal transition (EMT) (Kojima et al. 2010, Calon et al. 2014). Moreover, TGF-β secreted by CAFs stimulates IL-11 production, promoting cancer stemness properties and metastasis (Calon et al. 2012).

Intracellular calcium is a versatile second messenger in biochemical and physiological signaling and impacts almost every aspect of cellular activity (Monteith et al. 2017). Within the cells, calcium is predominantly stored in the endoplasmic reticulum and transferred into mitochondria under stress condition (Giorgi et al. 2012). The transfer of the intracellular calcium to the mitochondria is mediated via the mitochondrial calcium uniporter (MCU) that is located on the inner-outer membrane of the mitochondria (Patron et al. 2013). In many human cancers, MCU expression is upregulated and promotes tumor progression by increasing HIF-1α (Vultur et al. 2018). The mitochondrial calcium coordinates dehydrogenase activity and function, cell proliferation and death. By direct conjugation with calcium, the F0F1 site of ATP synthase in the mitochondria is activated to produce ATP (Monteith et al. 2017). In contrast, excessive mitochondrial calcium induces apoptosis through mitochondrial swelling and the release of cytochrome C to the cytoplasm (Szydlowska and Tymianski 2010, Rizzuto et al. 2012, Rossi et al. 2019).

This study illustrated that phenotypes of CAFs isolated from a tumor mass were heterogeneous in glucose deficient condition. And in contrast to normal fibroblasts (NFs), the glucose-starved CAFs showed a significant increase in calcium in mitochondria via upregulated MCU, resulting in the enhanced cell survival and proliferation. These results provide a clue for an alternative mechanism by which CAFs influence cancer cell biology in the hostile tumor microenvironment.

Materials and Methods

Xenograft assay

Three female BALB/c nude (4 weeks of age) mice were purchased from Jungang Lab Animal, Inc. (Seoul, Korea). One week after the animal acclimation, 1 x 10^6 NCI-H460 cells (H460, KCLB; Seoul, Korea) were injected subcutaneously in the back of the mice. After 4 weeks, the tumor mass which resected from the mice, underarm skin and lung tissues were collected for primary culture. A tumor mass was dissected into 6 pieces of equal size using a surgical scalpel.

Isolation and culture of cells

Complete medium and glucose-deficient medium were prepared as described (Hwang et al. 2019). Primary cell culture was conducted using the dissected pieces from the three tumor masses, underarm skin and lung tissues as described with slight modification (Cat et al. 2006). Primary culture cells from different areas of a tumor mass were referred to as Nos. 1 to 6. Fibroblasts different tumor pieces, skin and lung tissues were isolated using magnetically activated cell sorting (MACs) with anti-fibroblast activation protein (FAP; Abcam) antibody for preparation of CAFs and NFs, respectively (Huang et al. 2017). Briefly, following the individual cells by mincing and collagenase I treatment, the cells were incubated with FAP antibody for 1 hour in ice. After washing, microbead-conjugated secondary antibody (Miltenyi Biotec, Bergisch Gladbach, Germany) was added, and the FAP^+ cells into magnetic column were isolated by flushed

out. All of the experiments using the primary culture cells were conducted at passage 5.

Cell viability assay

The cells were seeded at 1 x 10^4 cells per well in 96-well plates. Cell culture media was replaced with complete or glucose deficient media and cultured for 1 day. Cell viability was assessed by MTT assay (Sigma-Aldrich) assay according to manufacturer's recommendations. Optical densities were measured at a wavelength of 570 nm by a microplate reader (Biotek Epoch Izasa).

Analysis of intracellular signaling molecules

Real-time PCR was performed to evaluate α-smooth muscle actin (α-SMA), vimentin, TGF-β, MCU, glucose transporter 1 (GLUT1), and hypoxia inducible factor 1-α (HIF-1α). The sequences of the primers for the genes are listed in Table 1. The relative gene expression level was normalized to 18S rRNA, and the $\Delta\Delta C_t$ method was applied (Rao et al. 2013). Western blot was performed as described (Hwang et al. 2019). The primary antibodies, including TGF-β receptor type I (TGF-βR I; Santa Cruz Biotechnology), p-Smad3 (Santa Cruz Biotechnology), MCU (Abcam), GAPDH (Santa Cruz Biotechnology) and β-actin (Santa Cruz Biotechnology), were diluted 1:1000 in PBS-T with 5% bovine serum albumin (BSA). And HRP-conjugated anti-rabbit (Santa Cruz Biotechnology) or anti-mouse secondary antibody (Santa Cruz Biotechnology) were diluted 1000:1 in PBS-T with 5% skim milk. Immunoblotting reactions were detected using

Luminata Forte Western HRP substrate (Millipore) and a chemiluminescence imaging system (Atto).

To determine the phenotype of isolated fibroblasts, surface staining for anti-CD90 (Novus Biologicals) and FAP (Abcam) was conducted using FACSVerse (BD Biosciences).

MCU was blocked with 5 μM Ru360 (Calbiochem, San Diego, CA, USA). ATP synthase and TGF-β signaling were inhibited by 1 μM oligomycin (Sigma-Aldrich) and 10 μM SB-431542 (Sigma-Aldrich) treatment for 1 day, respectively.

Measurement of calcium concentration

Intracellular calcium was stained with Fluo-4AM according to the manufacturer's instructions (Invitrogen, Carlsbad, CA, USA) and analyzed by a BD FACSVerse flow cytometer (BD Biosciences, San Jose, CA, USA) and LSM710 CLSM (Carl Zeiss). As negative and positive controls, cells were treated with EDTA and ionomycin, respectively, and P2 population in Fluo-4AM staining was established. Mitochondrial calcium was measured using Rhod-2AM staining according to the manufacturer's instructions. The P3 population for Rhod-2AM staining was established using negative and positive controls that were treated with EDTA and BAPTA-2AM, and ionomycin, respectively.

Analysis of mitochondrial integrity and activity

Activation of the mitochondrial permeability transition pore (mPTP) was analyzed using a commercial mPTP detection kit (Molecular Probe)

according to the manufacturer's instructions. Briefly, calcein, CoCl2 or ionomycin were mixed in Hanks' balanced salt solution (HBSS) (Gibco-Life Technology, Gaithersburg, MD, USA) at the final concentration of 2 μM. The fluorescence of the cells was measured using flow cytometry (Becton Dickinson).

CellTiter-Glo reagent (Promega, Madison, WI, USA) was used to measure the synthesis of adenosine triphosphate (ATP) synthesis. Detection reagent was added to each well, mixed thoroughly for 2 min, and incubated for 10 min at room temperature. Subsequently, the luminescence reaction was measured by a luminometer (Infinite M200 Pro; Tecan, Mannedorf, Switzerland).

Mitochondrial membrane potential was assessed using 5,5′,6,6′-tetrachloro-1,1′, 3,3′-tetraethylbenzimidazolylcarbocyanine iodide; JC-1, Molecular Probes) according to instruction's recommendation. Briefly, harvested cells were treated with JC-1 solution for 30 min in the dark, and analyzed with flow cytometry. The portion of green and red was divided based on depolarization control, which treated with carbonyl cyanide m-chlorophenyl hydrazone (CCCP).

H2DCFDA (Invitrogen) was used to evaluate the intensity of ROS according to the manufacturer's recommendations. Cells were incubated with 10 μM H2DCFDA for 15 min and analyzed with flow cytometry. For positive and negative control, N-acetyl Cysteine and hydroperoxide were treated for 1

day, respectively, and used to accomplished P2 population.

Statistical analysis

All experiments were repeated at least 3 times, and the data were presented as the means ± standard error of the mean (SEM). GraphPad Prism 5 software was used to perform statistical analysis, including one-way analysis of variance (ANOVA), and to generate all graphs. Statistical significance was determined at $P < 0.05$, $P < 0.01$ or $P < 0.001$.

Table 1. Primer sequences

GLUT1, HIF-1α, TGF-β, MCU and 18S rRNA primers for qRT-PCR are presented

Name		*Sequence*
α-SMA	Forward	5'-TGCTGACAGAGGCACCACTGAA-3'
	Reverse	5'-CAGTTGTACGTCCAGAGGCATAG-3'
Vimentin	Forward	5'-CGGAAAGTGGAATCCTTGCAGG-3'
	Reverse	5'-AGCAGTGAGGTCAGGCTTGGAA-3'
TGF-β	Forward	5'-CACCCGCGTGCTAATGG-3'
	Reverse	5'-ATGCTGTGTGTACTCTGCTTGAACT-3'
MCU	Forward	5'-CACACAGTTTGGCATTTTGG-3'
	Reverse	5'-CGTGACTTTTTGGCTCCTTT-3'
18s rRNA	Forward	5'-CGCCGCTAGAGGTGAAATTC-3'
	Reverse	5'-TTGGCAAATGCTTTCGCTC-3'

Results

Heterogeneity in cell proliferation and ATP production was detected in CAFs from a tumor mass

Xenograft assay was performed in three immunodeficient mice by subcutaneous injection of $1x10^6$ H460 cells. A tumor mass was dissected into 6 pieces to represent different areas (Fig. 1 A). After the mincing and treatment with collagenase IV, FAP^+ cells were isolated using MACs. CAFs isolated from the different pieces from individual tumor mass showed heterogeneities in phenotypes and molecular features under glucose starved condition. The fibroblastic phenotype of CAFs and NFs were examined by flow cytometry with fibroblast markers, CD90 and FAP. In isolated cells from tumor pieces, more than 90% was positive for FAP, but only a portion of cells were positive for CD90. In contrast, isolated cells from lung and skin tissues showed positive for FAP, while none were positive for CD90 (Fig. 1 B – G). NFs separated from both lung and skin tissues were only positive for FAP at 85% and 94%, respectively, but CD90 expression was not detected (Fig. 1 H, I). These experiments were performed as triplicates using cells from different tumor masses (Fig. 1 J – L). Additionally, the FAP^+ cells isolated from tumor pieces showed higher expression of α-SMA and vimentin, compared to those from skin and lung tissues (Fig. 1 M, N). As surrogates for glucose and oxygen concentrations, the expression levels of GLUT1 and HIF-1α were evaluated in CAFs and NFs. In CAFs, the expression levels of GLUT1 and HIF-1α were

heterogeneous and expression of GLUT1 was increased under glucose-deficient conditions, but HIF-1α was not changed except No.3 and 5 (Fig. 2 A). In contrast, those expressions were not changed in NFs which isolated from lung and skin tissue. Under glucose deficient conditions, CAFs showed significantly increased cell proliferation compared to those cultured in complete medium (Fig. 2 B). In contrast to CAFs, a marked decrease in cell viability was observed in NFs under glucose starvation conditions. Similar to viability, under glucose deprivation, proliferation of the cells was higher in CAFs at 1 day than in those cells at 2 and 3 days, but NFs showed consistent decrease (Fig. 2 C). The amount of ATP was significantly increased in glucose-starved CAFs compared to that of CAFs in complete medium. In contrast, the amount of ATP in NFs was not affected by glucose concentration (Fig. 2 D). Similar to the expression pattern of GLUT1 and HIF-1α, No. 3 CAFs showed significantly increased cell proliferation and ATP production compared to those of No. 4 CAFs under glucose deficient conditions. As an intracellular organelle for ATP production, mitochondrial integrity and activity were determined.

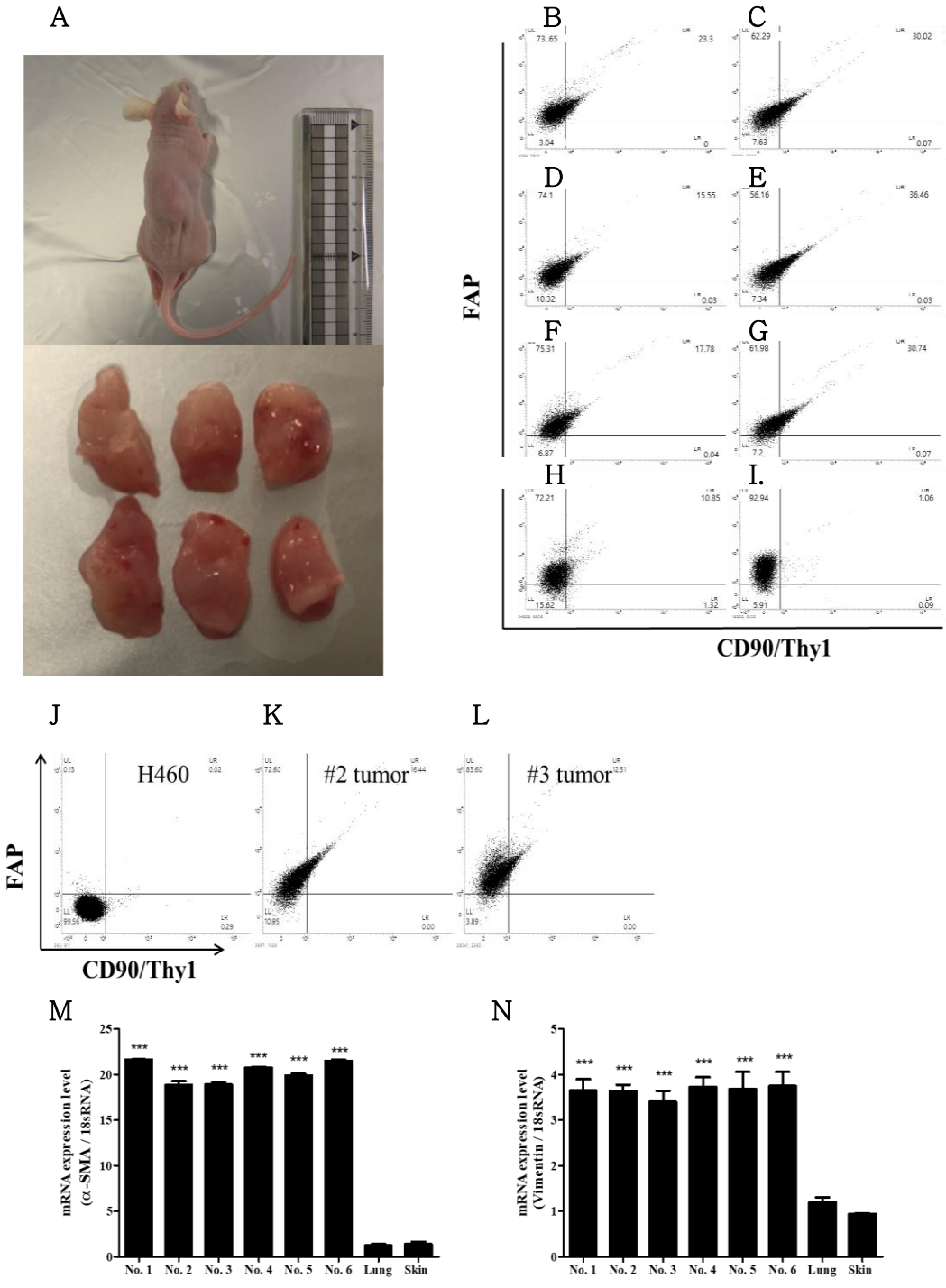
A
B
C
D
E
F
G
H
I.
FAP
CD90/Thy1
J
K
L
H460
#2 tumor
#3 tumor
FAP
CD90/Thy1
M
mRNA expression level (α-SMA / 18sRNA)
No. 1
No. 2
No. 3
No. 4
No. 5
No. 6
Lung
Skin
N
mRNA expression level (Vimentin / 18sRNA)
No. 1
No. 2
No. 3
No. 4
No. 5
No. 6
Lung
Skin

Figure 1. Isolation of fibroblasts from a tumor mass and lung and skin tissue and their characterization

(A) Image of xenografted mice and dissected 6 pieces. (B – G) Cell surface staining of CD90 and FAP and their population in No. 1 to 6 CAFs. The experiment was performed triplicate using individual tumor masses from each mouse. (H, I) CD90 and FAP staining and their population in fibroblasts from lung and skin tissue. (J – L) Cell surface staining in unstained cells and FAP^+ cells, which isolated from other 2 different tumor mass. H460 cells and FAP^+ cells isolated from #2 and #3 tumor mass indicated as L, M and N, respectively. (M, N) The mRNA expression of α-smooth muscle actin (α-SMA) and vimentin were measured in CAFs and NFs. $^{***}P < 0.001$.

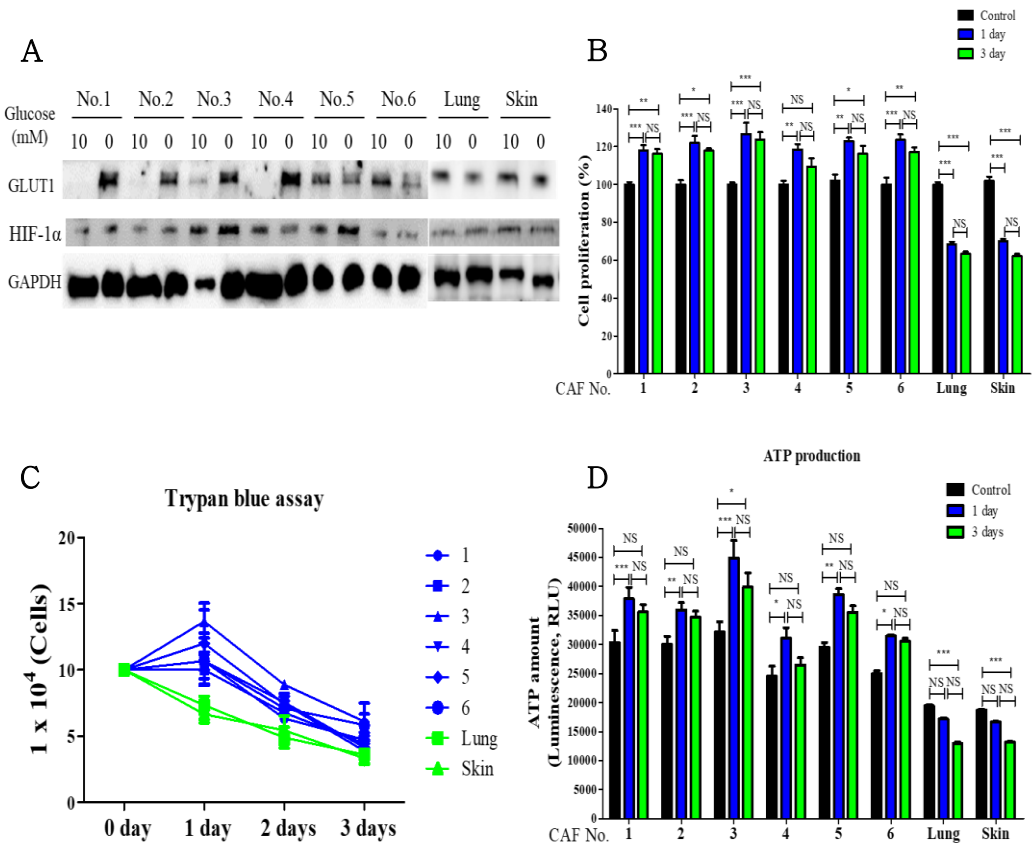

Figure 2. Heterogeneous characteristics of CAFs from a tumor mass

(A) Expression levels of GLUT1 and HIF-1α in CAFs and NFs which cultured in complete medium or glucose-deficient condition. (B) The viability of CAFs and NFs under glucose starved condition for 1 or 3 days. $^{*}P < 0.05$, $^{**}P < 0.01$, and $^{***}P < 0.001$ vs the cells cultured in complete medium. The data represent the mean ± SEM (n = 8). (C) Assessment of proliferation by trypan blue assay in CAFs and NFs under glucose-deficient condition for 3 days. (D) ATP production in CAFs and NFs cultured in complete medium or glucose starved condition for 1 or 3 days. $^{*}P < 0.05$, $^{**}P < 0.01$, and $^{***}P < 0.001$. The data indicate the mean ± SEM (n = 5).

TGF-β signaling was significantly activated in CAFs cultured under glucose deficient condition

Under glucose starved condition, CAFs showed significantly increased expression of TGF-β mRNA, while no change was observed in NFs (Fig. 3 A). Glucose starvation enhanced the expression of TGF-βR I and p-Smad3 in CAFs, but not in NFs (Fig. 3 B). Moreover, increased their expressions in glucose starved CAFs were reversed by treated with SB-431542, an inhibitor of TGF-β signaling for 1 day (Fig. 3 C). In NFs, expression of these proteins remained at basal levels regardless of glucose concentration and/or SB-431542 treatment. To determine the role of increased TGF-β in glucose starvation conditions, cell proliferation and ATP production were assessed following SB-431542 treatment. In CAFs, treatment with SB-431542 suppressed cell proliferation in complete medium and induced significantly reduced cell proliferation under glucose starvation conditions. However, the cell proliferation of NFs was not affected by SB-431542 treatment (Fig. 3 D). SB-431542 treatment significantly suppressed ATP production in CAFs under glucose starvation, while ATP production was not affected in CAFs in complete medium, except No. 4 CAFs (Fig. 3 E). In contrast to the effect in CAFs, ATP production in NFs was independent of either glucose concentration or SB-431542 treatment.

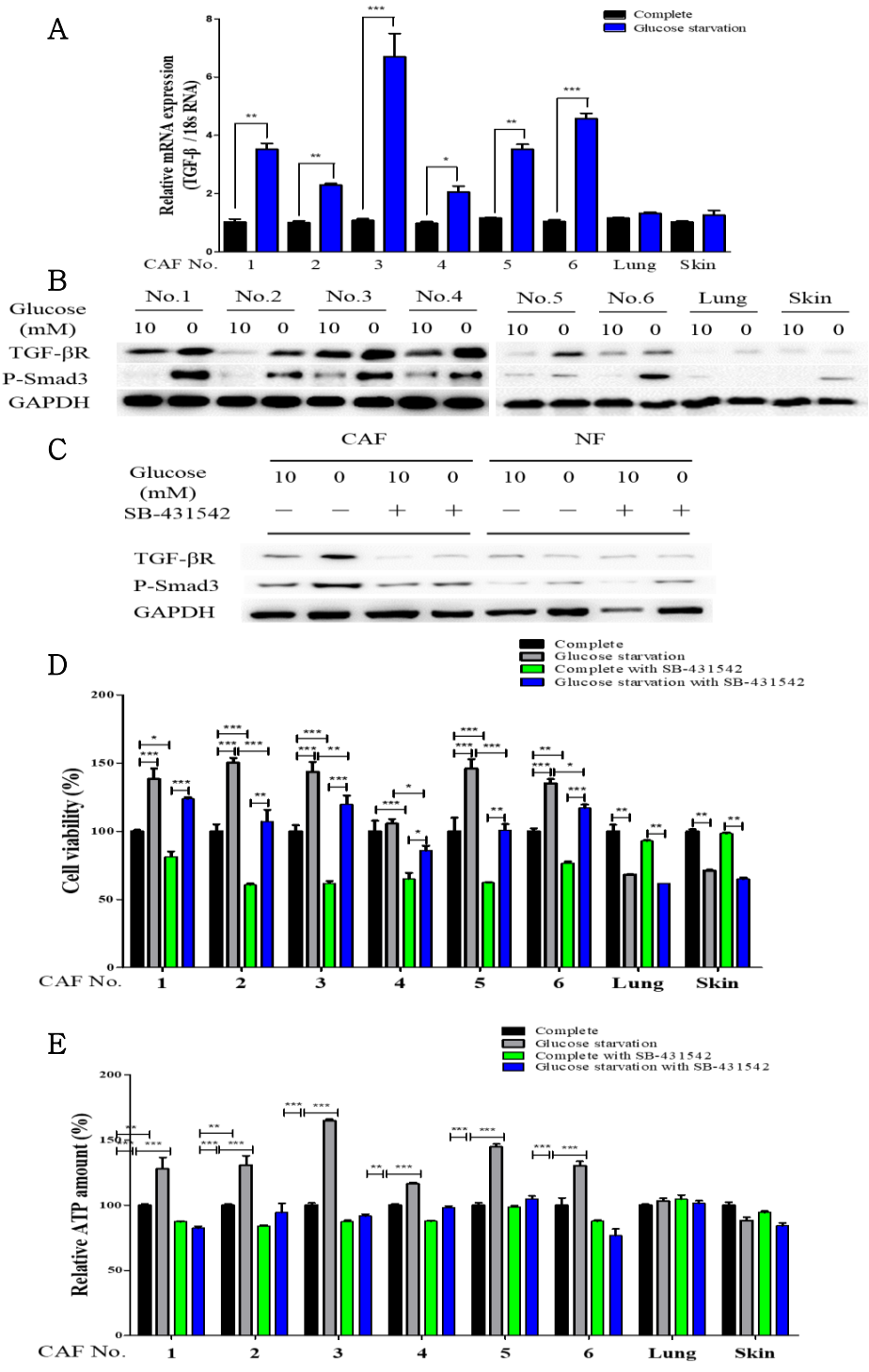
A
Complete
Glucose starvation
Relative mRNA expression (TGF-β /18s RNA)
CAF No. 1 2 3 4 5 6 Lung Skin
B
Glucose (mM)
No.1 No.2 No.3 No.4 No.5 No.6 Lung Skin
10 0 10 0 10 0 10 0 10 0 10 0 10 0 10 0
TGF-βR
P-Smad3
GAPDH
C
CAF NF
Glucose (mM)
SB-431542
10 0 10 0 10 0 10 0
— — + + — — + +
TGF-βR
P-Smad3
GAPDH
D
Complete
Glucose starvation
Complete with SB-431542
Glucose starvation with SB-431542
Cell viability (%)
CAF No. 1 2 3 4 5 6 Lung Skin
E
Complete
Glucose starvation
Complete with SB-431542
Glucose starvation with SB-431542
Relative ATP amount (%)
CAF No. 1 2 3 4 5 6 Lung Skin

Figure 3. Activated TGF-β signaling augments cell growth in CAFs cultured under glucose-deficient conditions

(A) The mRNA expression of TGF-β in CAFs and NFs cultured in complete medium or glucose starvation conditions for 1 day. $^{*}P < 0.05$, $^{**}P < 0.01$, and $^{***}P < 0.001$. (B) Protein expression of TGF-βR I and p-Smad3 expression in CAFs and NFs in complete medium or glucose-deficient condition. (C) Protein expression of TGF-βR I, p-Smad-3 and GAPDH in CAFs and NFs cultured in complete medium or glucose starvation with or without SB-431542 treatment. (D) The relative viability in CAFs and NFs was normalized with that of cells in complete medium. (N = 5), $^{*}P < 0.05$, $^{**}P < 0.01$, and $^{***}P < 0.001$. (E) The relative ATP production in CAFs and NFs was normalized with that of cells in complete medium. (N = 3), $^{*}P < 0.05$, $^{**}P < 0.01$, and $^{***}P < 0.001$.

Intracellular and mitochondrial calcium was increased by TGF-β signaling in CAFs under glucose-deficient conditions

As intracellular calcium is coordinated by TGF-β signaling, intracellular calcium was measured after treating CAFs with SB-431542. The P2 population for Fluo-4AM staining was established using negative and positive control. Intracellular calcium was significantly increased in glucose-starved CAFs compared to that of the cells in complete medium (Fig. 4 A). Increased intracellular calcium was detected in CAFs compared to that of NFs, and the level was heterogeneous between different CAFs. In particular, No. 3 CAFs showed an approximately 40% increase in intracellular calcium under glucose starvation conditions compared to those in complete medium (Fig. 4 B). Treatment with SB-431542 dramatically decreased the level of intracellular calcium. In contrast to the increased intracellular calcium in glucose-starved CAFs, NFs showed consistent expression, independent of SB-431542 treatment.

To assess the level of mitochondrial calcium, CAFs in complete medium were gated as the P3 population and were used as a comparator (Fig. 4 C). The mitochondrial calcium was significantly increased in glucose-starved CAFs compared to that of CAFs in complete medium. In contrast to the effect in CAFs, the P3 population of NFs was not affected by the glucose concentration. Moreover, treatment of glucose-starved CAFs with SB-431542 reduced the level of mitochondrial calcium by approximately 22% (Fig. 4 D). In contrast to the effect in CAF, NFs showed persistent levels,

regardless of SB-431542 treatment. Similar to the intracellular calcium amount, a heterogeneous increase in mitochondrial calcium was detected in different CAFs under glucose starvation. Intriguingly, the greatest increase in mitochondrial calcium was observed in No. 3. CAFs, which was the same as intracellular calcium, and the level was dramatically reduced by SB-431542.

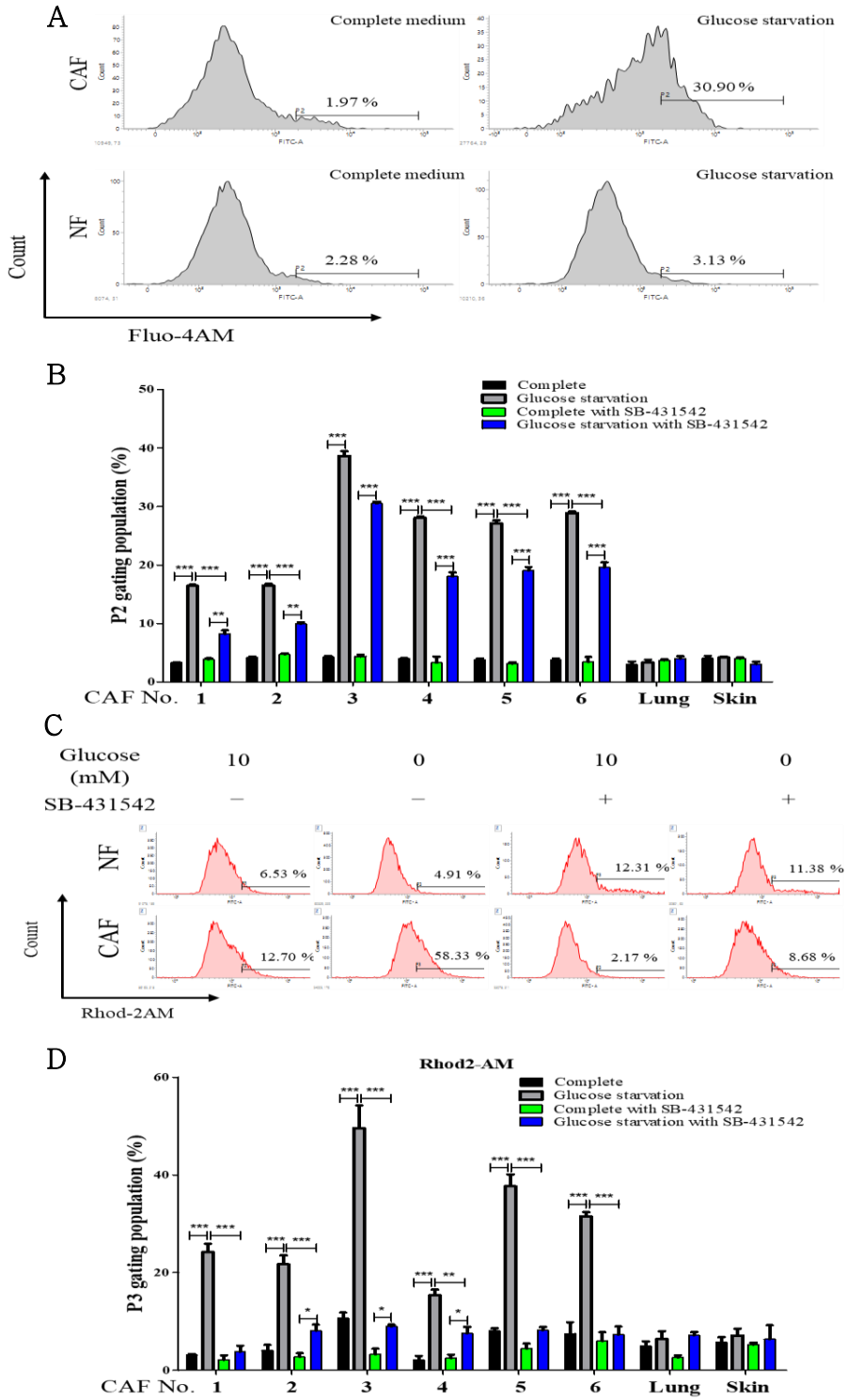
A
Complete medium
Glucose starvation
CAF
1.97 %
30.90 %
NF
2.28 %
3.13 %
Count
Fluo-4AM
B
Complete
Glucose starvation
Complete with SB-431542
Glucose starvation with SB-431542
P2 gating population (%)
CAF No. 1 2 3 4 5 6 Lung Skin
C
Glucose (mM)
10 0 10 0
SB-431542
− − + +
NF
CAF
6.53 %
4.91 %
12.31 %
11.38 %
12.70 %
58.33 %
2.17 %
8.68 %
Count
Rhod-2AM
D
Rhod2-AM
Complete
Glucose starvation
Complete with SB-431542
Glucose starvation with SB-431542
P3 gating population (%)
CAF No. 1 2 3 4 5 6 Lung Skin

Figure 4. Activation of TGF-β signaling significantly increases intracellular and mitochondrial calcium

(A) Representative data of Fluo-4AM staining in CAF and NF cultured in complete medium and glucose-starved condition. (B) Intracellular calcium was measured in CAFs and NFs cultured in complete medium or glucose starvation conditions for 1 day. $^{***}P < 0.001$. (C) Representative image of Rhod-2AM staining in CAF (No.3) and NF (Skin) under the complete medium or glucose deficient condition. Mitochondrial calcium was measured using Rhod-2AM staining. (D) The bar graph depicted the P3 population in Rhod-2AM staining of CAFs and NFs and analyzed with ANOVA. (N = 3), $^{**}P < 0.01$, and $^{***}P < 0.001$.

Calcium influx to mitochondria was stimulated by upregulated MCU in CAFs under glucose starvation

As a major player in transferring intracellular calcium to mitochondria, MCU was evaluated. CAFs under glucose starvation showed significantly higher expression of MCU mRNA than those cells in complete medium, while the MCU level in NFs was not altered by glucose starvation (Fig. 5 A). To determine the role of MCU in the process, an MCU inhibitor, Ru360, was utilized. The approximately 63% increase in the P3 population in glucose-starved CAFs was dramatically suppressed to 14% by Ru360 treatment but not in NFs (Fig. 5 B). Although a heterogeneous P3 population was detected in glucose-starved CAFs, the Ru360-induced suppression was generally observed in different CAFs (Fig. 5 C).

Subsequently, we determined the regulation of MCU by TGF-β signaling. Heterogeneous expression of TGF-βR I, p-Smad3 and MCU were observed in different CAFs with higher level in No.3 (Fig. 5 D). And, to determine the effect of TGF-β on MCU, the cells were treated with SB-431542. Under glucose-deficient condition, higher expression of MCU was detected in CAF than in NF, which was significantly suppressed by treatment with SB-431542 in both NF and CAF (Fig. 5 E). To ascertain the role of TGF-β signaling in MCU-mediated mitochondrial calcium influx, the expression of p-Smad3, a TGF-β downstream signaling molecule, was determined after Ru360 treatment. MCU expression was significantly increased in glucose-starved CAFs compared to the cells in complete medium, and was decreased

by Ru360 treatment. In contrast, in NFs, only a faint band was detected regardless of glucose concentrations. Furthermore, enhanced p-Smad3 expression in glucose-starved CAFs was significantly suppressed by Ru360 treatment (Fig. 5 F). Intriguingly, Ru360 treatment also suppressed expression of GLUT1 and HIF-1α in CAFs and NFs under glucose starvation (Fig. 5. G).

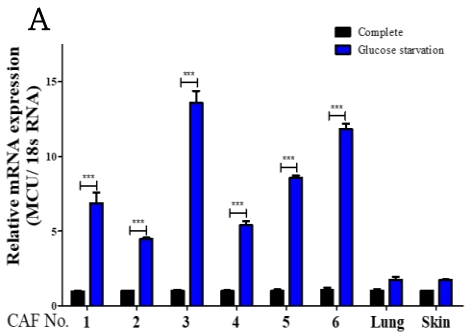
A
Complete
Glucose starvation
Relative mRNA expression (MCU/ 18s RNA)
CAF No. 1 2 3 4 5 6 Lung Skin

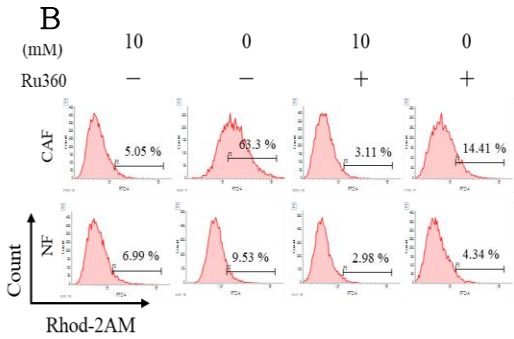
B
(mM) 10 0 10 0
Ru360 − − + +
CAF
5.05 %
63.3 %
3.11 %
14.41 %
NF
6.99 %
9.53 %
2.98 %
4.34 %
Count
Rhod-2AM

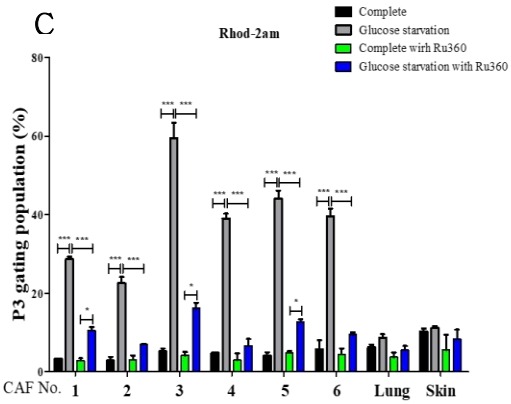
C
Rhod-2am
Complete
Glucose starvation
Complete wirh Ru360
Glucose starvation with Ru360
P3 gating population (%)
CAF No. 1 2 3 4 5 6 Lung Skin

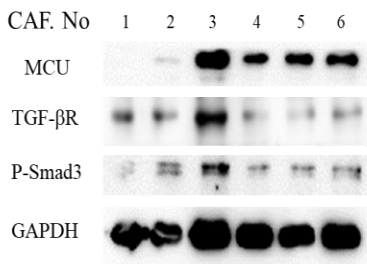
D
CAF. No 1 2 3 4 5 6
MCU
TGF-βR
P-Smad3
GAPDH

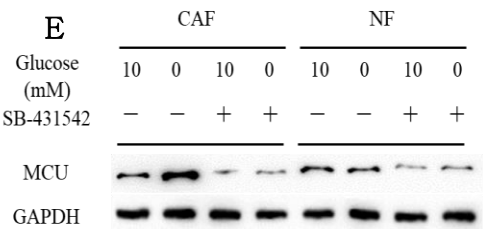
E
CAF
NF
Glucose (mM) 10 0 10 0 10 0 10 0
SB-431542 − − + + − − + +
MCU
GAPDH

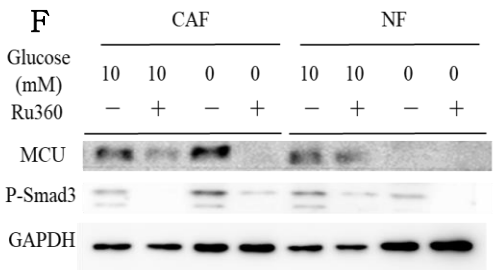
F
CAF
NF
Glucose (mM) 10 10 0 0 10 10 0 0
Ru360 − + − + − + − +
MCU
P-Smad3
GAPDH

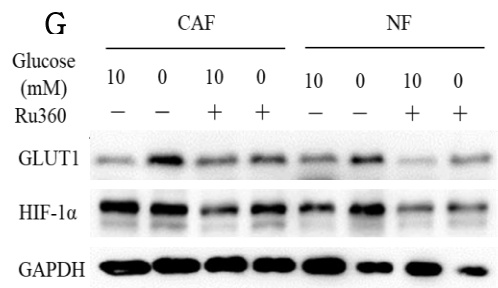
G
CAF
NF
Glucose (mM) 10 0 10 0 10 0 10 0
Ru360 − − + + − − + +
GLUT1
HIF-1α
GAPDH

Figure 5. MCU coordinated calcium influx into mitochondria of CAFs and TGF-β signaling under glucose-deficient conditions

(A) The mRNA levels of MCU in CAFs and NFs cultured in complete medium or glucose starvation for 1 day. $^{***}P < 0.001$. (B) Mitochondrial calcium was assessed using by Rhod-2AM in CAFs and NFs cultured under each glucose concentration in medium and treated with or without Ru360. (C) The P3 population in CAFs and NFs. $^{***}P < 0.001$. (D) Protein expression of TGF-βR I, p-Smad3 and MCU in CAFs. (E) Protein expression of MCU and GAPDH in CAF (No.3) and NF (Skin) in complete medium or glucose-deficient condition. (F) Protein expression of MCU and p-Smad3 in CAF (No.3) and NF (Skin) that were treated with Ru360 in complete medium or glucose-deficient condition. GAPDH was used a loading control. (G) Analysis of GLUT1 and HIF-1α expression in CAF (No.3) and NF (Skin) in complete medium or glucose-deficient condition with Ru360.

Increased mitochondrial calcium in glucose-starved CAFs was essential in maintaining cell survival by activating ATP synthase

Intracellular and mitochondrial calcium was chelated with EDTA and BAPTA-2AM, respectively, and followed by analysis of cell viability and ATP production. Calcium chelation decreased the viability of CAFs under glucose starvation but not that of cells in complete medium (Fig. 6 A). In contrast to the effect on the CAFs, the cell viability of NFs was not affected by glucose concentration or calcium chelation. Glucose-starved CAFs but not NFs showed a significant decrease in ATP production following calcium chelation (Fig. 7 A). To confirm the role of mitochondrial calcium in the activation of ATP synthase, oligomycin, an ATP synthase inhibitor was administered. In glucose-starved CAFs, oligomycin treatment increased mitochondrial calcium by more than 72%, but not in CAFs in complete medium or in NFs (Fig. 6 B). Treatment with oligomycin significantly decreased ATP levels in glucose-starved CAFs but not in CAFs in complete medium and NFs (Fig. 6 C). In particular, No. 3 CAFs showed a 20,000 RLU decrease in response to oligomycin treatment under glucose deficient conditions. ATP amount in NF which cultured in complete medium was not affected by treatment with oligomycin, whereas treatment with antimycin A and rotenone, inhibitors of mitochondrial complex I and III reduced its amount, but not in CAF (Fig. 7 B, C).

To determine inactivation of mitochondrial permeability transition pore (mPTP) enhanced the mitochondrial calcium by blockade of calcium efflux

from mitochondria, activation of mPTP was evaluated by calcien staining. The unstained population for calcein staining indicated the inactivation of mPTP. P1 population was established using inactivation marker and indicated the inactivation of mPTP. The P1 population was approximately 7% in CAFs cultured in complete medium. In contrast, glucose-starved CAFs showed a P1 population of 31%, which was increased to 95% by oligomycin treatment (Fig. 6 D). However, NFs showed a constant P1 population independent of glucose concentration or oligomycin treatment.

To determine significant mitochondrial calcium by mPTP inactivation induced the apoptosis, glucose-starved CAFs were treated with oligomycin and assessed the apoptosis. The total apoptosis ratio in glucose-starved CAFs was significantly increased by oligomycin treatment from approximately 7.15 to 73.15% (Fig. 6 E), while it was not affected in CAFs that were cultured in complete medium. In glucose-starved NFs, the total apoptosis ratio was increased by approximately 25% compared to that of cells in complete medium, but it was not changed by oligomycin treatment. However, calcium chelation in glucose-starved CAFs that were treated with oligomycin significantly decreased apoptosis from 73 to 30% (Fig. 6 F). In contrast to CAFs, glucose-starved NFs showed a similar apoptotic ratio independent of oligomycin and/or calcium chelation.

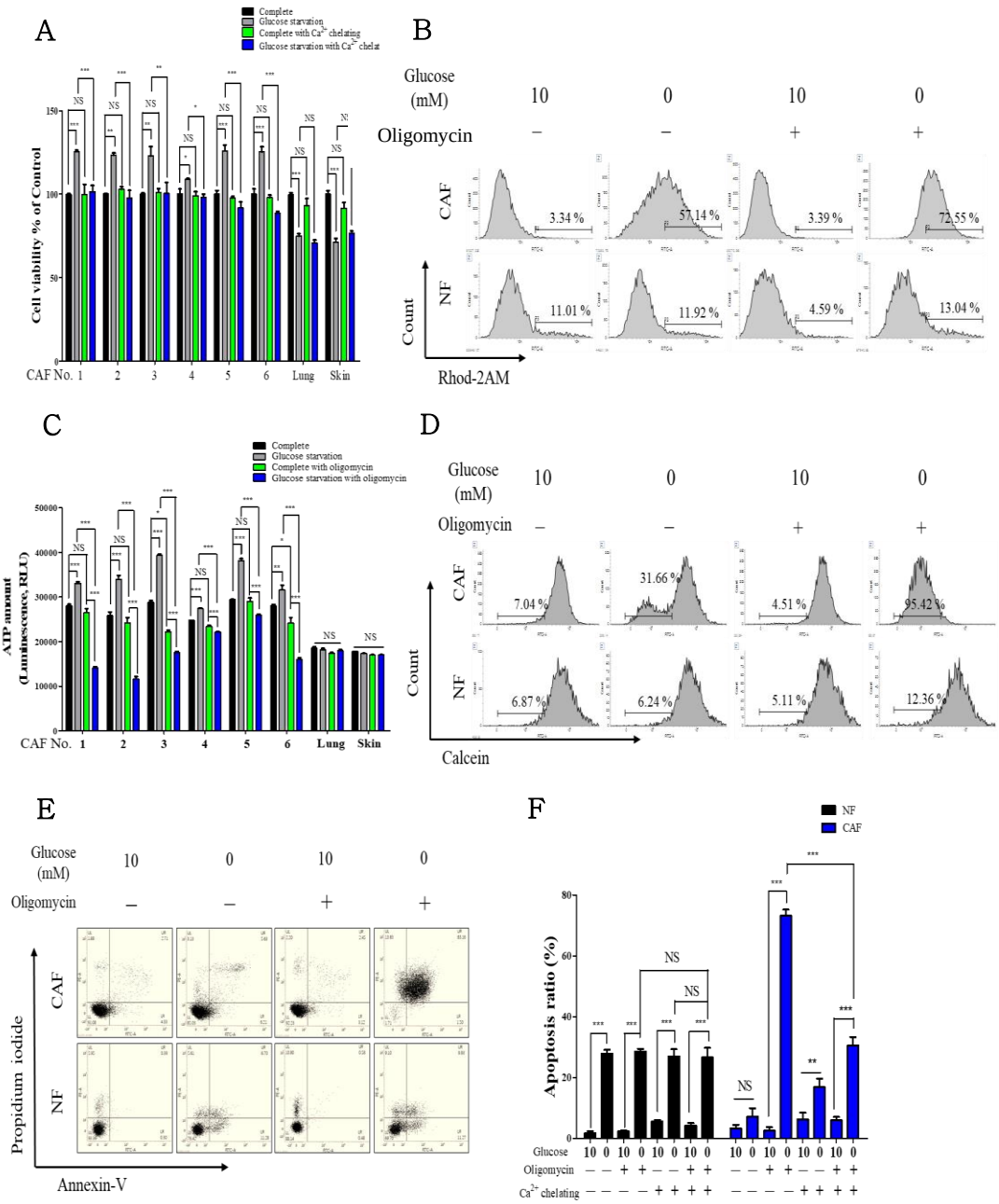
A
Complete
Glucose starvation
Complete with Ca2+ chelating
Glucose starvation with Ca2+ chelat
Cell viability % of Control
CAF No. 1 2 3 4 5 6 Lung Skin
B
Glucose (mM) 10 0 10 0
Oligomycin – – + +
CAF
NF
3.34 %
57.14 %
3.39 %
72.55 %
11.01 %
11.92 %
4.59 %
13.04 %
Count
Rhod-2AM
C
Complete
Glucose starvation
Complete with oligomycin
Glucose starvation with oligomycin
ATP amount (Luminescence, RLU)
CAF No. 1 2 3 4 5 6 Lung Skin
D
Glucose (mM) 10 0 10 0
Oligomycin – – + +
CAF
NF
7.04 %
31.66 %
4.51 %
95.42 %
6.87 %
6.24 %
5.11 %
12.36 %
Count
Calcein
E
Glucose (mM) 10 0 10 0
Oligomycin – – + +
CAF
NF
Propidium iodide
Annexin-V
F
NF
CAF
Apoptosis ratio (%)
Glucose 10 0 10 0 10 0 10 0 10 0 10 0 10 0 10 0
Oligomycin – – + + – – + + – – + + – – + +
Ca2+ chelating – – – – + + + + – – – – + + + +

Figure 6. Mitochondrial calcium is essential for cell viability and ATP production by ATP synthase

(A) The viability of CAFs and NFs cultured in complete medium or glucose starvation with or without oligomycin treatment for 1 day. $^{*}P < 0.05$, $^{**}P < 0.01$, and $^{***}P < 0.001$. (B) Assessment of mitochondrial calcium amount in CAFs and NFs cultured in complete medium or glucose starvation with or without oligomycin treatment for 1 day. $^{**}P < 0.01$, and $^{***}P < 0.001$. (C) ATP production in CAFs and NFs cultured in complete medium or glucose starvation with or without oligomycin treatment. $^{*}P < 0.05$, $^{**}P < 0.01$, and $^{***}P < 0.001$. (D) Activation of mPTP in CAFs and NFs cultured in complete medium or glucose starvation with or without oligomycin treatment. The P1 population in CAF cultured in complete medium was used as a comparison. $^{***}P < 0.001$. (E) Analysis of apoptosis in CAFs and NFs cultured in complete medium or glucose starvation with or without oligomycin treatment. $^{*}P < 0.05$, $^{**}P < 0.01$, and $^{***}P < 0.001$. (F) The viability of CAFs and NFs cultured in complete medium or glucose starvation with or without calcium chelator treatment (EDTA and BAPTA-2AM). $^{***}P < 0.001$.

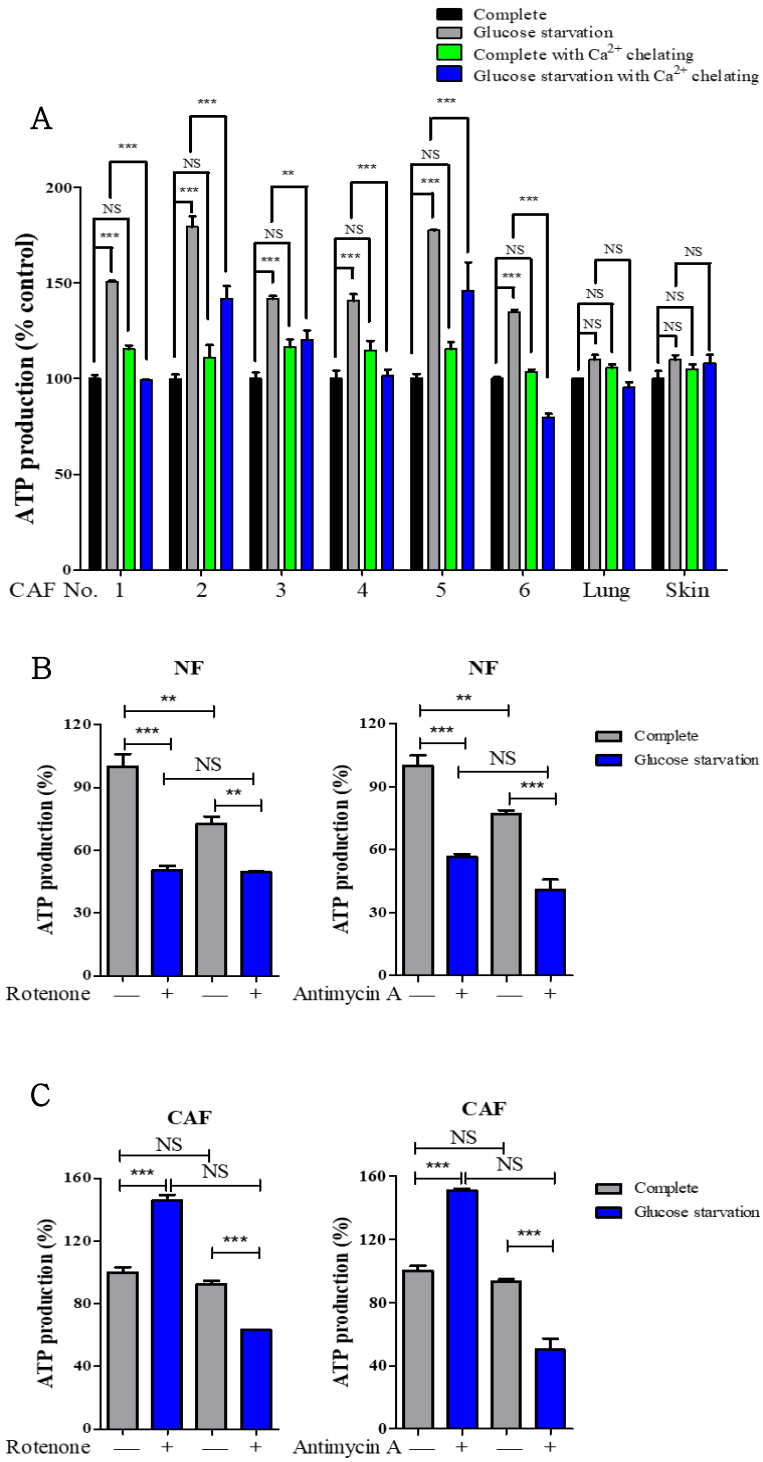
A
Complete
Glucose starvation
Complete with Ca2+ chelating
Glucose starvation with Ca2+ chelating
ATP production (% control)
CAF No. 1 2 3 4 5 6 Lung Skin
B
NF
ATP production (%)
Rotenone
Antimycin A
Complete
Glucose starvation
C
CAF
ATP production (%)
Rotenone
Antimycin A
Complete
Glucose starvation

Figure 7. Increased calcium coordinates ATP production in CAFs by activation of ATP synthase complex

(A) ATP production in CAFs and NFs that were cultured in complete medium/glucose starvation with or without the calcium chelator. $^{**}P < 0.01$ and $^{***}P < 0.001$. (B, C) ATP production in NFs and CAFs that were treated with antimycin A or rotenone, inhibitors of ATP synthase complex III or I, respectively. $^{***}P < 0.001$.

Discussion

The tumor mass consists of cancerous and noncancerous cells. CAFs are representative noncancerous cells that promote tumor malignancy through various interactions with cancer cells (Cat et al. 2006). Distinct microenvironment in a tumor mass is characterized by limited glucose diffusion and oxygen supply due to irregular angiogenesis, which exacerbates cancer cell malignancy via metabolic alteration and destabilization (Galluzzi et al. 2013, Chang et al. 2015, Endo et al. 2018). The present study revealed heterogeneity in the phenotypes and underlying molecular mechanisms in CAFs under glucose deficient conditions compared to those of NFs.

A distinct metabolism is activated in the hostile microenvironment, promoting tumor progression. HIF-1α and GLUT1 are representative markers of the cancer cell metabolism, including glycolysis and oxidative phosphorylation (Chen et al. 2015). HIF-1α subunits bind to CBP/p300, which induces transcriptional activation of oncogenes that promote poor prognosis with upregulation of VEGF and TGF-β signaling (Masoud 2015). The present study showed that GLUT1 and HIF-1α were significantly increased in CAFs compared to those of NFs, with heterogeneity in their expression depending on regions in the tumor mass. Intriguingly, ATP production also showed a similar pattern to these gene expression levels. Our data also revealed that the survival and proliferation of CAFs were significantly increased under glucose starved condition, while NFs were not.

TGF-β secreted from CAFs promotes tumor progression by enhancing the EMT, Wnt signaling and calcium influx (McGowan et al. 2002, Guido et al. 2012, Calon et al. 2014). Additionally, CAF-derived TGF-β influences cancer cells, tumor-associated macrophages and lymphocytes for tumor progression, immune suppression and limited differentiation, respectively (Ziani et al. 2018). Moreover, oxidative stress upregulates TGF-β expression in cancer cells by nutrient starvation (Guido et al. 2012). The present study showed that CAFs significantly upregulated TGF-β, subsequently enhancing cell viability and ATP production under glucose starvation, but not in NFs.

Moreover, activated TGF-β signaling increased intracellular and mitochondrial calcium in glucose-starved CAFs. Calcium is a critical second messenger for a variety of intracellular signaling pathways that are involved in cell proliferation and apoptosis. Intracellular calcium is mainly stored in the endoplasmic reticulum. However, in stimulated cells, a high concentration of calcium accumulates in mitochondria through MCU, mPTP and NCX (Pinto et al. 2015). Among these channels, the MCU is more predominantly involved in mitochondrial influx of calcium than the other channels (Clapham 2007, Griffiths and Rutter 2009, Santo-Domingo and Demaurex 2010). In this study, MCU expression was significantly increased in CAFs under glucose deficient conditions. Additionally, the significant increase in mitochondrial calcium was returned to normal levels by Ru360 treatment in glucose-starved CAFs, indicating the critical role of MCU in

this process. Ru360 treatment also suppressed the TGF-β signaling pathway, suggesting a positive feedback of MCU in TGF-β signaling. MCU overexpressing macrophage exhibits higher TGF-β expression via increase of mitochondrial ROS and ATP production compared with control, whereas the expression is significantly suppressed in MCU deleted mice (Gu et al. 2017). However, the precise interaction between TGF-β signaling and MCU in CAFs warrants further study.

In cancer cells, intracellular calcium promotes energy-dependent cellular processes such as cytoskeleton elongation, extracellular matrix remodeling and metastasis (Brini et al. 2013). However, the role of calcium in CAFs remains unclear. In mitochondria, calcium is conjugated with the F0 site of ATP synthase to produce ATP (Griffiths and Rutter 2009, Tarasov et al. 2012, Bonora et al. 2013). Our data demonstrated that ATP production was significantly increased in glucose-starved CAFs and was dependent on the calcium level in the mitochondria. Our data demonstrated that ATP production was significantly increased in glucose-starved CAFs which was dependent on mitochondrial calcium-mediated ATP synthase activation. However, ATP production by mitochondrial complex V was minor in NF, whereas it was critically affected by activation of complex I and III. Likewise, MCU-mediated mitochondrial calcium increase activates oxidative phosphorylation with enhancement of oxygen consumption, eliciting ATP production (Gu et al. 2017). Accordingly, depletion of calcium in the mitochondria by chelation or Ru360 treatment significantly suppressed ATP

production and cell proliferation in glucose-starved CAFs. However, NFs exhibited constant ATP production and cell viability independent of mitochondrial calcium or MCU levels.

Furthermore, our data revealed that inhibition of ATP synthase by oligomycin markedly suppressed cell proliferation and enhanced apoptosis in glucose-starved CAFs through excessive calcium entry into mitochondria. Cyclophilin D (CyPD), which is a regulator of the mPTP is binding with F0F1 site of ATP synthase and it is suppressed by ATP synthase inhibitor treatment (Giorgio et al. 2013). Additionally, CyPD aberrant model shows significantly higher mitochondrial calcium level compared with the control model (Elrod et al. 2010), and chronic irregular mPTP might release the cytochrome C, leading to apoptotic signaling (Giorgi et al. 2012).The present study also revealed that increased mitochondrial calcium activated ATP synthase and maintained calcium homeostasis through mPTP activation in glucose-starved CAFs. In particular, treatment of glucose-starved CAFs with oligomycin caused mPTP dysfunction that led to excessive mitochondrial calcium and a significant increase of apoptosis. Additionally, calcium chelation alleviated apoptosis induced by oligomycin in glucose-starved CAFs.

CHAPTER III.

Oleic acid from CAF promoted stemness in H460 cells through YAP nuclear translocation under glucose-deficient condition

Abstract

CAFs coordinate the malignancy of cancer cells via secretory regulators. Reprogrammed lipid metabolism and signaling play critical roles in cancer biology. Oleic-acid (OA) serves as a source of energy under glucose-deficient conditions, but its function in cancer progression remains unclear. The present study showed that CAFs in xenografted tumors had reprogrammed lipid metabolism with higher amounts of fatty acids, particularly OA, compared to normal fibroblasts. We further investigated the impact of the OA-derived from CAFs on phenotypes of lung adenocarcinoma cells under glucose-deficient condition. Transfer of the CAF-derived OA upregulated stearoyl-CoA desaturase (SCD) in cancer cells under glucose-deficient conditions, resulting in enhanced lipid metabolism and autophagosome maturation. By OA treatment under glucose deficient condition, cancer cell stemness was significantly enhanced through sequential activation of SCD, F-actin polymerization, and nuclear translocation of yes-associated protein (YAP). These findings were confirmed by experiments using chemical inhibitors, SCD-overexpressing cells and SCD-knockout (KO) cells. When xenografted, SCD-overexpressing cells produced larger tumors compared with parental cells, while SCD-KO cells resulted in much smaller tumors. Analysis of tissue microarray from lung adenocarcinoma patients revealed that SCD expression was the marker for poor prognosis involving tumor grade, clinical stage and survival rate. Our data indicate that CAFs-derived OA activated lipid metabolism in lung adenocarcinoma cells under glucose-deficient conditions, promoting stemness and progression toward malignancy.

Introduction

A hostile microenvironment for cancer cell is established by abnormal angiogenesis and affects the metabolic profile in the tumor tissue (Chang et al. 2015, Gupta et al. 2017). Cancer cells consume high amounts of glucose and oxygen to produce ATP, resulting in glucose deficiency. Glucose starvation confers metabolic reprogramming in cancer cells via dysregulated AMPK expression (Wang et al. 2018). For example, lipid metabolism is activated to compensate the energy demand through enhanced β-oxidation under glucose-deficient conditions (Van Cutsem and Arends 2005, Durham et al. 2018). Alternatively, lipids-mediated autophagy provides an energy source during glucose starvation (Dong and Czaja 2011, Li et al. 2017). Stearoyl-CoA desaturase (SCD) is essential for the earliest step of autophagosome formation that supports the undisturbed growth of cancer cells (Ogasawara et al. 2014). High expression of SCD is associated with poor prognosis and metastasis in patients with colorectal cancer (Ran et al. 2018).

CAFs modulate the microenvironment around cancer cells. They produce extracellular matrix and interact with cancer cells via secretory materials (Erdogan and Webb 2017). In tumor masses, various molecules are biosynthesized in CAFs, affecting cancer cell phenotypes (Chen et al. 2009, Sullivan et al. 2019). Moreover, CAFs supplement the metabolic needs of cancer cells by providing essential nutrients and energy-rich metabolites (Wu et al. 2017). Direct transfer of CAF-derived metabolites to cancer cells increases the mitochondrial activity via upregulation of SIRT1-dependent

peroxisome proliferator-activated receptor gamma coactivator 1-α (Ippolito et al. 2019).

Oleic acid (OA), a monounsaturated fatty acid (MUFA), is essential to produce energy by activation of β-oxidation in cancer cells (Lim et al. 2013). SCD catalyzes the biogenesis of MUFA from saturated fatty acid (SFA). Loss of SCD results in aberrant lipid metabolism, leading to insulin resistance and lipotoxicity (Paton and Ntambi 2009). SCD deficiency also impairs mitochondrial function and affects β-oxidation, ATP production, and oxidative phosphorylation (OXPHOS) (Dobrzyn et al. 2008, Wajner and Amaral 2016). In contrast to normal cells, cancer cells use of fatty acids to produce ATP for the rapid growth and actin polymerization (Dobrzyn et al. 2004, Kelley et al. 2019).

Although CSCs account for a very small portion, they are responsible for tumor initiation, metastasis and tumor recurrence. Compared to the more differentiated cells that mostly rely on OXPHOS, CSCs have increased glycolysis as well as OXPHOS (Wong et al. 2017). In CSCs, metabolic reprogramming from OXPHOS to glycolysis is facilitated by transcription factors including Sox2, Oct4 or Myc (De Francesco et al. 2018). Additionally, lipid desaturation is crucial for the maintenance of cancer cell stemness (Yi et al. 2018). Likewise, SCD1 is highly expressed in the CSC subpopulation of human bladder cancer (Piao et al. 2019), while silencing of SCD reduces CSC formation and mitigates cisplatin resistance (Pisanu et al. 2017).

The present study showed that lipogenesis is activated in CAFs via SCD upregulation under glucose-deficient conditions. And CAF-derived OA was

transferred to cancer cells where they increased SCD expression and promoted stemness via nuclear translocation of YAP. Our data suggested that deregulated lipid metabolism and lipid desaturases could be a valuable target for the development of cancer therapy.

Materials and Methods

Mouse xenograft models

Four five-week-old BALB/c nude mice were purchased from Jungang Lab Animal, Inc. (Seoul, South Korea) and were subcutaneously injected with 1×10^7 NCI-H460 (H460) cells suspended in Matrigel (Corning, New York, USA). The resultant tumor masses from the four mice were resected for primary culture as described in the *Primary culture and fibroblast isolation* section. Parental, SCD-KO, and SCD-pCDH H460 cells were prepared as described in the *Generation of genetically engineered cells with dysregulated SCD expression* section. Mice were sacrificed four weeks after injection of the cells and the resultant tumor masses were collected.

Cell culture and reagents

Complete medium contained 10 mM glucose and prepared according to (Hwang et al. 2019). Glucose-deficient medium was prepared as per the complete RPMI medium, but without glucose. Oleic acid (OA; Sigma-Aldrich) was dissolved in DMSO and cells were treated with 100 μM. SCD, lipid transporter, β-oxidation, and actin polymerization were chemically inhibited using CAY10566 (Cayman Chemical, Ann Arbor, MI, USA), sulfo-N-succinimidyl oleate (Cayman Chemical), etomoxir (Sigma-Aldrich), and latrunculin A (Cayman Chemical), respectively. Autophagy was blocked using CQ (Sigma-Aldrich) and 3-MA (Sigma-Aldrich).

Primary culture and fibroblast isolation

Tissues containing underarm skin and xenografted tumor mass from four individual mice were used for primary culture. Primary cells passaged up to

four times were used for further experiments. Fibroblasts were isolated from the primary cultured cells of tumor mass and skin tissues using a commercial kit (Miltenyi Biotec) according to manufacturer's instructions (Agorku et al. 2019). To confirm the phenotype of the isolated fibroblasts, flow cytometry was performed using FACSVerse (BD Biosciences) with antibodies against FAP (Abcam) and CD90 (Novus Biologicals).

Measurement of cell viability

Cell viability was measured using MTT assay (Sigma-Aldrich) (Hwang et al. 2019). The absorbance was measured at 570 nm using a microplate reader (BioTek Epoch).

Measurement of apoptosis

Apoptotic rate was measured using EzWay Annexin V-FITC apoptosis detection kits (Koma Biotech) as described in (Hwang et al. 2019). The cells analyzed with flow cytometry (BD Biosciences).

Analysis of fatty acid methyl esters

Lipid was extracted cell pellets and conducted fatty acid methyl esters (FAMEs) at NICEM of Seoul National University. Content of fatty acids was calculated as referred (Garces and Mancha 1993).

Analysis of cell lipid droplets

Cultured cells were stained with BODIPY 493/503 (BODIPY; Invitrogen) according to manufacturer's recommendation and analyzed by flow cytometry (BD Biosciences). Within BODIPY staining, P2 and P3 populations were established using untreated H460 cells. The staining of lipid droplets was assessed using a CLSM (Carl Zeiss).

Western blot assay

Membrane loaded with protein (10 ng) was incubated in blocking solution containing antibodies against SREBP (Santa Cruz Biotechnology), SCD (Cell-Signaling Technology), mTOR (Cell-Signaling Technology), BECN-1 (Santa Cruz Biotechnology), LC3 (Novus Biologicals), ATG5 (Cell-Signaling Technology), Oct4 (Santa Cruz Biotechnology), Nanog (Cell-Signaling Technology), Yes-associated protein (YAP; Santa Cruz Biotechnology), F-actin (Abcam), p-Cofilin (Cell-Signaling Technology), and β-actin (Cell-Signaling Technology) overnight at 4 °C. Secondary horseradish peroxidase (HRP)-conjugated anti-rabbit (Santa Cruz Biotechnology) or mouse (Santa Cruz Biotechnology) antibody was added and incubated for 2 h. The protein expression was detected by chemiluminescence imaging system (ATTO) following the spread of Luminata Forte Western HRP Substrate (Merck Millipore). Densitometric analysis was performed using the ImageJ program (NIH, Bethesda, MD, USA) (http://rsbweb.nih.gov/ij).

Immunofluorescence staining assay

H460 cells were cultured in confocal dishes (SPL Life Science) and performed fixation, permeabilization and incubated with antibodies including Oct4 (Santa Cruz Biotechnology), YAP (Santa Cruz Biotechnology), and F-actin (Abcam). The cells were incubated with either Alexa Fluor 488 or 647-conjugated secondary antibody (Molecular Probes). Nuclei were stained with DAPI contained mounting solution (Southern Biotechnology, Birmingham, AL, USA). Mitochondria in the H460 cells were stained using Mitotracker deep red (Invitrogen).

Measurement of free fatty acid (FFA)

The amount of FFA was measured using EZ-Free Fatty Acid Assay Kits (Dogen, Seoul, South Korea) according to manufacturer's instruction. The absorbance was measured using a microplate reader (BioTek Epoch), and the amount of FFA was calculated based on the value of the standards.

Quantitative real-time PCR

Total RNA was extracted using TRIzol reagent (Ambion) and quantified using a microplate reader (BioTek Epoch). A total of 500 ng of total RNA was used for cDNA synthesis using TOPscript cDNA Synthesis kits (Enzynomics). Gene expression was quantified using a SYBR Green Real-time PCR kit (Enzynomics). Relative expression levels were normalized using GAPDH, and calculated using the ΔΔCt method (Rao et al. 2013).

ATP measurement

ATP synthesis was assessed using the Cell-Titer-Glo Reagent (Promega) according to the manufacturer's instructions. Briefly, detection reagent was added and incubated at room temperature for 10 min. Subsequently, luminescence was measured using a luminometer (Infinite M200 Pro; Tecan, Mannedorf, Switzerland).

Flow cytometry

Harvested cells were incubated in blocking solution with primary antibodies against FAP (Abcam), CD90 (Novus Biologicals), CD133 (BD Biosciences), and CD44 (BD Biosciences) on ice. Cells were then further incubated with Alexa Fluor 488-conjugated anti-mouse secondary antibody (Molecular Probes) or Alexa Fluor 647-conjugated anti-rabbit secondary

antibody (Molecular Probes) on ice and in the dark. Flow cytometry was performed using FACSVerse (BD Biosciences) immediately after washing with PBS.

Autophagosome maturation detection

Autophagosome maturation was assessed using Cyto-ID autophagy detection kits (Enzo Life Sciences, Farmingdale, NY, USA) according to the instruction and analyzed by flow cytometry (BD bioscience). The level of autophagosome maturation in the cells was analyzed by comparing with the P2 population that was established using a negative control, untreated H460 cells.

Spheroid formation

H460 cells were mixed with 2% B27 (Invitrogen), basic fibroblast growth factor (20 ng/mL) (Invitrogen), and epithelial growth factor (20 ng/mL) (Invitrogen) in complete medium or glucose-deficient conditions and placed in 6-well ultralow attachment plates (SPL Life Science) for 72 h. Over 100 μm of spheroids were determined by ImageJ software (NIH) and counted.

Generation of genetically engineered cells with dysregulated SCD expression

A human SCD-coding sequence with corresponding restriction sites, NheI and BamHI, was cloned and inserted into pCDH-EF1-MCS-T2A-puro lentiviral vector (Biocat, Heidelberg, Germany) to produce an SCD-pCDH construct. The pCDH-EF1 lentiviral vector was used as a vehicle control. The SCD-pCDH lentiviral vector was transfected to 293T cells with second viral packaging reagents, and viral particles were collected. After incubation

of H460 cells with the viral particles and polybrene (Merck Millipore), SCD-pCDH positive cells were selected by treatment with puromycin.

Either SCD-sgRNA-U6 plasmid (Suppl. Table S1) (Toolgen, Seoul, South Korea) or control-sgRNA was transfected into H460 cells with CRISPR/Cas9-puromycin-CMV plasmid vector (Toolgen) and lipofectamine-3000 (Invitrogen). Cell colonies that survived treatment with puromycin were individually cultured and followed by assessment of SCD expression by Western blot and RT-PCR. Subclones of the SCD-KO cells were used for further experiments.

Analysis of the correlation between SCD expression and survival in lung cancer patients

Kaplan-Meier plotter tools were applied to analyze the correlation between expression of SCD and overall survival (OS), progression-free survival (PFS), and post-progression survival (PPS) in patients with lung adenocarcinoma using a web-based tool available at http://kmplot.com/analysis/index.php?p=service&cancer=lung (Győrffy et al. 2013). Hazard ratios, 95% confidence intervals, and log rank *P*-values were described for each result.

Analysis of SCD expression in lung adenocarcinoma tissue microarray

Immunohistochemistry (IHC) for SCD was performed in lung adenocarcinoma tissue microarray (US Biomax, Rockville, MD, USA) according to the manufacturer's instructions (Winslow et al. 2011). The prepared tissues microarray slides were incubated with SCD antibody (Cusabio technology, Houston, TX, USA) for overnight and incubated with

horse anti-rabbit secondary antibody (Vector Laboratories, Burlingame, CA, USA) for 2 h. Following treatment with 3,3'-diaminobenzidine solution (Vector Laboratories), slides were counterstained using hematoxylin, dehydrated in alcohol, and mounted in a xylene-based solution. The mean IHC staining intensity for SCD was quantified using ImageJ software and scored 0–3 as follows (Prasad and Prabhu 2012): 0, no staining; 1, <15 mean intensity; 2, 15–50 mean intensity; and 3, >50 mean intensity.

Statistical analysis

In vitro experiments were performed independently at least three times and data values were presented as the mean ± SD. Statistical analyses were performed using GraphPad Prism Software (GraphPad Software). *P*-values were calculated by one-way analysis of variance or Tukey's pairwise comparison. All results were considered statistically significant with *P*-values < 0.05, 0.01 and 0.001.

Results

CAF culture supernatant boosted cancer cell malignancy under glucose-deficient conditions

CAFs and normal fibroblasts (NFs) isolated from primary cultures of four tumor masses and skin were validated by flow cytometry using antibodies against FAP and CD90. In contrast to the negative staining in H460 cells, >91% of CAFs and NFs were positive for FAP and CD90 (Fig. 2 A). To determine the effects of cell free media, supernatants were collected from the culture media from H460 cells, NFs, and CAFs. H460 cells were treated with the supernatants for one day, followed by incubation for one further day in either complete or glucose-deficient media. The viability of H460 cell was significantly enhanced by CAF supernatant but was not affected by NF supernatant (Fig. 1 A). Moreover, pretreatment with CAF supernatant increased resistance to cisplatin under glucose-deficient conditions (Fig. 1 B). Treatment with cisplatin induced total apoptosis in H460 cells that were pretreated with H460 and NF supernatants by 80% and 38%, respectively. In contrast, the total apoptosis significantly decreased to 23% following pretreatment with CAF supernatant and was further suppressed to around 13% under glucose-deficient conditions. Although treatment with NF supernatant reduced total apoptosis compared with H460 supernatant under glucose-deficient conditions, it was lower than treatment with CAF supernatants (Fig. 1 C). Under glucose-deficient condition, incubation of H460 cells with CAF supernatants exhibited a constant rate of apoptosis regardless of cisplatin treatment.

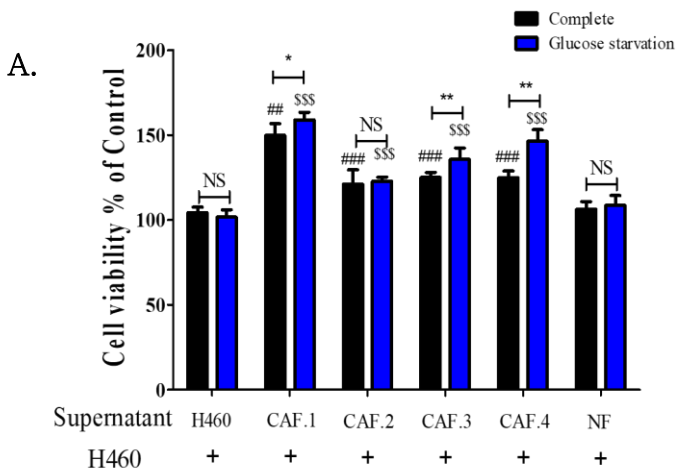
A.
Complete
Glucose starvation
Cell viability % of Control
200
150
100
50
0
NS
##
$$$
*
###
$$$
NS
###
$$$
**
###
$$$
**
NS
Supernatant
H460
CAF.1
CAF.2
CAF.3
CAF.4
NF
H460
+
+
+
+
+
+

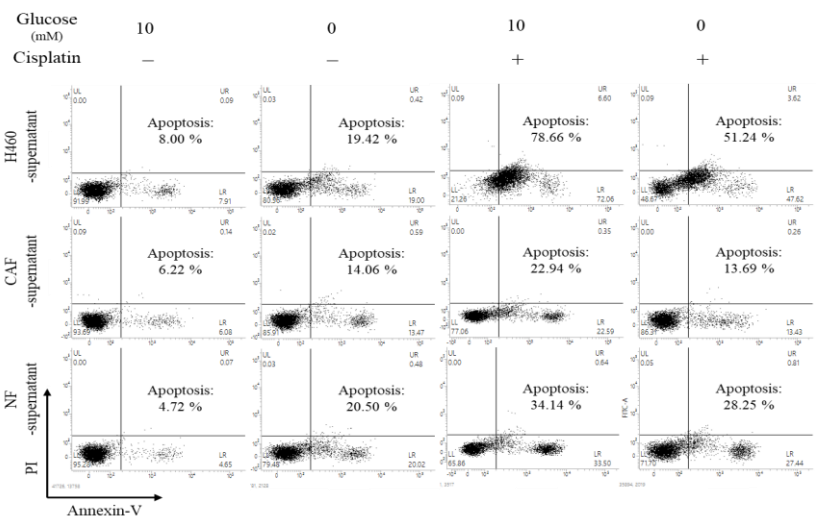
B.
Glucose (mM)
10
0
10
0
Cisplatin
–
–
+
+
H460 -supernatant
CAF -supernatant
NF -supernatant
Apoptosis: 8.00 %
Apoptosis: 19.42 %
Apoptosis: 78.66 %
Apoptosis: 51.24 %
Apoptosis: 6.22 %
Apoptosis: 14.06 %
Apoptosis: 22.94 %
Apoptosis: 13.69 %
Apoptosis: 4.72 %
Apoptosis: 20.50 %
Apoptosis: 34.14 %
Apoptosis: 28.25 %
PI
Annexin-V

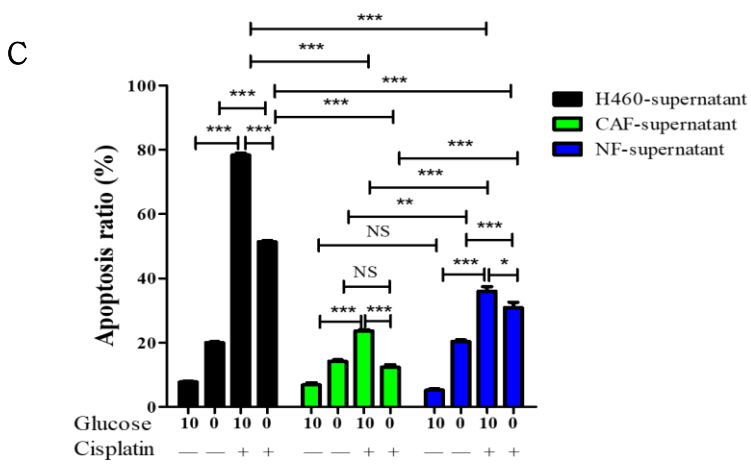
C
Apoptosis ratio (%)
100
80
60
40
20
0
H460-supernatant
CAF-supernatant
NF-supernatant
***
**
NS
*
Glucose
10 0 10 0 10 0 10 0 10 0 10 0
Cisplatin
— — + + — — + + — — + +

Figure 1. Cell viability and apoptosis of H460 cells that were treated with supernatant of CAFs culture under glucose-deficient condition

(A) Viability of H460 cells cultured in complete medium or glucose-deficient conditions for one day followed by treatment with supernatant of H460, CAFs, or NF for one day. CAFs. 1-4 was isolated from individual xenograft tumor mass. $^{\#\#}P < 0.01$, $^{\#\#\#}P < 0.001$ vs. H460 cells treated with H460 supernatant in complete medium. $^{\$\$\$}P < 0.001$ vs. H460 cells treated with H460 supernatant in glucose-deficient conditions. $^{**}P < 0.01$, $^{***}P < 0.001$. Error bars indicate the standard error of the mean (SEM; n = 8). (B) Representative dot plot showing flow cytometry for apoptosis assay in H460 cells that were pretreated with supernatant of H460, CAF, or NF, followed by culture in complete or glucose-deficient medium containing cisplatin (10 μM) for one day. (C) Statistical analysis of apoptotic rate. Error bars indicate SEM (n = 3). $^{*}P < 0.05$, $^{**}P < 0.01$ and $^{***}P < 0.001$.

SCD upregulation in CAFs stimulated lipogenesis and lipid transfer in cancer cells

In xenografted tumors, lipid levels were high in CAFs and gradually decreased away from the CAFs (Fig. 3 A). Oil red O staining revealed a similar pattern of lipids, which was exclusively detected in CAFs in tumor masses (Fig. 2 B). Analysis of fatty acids revealed that OA (C18:1n9) was higher than saturated fatty acids (SFA) involving palmitic acids (C16:0) and stearic acids (C18:0) in CAFs, but was lower in NFs (Fig. 2 B). In addition, CAFs isolated from individual tumor mass showed higher lipids amount than NFs and H460 cells (Fig. 2 C). Notably, SCD expression was significantly higher in CAFs than NFs (Fig. 3 C). To investigate the function of SCD in fatty acid synthesis, CAFs and NFs were treated with CAY10566, a selective inhibitor of SCD, and mRNA levels of ATP citrate lyase (ACLY), acetyl-CoA carboxylase (ACAC), and fatty acid synthase (FASN) were assessed. Comparative analyses revealed that high expression of SCD in CAFs increased the level of these genes but not in NFs (Fig. 3 D).

To determine whether CAF-derived lipids transferred to cancer cells, H460 cells were incubated with NF or CAF supernatant for one day, followed by measurement of lipid content. OA content was significantly higher in H460 cells treated with CAF supernatant than those treated with complete medium or NF supernatant, whereas content of SFAs was not changed by treatment with NF or CAF supernatants (Fig. 4 A). The P2 population in H460 cells treated with NF supernatant was used as a comparison. Treatment of H460 cells with CAF supernatant significantly

increased the P2 population to 31%, while it was reduced to 6.72% by CAY10566 treatment (Fig. 4 B). In contrast, the P2 population in H460 treated with NF supernatant was not affected by CAY10566 treatment. Likewise, SCD expression was increased in H460 cells treated with CAF supernatant, which was reversed by treatment with CAY10566 (Fig. 4 C). Additionally, H460 cells treated with CAF supernatant showed increased expression of the lipid transporters, CD36 and SLC27A1, but not ACLY, ACAC, and FASN (Fig. 4 D). Moreover, CAY10566 treatment significantly decreased the expression of CD36 and SLC27A1. In contrast, treatment with NF supernatant did not affect the expression of lipid transporters in cancer cells.

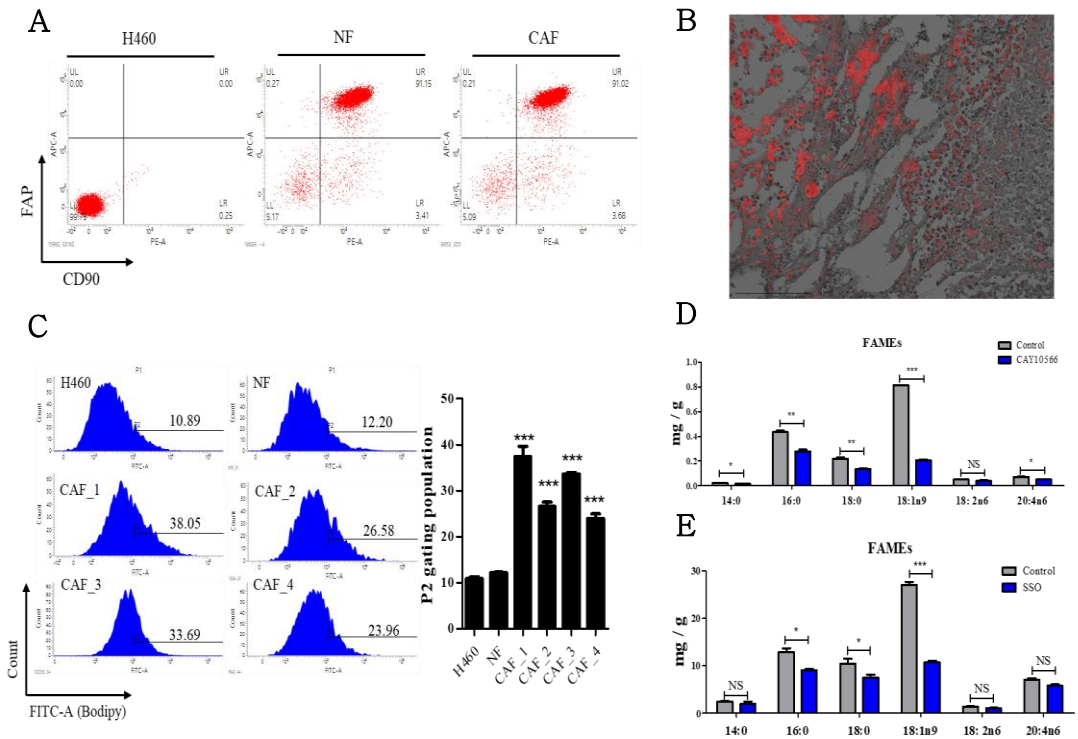

Figure 2. Phenotype of CAFs isolated from xenografted tumor mass

(A) Staining for CD90 and FAP in H460 cells, NFs and CAFs. (B) Representative image of oil red O staining in a xenografted tumor. Red fluorescence indicates oil red O staining. 4× magnification. Scale bar: 150 μm. (C) Representative histogram for BODIPY staining in H460 cells, CAFs and NFs. The P2 population was established using H460 cells. $^{***}P < 0.001$ vs. H460 cells. Data indicate the mean ± SEM (n = 3). (D) Profile of fatty acid contents in supernatant from nontreated and 1 μM CAY10566-treated CAFs. $^{***}P < 0.001$, Control vs CAY10566-treated CAFs. Data represent the mean ± SEM (n = 3). (E) Profile of fatty acid contents in H460 cells treated with 50 μM SSO and CAFs-supernatant for 1 day. $^{***}P < 0.001$, Control vs SSO-treated cells. Data represents the mean ± SEM (n = 3).

A

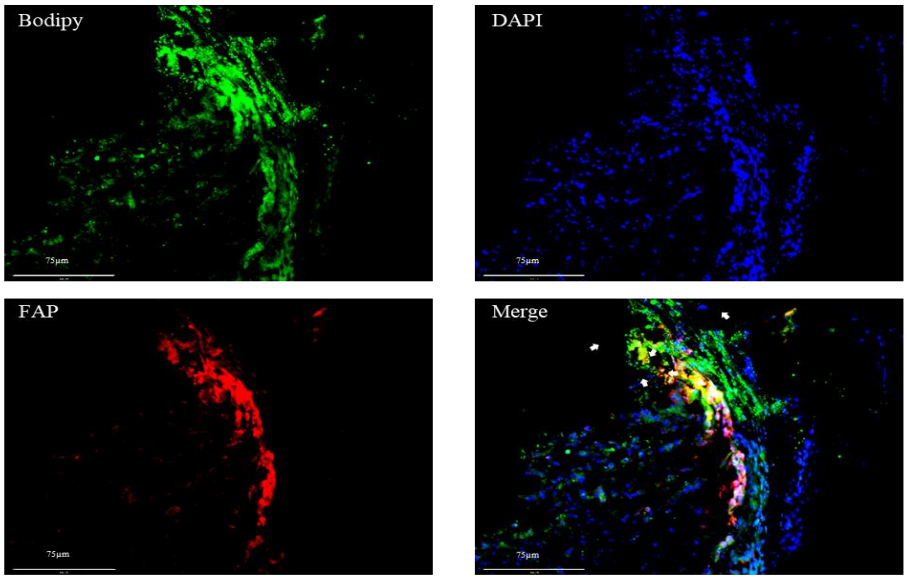
Bodipy
DAPI
FAP
Merge
75μm

B

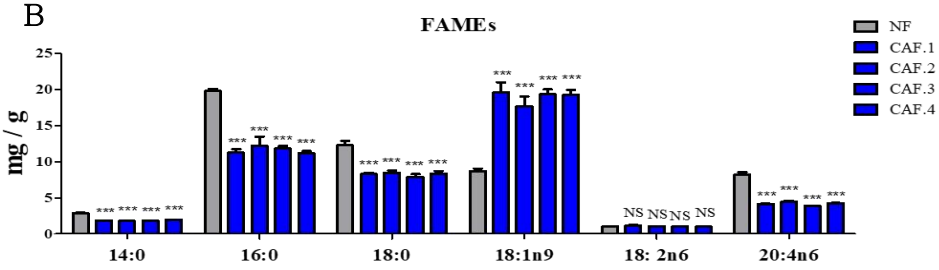
FAMEs
NF
CAF.1
CAF.2
CAF.3
CAF.4
mg / g
14:0
16:0
18:0
18:1n9
18: 2n6
20:4n6
NS

C

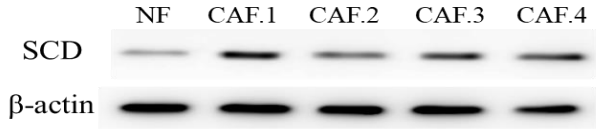
NF
CAF.1
CAF.2
CAF.3
CAF.4
SCD
β-actin

D

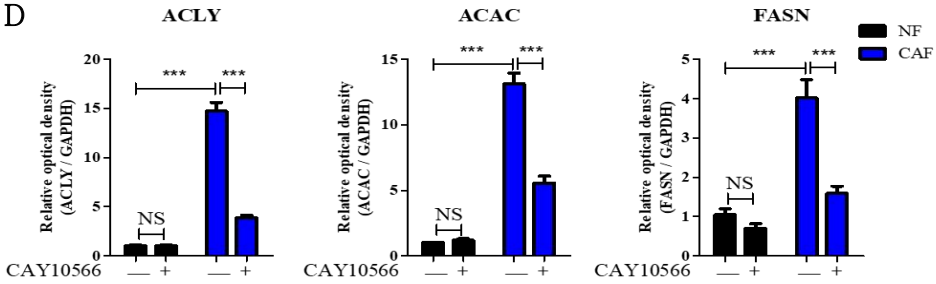
ACLY
ACAC
FASN
NF
CAF
Relative optical density (ACLY / GAPDH)
Relative optical density (ACAC / GAPDH)
Relative optical density (FASN / GAPDH)
NS
CAY10566

Figure 3. High amounts of lipid especially oleic acid in CAFs by SCD-mediated lipogenesis

(A) Representative fluorescence image of FAP, BODIPY, and DAPI staining in xenografted tumor. Red: FAP, green: BODIPY, blue: DAPI. 40× magnification. Arrowhead indicates co-localized FAP and BODIPY fluorescence. Scale bar: 75 μm. (B) Profile of fatty acids content in NF and CAF.1-4. $^{***}P < 0.001$, CAFs versus NF. Data represents the mean ± SEM (n = 3). (C) Expression of SCD and β-actin in NF and CAFs isolated from 1 to 4 individual tumor masses. (D) Transcription levels of ACLY, ACAC, and FASN in NF and CAF.1 which cultured in complete medium and treated with CAY10566 (1 μm). $^{***}P < 0.001$. Data represent the mean ± SEM (n = 4).

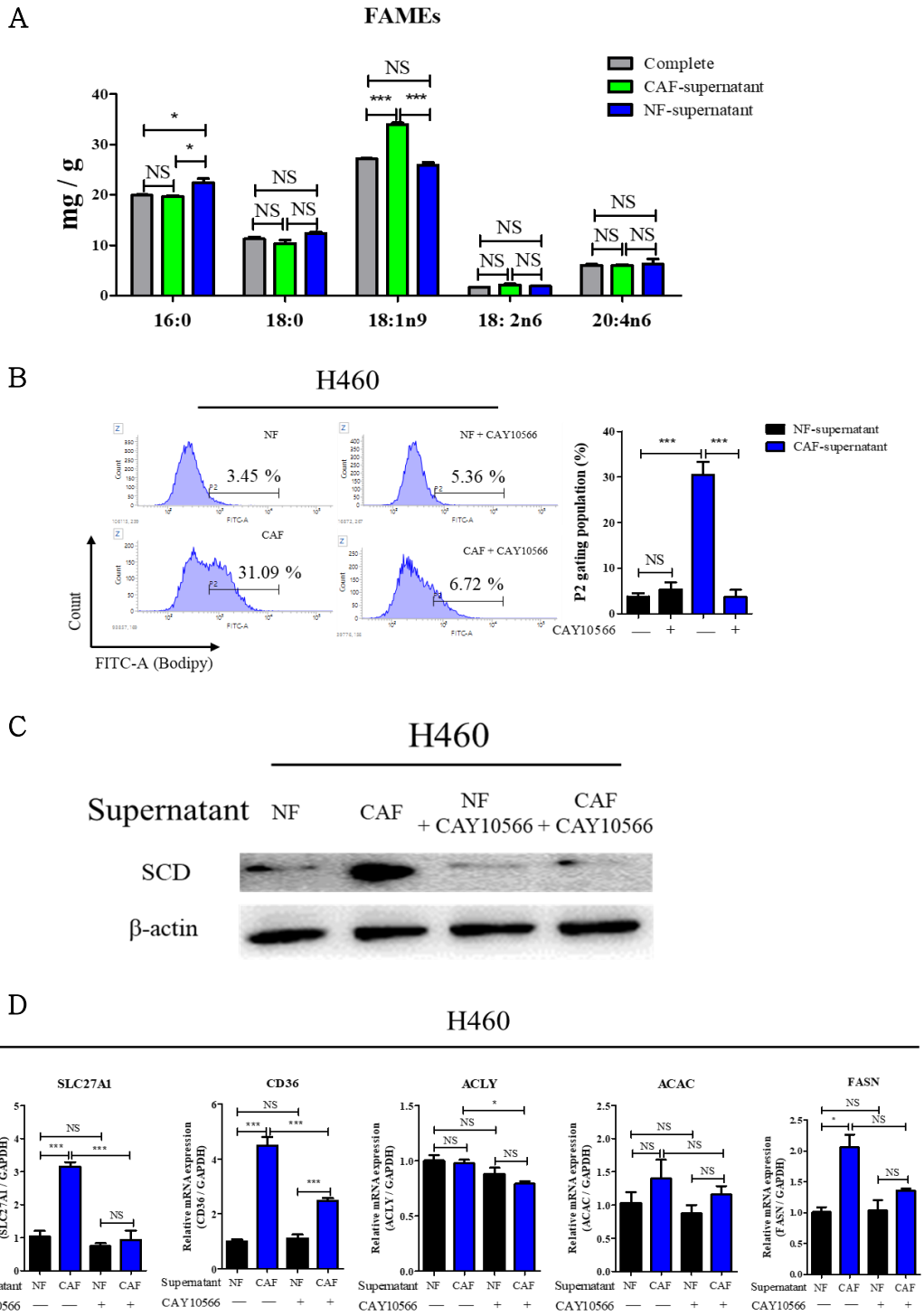
A
FAMEs
Complete
CAF-supernatant
NF-supernatant
mg / g
16:0
18:0
18:1n9
18: 2n6
20:4n6
B
H460
NF
3.45 %
NF + CAY10566
5.36 %
CAF
31.09 %
CAF + CAY10566
6.72 %
Count
FITC-A (Bodipy)
P2 gating population (%)
CAY10566
C
H460
Supernatant
NF
CAF
NF + CAY10566
CAF + CAY10566
SCD
β-actin
D
H460
SLC27A1
CD36
ACLY
ACAC
FASN
Relative mRNA expression (SLC27A1 / GAPDH)
Relative mRNA expression (CD36 / GAPDH)
Relative mRNA expression (ACLY / GAPDH)
Relative mRNA expression (ACAC / GAPDH)
Relative mRNA expression (FASN / GAPDH)
Supernatant
CAY10566

Figure 4. Transfer of CAF-derived oleic acid to cancer cells via upregulated lipid transporters

(A) Fatty acids profile in H460 cells treated with complete medium, NF and CAF.1 supernatant for 1 day. $^{*}P < 0.05$ and $^{***}P < 0.001$. Data represents the mean ± SEM (n = 3). (B) Representative histogram of BODIPY staining analysis in H460 cells incubated in complete medium with supernatant of NF or CAF.1 for one day and subsequently treated with CAY10566. Error bars represent SEM (n = 3). $^{***}P < 0.001$. (C) SCD protein expression and (D) mRNA expression of SLC27A1, CD36, ACLY, ACAC, and FASN in H460 cells incubated in complete medium with supernatant of NF or CAF.1 for one day and subsequently treated with CAY10566. $^{*}P < 0.05$ and $^{***}P < 0.001$. Data represents mean ± SEM (n = 4).

Stimulation of lipid catabolism by cell free lipid accelerated autophagosome maturation in cancer cells under glucose-deficient conditions

H460 cells treated with CAF supernatant showed greater fluorescence for lipids and FFA levels than those treated with NF supernatant and it was diminished under glucose-deficient conditions (Fig. 5 A, B). To further investigate of the role of cell free lipids, H460 culture media was supplemented with OA for one day. Lipid levels were evaluated in H460 cells using BODIPY staining. Addition of OA significantly increased the P3 population to approximately 85% in complete media, and to approximately 56% in glucose-deficient media (Fig. 6 A). Expression levels of SREBP and SCD were upregulated in H460 cells treated with CAF supernatant, which were further increased under glucose-deficient conditions (Fig. 5 C). Likewise, compared with cells cultured in complete media, lipid metabolism was further activated by OA treatment in glucose-starved cells, as indicated by upregulation of SREBP and SCD mRNA (Fig. 6 B, C). In glucose-starved H460 cells, OA treatment increased the expression of autophagy indicators, BECN1 and LC3, but reduced mammalian target of rapamycin (mTOR) (Fig. 7 A).

The P2 population of H460 cells were cultured in complete medium as a comparison to determine autophagosome maturation using Cyto-ID fluorescence. OA treatment increased the P2 population to 35%, which was further elevated to approximately 54% under glucose-deficient conditions (Fig. 7 B). Treatment with CAY10566 suppressed the P2 population by approximately 15% in glucose-starved H460 cells supplemented with OA

(Fig. 7 C). Additionally, under glucose-deficient conditions, OA treatment increased the expression of autophagosome markers, LC3-II and ATG5, which was reversed by treatment with CAY10566 (Fig. 5 D). Autophagosome maturation was targeted separately to assess the influence of autophagosome on SCD. Treatment with 3-methyladenine (3-MA) and chloroquine (CQ) blocked the autophagy response via inhibition of autophagosome formation and autophagosome-lysosome fusion, respectively (Mizushima et al. 2010). Intriguingly, in glucose-starved H460 cells supplemented with OA, CQ treatment augmented SCD expression, but 3-MA suppressed its expression (Fig. 7 D). Moreover, 3-MA and CQ treatment induced significant decrease and increase LC3-II expression, respectively.

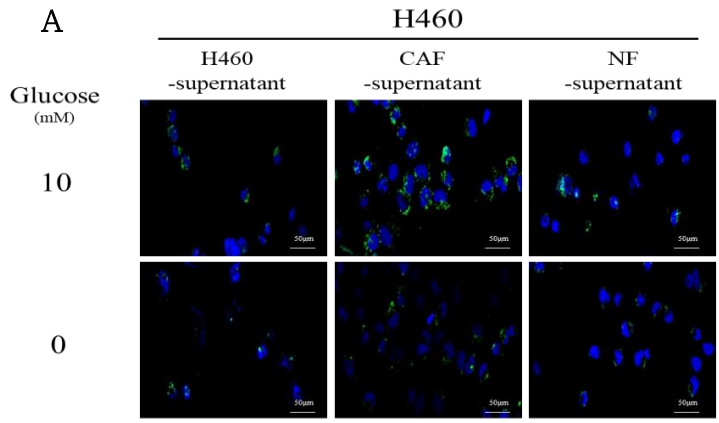
A
H460
H460
-supernatant
CAF
-supernatant
NF
-supernatant
Glucose
(mM)
10
0

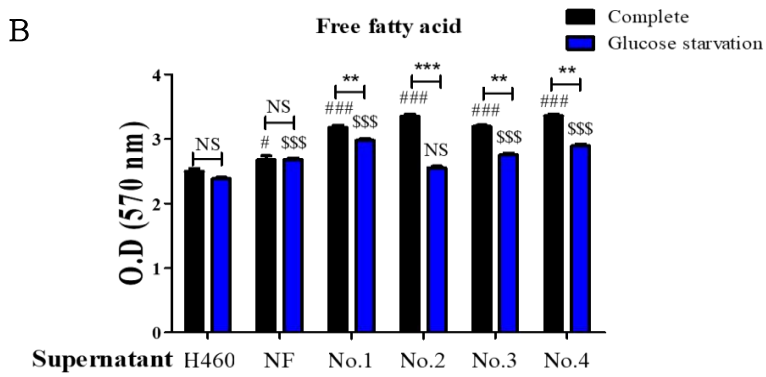
B
Free fatty acid
Complete
Glucose starvation
O.D (570 nm)
Supernatant H460 NF No.1 No.2 No.3 No.4

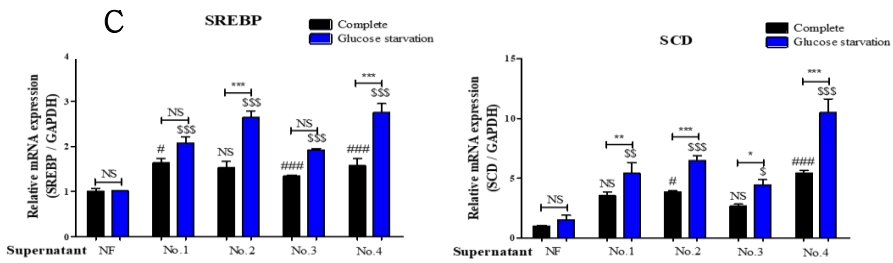
C
SREBP
SCD
Complete
Glucose starvation
Relative mRNA expression
(SREBP / GAPDH)
(SCD / GAPDH)
Supernatant NF No.1 No.2 No.3 No.4

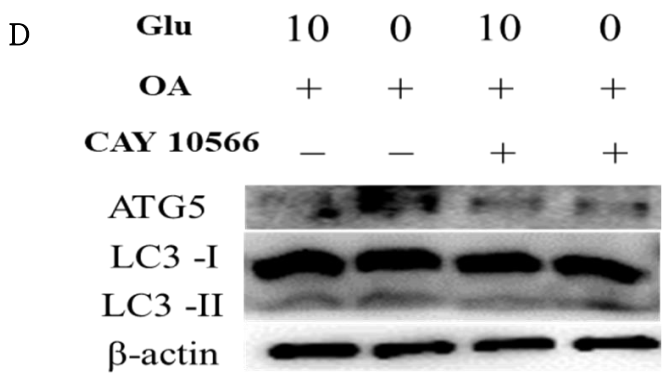
D
Glu 10 0 10 0
OA + + + +
CAY 10566 – – + +
ATG5
LC3 -I
LC3 -II
β-actin

Figure 5. Effect of glucose deficiency on lipid metabolism and autophagosome

(A) Representative fluorescence image of BODIPY staining in H460 cells incubated with NF or CAF supernatant in complete or glucose-deficient medium for one day. Green: BODIPY; blue: DAPI. 20× magnification. Scale bar: 50 μm. (B) Assessment of FFA levels in H460 cells incubated with supernatant of NF or CAF in complete or glucose-deficient medium for one day. $^{\$\$}P < 0.01$, $^{\$\$\$}P < 0.0001$ vs. treatment of H460 cells with H460 supernatant. $^{\#}P < 0.05$, $^{\#\#\#}P < 0.0001$ vs. treatment of glucose-starved H460 cells with H460 supernatant. $^{**}P < 0.01$ and $^{***}P < 0.001$. Error bars indicate SEM (n = 3). (C) Transcription levels of SREBP and SCD in H460 cells incubated with supernatant of NF or CAF and cultured in complete or glucose-deficient medium for one day. $^{\#}P < 0.05$, $^{\#\#}P < 0.01$, $^{\#\#\#}P < 0.001$ vs. treatment of H460 cells with H460 supernatant. $^{\$\$}P < 0.01$, $^{\$\$\$}P < 0.001$ vs. treatment of glucose starved H460 cells with H460 supernatant. $^{*}P < 0.05$, $^{**}P < 0.01$ and $^{***}P < 0.001$. Error bars indicate SEM (n = 4). (D) Expression of ATG5, LC3-I, LC3-II and β-actin in H460 cells treated with OA in complete or glucose-deficient medium.

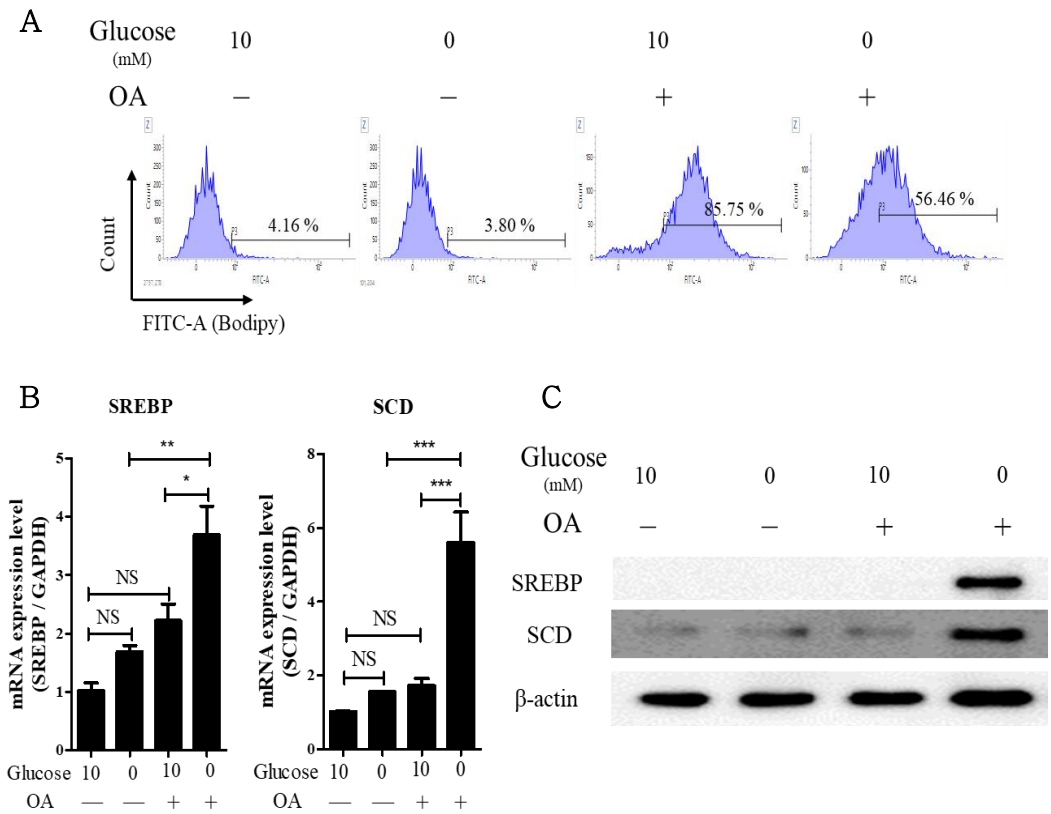

Figure 6. Significant enhancement of SCD in OA treated H460 cells under glucose-deficient condition

(A) Representative histogram showing BODIPY staining in H460 cells that were treated with OA in complete or glucose-deficient medium. Error bars represent the SEM (n = 4). $^{***}P < 0.001$. (B) Transcription levels and (C) protein expression of SREBP and SCD in H460 cells treated with OA in complete or glucose-deficient medium. $^{*}P < 0.05$, $^{**}P < 0.01$ and $^{***}P < 0.001$. Data indicate the mean ± SEM (n = 4).

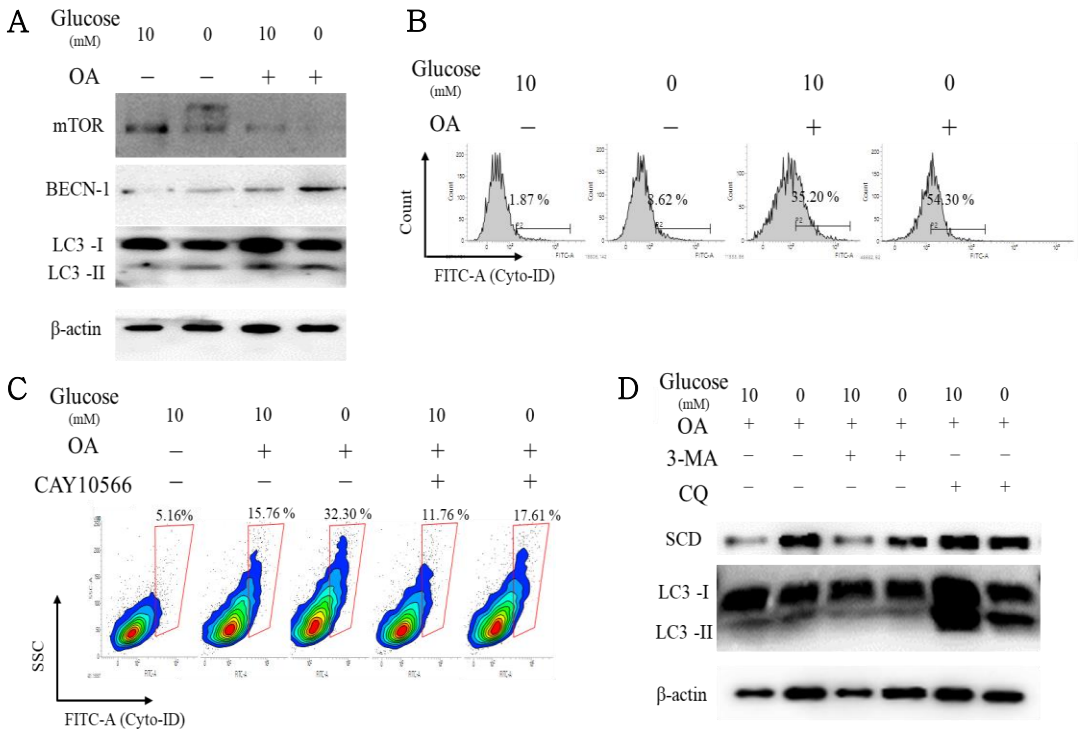

Figure 7. Increased SCD in glucose-starved H460 cells that were treated with OA enhances autophagic response

(A) Expression of mTOR, BECN-1, LC3-I, LC3-II, and β-actin in H460 cells treated with OA in complete or glucose-deficient medium. (B) Representative histogram of Cyto-ID staining of H460 cells treated with OA in complete or glucose-deficient medium. $^{***}P < 0.001$. The results from each experiment represent the mean ± SEM (n = 3). (C) Representative flow cytometric analysis of Cyto-ID staining in H460 cells treated with OA and CAY10566. $^{**}P < 0.01$ and $^{***}P < 0.001$. Data represent the mean ± SEM (n = 3). (D) Expression of SCD, LC3-I, LC3-II and β-actin in H460 cells treated with OA and either 3-MA or CQ in complete or glucose-deficient medium.

Cell free lipid augmented cancer cell stemness properties in glucose-deficient conditions

In H460 cells, expression of the stemness markers, Nanog and Oct4, were increased by OA treatment, which were further upregulated under glucose-deficient conditions (Fig. 8 A). In contrast, lipid levels determined by BODIPY staining were decreased in glucose-starved cells treated with OA (Fig. 8 B). These results indicated that digestion of lipids under glucose-deficient conditions augmented stemness. Approximately 35% of H460 cells treated with OA were positive for the CSC markers, CD133 and CD44, under glucose-deficient conditions, and the population was reduced to 20% following CAY10566 treatment (Fig. 8 C). Moreover, under glucose-deficient conditions, spheroid formation in H460 cells was enhanced by OA treatment, and was reversed by CAY10566 treatment (Fig. 8 D).

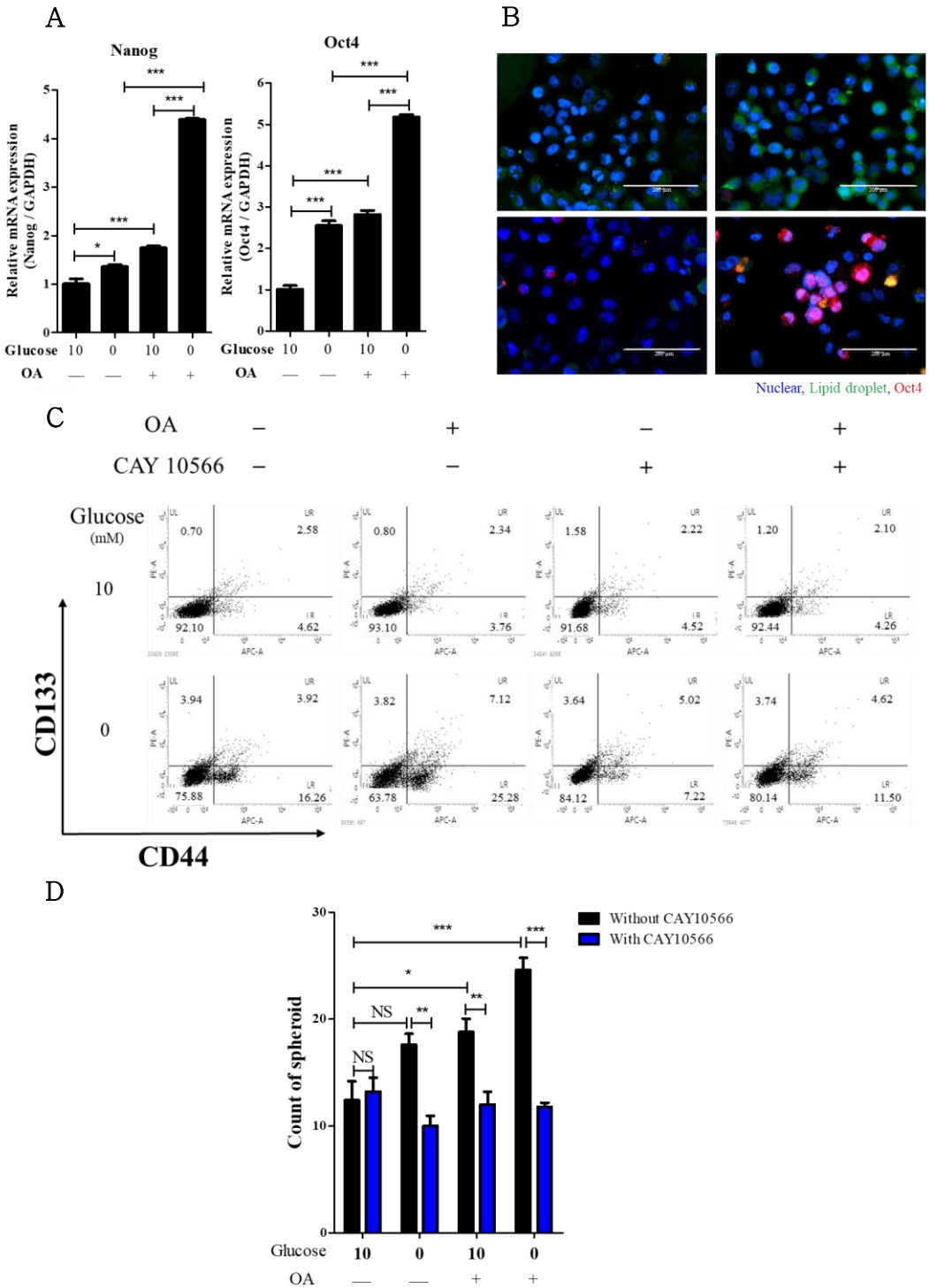
A
Nanog
Oct4
Relative mRNA expression (Nanog / GAPDH)
Relative mRNA expression (Oct4 / GAPDH)
Glucose 10 0 10 0
OA — — + +
B
Nuclear, Lipid droplet, Oct4
C
OA – + – +
CAY 10566 – – + +
Glucose (mM)
10
0
CD133
CD44
0.70
2.58
92.10
4.62
0.80
2.34
93.10
3.76
1.58
2.22
91.68
4.52
1.20
2.10
92.44
4.26
3.94
3.92
75.88
16.26
3.82
7.12
63.78
25.28
3.64
5.02
84.12
7.22
3.74
4.62
80.14
11.50
D
Without CAY10566
With CAY10566
Count of spheroid
NS
Glucose 10 0 10 0
OA — — + +

Figure 8. Effects of OA treatment on stemness of H460 cells under glucose-deficient condition

(A) Transcription levels of Nanog and Oct4 in H460 cells incubated with OA in complete or glucose-deficient medium for one day. $^{*}P < 0.05$ and $^{***}P < 0.001$. Data indicate the mean ± SEM (n = 4). (B) Representative fluorescent image of BODIPY and Oct4 staining in H460 cells cultured in complete medium and glucose-deficient conditions with/without OA treatment. Upper left: H460 cells in complete medium, upper right: H460 cells in complete medium with OA treatment, bottom left: H460 cells in glucose-deficient conditions, and bottom right: H460 cells in glucose-deficient conditions with OA. Green, BODIPY; red, Oct4; blue, DAPI. 20× magnification. Scale bar: 200 μm. (C) Staining for CD133 and CD44 in H460 cells treated with OA and CAY10566 in complete or glucose-deficient medium. (D) Number of spheroids derived from H460 cells treated with OA and CAY10566 in complete or glucose-deficient medium. Spheroids over 100 μm in diameter were counted using Image J. $^{*}P < 0.05$, $^{**}P < 0.01$, and $^{***}P < 0.001$. Data represent the mean ± SEM (n = 3).

SCD-enriched cancer stemness was achieved via F-actin-mediated nuclear translocation of YAP

Under glucose-deficient conditions, YAP and F-actin were mainly detected in the nuclei of H460 cells treated with CAF supernatant (Fig. 10 A). In contrast, only faint YAP fluorescence was detected in the cytoplasm of H460 cells treated with either H460 or NF supernatant, which was not affected by glucose starvation. The abundance of side populations (SPs) in H460 cells was increased by treatment with CAF supernatant, which was further enhanced by glucose starvation, but not in cells treated with H460 or NF supernatant (Fig. 10 B).

Genetically-engineered subclones of H460 cells were manufactured by lentiviral vector or CRISPR/cas9-based gene editing to elucidate the mechanisms involved in the control of cancer stemness by SCD. Compared with parental and mock cells, expression of SCD mRNA and protein were completely abrogated in SCD-KO cells (Fig. 9 A, B). SCD-pCDH cells had overexpressed SCD, while no change of SCD was observed in control Cas9 and pCDH transfected cells (Fig. 9 C). Additionally, analysis of fatty acids revealed that proportion of OA was higher in SCD-pCDH cells than other subclones (Fig. 9 D)

Higher expression levels of Nanog and Oct4 were observed in SCD-pCDH cells compared with the parental cells; however, their expression levels were significantly lower in SCD-KO cells (Fig. 10 C). While only 8% of SCD-KO cells were positive for CD133 and/or CD44, more than 45% of SCD-pCDH cells were positive for these markers (Fig. 10 D). SP analyses in

parental, SCD-KO, and SCD-pCDH cells revealed that the abundance of SPs was positively associated with SCD expression (Fig. 9 E). In contrast to the cytoplasmic localization in parental cells, high levels of YAP and F-actin were detected in the nuclei of SCD-pCDH cells (Fig. 10 E). SCD-KO cells showed lower expression of YAP and F-actin in the nuclei and cytoplasm compared with the parental cells. Cells were treated with an F-actin inhibitor, latrunculin A (Lat A), to evaluate the role of F-actin in the nuclear translocation of YAP. Lat A treatment significantly suppressed nuclear expression of YAP and F-actin in SCD-pCDH cells (Fig. 11 A), but not in parental or SCD-KO cells.

Strong fluorescence for F-actin levels were detected in the nuclei, with elongation of mitochondrial dynamics in SCD-pCDH cells (Fig. 12 A), whereas mitochondrial fragmentation was observed in SCD-KO cells. Moreover, analyses of mitochondrial membrane potential and mitochondrial calcium in parental, SCD-KO, and SCD-pCDH cells revealed that SCD played a crucial role in the integrity of mitochondrial function (Fig. 12 B, C). Since the ATP was required for actin polymerization was mainly generated in the mitochondria via β-oxidation, subclones of H460 cells were treated with the β-oxidation inhibitor, etomoxir (Eto). In SCD-pCDH cells, treatment with Eto suppressed ATP production and expression of F-actin, but increased p-cofilin (Fig. 11 B, C). The level of ATP was lower in SCD-KO cells than parental cells, and were not affected by Eto treatment in these subclones.

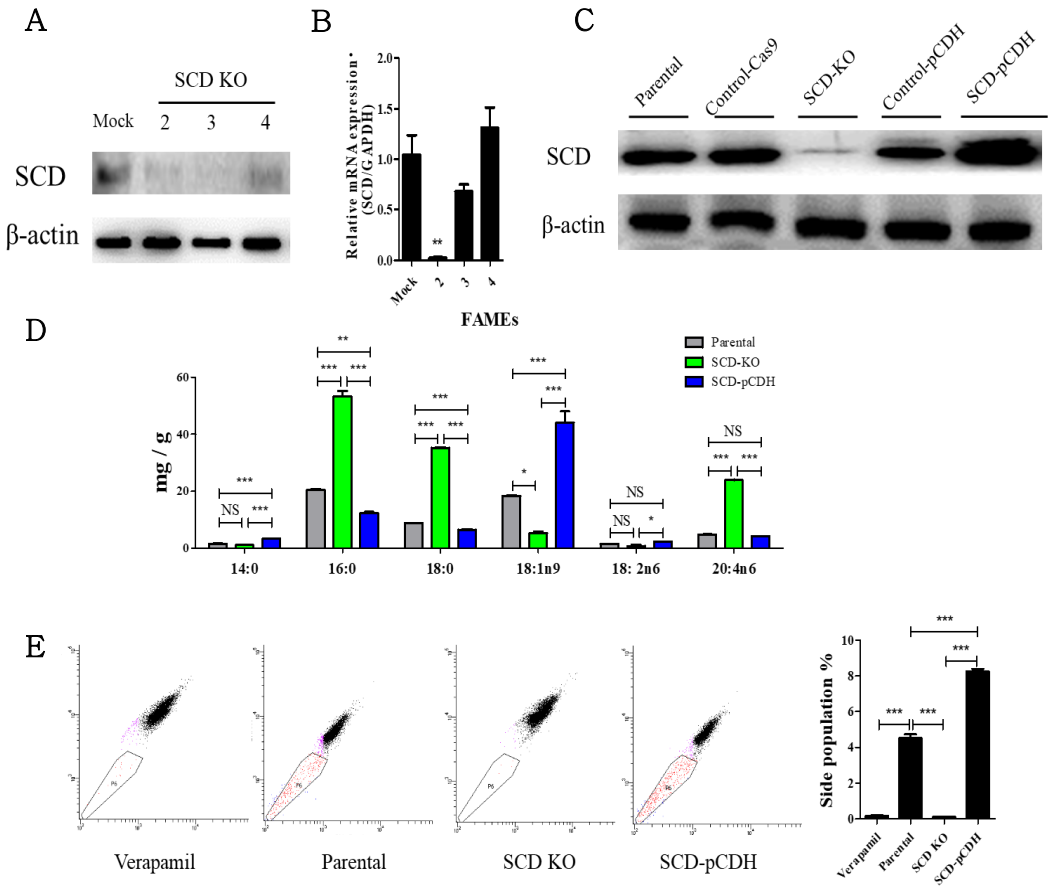

Figure 9. Characterization of SCD gene-manipulated cells and their side population (SP)

(A) Protein expression and (B) transcription level of SCD in control Cas9 (Mock) cells and colony of SCD-KO cells. $^{**}P < 0.01$ vs. mock cells. Data indicate the mean ± SEM (n = 4). (C) Expression of SCD in parental, control Cas9, SCD-KO, control-pCDH, and SCD-pCDH H460 cells. (D) Profile of fatty acid contents in subclones of H460 cells. $^{***}P < 0.001$, Data represents the mean ± SEM (n = 3). (E) Representative flow cytometry for SP assay in H460 cells treated with verapamil, parental, SCD-KO, and SCD-pCDH H460 cells. $^{***}P < 0.001$. Data indicate the mean ± SEM (n = 3).

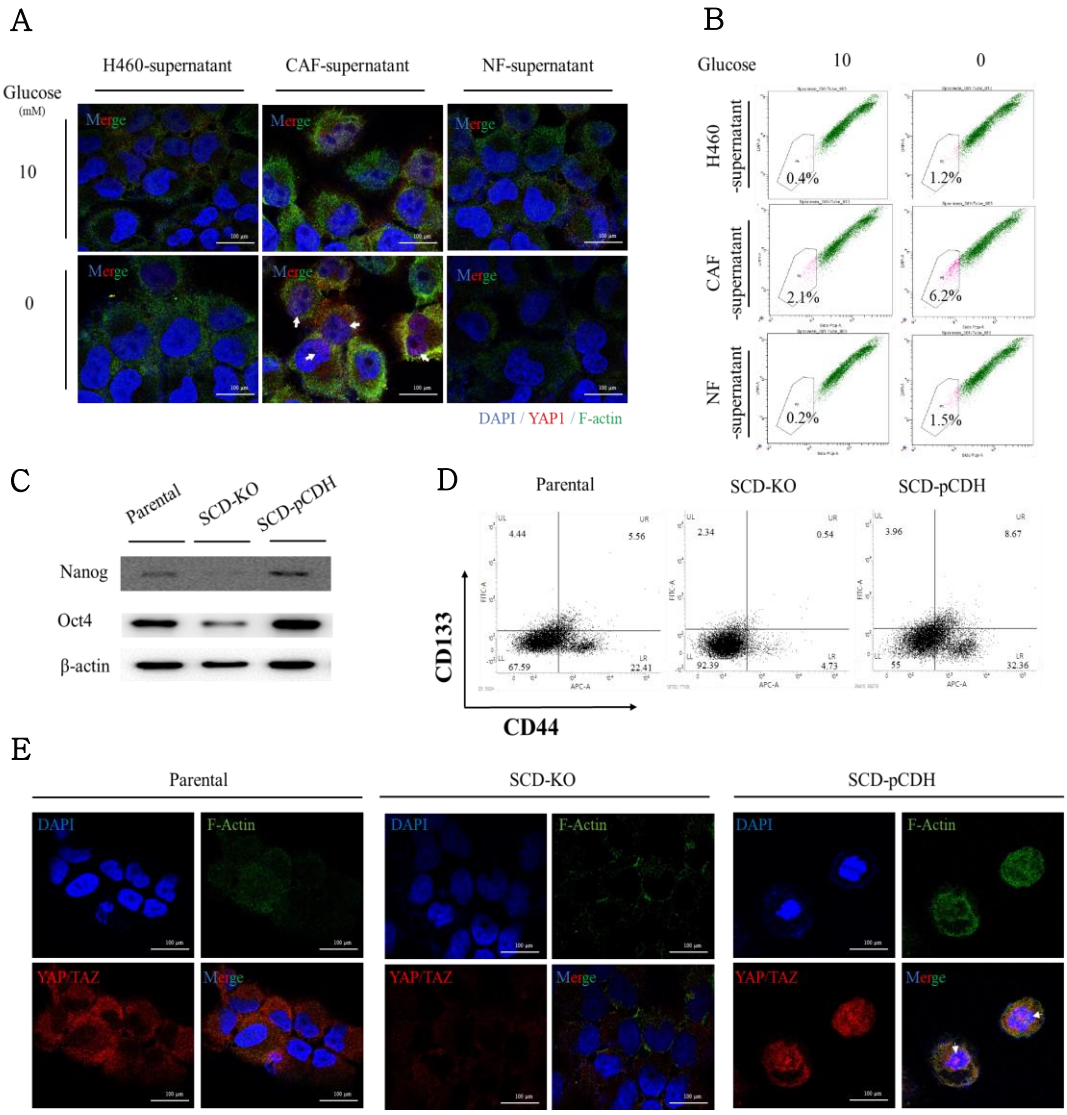
A
H460-supernatant
CAF-supernatant
NF-supernatant
Glucose
(mM)
10
0
Merge
DAPI / YAP1 / F-actin
B
Glucose
10
0
H460 -supernatant
CAF -supernatant
NF -supernatant
0.4%
1.2%
2.1%
6.2%
0.2%
1.5%
C
Parental
SCD-KO
SCD-pCDH
Nanog
Oct4
β-actin
D
Parental
SCD-KO
SCD-pCDH
CD133
CD44
4.44
5.56
67.59
22.41
2.34
0.54
92.39
4.73
3.96
8.67
55
32.36
E
Parental
SCD-KO
SCD-pCDH
DAPI
F-Actin
YAP/TAZ
Merge

Figure 10. Increased SCD promotes stemness via translocation of YAP into the nucleus

(A) Representative fluorescence image of YAP, F-actin and DAPI in H460 cells cultured with supernatant of H460, NF or CAF in complete or glucose-deficient medium for one day. Green: F-actin; red: YAP; blue: DAPI. 40× magnification. Arrowhead indicates co-localization of YAP and DAPI. Scale bar: 100 μm. (B) Representative dot plot of flow cytometry for side population assay. H460 cells incubated with supernatant of H460, NF or CAF followed by further culture in complete or glucose-deficient medium for one day. The P6 population was established using verapamil treatment (negative control). (C) Expression of Nanog, Oct4 and β-actin, and (D) staining for CD133 and CD44 in parental, SCD-KO and SCD-pCDH H460 cells. (E) Representative fluorescence image of YAP, F-actin and DAPI in parental, SCD-KO and SCD-pCDH H460 cells. Arrowhead indicates co-localized fluorescence of YAP and F-actin in the nucleus. Green, F-actin; Red, YAP; Blue, DAPI. 40× magnification. Scale bar: 100 μm.

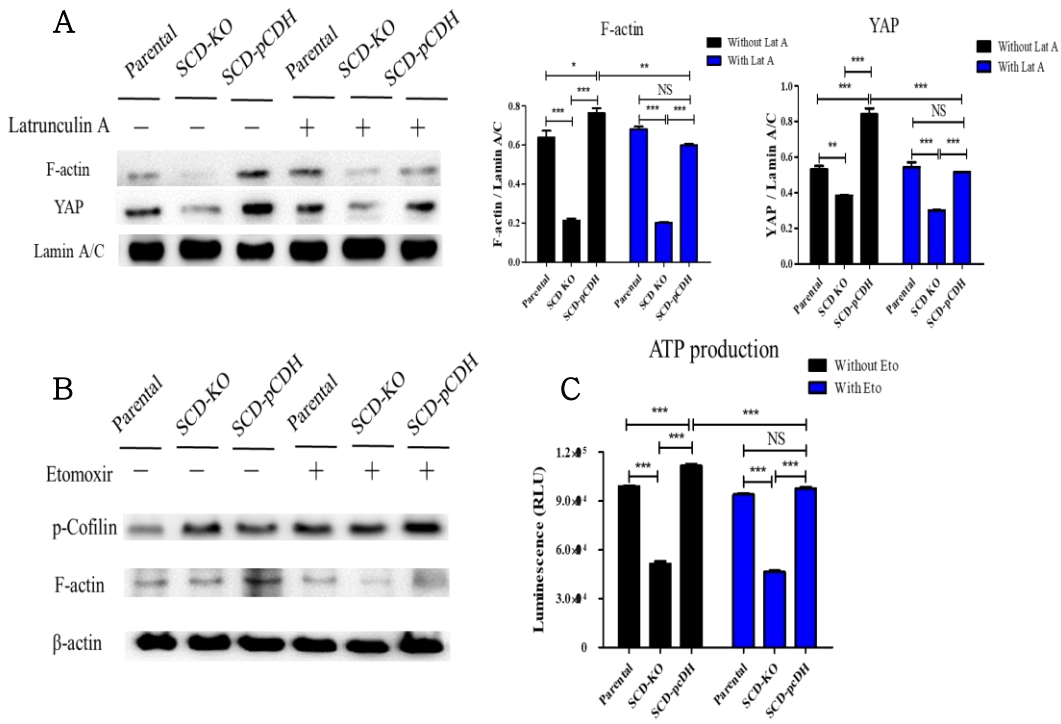

Figure 11. SCD enhanced actin polymerization by activation of β-oxidation and promoted YAP nuclear translocation

(A) Expression of F-actin, YAP and lamin A/C in the nucleus of parental, SCD-KO and SCD-pCDH H460 cells treated with Lat A and normalized using lamin A/C using ImageJ. $^{*}P < 0.05$, $^{**}P < 0.01$, and $^{***}P < 0.001$. Data represent the mean ± SEM (n = 3). (B) Expression of p-cofilin, F-actin, and β-actin and (C) level of ATP in parental, SCD-KO and SCD-pCDH H460 cells treated with etomoxir. $^{***}P < 0.001$. Data indicate the mean ± SEM (n = 9).

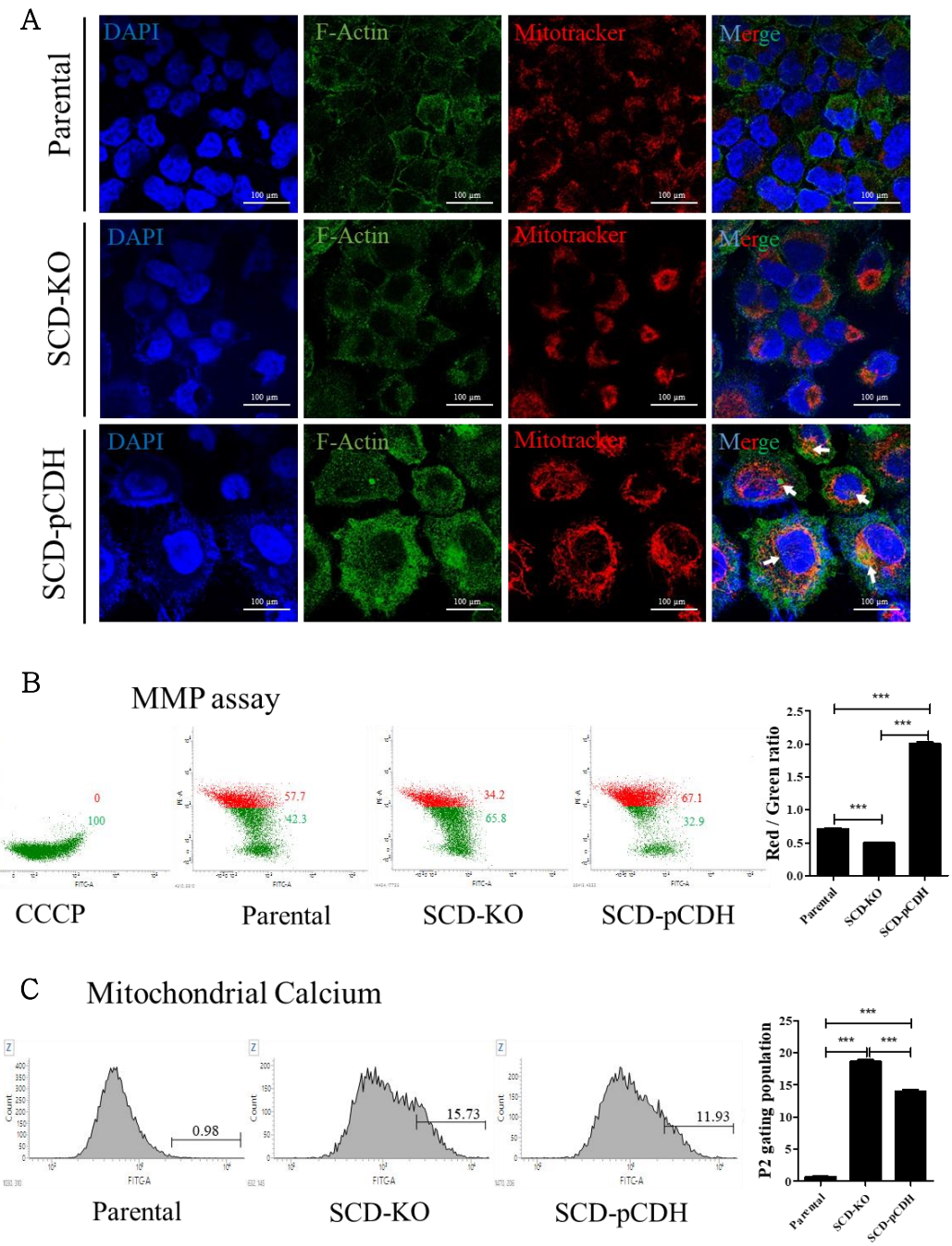
A
Parental
SCD-KO
SCD-pCDH
DAPI
F-Actin
Mitotracker
Merge
100 μm
B
MMP assay
0
100
57.7
42.3
34.2
65.8
67.1
32.9
CCCP
Parental
SCD-KO
SCD-pCDH
Red / Green ratio
***
C
Mitochondrial Calcium
0.98
15.73
11.93
Count
FITC-A
P2 gating population

Figure 12. Effects of SCD on mitochondrial function and dynamics machinery

(A) Representative fluorescence image of mitotracker, F-actin, and DAPI in parental, SCD-KO, and SCD-pCDH H460 cells. Red, mitotracker; green, F-actin; blue, DAPI. Arrow indicates co-localized fluorescence of F-actin and mitotracker. 40× magnification. Scale bar: 100 μm. (B) Representative flow cytometry for JC-1 staining in parental, SCD-KO, and SCD-pCDH H460 cells. CCCP was used as a positive control to determine the proportion of red and green regions. $^{***}P < 0.001$. Data indicate the mean ± SEM (n = 3). (C) Representative flow cytometry of Rhod-2AM staining in parental, SCD-KO, and SCD-pCDH H460 cells. The P2 population was established using parental H460 cells. $^{***}P < 0.001$. Data represents the mean ± SEM (n = 3).

SCD promoted tumorigenesis and nuclear translocation of YAP in a mouse xenograft model

Parental, SCD-KO, or SCD-pCDH subclones of H460 cells were subcutaneously injected into three immunodeficient mice, respectively. After four weeks, the tumor size was significantly larger in mice injected with SCD-pCDH cells than those with other subclones (Fig. 13 A). Furthermore, tumors generated from SCD-KO cells were smaller than those from parental cells. Histologically, a large amount of lipids was detected not only within cancer cells, but also in the extracellular space of the tumor tissues generated from SCD-pCDH cells, whereas lipids were not observed in the tumor tissues from parental or SCD-KO cells (Fig. 13 B). The SCD expression was higher in xenografted tumors produced by SCD-PCDH cells, than in those from parental cells, whereas its expression was not detected in tumors from SCD-KO cells (Fig. 11 A). Additionally, high level of lipids was also detected in the stromal cells. Additionally, aggressive features of cancer cells were observed in the SCD-pCDH subclone-derived tumor, as characterized by numerous mitotic figures, multiple large nucleoli, and necrosis (Fig. 13 B). Tumor tissue generated from parental cells showed tumor cells arranged in solid sheet and glandular structures. In contrast, tumors derived from the SCD-KO subclone were encapsulated and had diffuse glandular structures. YAP fluorescence was faintly detected in the cytoplasm of cancer cells in parental or SCD-KO cell-derived tumors, whereas high levels of fluorescence were detected in the nuclei of cancer cells in SCD-pCDH cell-derived tumors (Fig. 13 C).

To further assess the value of SCD expression as a prognostic biomarker of survival rate, Kaplan–Meier plots were implemented for patients with lung adenocarcinoma with follow-up analysis for 200 months (http://kmplot.com/analysis/index.php?p=service&cancer=lung). The analysis revealed that 1925 lung cancer and 719 adenocarcinoma patients with low expression of SCD had longer OS, FS, and PPS than the patients with high expression of SCD (Fig. 14 A). Specifically, the median FS in lung cancer and adenocarcinoma patients with low SCD expression was 27.14 and 41.4 months, respectively, and was 12.1 and 18.63 months, respectively, in patients with high SCD expression. Likewise, IHC for SCD expression on human lung tissue array revealed that the mean intensity score of SCD staining was higher in adenocarcinoma compared with normal lung tissue, and was positively associated with increase of tumor grade and clinical stage (Fig. 14 B, C). Indeed, the mean of SCD scores was positively associated with enhancement of the grade and stage in lung adenocarcinoma tissues (Fig. 14 D).

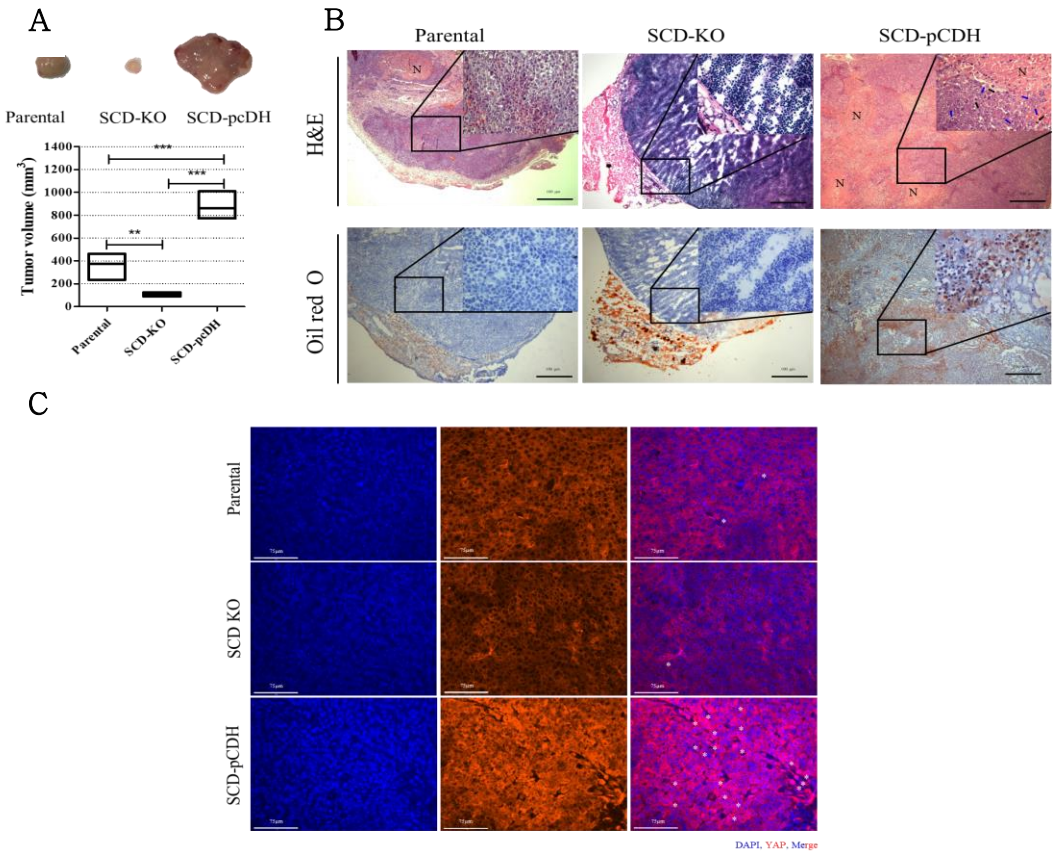

Figure 13. SCD promotes tumorigenesis with nuclear localization of YAP

(A) Size of xenografted tumor following injection of parental, SCD-KO and SCD-pCDH H460 cells. $^{**}P < 0.01$ and $^{***}P < 0.001$. Data indicate the mean ± SEM (n = 3). (B) Representative image of hematoxylin and eosin and oil red O staining in xenografted tumors from parental, SCD-KO and SCD-pCDH H460 cells. 4× and 40× magnification. Black and blue arrows indicate mitotic cell and multi nucleolus, respectively. N: necrosis region. (C) Representative fluorescence image of YAP and DAPI staining in xenografted tumors from parental, SCD-KO and SCD-pCDH H460 cells. Red, YAP; Blue, DAPI. 20× magnification. Scale bar: 75 μm. Asterisk indicates co-localized YAP and DAPI.

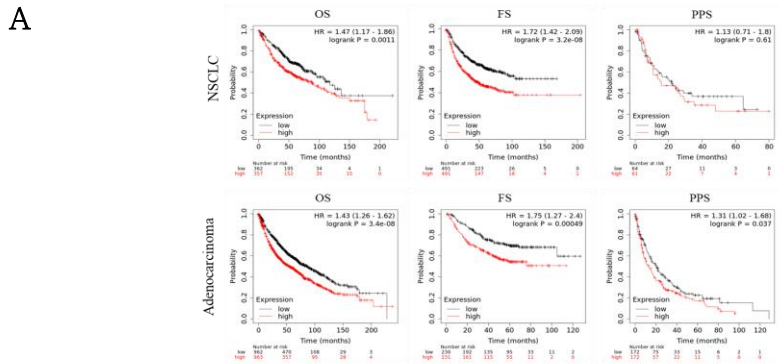
A
NSCLC
Adenocarcinoma
OS
FS
PPS
HR = 1.47 (1.17 - 1.86)
logrank P = 0.0011
HR = 1.72 (1.42 - 2.09)
logrank P = 3.2e-08
HR = 1.13 (0.71 - 1.8)
logrank P = 0.61
HR = 1.43 (1.26 - 1.62)
logrank P = 3.4e-08
HR = 1.75 (1.27 - 2.4)
logrank P = 0.00049
HR = 1.31 (1.02 - 1.68)
logrank P = 0.037
Probability
Expression
low
high
Time (months)
Number at risk

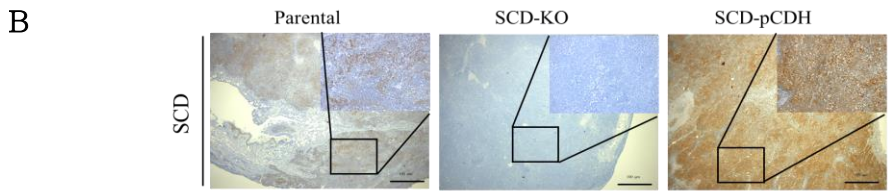
B
Parental
SCD-KO
SCD-pCDH
SCD

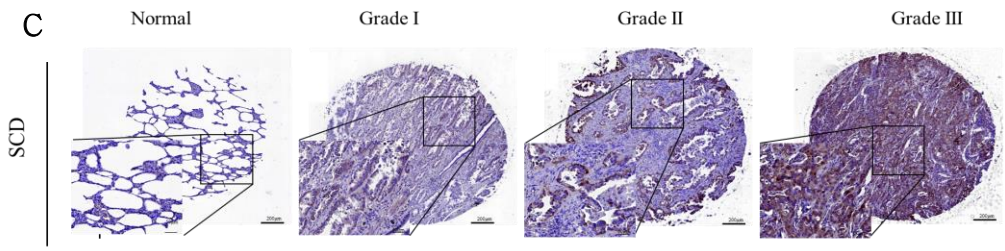
C
Normal
Grade I
Grade II
Grade III
SCD

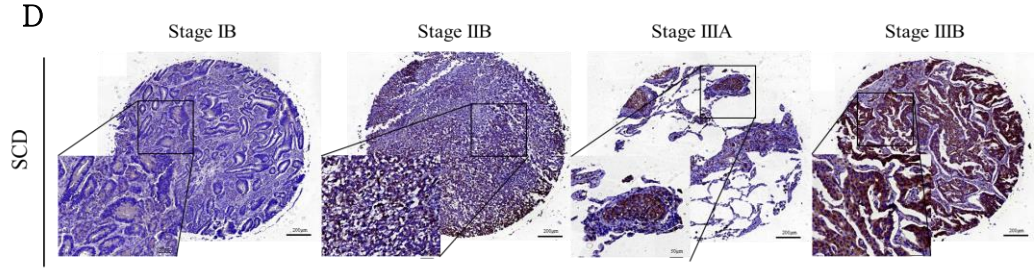
D
Stage IB
Stage IIB
Stage IIIA
Stage IIIB
SCD

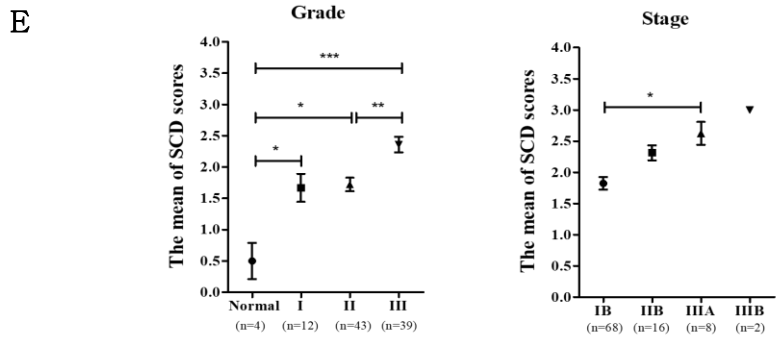
E
Grade
Stage
The mean of SCD scores
Normal
I
II
III
IB
IIB
IIIA
IIIB
(n=4)
(n=12)
(n=43)
(n=39)
(n=68)
(n=16)
(n=8)
(n=2)

Figure 14. Association of SCD expression in tissues of lung cancer patients

(A) Analysis of survival rate (OS, FS and PPS) in patients with lung cancer (n = 1925, 982, and 344, respectively) or lung adenocarcinoma (n = 719, 461, and 125, respectively) based on SCD expression using Kaplan–Meier plot of follow-up for 200 months. The level of SCD expression is divided with a median cutoff value. (B) Representative IHC staining for SCD in xenografted tumors generated from parental, SCD-KO and SCD-pCDH cells. 5× and 20× magnification. (C, D) Representative IHC staining for SCD in normal lung tissue and lung adenocarcinoma tissue microarray. 5× and 20× magnification. (E) Statistic analysis of mean of SCD scoring in lung tissue microarray. The mean of SCD staining scoring was quantified using ImageJ software. $^{*}P < 0.05$, $^{**}P < 0.01$ and $^{***}P < 0.001$. Data indicate the mean ± SEM.

Discussion

Functional changes of non-cancerous stromal cells influence cancer cell malignancy. CAFs are the main component of the tumor stroma and interact with cancer cells via direct or indirect crosstalk within the tumor microenvironment (Paton and Ntambi 2009). Mediators released from the CAFs contribute to cancer cell growth and chemoresistance (Baenke et al. 2013, Beloribi-Djefaflia et al. 2016, Sullivan et al. 2019). The present study revealed that CAFs significantly increased the synthesis of OA that was transferred to neighboring cancer cells. Moreover, the CAF-derived OA enhanced cancer cell stemness via upregulation of SCD and downstream signaling pathways in *in vitro* and *in vivo* models.

Compared with NFs, lipid metabolism is significantly enhanced in CAFs (Santi et al. 2015, Gupta et al. 2017). Our study also showed that the lipid metabolism was reprogrammed to increase the OA in CAFs under glucose deficient condition through activation of SCD. Furthermore, we found that the OA released from the CAFs was transferred to the lung adenocarcinoma cells through the lipid transporters. Analogously, our xenograft model revealed that lipid was predominantly detected in CAFs and its concentration was higher in the areas near CAFs. Our data indicated that OA derived from CAFs contributed to the reprogramming of lipid metabolism in cancer cells.

Unlike normal tissue, tumor growth requires a massive supply of glucose and oxygen for ATP production, resulting in glucose-deficient conditions (Zheng 2012, Sullivan et al. 2019). In turn, glucose deficiency modifies

mitochondrial activity that affects the cancer cell phenotype (Porporato et al. 2018). Under glucose-deficient condition, lipid metabolism is activated by the autophagic response in cancer cells, which functions as an alternative energy source (Rambold et al. 2015). We demonstrated that autophagy and lipid metabolism were highly activated in cancer cells by OA-transferred from CAFs under glucose-deficient condition. Additionally, we showed that SCD is essential for autophagosome maturation, particularly in the fusion with lysosomes. In line with our results, previous study reported that silencing of SCD interferes the fusion of autophagosome and lysosome (Janikiewicz et al. 2015). Furthermore, we revealed that autophagosome synthesis regulated the SCD expression in cancer cells under the glucose deficient condition. The importance and detailed mechanisms involved in SCD regulation by autophagosome are limited and warrant further investigation.

Growing body of evidence indicates that CSCs exbibit a self-renewal capacity and express stemness markers like OCT4, NANOG and SOX2. And their stemness properties are maintained by intracellular mechanisms such as Wnt/β-catenin and Hippo pathways. Recent studies have shown that increased expression of SCD is correlated with cancer malignancy and promotes cancer stemness (Li et al. 2017, Yi et al. 2018). In lung adenocarcinoma, an effector of Hippo pathway, YAP, plays a crucial role in the maintenance of stemness by physical interaction with Sox2 and Oct4 (Bora-Singhal et al. 2015). Nuclear translocation of YAP is essential for the maintenance of stemness, which is mediated by F-actin polymerization

(Sansores-Garcia et al. 2011). Intriguingly, expression of F-actin is significantly suppressed by SCD-inhibitor in lung adenocarcinoma (Noto et al. 2017). Thus far, the molecular mechanism involved in SCD regulation of F-actin formation and nuclear YAP translocation was not comprehensively understood. Our study demonstrated that ATP production by β-oxidation was significantly increased in SCD-overexpressing cancer cells and was provided as a fuel for F-actin polymerization and nuclear translocation of YAP. Moreover, our xenograft model using cancer cell subclones with manipulated SCD expression also supported the role of SCD in the maintenance of CSC properties. The SCD-overexpressing subclones produced larger tumor masses that comprised of more malignant cells with higher level of nuclear YAP than those from the parental or KD subclones. Our data indicated that activation of the lipid metabolism by SCD is critical for the maintenance of stemness of cancer cells under glucose deficient condition.

The present study also explored the clinical relevance of SCD expression in lung cancer patients. Our data indicated that SCD expression was negatively correlated with survival rate in patients with lung adenocarcinomas. Moreover, SCD expression levels were increased along with tumor grade and stage, but was not detected in normal lung tissue. Previous reports showed that SCD expression was associated with stemness markers, such as CD24, CD133, SOX2, and CD44 (Von Roemeling et al. 2013, Pisanu et al. 2017). Collectively, our data indicate that increased

level of SCD is associated with aggressiveness and poor prognosis of lung adenocarcinoma.

Taken together, our study illustrated that reprogrammed lipid metabolism in CAFs under glucose deficient condition enhanced the transfer of OA, subsequently upregulating SCD expression and stemness in cancer cells. These findings suggest that regulation of the lipid metabolism by targeting SCD could be a potential way to develop clinically relevant therapies.

CHAPTER IV.

Crosstalk between CAF-derived oleic acid and $CD4^+$ T cells enhanced the phenotype of Th1 cells under glucose-deficient condition

Abstract

Within tumor microenvironment, abundant FAs promote cancer cells malignancy, but comprehensive role of OA and SCD in T cells under glucose-deficient conditions remains poorly understood. Here, we demonstrated that SCD expression was enhanced in $CD4^+$ tumor-infiltrating lymphocytes (TILs) by CAFs-derived OA and glucose-deficient conditions. SCD augmented the phenotype of Th1 cell rather than regulatory T (Treg) cell. Moreover, robust C-X-C chemokine 11 (CXCL11) production from SCD-upregulated $CD4^+$ splenic T cells augmented the cancer-killing effect of $CD8^+$ T cells dependent on C-X-C chemokine receptor 3 (CXCR3).

OA content and SCD expression were higher in $CD4^+$ TILs than $CD4^+$ splenic T cells, and more enhanced by CAFs-derived OA and glucose-deficiency. Comparative analysis of FAs in parental, SCD-KO and SCD-pLenti Jurkat cells revealed that palmitic acid was dominant in SCD-KO cells and enhanced Treg cell phenotypes by upregulation of mitochondrial superoxide. Meanwhile, high content of OA in SCD-pLenti cells augmented the Th1 cell phenotype compared to other subclones. A robust CXCL11 production from SCD-upregulated $CD4^+$ T cells substantially augmented cancer-killing effect of $CD8^+$ T cells by CXCR3 in 4T1 mouse model. The CXCL11/CXCR3-axis enhanced activity of $CD8^+$ T cells by phosphorylation of Src, Lck and Erk.

The present study demonstrated the OA-induced SCD in $CD4^+$ T cells enhanced Th1 cell phenotype and immunosurveillance of $CD8^+$ T cells that could improve clinical outcomes.

Introduction

In tumor mass, the Warburg effect rapidly produces the acetyl-CoA and pyruvate in cancer cells and induces the abnormal metabolism in cancerous and non-cancerous cells (Liberti 2016). CAFs are the main components of non-cancerous stromal cells and assist tumor growth by physical and physiological interaction with cancer cells (Santi et al. 2018). Unlike the normal fibroblasts, excessive amounts of lipid are produced in CAFs. There are provided to neighboring cells and promote the lipid metabolic reprogramming which is called as 'Reverse Warburg effect' (Pavlides et al. 2009, Fu et al. 2017). Transition of lipids from CAFs to neighboring cancer cells reprograms the lipid metabolism and augments the migration and epithelial-mesenchymal transition (Santi et al. 2015, Gong et al. 2020). Despite the importance of CAFs-induced metabolic reprogramming in tumor microenvironment, how it affects the functional change of $CD4^+$ T cells subtypes has not been delineated.

Within tumor microenvironment, interaction between CAFs and $CD4^+$ tumor-infiltrating lymphocytes (TILs) renders metabolic shift from glycolysis to lipid metabolism in $CD4^+$ TILs (Ino et al. 2013, Pacella et al. 2018). Additionally, lipid metabolism is activated in $CD4^+$ TILs by cancer cell-induced glucose hijacking and regulates the functional change of subtypes (Michalek et al. 2011, Chang et al. 2015). Notably, lipid metabolism augments the expansion of regulatory T (Treg) cells with upregulation of AMP-activated protein kinase (AMPK), resulting in immunosuppressive tumor microenvironment (Michalek et al. 2011).

Moreover, the activity of lipid metabolism also enhances the expansion and phenotype of Th1 cell. Lipid metabolism upregulates the differentiation from naïve T cells to interferon-ɣ (IFN-ɣ)$^{+}$CD4^{+} T cells and their proliferation (Haghikia et al. 2015). However, inhibition of lipid metabolism suppresses the phenotype of Th1 cell including population of IFN-ɣ positive cells and interleukin-10 (IL-10) level by reduction of c-Maf expression in CD4^{+} T cells (Perucha et al. 2019). These published studies report that the impact of lipid metabolism is different in CD4^{+} T cells subtype, therefore, a better understanding of the metabolism is necessary to regulate the phenotype.

FAs re major components of lipids and their oxidation and synthesis orchestrate the activation of lipid metabolism. According to the presence of double bonds, FAs are classified as saturated and unsaturated ones and they play a different role in T cells (de Jong et al. 2014). In stimulated T cells, treatment of palmitic acid (PA), a saturated FA (SFA) augments the cell death and suppresses activity with cell cycle arrest, but it is substantially ameliorated by oleic acid (OA) treatment (Gorjao et al. 2007). Particularly, treatment of OA enhances the phenotype of Th1 cells including IL-2 and IFN-ɣ concentration in CD4^{+} T cells, but their concentrations are consistent by treatment with SFAs (Ioan-Facsinay et al. 2013, de Jong et al. 2014, Passos et al. 2016, Passos et al. 2016). Thus, biosynthesis of UFA especially OA from SFA is essential to enhance the phenotype of Th1 cells. Stearoyl-CoA desaturase (SCD) is an enzyme to convert the SFA to UFA and increases the differentiation of naïve CD4^{+} T cell to

conventional $CD4^+$ T cells rather than Treg cell (Yi et al. 2018, Son et al. 2020).

Furthermore, SCD is a key factor to activate FA metabolism by upregulation of peroxisome proliferator-activated receptor, carnitine palmitoyltransferase-1 and acyl-CoA enzymes (Miyazaki and Ntambi 2003). In $CD4^+$ T cells, activated FA metabolism substantially enhances the production of IFN-ɣ that is priming the cytotoxic effect of $CD8^+$ T cells (Rocha et al. 2008, Bhat et al. 2017). Additionally, reprogrammed FA metabolism in $CD8^+$ T cells by glucose deficiency remarkably augments the cancer-killing effect through blockade of PD-1 compared to normal cells (Zhang et al. 2017). In contrast to glycolysis, FA metabolism substantially upregulates the proliferation of $CD8^+$ T cells by AMPK-signaling and increases the survival rate of tumor mouse model (Pearce et al. 2009). These data suggest that reprogrammed FA metabolism in T cells has potential as anticancer therapy.

We discovered that CAF-derived OA enhanced the SCD expression and FA metabolism in $CD4^+$ T cells under glucose-deficient condition. High amounts of OA by SCD-overexpression enhanced the phenotype of the Th1 cell. Furthermore, a robust secretion of C-X-C chemokine 11 (CXCL11) from SCD-upregulated $CD4^+$ T cells activated C-X-C chemokine receptor 3 (CXCR3)-signaling in $CD8^+$ T cells, resulting in a significant cancer-killing effect in our *in vitro* and *in vivo* model.

Materials and Methods

Cell lines and reagents

Mouse mammary carcinoma cell, 4T1 and human leukemia T cells, Jurkat cells were cultured in a complete RPMI medium (Gibco) supplemented with 10 mM glucose, 100 μg/mL penicillin/streptomycin (Gibco), 1 mM sodium pyruvate (Sigma-Aldrich), 10 mM HEPES (Sigma-Aldrich), 10 mM sodium carbonate (Sigma-Aldrich), and 10% fetal bovine serum (FBS; Gibco). Glucose deficient medium was prepared by excluding the glucose from a complete RPMI medium. The mouse melanoma, B16F10 and colon cancer, CT26 cells were incubated in a Dulbecco's Modified Eagle Medium (DMEM; Sigma-Aldrich) supplemented with the same components as above. Luc2-4T1 cells were prepared by transfected with Luc2-vector (Promega) and selected with G418 solution (Sigma-Aldrich).

Sulfosuccinimidyl Oleate (SSO; Cayman-Chemical) and AMG487 (Cayman-chemical) inhibited lipid transporter and C-X-C chemokine receptor 3 (CXCR3). Oleic acid (OA; Sigma-Aldrich) and palmitic acid (PA; Sigma-Aldrich) were dissolved in DMSO (Sigma-Aldrich). CAY10566 (Cayman-Chemical) and T0901317 (Cayman-Chemical) inhibited and enhanced the SCD expression. Recombinant C-X-C chemokine 11 (rCXCL11; R&D systems, Minneapolis, Minnesota, USA) and programmed-death ligand 1 (rPD-L1; R&D systems) were dissolved in complete media as 10 ng/mL and 1 μg/mL, respectively and treated to cells for 1 day.

Animal models for primary culture and tumor growth assay

All of the animal experiments were approved by the Institutional Animal Care and Use Committee at Seoul National University, South Korea (SNU-200309-9). For establishment of 4T1-mouse model, 4 weeks-old BALB/c mice were purchased from Jungang Lab Animal, Inc. (Seoul, South Korea), and injected 2×10^5 4T1 or Luc2-4T1 cells to mammary fat pad. After 5 days, the resultant tumor masses were resected and subjected to the primary culture for CAF and TIL. Spleens collected from 5weeks-old female BALB/c mice were used for primary culture of lymphocytes according to the published method (Yonesaka et al. 2018). The separation of lymphocyte subsets in TIL and splenic T cells was carried out as described below.

To visualize tumor growth by bioluminescence, we subjected to Luc2-4T1 mouse models as above. Prepared PBS, 2×10^6 $CD8^+$ T cells and CXCR3-$CD8^+$ T cells in *'Establishment of genetically engineered cells'* as below were intratumorally injected in Luc2-4T1 mouse model and visualized the tumor using IVIS Lumina XR (Caliper-Life Sciences, Waltham, MA, USA) after intraperitoneal injection of 150 μg VivoGlow Luciferin (Promega). The images were analyzed by Living Image software (Caliper-Life sciences). The background bioluminescence was 2.1×10^7 photon/s.

To evaluate the growth of tumor in CT26-mouse model, 2×10^5 CT26 cells were subcutaneously injected into backside of 5 weeks-old BALB/c mice. After 7 days, resultant tumor masses were

intratumorally injected with prepared PBS, 2×10^6 $CD8^+$ T cells and CXCR3-$CD8^+$ T cells and anti-PD1 antibody (200 μg, RMP1-14, Bio-X Cell, New Hampshire, USA) for 1 time and 3 times, respectively. Tumor volumes were measured by caliper and calculated as length × $width^2/2$.

Separation of CAFs and T lymphocyte subsets from primary culture

Collected tumor masses and spleens from five mice were used for primary culture of TILs and splenocytes, respectively (Yonesaka et al. 2018). $CD3^+CD4^+$ and $CD3^+CD8^+$ were separated from primary cultured TILs and splenocytes using a commercial kit (Miltenyi Biotec) in accordance with the manufacturer's instructions. Separated cells were cultured in a complete RPMI medium. To evaluate the purity of the separated cells, we stained the cells with antibodies for CD3 (Invitrogen), CD4 (Invitrogen), and CD8 (Invitrogen), followed by flow cytometric analysis using a FACSVerse (BD Biosciences).

To isolate CAFs in resultant tumors from 4T1 mouse model, tumor masses were minced and digested using type I collagenase (Gibco) for 30 min and neutralized with equal volume of complete medium. Digested cells from tumor masses were filtered d using a 70-mm cell strainer (SPL Life Science) and cultured in complete media. To isolate fibroblasts from the primary cultured cells, a commercial kit (Miltenyi Biotec) was used according to manufacturer's instructions (Agorku et al. 2019) and cultured further in complete media. Purity of the isolated CAFs was assessed using a FACSVerse (BD Biosciences) with

antibody against FAP (Abcam). Passaged up to 5 was not used for further study.

Establishment of genetically engineered cells

To verify the role of SCD in T cells, we genetically manipulated the SCD-KO and SCD-overexpressed Jurkat cells using CRISPR and lentiviral vector. Jurkat cells were transfected with control or SCD-sgRNA-U6 plasmid (Toolgen) and CRISPR/Cas9-puromycin-CMV plasmid vector (Toolgen) through lipofectamine-3000 (Invitrogen). After 3 days, survived cells from puromycin treatment were individually collected and cultured following the assessment of SCD expression by Western blot. Compared to parental and control-sgRNA transfected cells, SCD expression depleted cells were used for further experiments. Amplified PCR product for SCD coding sequence was inserted into TOPO vector (Invitrogen) which contained attR region. Then, the product was ligated with pLenti6.3/V5-DEST vector (Invitrogen) and transformed into E-coli DH5α. Prepared SCD-pLenti vector and empty-pLenti vector were transfected into 293T cells with 2nd lentivirus packaging solution (Applied Biological Materials, Richmond, BC, Canada) and lentifectin (Applied Biological Materials) for 1 day and replaced with fresh media. After 2 days, viral supernatant was harvested and concentrated using Lenti-X concentrator (Takara, Otsu, Japan). Jurkat cells were infected with control or SCD-pLenti viral supernatant with polybrene (Merck Millipore) for 2 days and rested in complete media for 1 day. The expression of SCD was

evaluated in parental and control-sgRNA transfected cells, SCD-KO cells, pLenti and SCD-pLenti cells by western blot and SCD-KO and overexpressed cells were used for further study.

To evaluate the role of CXCR3 in $CD8^+$ splenic T cells, we manipulated CXCR3-overexpressed cells using lentiviral vector. As mentioned above, supernatant of pLenti and CXCR3-pLenti vector was prepared from 293T cells and was infected to $CD8^+$ T cells.

Apoptosis assay

Cancer cells, 4T1, CT26 and B16F10 were co-cultured with $CD8^+$ T cells as 1:10 ratio for 1 day. After 1 day, $CD8^+$ T cells were discarded. Cancer cells were harvested after washing with PBS and performed apoptosis assay as below. To assess the apoptotic rate, cancer cells were stained with Annexin-V and PI using Ezway apoptosis detection kit (Koma Biotech) (Kim et al. 2018). Briefly, harvested the cells were incubated with Annexin-V reagent for 15 min in the dark. After washing with 1×binding buffer, the cells were resuspended with PI and analyzed with FACSVerse (BD Biosciences). Remained $CD8^+$ T cells were excluded according to different size of forward and side scatter. In dot blot analysis, quadrants were divided using negative control.

Measurement of lipid content and FAs subtype

Lipid amounts in cultured cells were stained with BODIPY (Invitrogen). For 30 min, cultured cells were incubated with 10 μM of BODIPY solution at 37°C in the dark and analyzed by FACSVerse (BD Biosciences) subsequent washing with PBS for three times.

In cell pellets, extracted fatty acids (FAs) were analyzed the proportion by FAMEs at NICEM in Seoul National University. The result of fatty acids proportion was calculated according to (Garces and Mancha 1993).

Measurement of reactive oxygen species

Intracellular total reactive oxygen species (ROS) and mitochondrial superoxide were determined by 2,7-dichlorodihydrogluorescein diacetate assay (DCF-DA, Invitrogen) and MitoSOX (Invitrogen) according to each manufacturer's instruction. For detection of ROS, harvested cells were treated with 2 mM of DCF-DA stock solution as 1000:1 ratio and incubated for 30 min. After washing with PBS, the cells were analyzed with flow cytometry FACSVerse (BD Biosciences). To assess the mitochondrial superoxide, 5 mM of MitoSOX stock solution as 1000:1 ratio was treated to collected cells for 15 min. The fluorescence of MitoSOX-PE was immediately analyzed with FACSVerse (BD Biosciences).

Expression analysis by quantitative RT-PCR and Western blot assay

TRIzol reagent (Ambion) was used to extract total RNA and it was quantified using a microplate reader (BioTek Epoch). To synthesize the cDNA, 500ng of total RNA was used with a TOPscript^{TM} cDNA Synthesis kit (Enzynomics). The mRNA expression was evaluated using SYBR Green RT-PCR kit (Enzynomics). Relative expression levels were normalized using GAPDH and it was calculated according to ΔΔCt method (Rao et al. 2013).

Protein was extracted using EzRIPA buffer (ATTO) and its concentration was assessed by Bradford assay (BiodRad, Hercules, CA, UA). The membrane which loaded with 10 ng of protein lysate was incubated with skim milk solution (PBS-T + 5% of skim milk) for 1 h. After three times washing with PBS-T, blocking solution (PBS-T + 5% of BSA) with antibodies including SCD (Cell-Signaling Technology), SREBP (Santa Cruz Biotechnology) and GAPDH (Santa Cruz Biotechnology) for overnight at 4°C. After washing with PBS-T, the membrane was incubated with secondary HRP-conjugated anti-rabbit and mouse (Santa Cruz Biotechnology) antibodies contained skim milk solution for 2 h. The protein expression was detected by a chemiluminescence imaging system (ATTO) after dropping of Luminata Forte Western HRP Substrate (Merck Millipore).

Flow cytometric analysis

To evaluate the expression of CD25 and interferon-ɣ (IFN-ɣ) in Jurkat cells and $CD4^+$ TILs, $CD4^+$ splenic T cells and $CD8^+$ splenic T cells, they were stimulated by a cell stimulation cocktail 500× (Invitrogen) for 18 hours and treated with CAY10566, OA or rCXCL11 (R&D systems) for 1 day. After washing with PBS, the cells were fixed and permeabilized using Intracellular Fixation & Permeabilization solution (Invitrogen) and incubated with permeabilization solution containing CD25 (Invitrogen) and IFN-ɣ (Invitrogen) antibodies as 100:1 ratio. After washing with PBS, we immediately analyzed using FACSVerse (BD Biosciences). To evaluate the intracellular protein

expressions in $CD8^+$ T cells, fixation and permeabilization was performed in $CD8^+$ T cells as above and incubated with the permeabilization solution with the antibody against to phosphor-ZAP70 (Invitrogen), Src (Invitrogen), -Lck (Invitrogen) and -Erk (Cell-Signaling Technology) and CXCR3 (Invitrogen) as 100:1 ratio. Their expressions were analyzed using FACSVerse (BD Biosciences). The concentrations of TGF-β, interleukin-2 (IL-2) and tumor-necrosis factor-α (TNF-α) were assessed using a commercial ELISA kits (Duoset, Minneapolis, MN, USA). Briefly, collected supernatant and standards was suspended on the pre-coated plate with each antibody and incubated for 2 h. After three times of washing with PBS-T (0.1% tween20 in PBS), detection antibody and streptavidin-horseradish-peroxidase (HRP) solution were added in the plate for 2 h and 30 min, respectively. Tetramethylbenzidine (TMB; Sigma-Aldrich) was added for 20 min to monitor the color change and 2N HCL was treated to stop the overreaction. Optical density was measured at 450 nm using a microplate reader (BioTek Epoch) and calculated according to standards.

To identify the cytokine candidate, we performed cytokine array (Abcam) according to manufacturer's instructions. The membranes targeting 96 cytokines were incubated with collected supernatants for 2 h. After three times washing with washing buffer I and II, biotinylated antibody cocktail and HRP-conjugated streptavidin were added and incubated for 2 h. Detection mixture was spread to the membranes and

cytokines expression was observed using a chemiluminescence imaging system (ATTO). Signal intensity was normalized with positive control spots in membranes.

Chemotaxis assay

To evaluate the migratory potential by CXCR3-CXCL11 conjugation, $CD8^+$ or CXCR3-$CD8^+$ T cells was plated in upper side of 24-well hanging plate (SPL Life Science) and control or CXCL11 siRNA-transfected 4T1 cells were seeded at bottom side. Control and CXCL11 siRNA (Bioneer, Seoul, South Korea) were mixed with lipofectamine 3000 (Invitrogen) and transfected in 4T1 cells according to manufacturer's recommendation (Kim et al. 2009). $CD8^+$ T cells alone and rCXCL11 treatment in bottom side were used as negative and positive control, respectively. After 1day, harvested cells in bottom side were stained with $CD3^+$ and counted using flow cytometry (BD Biosciences).

Statistical analysis

In this study, experiments were performed independently at least 3 times. Data values were described as the mean ± standard deviation (SD). GraphPad Prism Software (GraphPad Software) was applied to statistical analyses. One-way analysis of variance (ANOVA) was used to calculated *P*-values. Statistical significance was considered with *P*-values < 0.05, 0.01 and 0.001.

Result

CAF-derived lipids enhanced OA amounts in $CD4^+$ TILs with SCD expression

In 4T1 mouse model, we isolated $CD4^+$ T cells from tumor-infiltrating lymphocytes (TILs) in tumor mass and splenocytes in age-matched mice using magnetically activated cell sorting (Fig. 1 A). The mRNA expressions of *T-bet* and *Foxp3*, indicator for Th1 and regulatory T (Treg) cells were higher in $CD4^+$ TILs than $CD4^+$ splenic T cells, but *GATA* and *ROR-γ* mRNA expressions were not changed (Fig. 1 B). Higher lipids content was observed in $CD4^+$ TILs than $CD4^+$ splenic T cells (Fig. 2 A). Particularly, amount of 16:0 (palmitic acid), 18:0 (stearic acid), 18:1n9 (oleic acid) and 22:6n3 (docosahexaenoic acid) was substantially higher in $CD4^+$ TILs than $CD4^+$ splenic T cells (Fig. 1 C). Our previous study reported that CAFs had a massive lipid amounts than normal counterparts, and transferred into neighboring cancer cells through supernatant. In resultant tumor from 4T1-mouse model, most of the fluorescence of $CD3^+$ cells were located adjacent to FAP positive CAFs (Fig. 2 B). To determine high lipids in $CD4^+$ TILs were provided from CAFs, both $CD4^+$ TILs and splenic T cells were incubated with CAFs-supernatant for 1 day and evaluated lipid contents. CAFs were isolated from tumor mass in 4T1-mouse model using a commercial kit and more than 97% were positive to FAP (Fig. 1 D). Incubation of both $CD4^+$ TILs and splenic T cells with CAFs-supernatant enhanced the amount of lipids compared to non-treatment

(Fig. 2 C). Moreover, mRNA expressions of lipid transporter, CD36 and SLC27A1 were higher in $CD4^+$ TILs than $CD4^+$ splenic T cells, and incubation of CAFs-supernatant enhanced mRNA expressions in both cells (Fig. 2 D). However, treatment of $CD4^+$ TILs with sulfo-N-succinimidyl oleate (SSO), an inhibitor for lipid transporter, showed consistent lipid contents compared to non-treatment regardless of CAFs-supernatant incubation (Fig. 2 E). Moreover, expression of stearoyl-CoA desaturase (SCD) was overexpressed in $CD4^+$ TILs than $CD4^+$ splenic T cells and more enhanced when incubated with CAFs-supernatant (Fig. 2 F). Result of FA analysis revealed that incubation of CAFs-supernatant significantly augmented the proportion of oleic acid (OA) in $CD4^+$ TILs more than other FAs (Fig. 2 G).

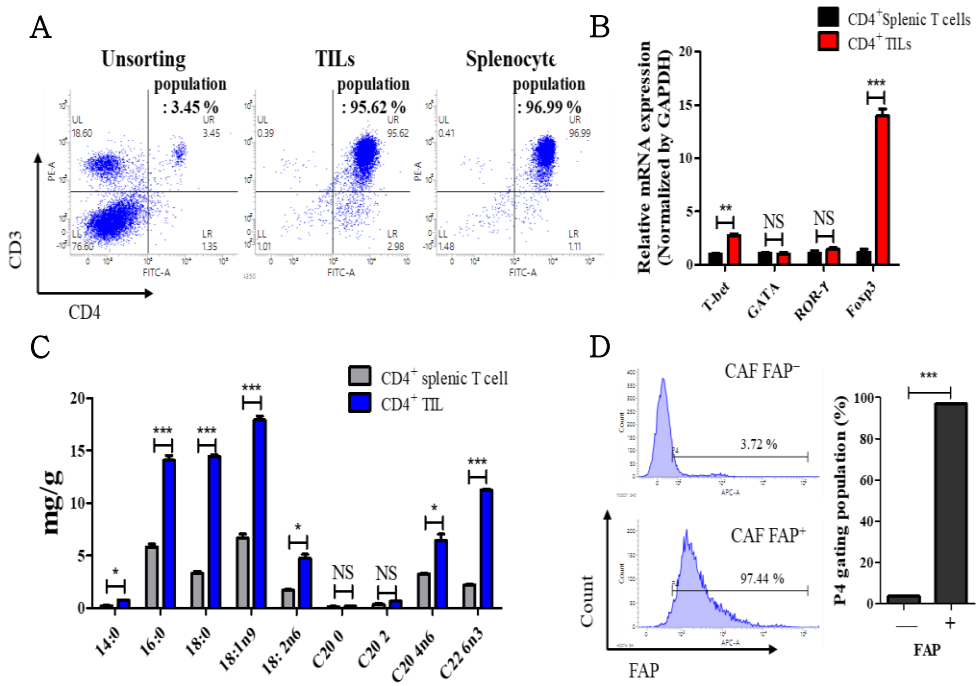

Figure 1. Characterization of lipid metabolism in TILs incubated with CAFs-supernatant

(A) Representative dot plot image of CD3 and CD4 staining in isolated $CD4^+$ splenocytes and TILs. (B) Transcription levels of *T-bet, GATA*, *ROR-γ* and *Foxp3* in $CD4^+$ splenic T cells and TILs cultured in complete media for 1 day. $^{**}P < 0.01$ and $^{**}P < 0.01$. Data indicate the mean ± SEM (n = 4). (C) Profile of fatty acids contents in $CD4^+$ splenic T cells and TILs. $^{***}P < 0.001$. Data represents the mean ± SEM (n = 3). (D) Representative image of FAP staining in FAP^- and FAP^+ cells isolated from tumor mass in 4T1 model. The P4 population was established using FAP^- cells. $^{***}P < 0.001$. Data indicate the mean ± SEM (n = 3).

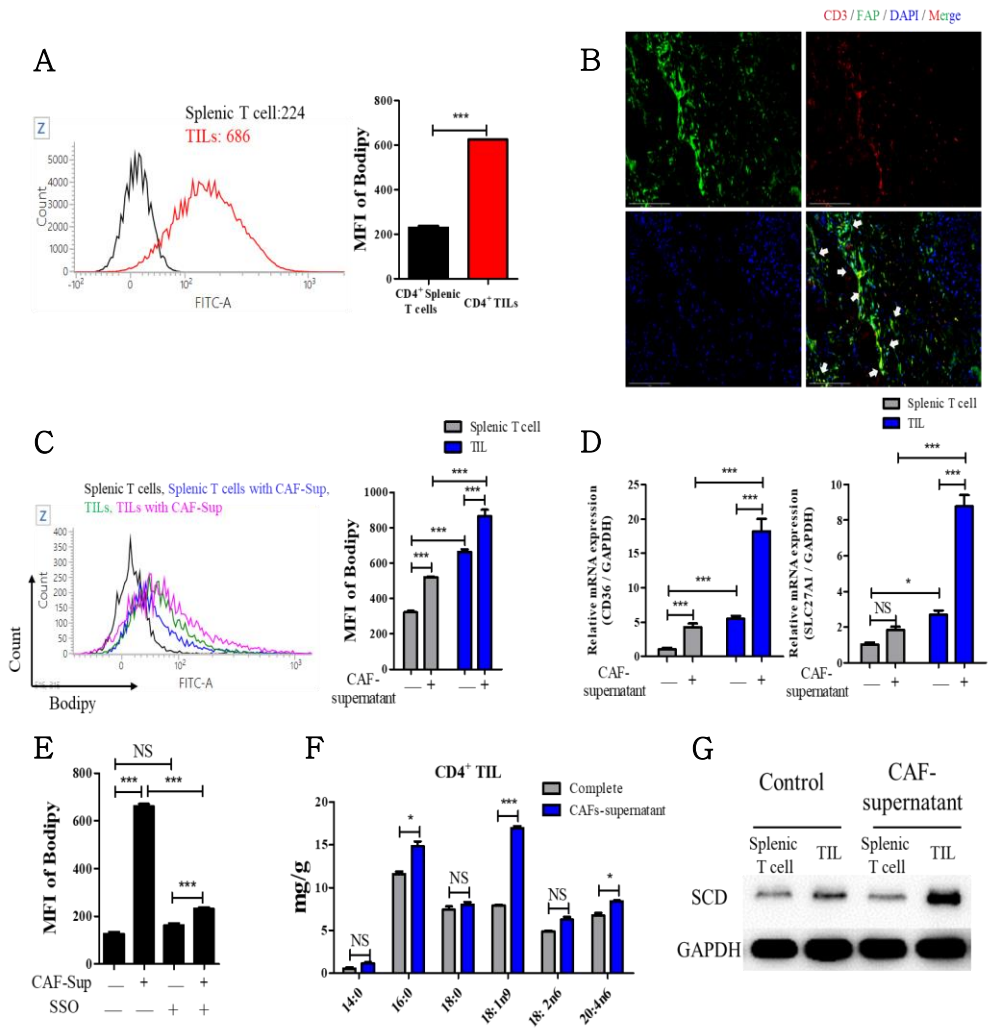
A
Splenic T cell:224
TILs: 686
Count
FITC-A
MFI of Bodipy
CD4+ Splenic T cells
CD4+ TILs
B
CD3 / FAP / DAPI / Merge
C
Splenic T cell
TIL
Splenic T cells, Splenic T cells with CAF-Sup,
TILs, TILs with CAF-Sup
Count
Bodipy
FITC-A
MFI of Bodipy
CAF-supernatant
D
Splenic T cell
TIL
Relative mRNA expression (CD36 / GAPDH)
Relative mRNA expression (SLC27A1 / GAPDH)
NS
CAF-supernatant
E
MFI of Bodipy
NS
CAF-Sup
SSO
F
CD4+ TIL
Complete
CAFs-supernatant
mg/g
NS
14:0
16:0
18:0
18:1n9
18: 2n6
20:4n6
G
Control
CAF-supernatant
Splenic T cell
TIL
SCD
GAPDH

Figure 2. Oleic acid (OA) in CAFs-supernatant was transition into $CD4^+$ TILs via lipid transporter

(A) Representative histogram for BODIPY staining in $CD4^+$ splenic T cells and TILs cultured in complete media for 1 day. Black: $CD4^+$ splenic T cells, Red: $CD4^+$ TILs. The graph indicated the mean fluorescence intensity (MFI) of BODIPY staining. $^{***}P < 0.001$. Data indicate the mean ± SEM (n = 3). (B) Representative fluorescence image of staining for CD3 and FAP in tumor mass from 4T1 mouse model. Red: CD3, Green: FAP, Blue: DAPI. 40× magnification. Scale bar: 75 μm. White arrow indicates co-localized fluorescence of CD3 and FAP. (C) Representative histogram for BODIPY staining in $CD4^+$ splenic T cells and TILs incubated with CAF-supernatant for 1 day. Black: $CD4^+$ splenic T cells, Blue: Incubation of $CD4^+$ splenic T cells with CAFs-supernatant, Green: $CD4^+$ TILs, Pink: Incubation of $CD4^+$ TILs with CAFs-supernatant. The graph indicated the MFI of BODIPY staining. $^{***}P < 0.001$. Data indicate the mean ± SEM (n = 3). (D) Transcription levels of *CD36* and *SLC27A1* in $CD4^+$ splenic T cells and TILs incubated with CAF-supernatant for 1 day. $^{*}P < 0.05$ and $^{***}P < 0.001$. Data indicate the mean ± SEM (n = 4). (E) The graph indicated the quantified MFI value of BODIPY staining in $CD4^+$ TIL incubated with CAF-supernatant subsequent to treatment with 50 μM SSO. $^{***}P < 0.001$. Data indicate the mean ± SEM (n = 3). (F) Expression of SCD and GAPDH in $CD4^+$ splenic T cells and TILs incubated with CAF-supernatant for 1 day. (G) Profile of fatty acid contents in $CD4^+$ TILs treated with CAF-supernatant and control. $^{*}P < 0.05$ and $^{***}P < 0.001$. Data indicate the mean ± SEM (n = 3).

Enhanced SCD expression by glucose deficiency and OA supplement increased phenotype of Th1 cell, but mitigated Treg cell

In tumor microenvironment, glucose in TILs is deficient by competition with cancer cells, leading to immune escape by enhancement of Treg cell population (Chang et al. 2015, Liberti 2016). To determine the effect of OA which was the most predominant FAs in CAFs-derived lipids under glucose-deficient conditions, OA was supplemented to Jurkat cells and cultured under glucose-deficient conditions for 1 day. In contrast to non-supplement, lipids content and expressions of SCD and sterol regulatory-element binding protein were enhanced in Jurkat cells by OA supplement and more increased under glucose-deficient conditions (Fig. 3 A, B). The schematic diagram of the procedure was described in Figure. 3 C. Additionally, mRNA expressions of *T-bet* and *Foxp3* were significantly increased in glucose-deficient Jurkat cells supplemented with OA compared to non-supplement (Fig. 4 A). Treatment of CAY10566, a selective SCD inhibitor to the cells substantially suppressed mRNA expression of *T-bet*, whereas *Foxp3* mRNA expression was more enhanced. Under glucose-deficient conditions, OA supplemented Jurkat cells showed enhanced phenotypes of Treg cells including CD25 positive cells population and transforming growth factor-β (TGF-β) concentration and furtherly enhanced by treated with CAY10566 (Fig. 4 B, C). However, CAY10566 treatment suppressed phenotypes of Th1 cells, population of IFN-γ positive cells and IL-2 concentration in OA supplemented glucose-deficient Jurkat cells.

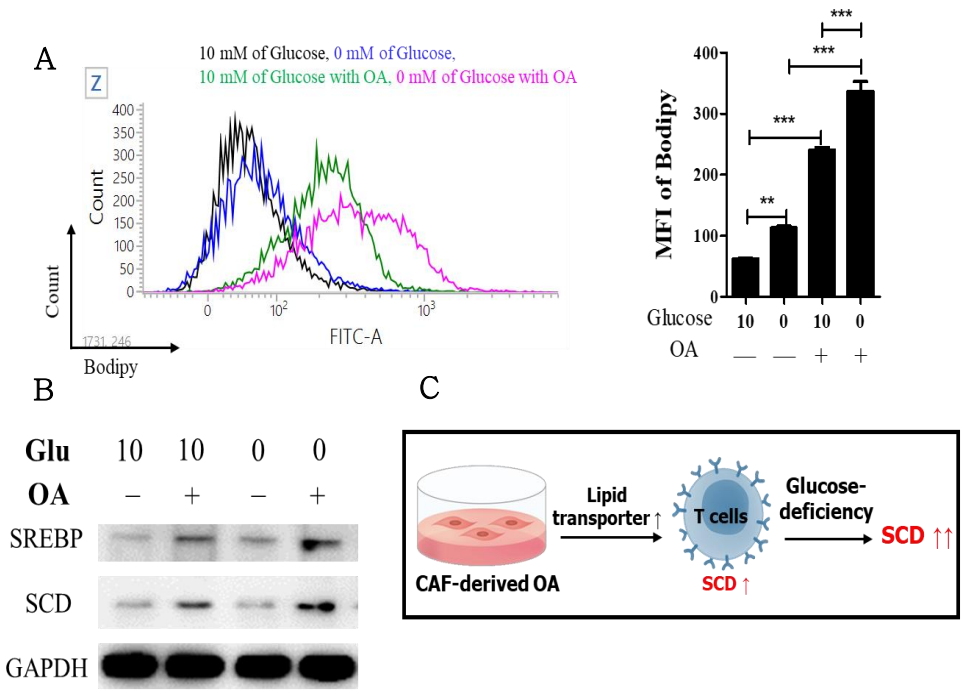

Figure 3. Under glucose-deficient conditions, SCD was enhanced by treatment with OA

(A) Representative histogram for BODIPY staining in Jurkat T cells treated with 100 μM OA and cultured in 10 or 0 mM glucose contained medium for 1 day. The graph indicated the quantified MFI value of BODIPY staining. $^{**}P < 0.01$ and $^{***}P < 0.001$. Data indicate the mean ± SEM (n = 3). (B) Expression of SCD, SREBP and GAPDH in Jurkat T cells treated with 100 μM OA and cultured in 10 or 0 mM glucose contained medium for 1 day. (C) Schematic image of how SCD was enhanced in incubated T cells CAF-supernatant under glucose-deficient conditions.

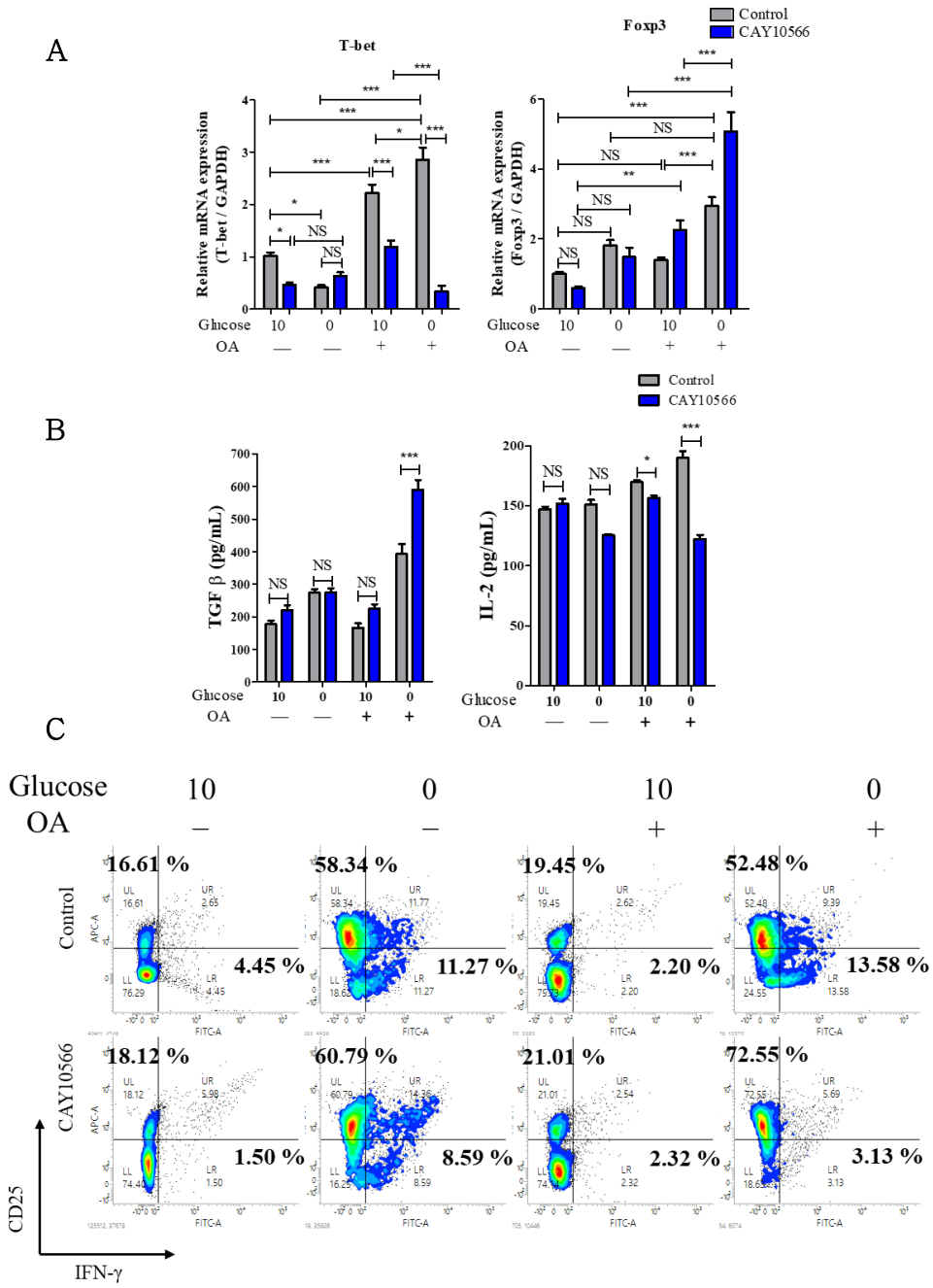
A
T-bet
Foxp3
Control
CAY10566
Relative mRNA expression (T-bet / GAPDH)
Relative mRNA expression (Foxp3 / GAPDH)
Glucose 10 0 10 0
OA — — + +
B
TGF β (pg/mL)
IL-2 (pg/mL)
C
Glucose 10 0 10 0
OA — — + +
Control
CAY10566
16.61 %
4.45 %
58.34 %
11.27 %
19.45 %
2.20 %
52.48 %
13.58 %
18.12 %
1.50 %
60.79 %
8.59 %
21.01 %
2.32 %
72.55 %
3.13 %
CD25
IFN-γ

Figure 4. Inhibition of SCD enhanced the phenotype of Treg cell, whereas suppressed Th1 cell phenotype

(A) Transcription levels of *T-bet* and *Foxp3* in Jurkat T cells treated with 100 μM OA and 1μM CAY10566 in 10 or 0 mM glucose contained medium for 1 day. $^{*}P < 0.05$. $^{**}P < 0.01$ and $^{***}P < 0.001$. Data indicate the mean ± SEM (n = 4). (B) Representative image of staining for CD25 and IFN-ɣ in Jurkat T cells treated with 100 μM OA and 1 μM CAY10566 in 10 or 0 mM glucose contained medium for 1 day. The quadrant was divided according to an unstained negative control. (C) The concentration of TGF-β and IL-2 in Jurkat T cells treated with 100 μM OA and 1 μM CAY10566 in 10 or 0 mM glucose contained medium for 1 day. $^{*}P < 0.05$ and $^{***}P < 0.001$. Data indicate the mean ± SEM (n = 4).

Regulation of SFA and UFA by SCD promoted phenotype of Treg and Th1 cell

We produced genetically engineered SCD subclones of Jurkat cells by pLenti-viral vector and CRISPR/Cas9 system to verify the role of SCD on biological function. Compared to parental, control-cas9 and pLenti transfected cells, SCD expression was depleted in SCD-KO cells and overexpressed in SCD-pLenti cells (Fig. 5 A). The phenotypes of Treg cells, including population of CD25 positive cells, TGF-β concentration and *Foxp3* mRNA expression were higher in SCD-KO cells than parental and SCD-pLenti cells. Meanwhile, SCD-pLenti cells showed significantly enhanced Th1 cells phenotypes including IFN-α positive cells population, IL-2 and tumor necrosis factor-α (TNF-α) concentration and *T-bet* mRNA expression compared to other subclones (Fig. 6 A-C). To examine FAs proportion was affected by SCD expression, the profile of FA was analyzed in subclones. The proportion of OA (18:1n9) was dominant in SCD-pLenti cells, whereas palmitic acids (PA; 16:0) proportion was higher in SCD-KO cells than other subclones (Fig. 6 D). Additionally, SCD-KO cells showed higher intensity of reactive oxygen species (ROS) and reduction of mitochondrial membrane potential (MMP) compared to other subclones (Fig. 5 B, C). These results were consistent in parental cells when treated with 50 μM PA. Particularly, intensity of mitochondrial superoxide was dramatically enhanced in SCD-KO cells compared to parental and SCD-pLenti cells (Fig. 7 A). And treatment

of parental cells with PA increased the intensity and CD25 positive cells population (Fig. 5 D). To determine the mitochondrial superoxide augmented the phenotype of Treg cells, mitotempo, a selective mitochondrial superoxide inhibitor was treated to subclones. In SCD-KO cells, population of CD25 positive cells and TGF-β concentration were attenuated from 22.97 to 14.33% and 748 to 596 pg/mL by mitotempo treatment (Fig. 7 B, C). Intriguingly, mitotempo treatment suppressed CD25 positive cells population from 15.24 to 8.64% in SCD-pLenti cells, but the treatment enhanced the population of IFN-ɣ positive cells and IL-2 concentration from 12.16% to 28.82% and 775 to 902 pg/mL. CXCL9, 10 and 11 are IFN-ɣ-inducible chemokines and enhance the T-bet expression in $CD4^+$ T cells, leading to upregulation of Th1 cell phenotype (Kriegova et al. 2011, Zohar et al. 2014). In SCD-pLenti cells, mRNA expressions of *CXCL9, 10* and *11* were dramatically enhanced compared to other subclones (Fig. 5 E). Especially CXCL11 expression was increased more than 10-fold-change. To determine OA which was the most dominant FA in SCD-pLenti cells was affected on the CXCL11 expression, 100 μM OA was treated to subclones and evaluated the expression of CXCL11. Treatment of parental and SCD-pLenti cells with OA substantially enhanced the mRNA expression of *CXCL11* compared to non-treatment, but not in SCD-KO cells (Fig. 7 D). Moreover, population of IFN-ɣ positive cells was increased in parental cells by treated with recombinant CXCL11 (Fig. 7 E).

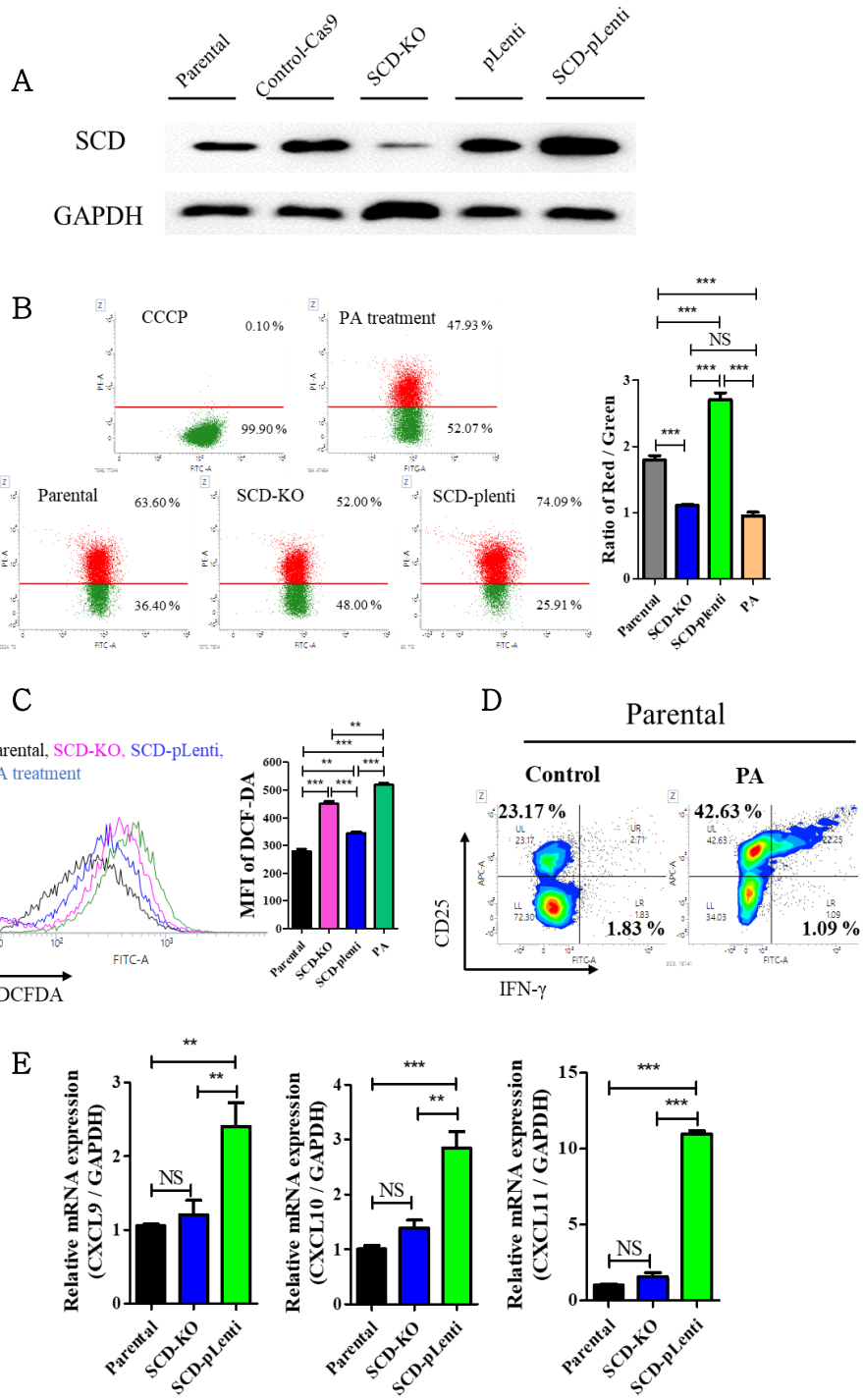
A
Parental
Control-Cas9
SCD-KO
pLenti
SCD-pLenti
SCD
GAPDH
B
CCCP
0.10 %
99.90 %
PA treatment
47.93 %
52.07 %
Parental
63.60 %
36.40 %
SCD-KO
52.00 %
48.00 %
SCD-plenti
74.09 %
25.91 %
Ratio of Red / Green
Parental
SCD-KO
SCD-plenti
PA
C
Parental, SCD-KO, SCD-pLenti,
PA treatment
Count
FITC-A
H2DCFDA
MFI of DCF-DA
D
Parental
Control
PA
23.17 %
1.83 %
42.63 %
1.09 %
CD25
IFN-γ
E
Relative mRNA expression (CXCL9 / GAPDH)
Relative mRNA expression (CXCL10 / GAPDH)
Relative mRNA expression (CXCL11 / GAPDH)
NS

Figure 5. General function of mitochondria in Jurkat cells according to SCD

(A) Expression of SCD and GAPDH in parental, Control-Cas9-transfected cells, SCD-KO cells, empty-pLenti-infected cells and SCD-pLenti cells. (B) Flow cytometric analysis of MMP in SCD subclones of Jurkat cells. Red and Green portion were divided according to positive control which treated with 50 μM carbonyl cyanide m-chlorophenyl hydrazine (CCCP). The graph indicated the value of red to green ratio. $^{**}P < 0.01$ and $^{***}P < 0.001$. Data indicate the mean ± SEM (n = 3). (C) Representative histogram for H_2-DCFDA staining in SCD subclones of Jurkat cells. The graph indicated the quantified MFI value of H_2-DCFDA staining. $^{**}P < 0.01$ and $^{***}P < 0.001$. Data indicate the mean ± SEM (n = 3). (D) Representative staining for CD25 and IFN-γ in parental cells treated with 50 μM PA and CCCP for 1 day. (E) Transcription levels of CXCL9, 10 and 11 in SCD subclones. $^{**}P < 0.01$ and $^{***}P < 0.001$. Data indicate the mean ± SEM (n = 4).

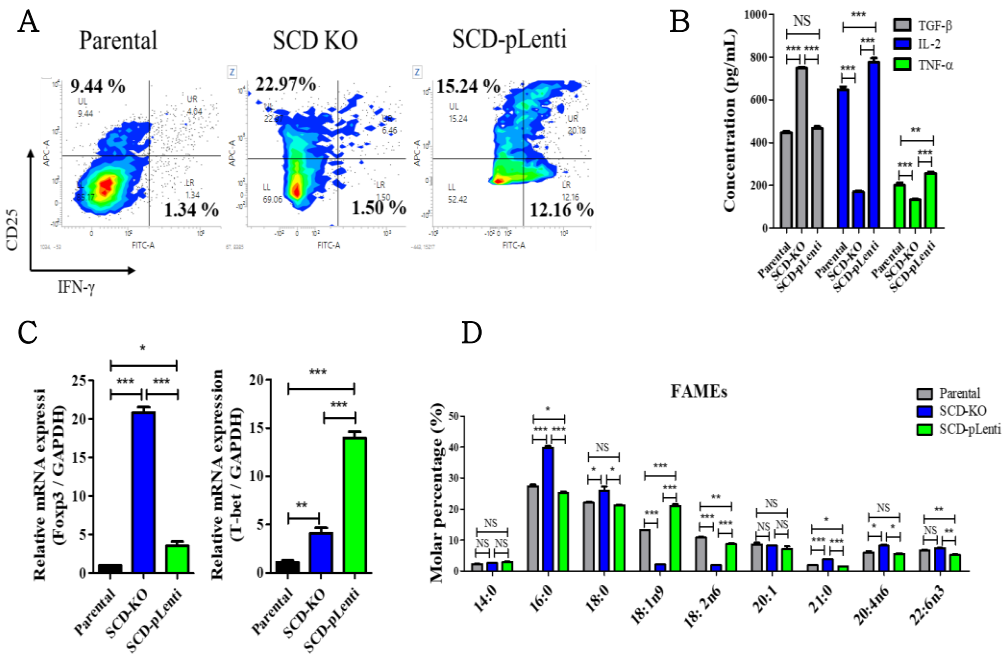

Figure 6. Increased OA amounts by SCD overexpression enhanced phenotype of Th1 cells rather than Treg cells

(A) Representative image of staining for CD25 and IFN-ɣ in SCD subclones of Jurkat T cells. The quadrant was divided according to an unstained negative control. (B) The concentration of TGF-β, IL-2 and TNF-α in SCD subclones of Jurkat T cells. $^{*}P < 0.05$, $^{**}P < 0.01$ and $^{***}P < 0.001$. Data indicate the mean ± SEM (n = 4). (C) Transcription levels of *Foxp3* and *T-bet* in SCD subclones of Jurkat T cells. $^{*}P < 0.05$, $^{**}P < 0.01$ and $^{***}P < 0.001$. Data indicate the mean ± SEM (n = 4). (D) The profile of major FAs molar percentages in SCD subclones of Jurkat T cells. $^{*}P < 0.05$, $^{**}P < 0.01$ and $^{***}P < 0.001$. Data indicate the mean ± SEM (n = 3). Gray: parental, Blue: SCD-KO cells, Green: SCD-pLenti cells.

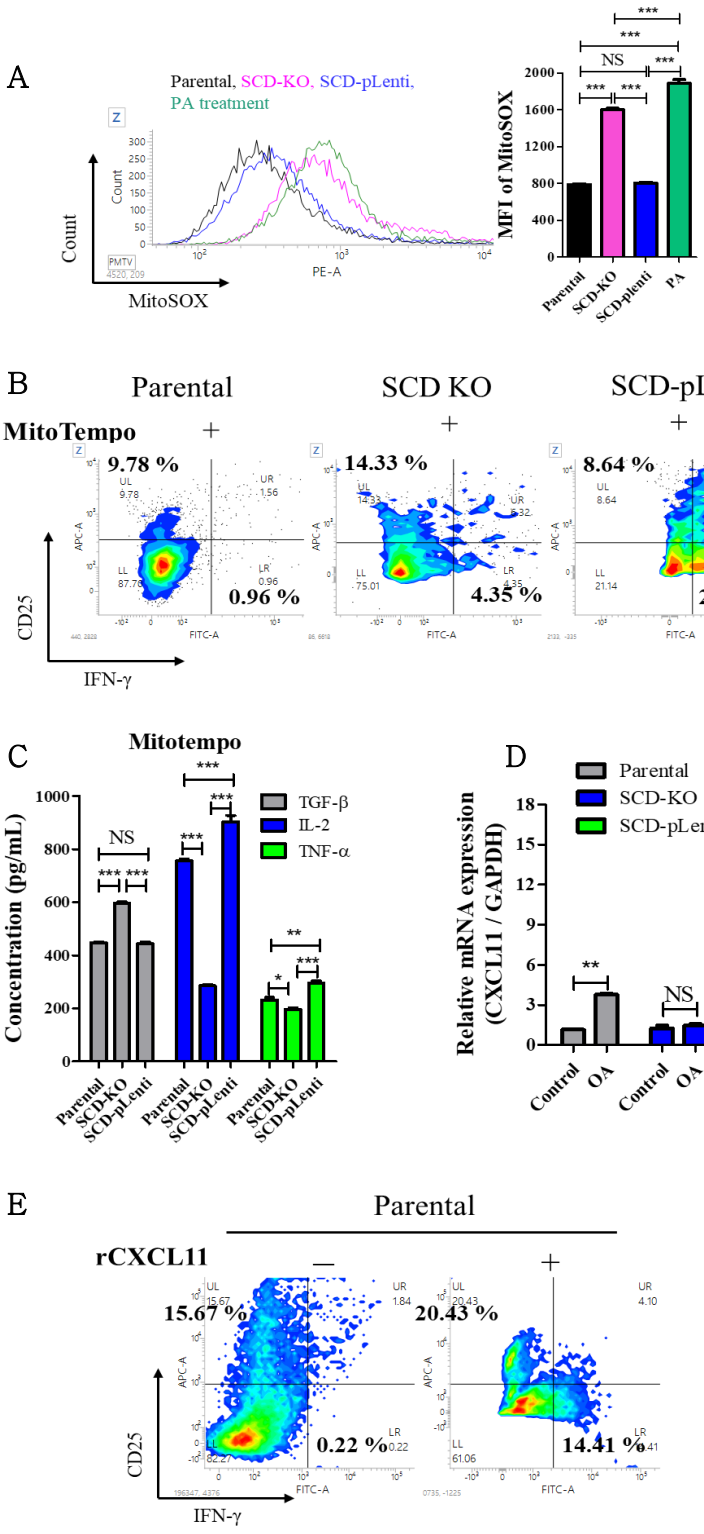
A
Parental, SCD-KO, SCD-pLenti,
PA treatment
Count
MitoSOX
PE-A
MFI of MitoSOX
Parental
SCD-KO
SCD-plenti
PA
B
Parental
SCD KO
SCD-pLenti
MitoTempo
9.78 %
14.33 %
8.64 %
0.96 %
4.35 %
28.82 %
CD25
IFN-γ
FITC-A
APC-A
C
Mitotempo
Concentration (pg/mL)
TGF-β
IL-2
TNF-α
NS
D
Relative mRNA expression
(CXCL11 / GAPDH)
Parental
SCD-KO
SCD-pLenti
Control
OA
E
Parental
rCXCL11
15.67 %
20.43 %
0.22 %
14.41 %

Figure 7. SCD-KO cell enhanced Treg cell phenotype by PA, whereas OA augmented phenotype of Th1 cells by OA

(A) Representative histogram for MitoSOX staining in SCD subclones of Jurkat T cells and 100 μM PA treated parental cells. The graph indicated the quantified MFI value of MitoSOX staining. $^{***}P < 0.001$. Data indicate the mean ± SEM (n = 3). Black: Parental, Pink: SCD-KO cells, Blue: SCD-pLenti cells, Green: PA treated parental cells. (B) Representative image of staining for CD25 and IFN-ɣ in SCD subclones of Jurkat T cells treated with 5 μM mitotempo for 1 day. (C) The concentration of TGF-β, IL-2 and TNF-α in SCD subclones of Jurkat T cells treated with 5 μM mitotempo for 1 day. $^{*}P < 0.05$, $^{**}P < 0.01$ and $^{***}P < 0.001$. Data indicate the mean ± SEM (n = 4). (D) Transcription levels of *CXCL11* in SCD subclones of Jurkat T cells treated with 100 μM OA for 1 day. $^{**}P < 0.01$ and $^{***}P < 0.001$. Data indicate the mean ± SEM (n = 4). (E) Representative image of staining for CD25 and IFN-ɣ in parental cells with 10 ng/mL rCXCL11 for 1 day.

CXCL11 produced from SCD-upregulated $CD4^+$ T cells upregulated the activity of $CD8^+$ T cells by coupled with CXCR3

To determine the effect of SCD on T cells, we isolated $CD4^+$ T cells from splenocytes in female BALB/c mice (5 weeks) and treated them with either CAY10566 or T0901317, SCD increased chemical. CAY10566 suppressed SCD expression in $CD4^+$ T cell, while its expression was enhanced by T0901317 treatment (Fig. 9 A). Concentration of IL-2 and population of IFN-ɣ positive cells were enhanced in T0901317 treated $CD4^+$ T cells compared to control, whereas TGF-β concentration and CD25 positive cells population were suppressed (Fig. 8 A, B). In contrast, CAY10566 treatment augmented TGF-β level. Cell proliferation was consistent in $CD4^+$ T cells regardless of CAY10566 or T0901317 treatment (Fig. 8 C).

To determine supernatant from $CD4^+$ splenic T cells could enhance the activity of $CD8^+$ splenic T cells (Fig. 11 A), co-cultured 4T1 cells with $CD8^+$ T cells were incubated with supernatant from control, CAY10566 or T0901317 treated $CD4^+$ splenic T cells for 1 day and assessed the apoptosis rate. The apoptosis rate of 4T1 cells was augmented more than 80% when co-cultured with $CD8^+$ T cells incubated with supernatants from T0901317-treated $CD4^+$ T cells, but the rate was suppressed when co-cultured with $CD8^+$ T cells with CAY10566-treated $CD4^+$ T cells supernatant (28.2%) (Fig. 9 B). Comparable result was obtained in B16F10 (70.09%) and CT26 cells (70.51%) (Fig. 11 B). Analogously, treatment of $CD8^+$ splenic T cells with T0901317 increased the apoptosis rate of 4T1 (40.42%), B16F10

(40.83%) and CT26 (64.91%) cells compared to non-treatment (4T1; 30.81%, B16F10; 31.77%, CT26; 39.42%) (Fig. 11 C). However, CAY10566 treatment attenuated the rate (4T1; 22.34%, B16F10; 27.14%, CT26; 30.71%). Although a comparable pattern of cancer cells apoptosis rate was observed in T0901317-treated $CD8^+$ T cells, the degree was lower than preincubation of $CD8^+$ T cells with supernatant from T0901317-treated $CD4^+$ T cells. Incubation of $CD8^+$ T cells with supernatant from T0901317-treated $CD4^+$ T cells enhanced mRNA levels of *perforin* and *granzyme B* compared to incubation with untreated $CD4^+$ T cells supernatant, while those levels did not change when incubated with supernatant from CAY10566-treated $CD4^+$ T cells (Fig. 9 C). Consistent pattern was obtained in $CD8^+$ T cells treated with CAY10566 and T0901317, the degree of change was low (Fig. 12 A).

To identify which soluble factors were affected by SCD expression, we performed a cytokine array using supernatant from CAY10566 and T0901317 treated $CD4^+$ T cells. In supernatant of T0901317-treated $CD4^+$ T cells, expressions of CXCL11, CXCL13, CXCL15, FGF2, TROY, IGFBP3, Resistin and IGF1 were significantly higher than in control and CAY10566 treatment (Fig. 12 B). Analogously, mRNA expressions of *CXCL11*, *CXCL13*, *CXCL15*, *FGF2*, *TROY*, *IGFBP3*, *Resistin*, and *IGF1* were enhanced in T0901317 treated $CD4^+$ T cells than control and CAY10566 treated cells (Fig. 12 C). Especially expression of *CXCL11* was substantially augmented in T0901317 treated $CD4^+$ T cells more than 12-fold-change in control and CAY10566 treated cells

(Fig. 9 D). However, other IFN-γ inducible chemokines, CXCL9 and -10 did not change (Fig. 12 D). Moreover, mRNA expression of *CXCR3*, a receptor for CXCL11 was increased in $CD8^+$ T cells when incubated with supernatant from T0901317-treated $CD4^+$ T cells (Fig. 9 E), but treatment of T0901317 only did not affect the expression (Fig. 12 E). Moreover, rCXCL11 treatment augmented activation markers of $CD8^+$ T cells including CD25 and IFN-γ (Fig. 10 A) and mRNA expressions of *perforin* and *granzyme B* compared to non-treatment (Fig. 12 F). Treatment of $CD8^+$ T cells with rCXCL11 increased apoptosis rate of 4T1 cells more than 40% compared to non-treatment (23.55%), indicating CXCL11 was required to activate $CD8^+$ T cells (Fig. 10 B). However, pretreatment of AMG 487, CXCR3 antagonist restrained the apoptosis rate of 4T1 cells when co-cultured with rCXCL11-treated $CD8^+$ T cells (Fig. 10 C), while only AMG487 treatment did not change the apoptosis of 4T1 cells (Fig. 13 A). Comparable results were observed in B16F10 and CT26 cells (Fig. 13 B). Additionally, expressions of CD25 and IFN-γ in $CD8^+$ T cells and mRNA expression of *perforin* and *granzyme B* were suppressed by treatment of AMG487 (Fig. 10 D) (Fig. 13 C). Furthermore, incubation of $CD8^+$ T cells with supernatants from T0901317-treated $CD4^+$ T cell enhanced apoptosis rate of 4T1 more than the supernatants from non and CAY10566 treated $CD4^+$ T cells, but it was reversed by AMG487 treatment (Fig. 13 D).

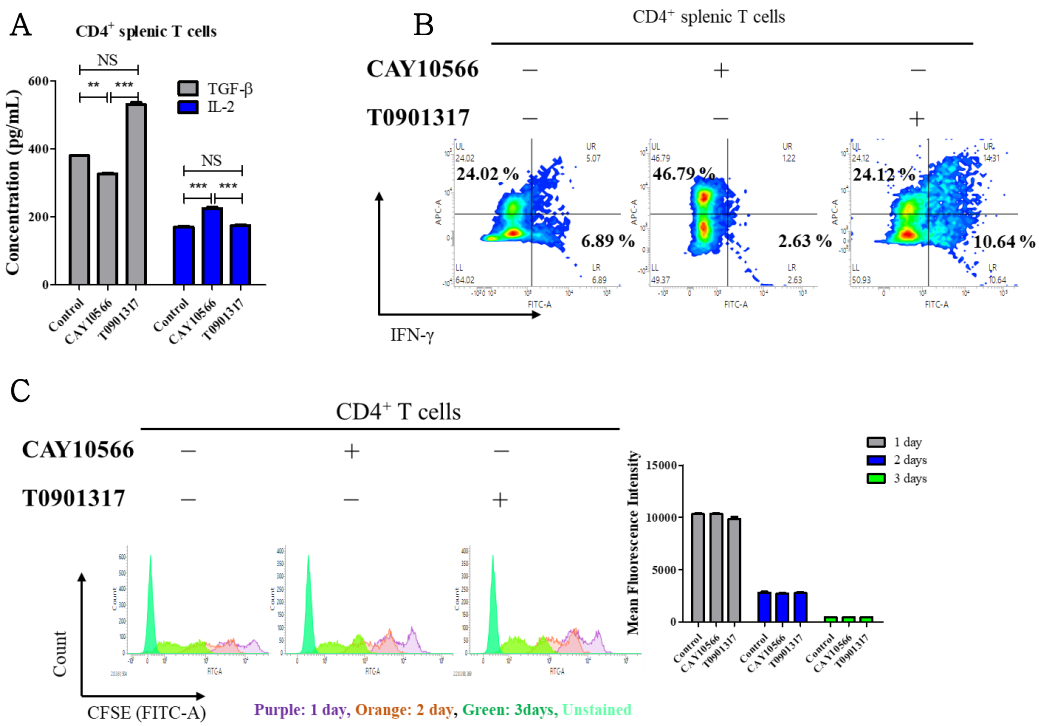

Figure 8. The effect of SCD in CD4$^+$ splenic T cells

(A) The concentration of TGF-β and IL-2 in CD4$^+$ splenic T cells treated with control, 1 μM CAY10566 and 10 μM T0901317 for 1 day. $^{*}P < 0.05$, $^{**}P < 0.01$ and $^{***}P < 0.001$. Data indicate the mean ± SEM (n = 4). (B) Representative staining for CD25 and IFN-ɣ in CD4$^+$ T cells treated with control, 1 μM CAY10566 and 10 μM T0901317 for 1 day. (C) CFSE staining in CD4$^+$ T cells treated with control, 1 μM CAY10566 and 10 μM T0901317 for 1 day. These cells were stained with CFSE and the fluorescent was measured for 3 days. The graph indicated the quantified MFI value of CFSE staining.

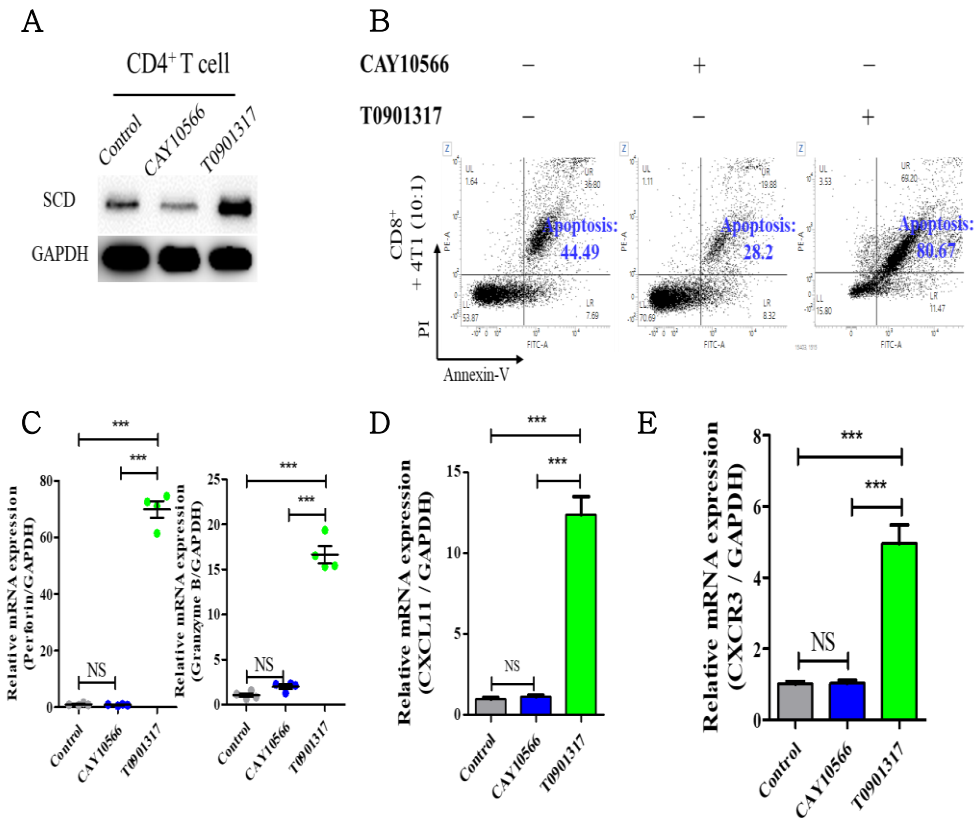
A
CD4+ T cell
Control
CAY10566
T0901317
SCD
GAPDH
B
CAY10566
T0901317
CD8+ + 4T1 (10:1)
PI
Annexin-V
Apoptosis: 44.49
Apoptosis: 28.2
Apoptosis: 80.67
C
Relative mRNA expression (Perforin/GAPDH)
Relative mRNA expression (Granzyme B/GAPDH)
NS
***
Control
CAY10566
T0901317
D
Relative mRNA expression (CXCL11 / GAPDH)
E
Relative mRNA expression (CXCR3 / GAPDH)

Figure 9. SCD-upregulated $CD4^+$ T cells-induced CXCL11 stimulated $CD8^+$ T cells activity by conjugated with CXCR3

(A) Expression of SCD and GAPDH in $CD4^+$ splenic T cells treated with control, 1 μM CAY10566 and 10 μM T0901317 for 1 day. (B) Representative dot plot of staining for annexin-V and PI in 4T1 cells which co-cultured with $CD8^+$ T cells as ratio 1:10 after incubation with supernatant of $CD4^+$ T cells treated with control, 1 μM CAY10566 and 10 μM T0901317 for 1 day. The quadrant was divided according to 4T1 cells. Apoptosis: Upper right + Lower right. (C) Transcription levels of *Perforin* and *Granzyme B* in $CD8^+$ T cells incubated with supernatant of $CD4^+$ T cells treated with control, 1 μM CAY10566 and 10 μM T0901317 for 1 day. $^{***}P < 0.001$. Data indicate the mean ± SEM (n = 4). (D) Transcription level of *CXCL11* in $CD4^+$ T cells treated with 1 μM CAY10566 and 10 μM T0901317 for 1 day. $^{***}P < 0.001$. Data indicate the mean ± SEM (n = 4). (E) Transcription level of *CXCR3* in $CD8^+$ T cells incubated with supernatant of $CD4^+$ T cells treated with control, 1 μM CAY10566 and 10 μM T0901317 for 1 day. $^{***}P < 0.001$. Data indicate the mean ± SEM (n = 4).

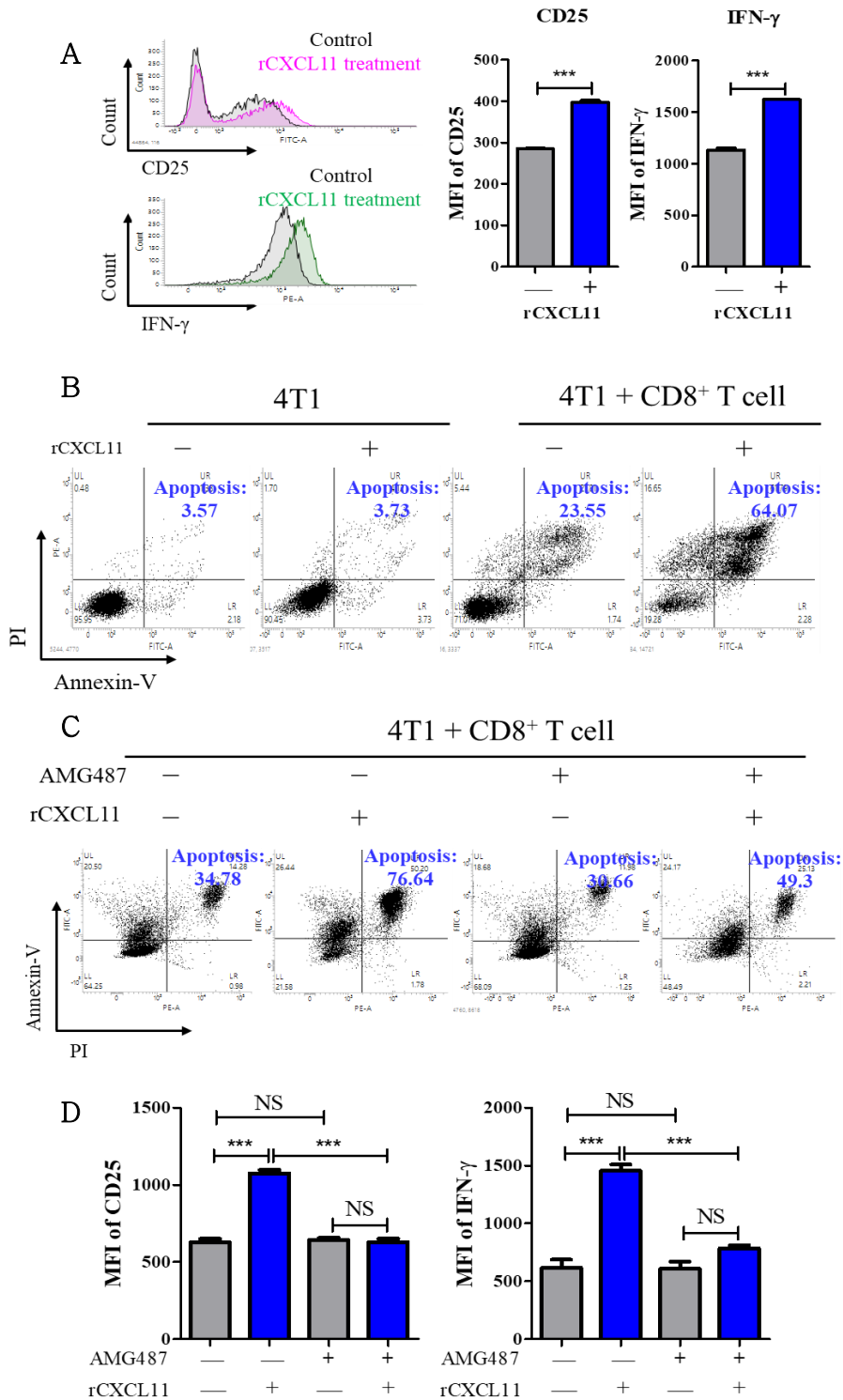
A
Control
rCXCL11 treatment
Count
CD25
Control
rCXCL11 treatment
Count
IFN-γ
CD25
IFN-γ
MFI of CD25
MFI of IFN-γ
***
***
rCXCL11
rCXCL11
B
4T1
4T1 + CD8+ T cell
rCXCL11
Apoptosis: 3.57
Apoptosis: 3.73
Apoptosis: 23.55
Apoptosis: 64.07
PI
Annexin-V
C
4T1 + CD8+ T cell
AMG487
rCXCL11
Apoptosis: 34.78
Apoptosis: 76.64
Apoptosis: 30.66
Apoptosis: 49.3
Annexin-V
PI
D
NS
***
***
NS
MFI of CD25
MFI of IFN-γ
AMG487
rCXCL11

Figure 10. CXCL11 augmented the activity of $CD8^+$ T cells by CXCR3

(A) Representative histogram for CD25 and IFN-γ staining in $CD8^+$ T cells treated with 10 ng/mL rCXCL11 for 1 day. The graph indicated the quantified MFI value of CD25 and IFN-γ staining. $^{***}P < 0.001$. Data indicate the mean ± SEM (n = 3). (B) Representative dot plot of staining for annexin-V and PI in 4T1 cells which co-cultured with $CD8^+$ T cells treated with 10 ng/mL rCXCL11 for 1 day. The quadrant was divided according to 4T1 cells. Apoptosis: Upper right + Lower right. (C) Representative dot plot of staining for annexin-V and PI in 4T1 cells which co-cultured with rCXCL11 treated $CD8^+$ T cells for 1 day after 18 hours pretreatment of 10 nM AMG487. Apoptosis: Upper left + Upper right. (D) The graph indicated the quantified MFI value of CD25 and IFN-γ staining in rCXCL11 treated $CD8^+$ T cells for 1 day after 18 hours pretreatment of 10 nM AMG487. $^{***}P < 0.001$. Data indicate the mean ± SEM (n = 3).

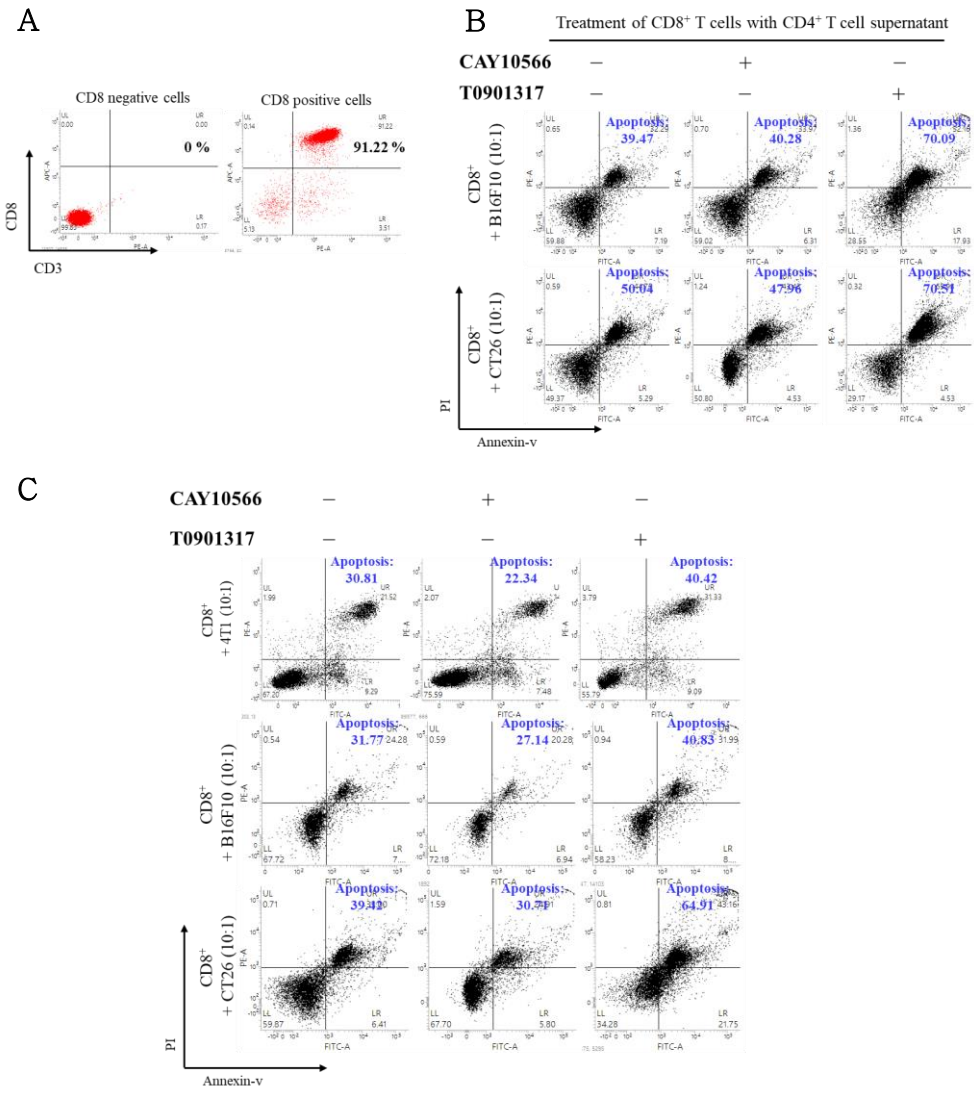
A
CD8 negative cells
CD8 positive cells
0 %
91.22 %
CD8
CD3
B
Treatment of CD8+ T cells with CD4+ T cell supernatant
CAY10566 – + –
T0901317 – – +
CD8+ + B16F10 (10:1)
CD8+ + CT26 (10:1)
Apoptosis: 39.47
Apoptosis: 40.28
Apoptosis: 70.09
Apoptosis: 50.04
Apoptosis: 47.96
Apoptosis: 70.51
PI
Annexin-v
C
CAY10566 – + –
T0901317 – – +
CD8+ + 4T1 (10:1)
CD8+ + B16F10 (10:1)
CD8+ + CT26 (10:1)
Apoptosis: 30.81
Apoptosis: 22.34
Apoptosis: 40.42
Apoptosis: 31.77
Apoptosis: 27.14
Apoptosis: 40.83
Apoptosis: 39.42
Apoptosis: 30.75
Apoptosis: 64.91
PI
Annexin-v

Figure 11. Treatment of supernatant from SCD-upregulated $CD4^+$ T cells enhanced cancer killing effect of $CD8^+$ T cells

(A) Representative dot plot image of CD3 and CD8 staining in isolated $CD8^+$ T cells from splenocytes. (B) Representative dot plot of staining for annexin-V and PI in B16F10 and CT26 cells which co-cultured with $CD8^+$ T cells after incubation with supernatant of $CD4^+$ T cells treated with control, 1 μM CAY10566 and 10 μM T0901317 for 1 day. The quadrant was divided according to untreated B16F10 and CT26 cells. Apoptosis: Upper right + Lower right. (C) Representative dot plot of staining for annexin-V and PI in 4T1, B16F10 and CT26 cells which co-cultured with $CD8^+$ T cells treated with 1 μM CAY10566 and 10 μM T0901317 for 1 day. Apoptosis: Upper right + Lower right.

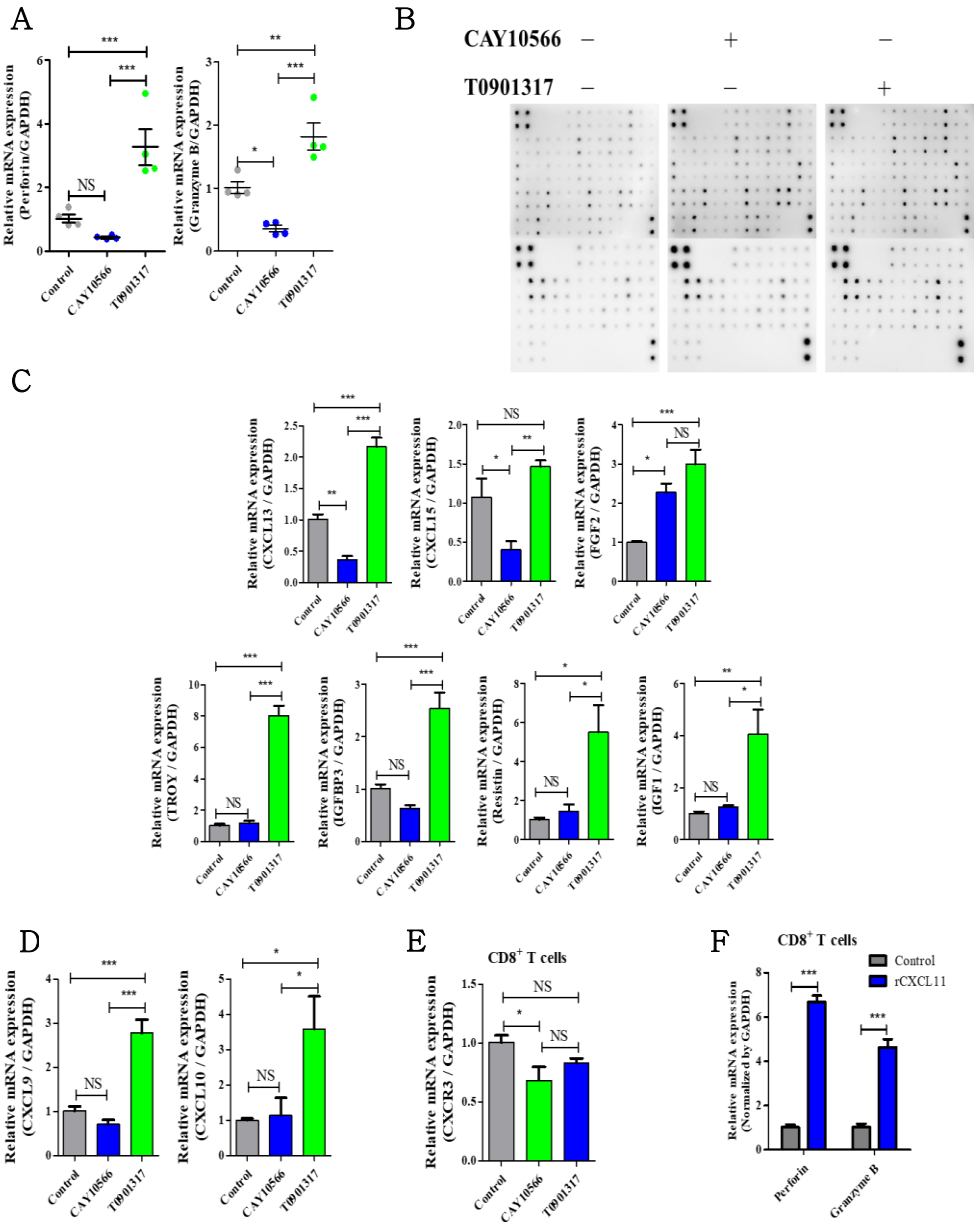
A
Relative mRNA expression (Perforin/GAPDH)
Relative mRNA expression (Granzyme B/GAPDH)
Control
CAY10566
T0901317
B
CAY10566
T0901317
C
Relative mRNA expression (CXCL13 / GAPDH)
Relative mRNA expression (CXCL15 / GAPDH)
Relative mRNA expression (FGF2 / GAPDH)
Relative mRNA expression (TROY / GAPDH)
Relative mRNA expression (IGFBP3 / GAPDH)
Relative mRNA expression (Resistin / GAPDH)
Relative mRNA expression (IGF1 / GAPDH)
D
Relative mRNA expression (CXCL9 / GAPDH)
Relative mRNA expression (CXCL10 / GAPDH)
E
CD8+ T cells
Relative mRNA expression (CXCR3 / GAPDH)
F
CD8+ T cells
Control
rCXCL11
Relative mRNA expression (Normalized by GAPDH)
Perforin
Granzyme B

Figure 12. Robust CXCL11 secretion from SCD-upregulated $CD4^+$ T cells increased the activity of $CD8^+$ T cells

(A) Transcription levels of *Granzyme B* and *Perforin* in $CD8^+$ T cells treated with 1 μM CAY10566 and 10 μM T0901317 for 1 day. $^{*}P < 0.05$, $^{**}P < 0.01$ and $^{***}P < 0.001$. Data indicate the mean ± SEM (n = 4). (B) The membrane image of cytokine array which incubated with supernatant from $CD4^+$ T cells treated with control, 1 μM CAY10566 and 10 μM T0901317 for 1 day. (C) Transcription levels of *CXCL13, CXCL15, FGF2, TROY, IGFBP3, Resistin* and *IGF1* in $CD8^+$ T cells incubated with supernatant from $CD4^+$ T cells treated with control, 1 μM CAY10566 and 10 μM T0901317 for 1 day. $^{*}P < 0.05$, $^{**}P < 0.01$ and $^{***}P < 0.001$. Data indicate the mean ± SEM (n = 4). (D) Transcription levels of *CXCL9* and *10* in $CD4^+$ T cells treated with control, 1 μM CAY10566 and 10 μM T0901317 for 1 day. Data indicate the mean ± SEM (n = 4). (E) Transcription level of *CXCR3* in $CD8^+$ T cells treated with control, 1 μM CAY10566 and 10 μM T0901317 for 1 day. Data indicate the mean ± SEM (n = 4). (F) Transcription levels of *Granzyme B* and *Perforin* in $CD8^+$ T cells treated with 10 ng/mL rCXCL11 for 1 day. $^{***}P < 0.001$. Data indicate the mean ± SEM (n = 4).

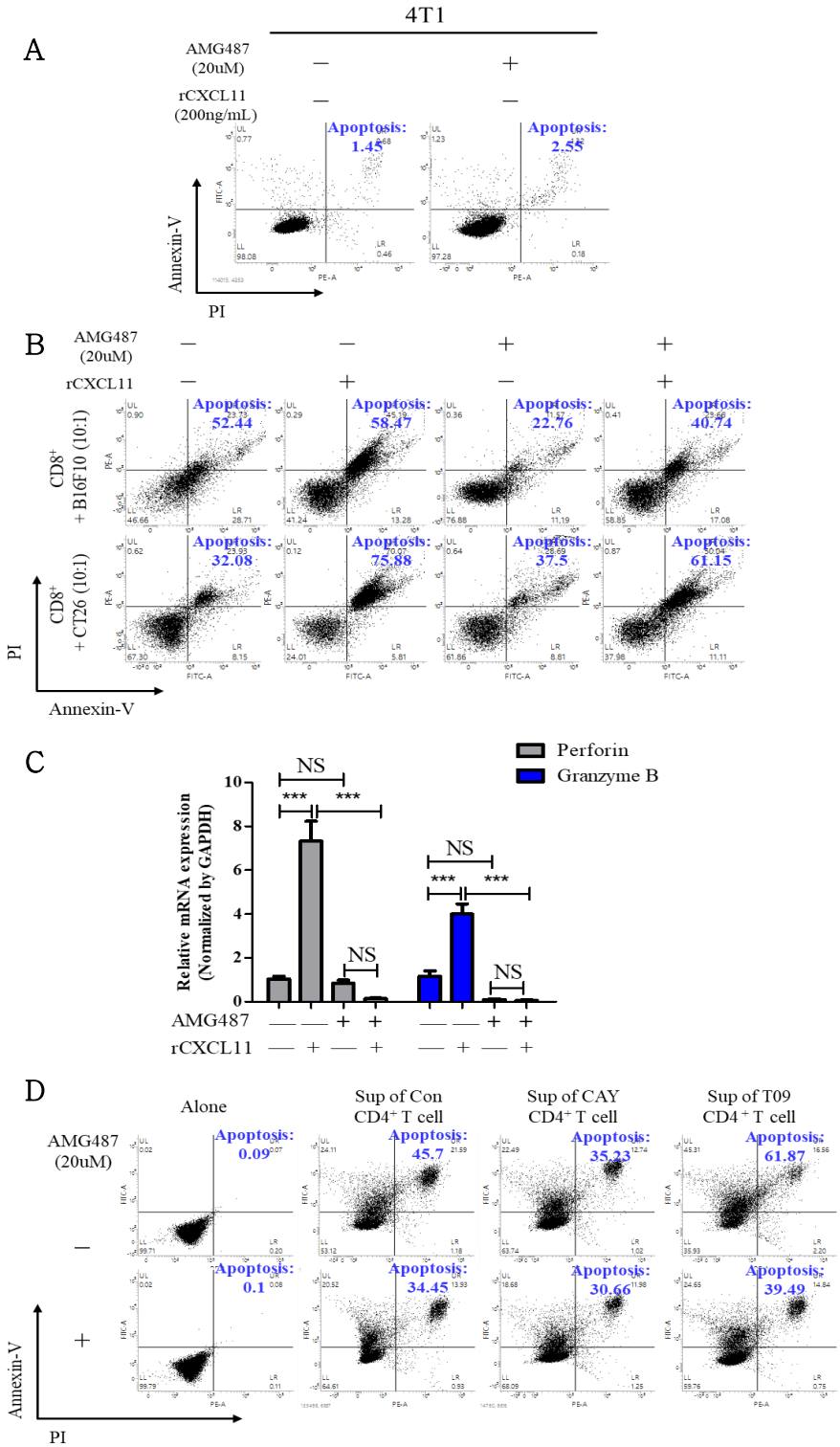
A
4T1
AMG487 (20uM)
rCXCL11 (200ng/mL)
Apoptosis: 1.45
Apoptosis: 2.55
Annexin-V
PI
B
AMG487 (20uM)
rCXCL11
CD8+ + B16F10 (10:1)
CD8+ + CT26 (10:1)
Apoptosis: 52.44
Apoptosis: 58.47
Apoptosis: 22.76
Apoptosis: 40.74
Apoptosis: 32.08
Apoptosis: 75.88
Apoptosis: 37.5
Apoptosis: 61.15
PI
Annexin-V
C
Perforin
Granzyme B
Relative mRNA expression (Normalized by GAPDH)
NS
***
AMG487
rCXCL11
D
Alone
Sup of Con CD4+ T cell
Sup of CAY CD4+ T cell
Sup of T09 CD4+ T cell
AMG487 (20uM)
Apoptosis: 0.09
Apoptosis: 45.7
Apoptosis: 35.23
Apoptosis: 61.87
Apoptosis: 0.1
Apoptosis: 34.45
Apoptosis: 30.66
Apoptosis: 39.49
Annexin-V
PI

Figure 13. CXCL11/CXCR3-axis enhanced cancer-killing effect in in $CD8^+$ T cells

(A) Representative dot plot of staining for annexin-V and PI in 4T1 cells treated with 20 μM AMG487 for 18 hours. The quadrant was divided according to untreated 4T1 cells. Apoptosis: Upper left + Upper right. (B) Representative dot plot of staining for annexin-V and PI in B16F10 and CT26 cells co-cultured with $CD8^+$ T cells treated with rCXCL11 for 1 day after preincubation with AMG487 for 18 hours. The quadrant was divided according to untreated B16F10 and CT26 cells Apoptosis: Upper right + Lower right. (C) Transcription levels of *Perforin* and *Granzyme B* in $CD8^+$ T cells treated with rCXCL11 for 1 day after preincubation with AMG487 for 18 hours. $^{***}P < 0.001$. Data indicate the mean ± SEM (n = 4). (D) Representative dot plot of staining for annexin-V and PI in 4T1 cells co-cultured with $CD8^+$ T cells treated with AMG487 for 1 day after incubation with supernatants of $CD4^+$ T cells treated with CAY10566 and T0901317 for 1 day. The quadrant was divided according to untreated 4T1 cells Apoptosis: Upper left + Upper right.

Suppression of CXCR3-$CD8^+$ T cells by upregulation of TCR signaling

We produced CXCR3-$CD8^+$ T cells infected with CXCR3-pLenti viral particle and verified the expression of CXCR3. Expression of CXCR3 was higher in CXCR3-$CD8^+$ T cells than parental and pLenti-$CD8^+$ T cells (Fig. 14 A). Expressions of CD25 and IFN-ɣ were higher in CXCR3-$CD8^+$ T cells than parental and pLenti-$CD8^+$ T cells, and more enhanced by rCXCL11 treatment (Fig. 14 B). Additionally, apoptosis of 4T1 cells was increased to 56.23% when co-cultured with CXCR3-$CD8^+$ T cells compared to parental (31.92%) and pLenti-$CD8^+$ T cells (34.78%) (Fig. 14 C). Comparable results were obtained in B16F10 and CT26 cells (Fig. 14 D). To examine the molecular mechanism of how CXCR3/CXCL11-axis activated $CD8^+$ T cells, we evaluated T-cell receptor (TCR) signaling pathway. In CXCR3-$CD8^+$ T cells, expressions of phosphor-Src, and phosphor-Lck and phosphor-Erk were substantially increased compared to $CD8^+$ T cells, but phosphor-ZAP70 expression was not (Fig. 15 A). However, treatment of PP2, a selective inhibitor for Src suppressed their expressions in $CD8^+$ T cells and CXCR3-$CD8^+$ T cells (Fig. 15 B). Additionally, PP2 treatment diminished activation markers of $CD8^+$ T cells including CD25 and IFN-ɣ expressions and mRNA expressions of *Perforin* and *Granzyme B* (Fig. 15 C, D).

We further analyzed the acute cancer-killing effect of CXCR3-$CD8^+$ T cells in 4T1-mouse model. Five days after administration of Luc2-

4T1 cells (0 day), PBS, $CD8^+$ T cells or CXCR3-$CD8^+$ T cells was intratumorally injected and the bioluminescence was assessed for 12 days. Administration of CXCR3-$CD8^+$ T cells greatly suppressed tumor growth and invasiveness in 4T1 mouse model compared to PBS and $CD8^+$ T cells administrated groups (Fig. 15 A). Although $CD8^+$ T cell injection regressed tumor growth compared to injection of PBS, the intensity of bioluminescence was higher than CXCR3-$CD8^+$ T cell (Fig. 15 B). Compared to PBS and $CD8^+$ T cells injected tumors, size and weight were smaller and lower in the tumors injected with CXCR3-$CD8^+$ T cells (Fig. 15 C). Percentage of $CD45^+CD3^+CD8^+$ cells were higher in CXCR3-$CD8^+$ T cell injected tumor (21.42%) than PBS (5.94%) and $CD8^+$ T cells (12.05%) injected tumors (Fig. 15 D). CXCR3 highly expressed $CD8^+$ T cells were observed in CXCR3-$CD8^+$ T cells injected tumors, but not in PBS and $CD8^+$ injected ones (Fig. 16 A). Moreover, in tumor mass administrated with CXCR3-$CD8^+$ T cells, more $CD8^+$ T cells were surrounding the cancer cells compared to PBS and $CD8^+$ T cells administrated ones. To determine $CD8^+$ T cells were migrated toward 4T1 cells by CXCR3 and CXCL11 conjugation, we performed a chemotaxis assay using CXCL11 siRNA transfected cancer cells and counted the number of $CD8^+$ cells in bottom wells. Migratory potential of CXCR3-$CD8^+$ T cells toward 4T1 cells was higher than $CD8^+$ T cells, but it was mitigated in CXCL11 siRNA transfected 4T1 cells (Fig. 16 B).

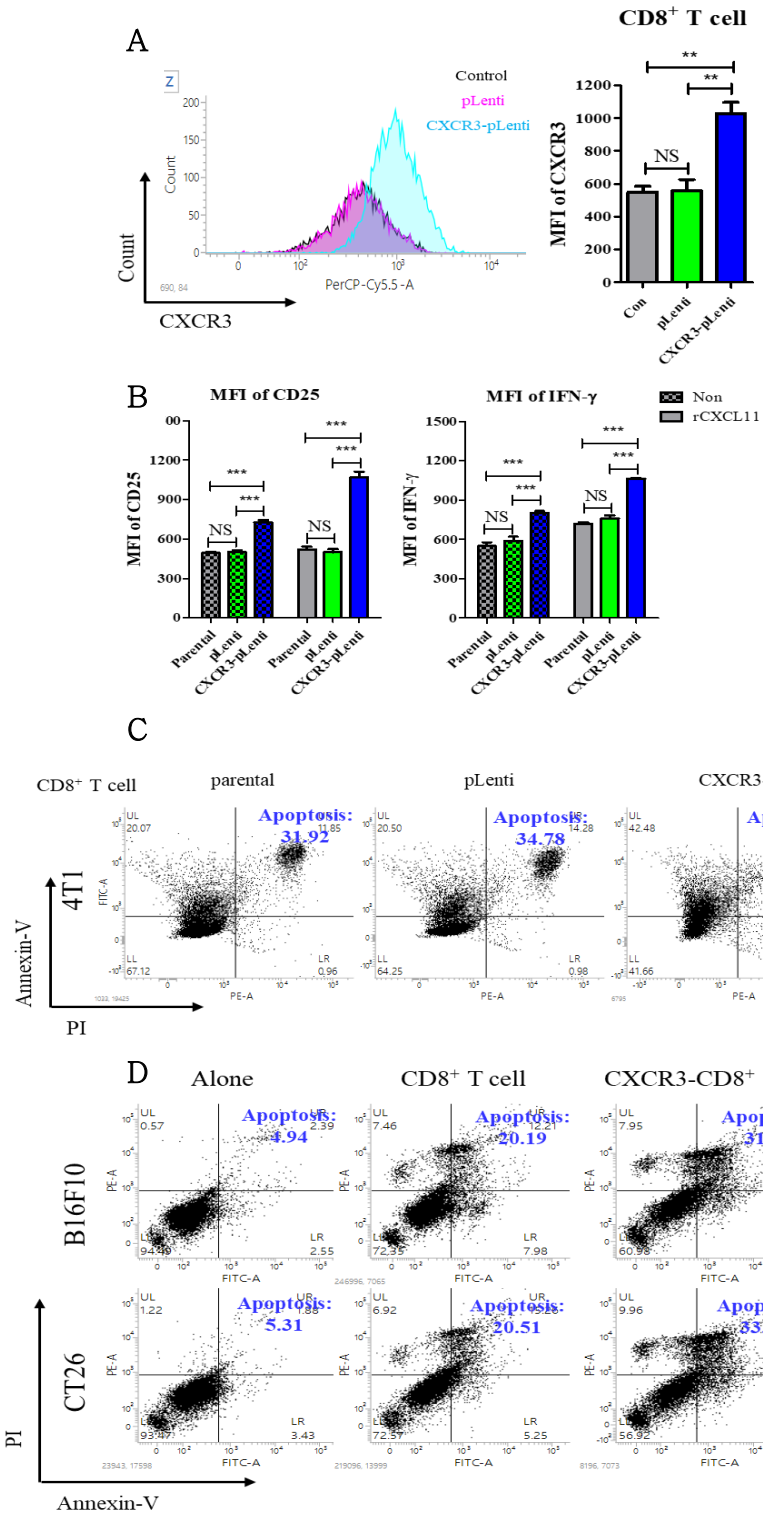
A
CD8+ T cell
Control
pLenti
CXCR3-pLenti
Count
CXCR3
PerCP-Cy5.5-A
MFI of CXCR3
NS
Con
pLenti
CXCR3-pLenti
B
MFI of CD25
MFI of IFN-γ
Non
rCXCL11
Parental
pLenti
CXCR3-pLenti
C
CD8+ T cell
parental
pLenti
CXCR3-pLenti
4T1
Annexin-V
PI
Apoptosis: 31.92
Apoptosis: 34.78
Apoptosis: 56.23
D
Alone
CD8+ T cell
CXCR3-CD8+ T cell
B16F10
CT26
Apoptosis: 4.94
Apoptosis: 20.19
Apoptosis: 31.07
Apoptosis: 5.31
Apoptosis: 20.51
Apoptosis: 33.12

Figure 14. The role of CXCR3-axis in $CD8^+$ T cells

(A) Representative histogram of CXCR3 staining in parental, pLenti and CXCR3-pLenti infected $CD8^+$ T cells. $^{**}P < 0.01$. Data indicate the mean ± SEM (n = 3). (B) The graph indicated the quantified MFI value of staining for CD25 and IFN-γ in parental, pLenti and CXCR3-pLenti infected $CD8^+$ T cells treated with rCXCL11 for 1 day. $^{***}P < 0.001$. Data indicate the mean ± SEM (n = 3). (C) Representative dot plot of staining for annexin-V and PI in 4T1 cells co-cultured with parental, pLenti and CXCR3-pLenti infected $CD8^+$ T cells for 1 day. The quadrant was divided according to untreated 4T1 cells Apoptosis: Upper left + Upper right. (D) Representative dot plot of staining for annexin-V and PI in B16F10 and CT26 cells co-cultured with alone, parental and CXCR3-pLenti infected $CD8^+$ T cells for 1 day. The quadrant was divided according to untreated B16F10 and CT26 cells Apoptosis: Upper right + Lower right.

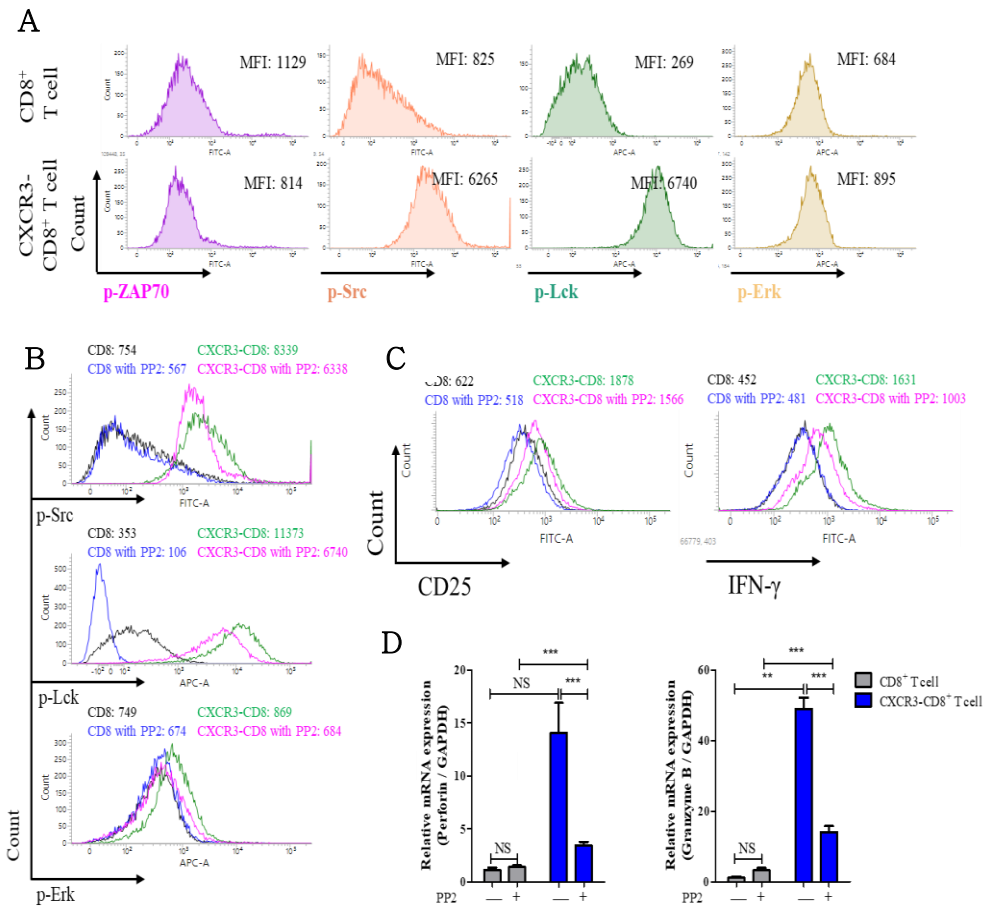

Figure 15. CXCL11/CXCR3-axis activated Src-signaling to enhance activity in CD8$^+$ T cells

(A) Representative histogram of staining for p-ZAP70, p-Src, p-Lck and p-Erk in CD8$^+$ and CXCR3-CD8$^+$ T cells. (B, C) Representative histogram of staining for p-Src, p-Lck, p-Erk, CD25 and IFN-γ in parental and CXCR3-CD8$^+$ T cells treated with 10 nM PP2 for 1 day. (D) Transcription levels of *Perforin* and *Granzyme B* in parental and CXCR3-CD8$^+$ T cells treated with 10 nM PP2 for 1 day. $^{**}P < 0.01$ and $^{***}P < 0.001$. Data indicate the mean ± SEM (n = 4).

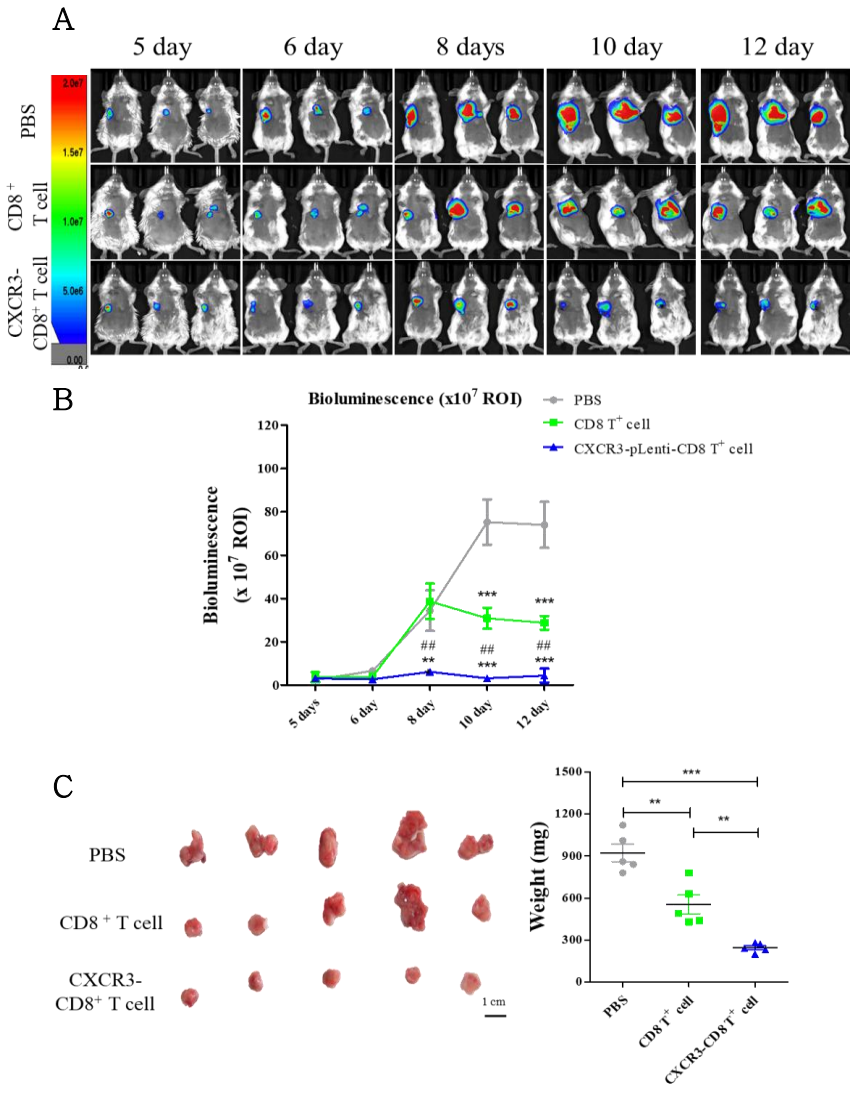
A
5 day
6 day
8 days
10 day
12 day
PBS
CD8 + T cell
CXCR3-CD8+ T cell
B
Bioluminescence (x10^7 ROI)
PBS
CD8 T+ cell
CXCR3-pLenti-CD8 T+ cell
Bioluminescence (x 10^7 ROI)
5 days
6 day
8 day
10 day
12 day
C
PBS
CD8 + T cell
CXCR3-CD8+ T cell
1 cm
Weight (mg)
PBS
CD8 T+ cell
CXCR3-CD8 T+ cell
D
PBS
CD8 + T cell
CXCR3-pLenti-CD8+ T cell
SSC
FITC-CD45
PE-CD3
APC-CD8
5.94
12.05
21.42

Figure 15. Outstanding cancer killing effect of CXCR3-$CD8^+$ T cells

(A) After 5 days of 2×10^5 4T1-Luc cells injection in mammary fat pad of mice, PBS, 2×10^6 $CD8^+$ T cells and CXCR3-$CD8^+$ T cells were administrated, respectively and measured the bioluminescence after luciferin-substrate injection (n = 3). (B) The bioluminescence intensity was quantified in the mice. PBS vs $^{***}P < 0.001$. $CD8^+$ T cells vs $^{\#\#}P < 0.01$ and $^{\#\#\#}P < 0.001$. Data indicate the mean ± SEM (n = 5). (C) The size and weight of tumors separated from those mice. Scale bar: 1 cm. $^{**}P < 0.01$ and $^{***}P < 0.001$. Data indicate the mean ± SEM (n = 5). (D) Flow cytometric analysis of CD3 and CD8 staining from CD45 positive cells (P1) in tumor-infiltrating leukocytes. The quadrant was divided according to unstained negative control.

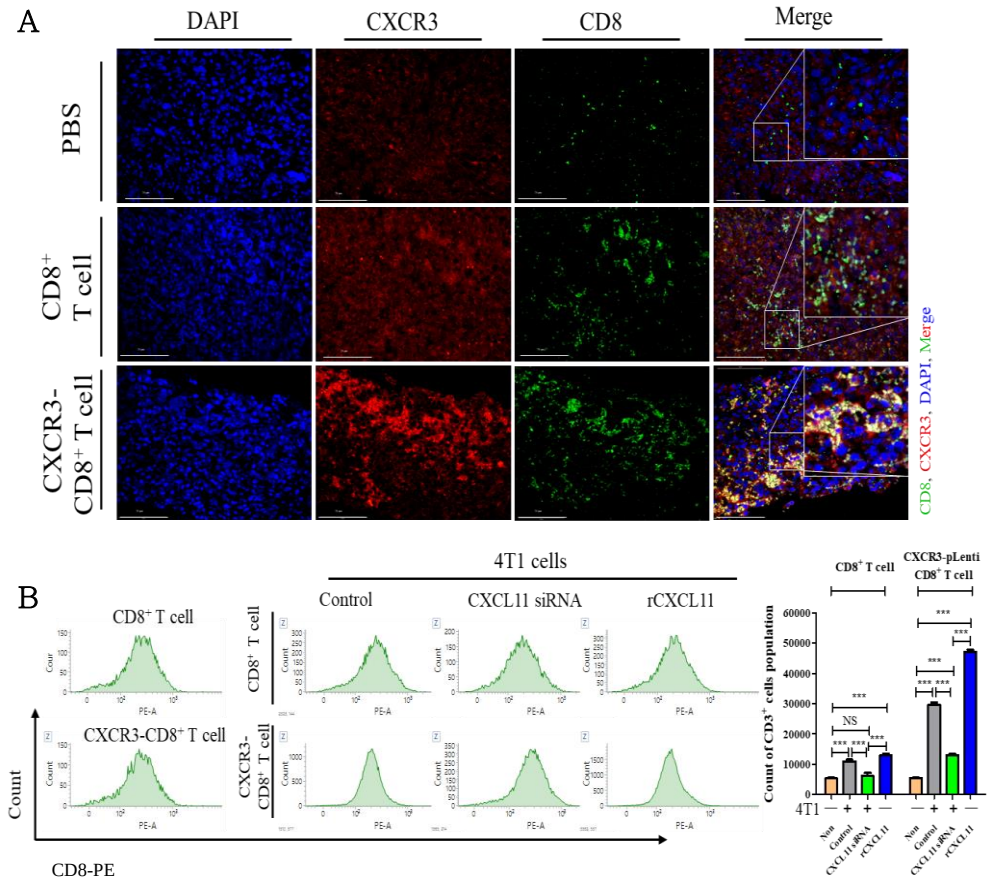

Figure 16. CXCR3-CD8$^+$ T cells migrated to cancer cells via conjugation with CXCL11

(A) Representative fluorescence staining for CD8 and CXCR3 in separated tumors. Green: CD8, Red: CXCR3, Blue: DAPI. 40× magnification. Scale bar: 75 μm. Enlarged image indicated the co-localization of CD8 and CXCR3. (B) Representative histogram of staining for CD8 in the bottom well. The graph indicated the counting of CD8$^+$ cells in bottom well. $^{***}P < 0.001$. Data indicate the mean ± SEM (n = 3).

Evaluation of synergetic effect in anti-PD1 antibody and $CD8^+$ T cells

To determine whether the programmed death (PD)-1 and PD-ligand1 (PD-L1) pathway could suppress the activity of parental and CXCR3-$CD8^+$ T cells, recombinant PD-L1 (rPD-L1) was treated to both cells and assessed expressions of activation markers. Treatment of rPD-L1 attenuated the intensity of CD25 and IFN-γ in parental and CXCR3-$CD8^+$ T cells, but it was reversed by treatment of anti-PD1 antibody (Fig. 17 A). Likewise, apoptosis of 4T1 cells was augmented when parental and CXCR3-$CD8^+$ T cells were treated with anti-PD1 antibody (Fig. 17 B). Additionally, treatment of anti-PD1 antibody enhanced the expressions of phosphor-Src, -Lck and Erk in parental and CXCR3-$CD8^+$ T cells compared to non-treatment (Fig. 17 C).

To examine the therapeutic efficacy of anti-PD1 antibody, 4T1 mouse model was injected with anti-PD1 antibody 3 times with a PBS, $2x10^6$ parental and CXCR3-$CD8^+$ T cells (Fig. 18 A). In 4T1 mouse model, administration of anti-PD1 antibody suppressed tumor size compared to non-treatment (Fig. 18 B). Co-administration of anti-PD1 antibody and $CD8^+$ T cells mitigated the tumor growth more than single injection of anti-PD1 antibody or $CD8^+$ T cells (Fig. 18 C). However, CXCR3-$CD8^+$ T cells did not show the synergetic effect with anti-PD1 antibody. In our 4T1-mouse model, cancer-killing efficacy of CXCR3-$CD8^+$ T cells alone was favorable, but anti-PD1 antibody was necessary for $CD8^+$ T cells to enhance the efficacy. The weights of tumors were lower in co-administration of CXCR3-$CD8^+$ T cells and

anti-PD1 antibody compared to $CD8^+$ T cells and anti-PD1 antibody administrated ones (Fig. 18 D). However, CXCR3-$CD8^+$ T cells did not show the synergetic effect when injected with anti-PD1 antibody at 12 day monitored model. In our 12 days 4T1-mouse model, cancer-killing efficacy of CXCR3-$CD8^+$ T cells was favorable, but anti-PD1 antibody was necessary for $CD8^+$ T cells to enhance the efficacy. Furthermore, we monitored the size of tumor for 21 days after injection with anti-PD1 antibody and PBS, $CD8^+$ T cells or CXCR3-$CD8^+$ T cells (Fig. 19 A). Analogous to the bioluminescence, the size of tumor was smaller in CXCR3-$CD8^+$ T cells administrated ones compared to others. At 21 days, co-injection with anti-PD1 antibody and CXCR3-$CD8^+$ T cells significantly suppressed the size of tumors compared to single injection (Fig. 19 B, C).

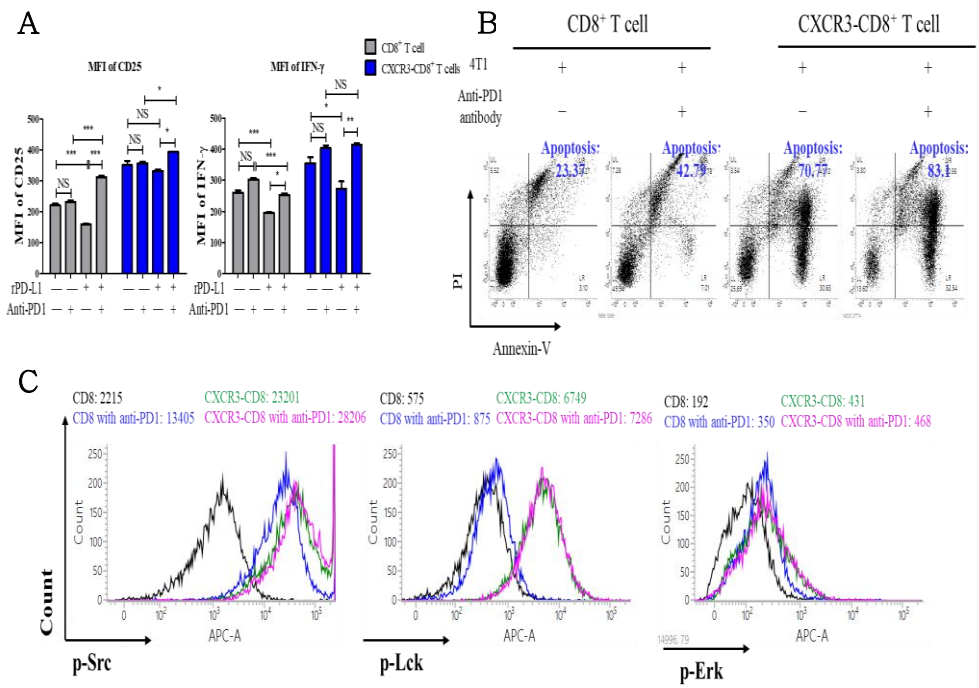

Figure 17. Treatment of anti-PD1 antibody enhanced Src-signaling in CD8$^+$ T cells

(A) The graph indicated the quantified MFI value of CD25 and IFN-ɣ staining in CD8$^+$ and CXCR3-CD8$^+$ T cells treated with 1 μg/mL anti-PD1 antibody and 1 μg/mL rPD-L1 for 1 day. $^{*}P < 0.05$, $^{**}P < 0.01$ and $^{***}P < 0.001$. Data indicate the mean ± SEM (n = 3). (B) Representative dot plot of staining for annexin-V and PI in 4T1 cells which co-cultured with CD8$^+$ T cells treated with 1 μg/mL anti-PD1 antibody for 1 day. Apoptosis: Upper right + Lower right. (C) Representative histogram of staining for p-Src, p-Lck and p-Erk in CD8$^+$ T cells treated with 1 μg/mL anti-PD1 antibody for 1 day.

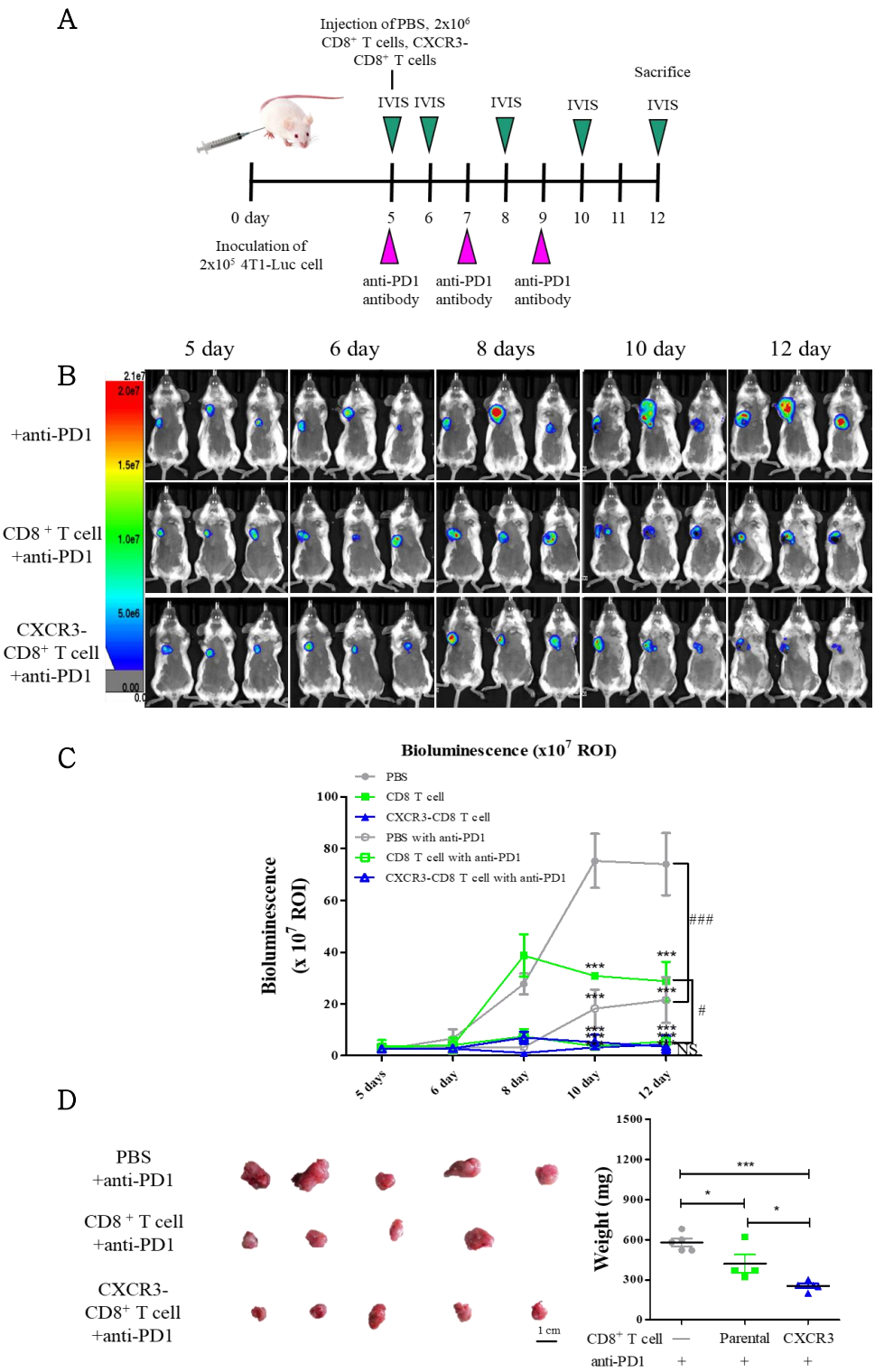
A
Injection of PBS, 2x10^6 CD8+ T cells, CXCR3- CD8+ T cells
Sacrifice
IVIS IVIS IVIS IVIS IVIS
0 day
5 6 7 8 9 10 11 12
Inoculation of 2x10^5 4T1-Luc cell
anti-PD1 antibody
anti-PD1 antibody
anti-PD1 antibody
B
5 day
6 day
8 days
10 day
12 day
+anti-PD1
CD8 + T cell +anti-PD1
CXCR3- CD8+ T cell +anti-PD1
C
Bioluminescence (x10^7 ROI)
PBS
CD8 T cell
CXCR3-CD8 T cell
PBS with anti-PD1
CD8 T cell with anti-PD1
CXCR3-CD8 T cell with anti-PD1
Bioluminescence (x 10^7 ROI)
5 days
6 day
8 day
10 day
12 day
###
#
NS
D
PBS +anti-PD1
CD8 + T cell +anti-PD1
CXCR3- CD8+ T cell +anti-PD1
1 cm
Weight (mg)
CD8+ T cell
Parental
CXCR3
anti-PD1

Figure 18. Treatment of anti-PD1 antibody-induced synergetic effect was minor in CXCR3$^+$ T cells

(A) Schedule of animal experiments treated with anti-PD1 antibody and PBS, CD8$^+$ and CXCR3-CD8$^+$ T cells. (B) PBS, 2×10^6 CD8$^+$ T cells and CXCR3-CD8$^+$ T cells were administrated in the mice after 5 days of 2×10^5 4T1-Luc cells injection. Two hundred microgram of Anti-PD1 antibody was directly injected in tumors at 5, 7 and 9 day (n = 3). (C) The bioluminescence intensity was quantified in the mice. PBS vs $^{***}P < 0.001$. Data indicate the mean ± SEM (n = 5). (D) The size and weight of tumors separated from mice injected with anti-PD1 antibody and PBS (n = 5), CD8$^+$ T cells (n = 4), CXCR3-CD8$^+$ T cells (n = 5). Scale bar: 1 cm. $^{*}P < 0.05$ and $^{***}P < 0.001$. Data indicate the mean ± SEM.

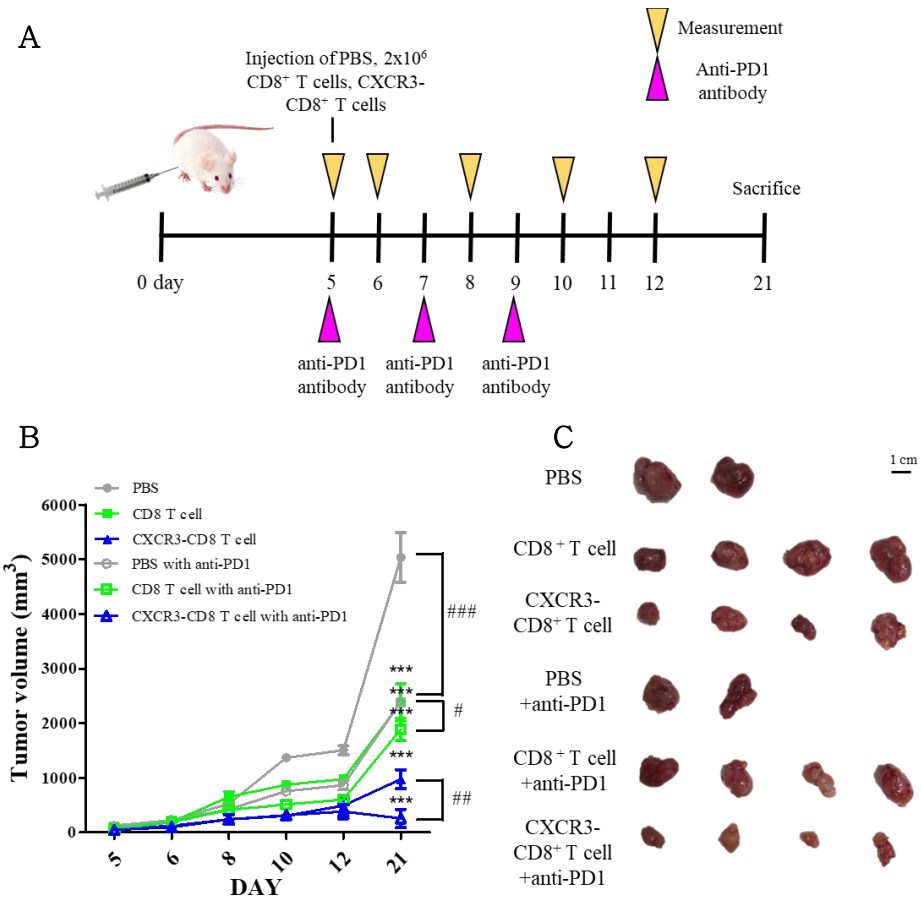

Figure 19. Synergetic effect of anti-PD1 antibody and CXCR3-CD8^{+} T cells injection at 21days

(A) Schedule of 4T1-mice model study for 21 days. (B, C) Assessment of tumor volume for 21 days. (C) Measurement of size of tumor separated from 4T1 mouse model at 21 days. PBS vs $^{***}P < 0.001$. $^{\#}P < 0.05$, $^{\#\#}P < 0.01$ and $^{\#\#\#}P < 0.001$. Data indicate the mean ± SEM (n = 4).

Discussion

Within tumor microenvironment, functional changes of fibroblasts and T cells promote tumor malignancy. Cancer cells escape the immune surveillance by TILs that is major obstacle to innate anticancer therapy (Swann and Smyth 2007). In contrast to normal counterparts, high amount of lipids from CAFs interact with neighboring cancer cells, advancing the tumorigenesis by metabolic reprogramming (Santi et al. 2015, Gupta et al. 2017, Sullivan et al. 2019), but comprehensive network between CAFs-derived fatty acids and T cells remains unclear. Our study demonstrated that oleic acid (OA) was higher than other FAs in CAFs-supernatant and transferred into $CD4^+$ TILs with upregulation of lipid transporter. Moreover, CAFs-derived OA augmented the SCD expression in $CD4^+$ TILs and more increased under glucose-deficient conditions. In T cells, SCD expression augmented the OA-induced CXCL11 expression and phenotype of Th1 cells, but silencing its expression led to enhancement of Treg cells phenotype by PA-mediated mitochondrial oxide production. Moreover, considerable CXCL11 production from SCD-upregulated $CD4^+$ T cells activated CXCR3-signaling in $CD8^+$ T cells with upregulation of phosphor-Src and Lck and augmented cancer killing effect *in vitro* and *in vivo*.

Lipids are highly generated by results of Warburg effects including glycolysis, pentose phosphate and NADPH pathway, and they are utilized to generate energy under glucose-deficient condition (Vander

Heiden et al. 2009, Raulien et al. 2017). In TILs, FA amounts are enhanced under glucose-deficient conditions by the Warburg effect and hijacking of glucose by cancer cells, producing energy to meet the energy demand (Chang et al. 2015, Rambold et al. 2015, Liberti 2016). Intriguingly, dependent on FAs saturation, activation and proliferation are changed in T cells (de Jong et al. 2014). Indeed, UFAs are beneficial to activate lipid metabolism and play as fuel for bioenergetics for proliferation (Jump 2011). In contrast, SFA enhances the lipotoxicity with endoplasmic reticulum stress even at low dose (Gorjao et al. 2007, Zeng et al. 2020). In our study, OA proportion was higher in $CD4^+$ T cells incubated with CAFs-supernatant than other FAs and its treatment augmented expression of SCD compared to non-treatment. Reversely, OA was highly synthesized in T cells according to SCD expression as consistent with (Polo-Hernandez et al. 2014). OA augmented CXCL11 and T-bet expression and concentration of IL-2 in parental and SCD-pLenti cells, but their expressions did not change in SCD-KO cells. It suggested that SCD was required to OA-induced Th1 cell phenotype enhancement. In contrast to other subclones, proportion of PA was higher in SCD-KO cells due to converting from SFA to UFA was blocked, leading to mitochondrial dysfunction.

SCD plays an important role which converts SFA to UFA, as well as orchestrates the pro-inflammatory response (Liu et al. 2011). Comparative analysis of microarray in wild-type and SCD-KO mice

revealed that SCD absence suppressed the detoxification, lipid metabolism and ER-stress-related gene expression under stressful conditions, whereas expressions of inflammation-related genes including *Lcn2, Afp, Fos* and *Jun* were enhanced (Flowers et al. 2008). Furthermore, the profiles of cytokines and chemokines in $CD4^+$ splenic T cells from wild-type and SCD-KO mice model indicate that loss of SCD greatly enhances the secretion of pro-inflammatory cytokines and chemokines compared to wild-type (Yeoh et al. 2016). In contrast, treatment of T0901317 enhances the proportion of OA and protects the stromal cells from lipotoxicity-induced cell death via reduction of endoplasmic reticulum stress and IL-6 and -8 concentration (Dalla Valle et al. 2019). Our data revealed that SCD-upregulated $CD4^+$ T cells enhanced the levels of chemokine and cytokines especially CXCL11 compared to control and SCD-downregulated $CD4^+$ T cells. Secretion of CXCL11 from docetaxel-treated cancer cells and vaccinia virus administration is beneficial for attracting $CD8^+$ T cells and suppresses tumor growth (Liu et al. 2016, Gao et al. 2019), but CXCL11 also plays a crucial role in cancer cells malignancy by upregulation of migration and epithelial-mesenchymal transition (Koo et al. 2017, Puchert et al. 2020). Thus, better understanding of CXCL11/CXCR3-axis in T cells is urgently required.

CXCR3 is a receptor for CXCL11 and necessary for induction of $CD8^+$ T cells priming and migration toward cancer cells via conjugation with its ligands (Ogasawara et al. 2002, Groom and Luster 2011), however,

detailed molecular mechanism of CXCR3/CXCL11-axis in activation of $CD8^+$ T cells has not been delineated. In T-cell receptor (TCR) signaling of $CD8^+$ T cells, Src-tyrosine kinase family is central to initiate the signaling and promotes the activation, development and differentiation (Salmond et al. 2009). In this study, compared to parental cells, CXCR3-$CD8^+$ T cells substantially augmented the expression of phosphorylation of Src and Lck after rCXCL11 treatment, increasing the activation. In 4T1-mouse model, administration of CXCR3-$CD8^+$ T cells remarkably suppressed tumor growth and invasiveness with migration toward cancer cells compared to PBS and $CD8^+$ T cells. Although administration of CXCR3-$CD8^+$ T cells could affect the activity of other immune cells warrants further investigation, the tumor growth was successfully diminished. Moreover, blocking PD-1 is well compelling as cancer therapy by enhancement of $CD8^+$ T cells activity and its therapy is usually combined with anticancer drugs for enhancement of efficacy (Bailly et al. 2020). In contrast to substantial suppression of tumor growth in 4T1 mouse model by administration of $CD8^+$ T cells with anti-PD1 antibody in 4T1 mouse model, synergetic effect of anti-PD1 antibody and CXCR3-$CD8^+$ was not observed compared to only CXCR3-$CD8^+$ T cells administration. We thought that CXCR3-$CD8^+$ T cells were enough to kill cancer cells without anti-PD1 antibody at 12 days. However, $CD8^+$ T cells required the combination with anti-PD1 antibody to enhance the efficacy. Analogously, tumor growth was substantially suppressed by

administration of CXCR3-$CD8^+$ T cells and comparable regardless of anti-PD1 antibody injection after 14 days from CT26 injection in mice. However, at 21 days, tumor volume and weight were dramatically suppressed by administration of CXCR3-$CD8^+$ T cells and anti-PD1 antibody more than CXCR3-$CD8^+$ T cells alone. In our 4T1 mouse model, synergetic effect of anti-PD1 antibody could have been observed in CXCR3-$CD8^+$ T cells administrated ones. However, severe cachexia was observed at 12 days in 4T1 mouse models, thus we ended the experiment. Based on our data, a combination of anti-PD1 and CXCR3-$CD8^+$ T cells could be excellent to cancer-killing efficacy at severe tumors than an only CXCR3-$CD8^+$ T cells administration.

The present study demonstrated that CAFs-derived OA enhanced SCD expression and its expression augmented Th1 cells phenotype with upregulation of CXCL11 rather than Treg cells. Furthermore, considerable CXCL11 secretion for SCD-upregulated $CD4^+$ T cells stimulate CXCR3 signaling in $CD8^+$ T cells with phosphorylation of Src and Lck, resulting in a significant cancer-killing effect in the mouse model. Moreover, synergetic effect of anti-PD1 antibody was worth consideration in tumors with a bad prognosis. Taken together, our study suggested that role of SCD in CXCL11/CXCR3-axis enhances cancer-killing effect of $CD8^+$ T cells and it could be applied for adoptive T cell therapy.

GENERAL CONCLUSION

Within the tumor microenvironment, glucose is deficient by irregular vasculature and aerobic glycolysis by cancer cells and induces metabolic reprogramming in cancerous and non-cancerous cells. It is well established that glucose deficiency enhances cancer malignancy, but the effect on cancer cells, CAFs, and $CD4^+$ TILs remain unclear. We demonstrated that adaptation to glucose deficiency enhanced the resistance to metformin in HMM cells by mitochondrial MDR1 expression. Additionally, glucose deficiency increased the TGF-β signaling and MCU expression in CAFs, but not in NFs. Enhancement of MCU-mediated calcium influx into mitochondria activated ATP synthase and produced ATP for survival, but blockade of ATP synthase augmented cell death. Moreover, higher lipogenesis in CAFs than in NFs provided the OA to cancer cells and enhanced SCD expression, leading to the promotion of stemness under glucose-deficient conditions. SCD-mediated cancer stemness was activated by YAP nuclear localization via actin-polymerization. SCD expression was positively correlated with tumorigenesis and poor prognosis in patients with lung cancer. Additionally, CAFs-derived OA enhanced SCD expression in $CD4^+$ TILs under glucose-deficient conditions. Biosynthesis of OA by SCD augmented the phenotype of Th1 cells and induced a robust secretion of CXCL11 that improved a cancer-killing effect of $CD8^+$ T cells by activation of CXCR3 signaling.

Reference

Abolhoda, A., A. E. Wilson, H. Ross, P. V. Danenberg, M. Burt and K. W. Scotto (1999). "Rapid activation of MDR1 gene expression in human metastatic sarcoma after in vivo exposure to doxorubicin." Clin Cancer Res 5(11): 3352-3356.

Agorku, D. J., A. Langhammer, U. Heider, S. Wild, A. Bosio and O. Hardt (2019). "CD49b, CD87, and CD95 are markers for activated cancer-associated fibroblasts whereas CD39 marks quiescent normal fibroblasts in murine tumor models." Front Oncol 9: 716.

Anderberg, C., H. Li, L. Fredriksson, J. Andrae, C. Betsholtz, X. Li, U. Eriksson and K. Pietras (2009). "Paracrine signaling by platelet-derived growth factor-CC promotes tumor growth by recruitment of cancer-associated fibroblasts." Cancer Res 69(1): 369-378.

Anderson, A. C., N. Joller and V. K. Kuchroo (2016). "Lag-3, Tim-3, and TIGIT: Co-inhibitory receptors with specialized functions in immune regulation." Immunity 44(5): 989-1004.

Aue, G., C. Sun, D. L. Liu, J. H. Park, S. Pittaluga, X. Tian, E. Lee, S. Soto, J. Valdez, I. Maric, M. Stetler-Stevenson, C. Yuan, Y. Nakamura, P. Muranski and A. Wiestner (2018). "Activation of Th1 immunity within the tumor microenvironment is associated with clinical response to lenalidomide in chronic lymphocytic leukemia." J Immunol 201(7): 1967-1974.

Baenke, F., B. Peck, H. Miess and A. Schulze (2013). "Hooked on fat: the role of lipid synthesis in cancer metabolism and tumour development." Dis Model Mech 6(6): 1353-1363.

Bailey, A. P., G. Koster, C. Guillermier, E. M. Hirst, J. I. MacRae, C. P. Lechene, A. D. Postle and A. P. Gould (2015). "Antioxidant role for lipid droplets in a stem cell niche of drosophila." Cell 163(2): 340-353.

Bailly, C., X. Thuru and B. Quesnel (2020). "Combined cytotoxic chemotherapy and immunotherapy of cancer: modern times." NAR Cancer 2(1): zcaa002.

Begicevic, R. R. and M. Falasca (2017). "ABC Transporters in cancer stem cells: Beyond chemoresistance." Int J Mol Sci 18(11): 2362.

Beloribi-Djefaflia, S., S. Vasseur and F. Guillaumond (2016). "Lipid metabolic reprogramming in cancer cells." Oncogenesis 5(1): e189.

Bhat, P., G. Leggatt, N. Waterhouse and I. H. Frazer (2017). "Interferon-γ derived from cytotoxic lymphocytes directly enhances their motility and cytotoxicity." Cell Death Dis 8(6): e2836-e2836.

Bhattacharya, B., S. H. H. Low, C. Soh, N. K. Mustapa, M. Beloueche-Babari, K. X. Koh, J. Loh and R. Soong (2014). "Increased drug resistance is associated with reduced glucose levels and an enhanced glycolysis phenotype." Br J Pharmacol 171(13): 3255-3267.

Bonora, M., A. Bononi, E. De Marchi, C. Giorgi, M. Lebiedzinska, S. Marchi, S. Patergnani, A. Rimessi, J. M. Suski, A. Wojtala, M. R. Wieckowski, G. Kroemer, L. Galluzzi and P. Pinton (2013). "Role of the c subunit of the FO ATP synthase in mitochondrial permeability transition." Cell Cycle 12(4): 674-683.

Bora-Singhal, N., J. Nguyen, C. Schaal, D. Perumal, S. Singh, D. Coppola and S. J. S. c. Chellappan (2015). "YAP 1 regulates OCT 4 activity and SOX 2 expression to facilitate self-renewal and vascular mimicry of stem-like cells." Stem Cells 33(6): 1705-1718.

Brini, M., T. Calì, D. Ottolini and E. Carafoli (2013). "Intracellular calcium homeostasis and signaling." Metallomics and the Cell, Springer: 119-168.

Buono, R. and V. D. Longo (2018). "Starvation, Stress Resistance, and Cancer." Trends Endocrinol Metab 29(4): 271-280.

Calon, A., E. Espinet, S. Palomo-Ponce, D. V. Tauriello, M. Iglesias, M. V. Céspedes, M. Sevillano, C. Nadal, P. Jung and X. H.-F. Zhang (2012). "Dependency of colorectal cancer on a TGF-β-driven program in stromal cells for metastasis initiation." Cancer Cell 22(5): 571-584.

Calon, A., D. Tauriello and E. Batlle (2014). "TGF-beta in CAF-mediated tumor growth and metastasis." Seminars in cancer biology, Elsevier.

Cat, B., D. Stuhlmann, H. Steinbrenner, L. Alili, O. Holtkotter, H. Sies and P. Brenneisen (2006). "Enhancement of tumor invasion depends on transdifferentiation of skin fibroblasts mediated by reactive oxygen species." J Cell Sci 119(Pt 13): 2727-2738.

Cat, B., D. Stuhlmann, H. Steinbrenner, L. Alili, O. Holtkötter, H. Sies and P. Brenneisen (2006). "Enhancement of tumor invasion depends on transdifferentiation of skin fibroblasts mediated by reactive oxygen species." J Cell Sci 119(13): 2727-2738.

Cavalcanti, Y. V., M. C. Brelaz, J. K. Neves, J. C. Ferraz and V. R. Pereira (2012). "Role of TNF-alpha, IFN-gamma, and IL-10 in the development of pulmonary tuberculosis." Pulm Med 2012: 745483.

Chang, C.-H., J. Qiu, D. O'Sullivan, M. D. Buck, T. Noguchi, J. D. Curtis, Q. Chen, M. Gindin, M. M. Gubin and G. J. Van Der Windt (2015). "Metabolic competition in the tumor microenvironment is a driver of cancer progression." Cell 162(6): 1229-1241.

Chen, C. L., D. B. U. Kumar, V. Punj, J. Xu, L. Sher, S. M. Tahara, S. Hess and K. Machida (2016). "NANOG metabolically reprograms tumor-initiating stem-like cells through tumorigenic changes in oxidative phosphorylation and fatty acid metabolism." Cell Metab 23(1): 206-219.

Chen, D., R. Jiang, C. Mao, L. Shi, S. Wang, L. Yu, Q. Hu, D. Dai and H. Xu (2012). "Chemokine/chemokine receptor interactions contribute to the accumulation of Th17 cells in patients with esophageal squamous cell carcinoma." Hum Immunol 73(11): 1068-1072.

Chen, T., Z. Ren, L.-C. Ye, P.-H. Zhou, J.-M. Xu, Q. Shi, L.-Q. Yao and Y.-S. Zhong (2015). "Factor inhibiting HIF1α (FIH-1) functions as a tumor suppressor in human colorectal cancer by repressing HIF1α pathway." Cancer Biol. Ther. 16(2): 244-252.

Chen, W., Z. Sun, X.-J. Wang, T. Jiang, Z. Huang, D. Fang and D. D. Zhang (2009). "Direct interaction between Nrf2 and p21Cip1/WAF1 upregulates the Nrf2-mediated antioxidant response." Mol. Cell 34(6): 663-673.

Chen, X. and E. Song (2019). "Turning foes to friends: targeting cancer-associated fibroblasts." Nat Rev Drug Discov 18(2): 99-115.

Cheng, Y., H. Li, Y. Deng, Y. Tai, K. Zeng, Y. Zhang, W. Liu, Q. Zhang and Y. Yang (2018). "Cancer-associated fibroblasts induce PDL1+ neutrophils through the IL6-STAT3 pathway that foster immune suppression in hepatocellular carcinoma." Cell Death Dis 9(4): 422.

Ciardiello, C., L. Cavallini, C. Spinelli, J. Yang, M. Reis-Sobreiro, P. de Candia, V. R. Minciacchi and D. Di Vizio (2016). "Focus on extracellular vesicles: New frontiers of cell-to-cell communication in cancer." Int J Mol Sci 17(2): 175.

Clapham, D. E. (2007). "Calcium signaling." Cell 131(6): 1047-1058.

Corominas-Faja, B., E. Cuyas, J. Gumuzio, J. Bosch-Barrera, O. Leis, A. G. Martin and J. A. Menendez (2014). "Chemical inhibition of acetyl-CoA carboxylase suppresses self-renewal growth of cancer stem cells." Oncotarget 5(18): 8306-8316.

Coscia, M., E. Quaglino, M. Iezzi, C. Curcio, F. Pantaleoni, C. Riganti, I. Holen, H. Monkkonen, M. Boccadoro, G. Forni, P. Musiani, A. Bosia, F. Cavallo and M. Massaia (2010). "Zoledronic acid repolarizes tumour-associated macrophages and inhibits mammary carcinogenesis by targeting the mevalonate pathway." J Cell Mol Med 14(12): 2803-2815.

Cribbs, J. T. and S. Strack (2007). "Reversible phosphorylation of Drp1 by cyclic AMP-dependent protein kinase and calcineurin regulates mitochondrial fission and cell death." EMBO Rep 8(10): 939-944.

Dalla Valle, A., P. Vertongen, D. Spruyt, J. Lechanteur, V. Suain, N. Gaspard, J. P. Brion, V. Gangji and J. Rasschaert (2019). "Induction of stearoyl-CoA 9-desaturase 1 protects human mesenchymal stromal

cells against palmitic acid-induced lipotoxicity and inflammation." Front Endocrinol (Lausanne) 10: 726.

Daniel, C., C. Bell, C. Burton, S. Harguindey, S. J. Reshkin and C. Rauch (2013). "The role of proton dynamics in the development and maintenance of multidrug resistance in cancer." Biochim Biophys Acta (BBA) Mol Basis of Disease 1832(5): 606-617.

De Francesco, E. M., F. Sotgia and M. P. J. B. J. Lisanti (2018). "Cancer stem cells (CSCs): metabolic strategies for their identification and eradication." Biochem J. 475(9): 1611-1634.

de Jong, A. J., M. Kloppenburg, R. E. Toes and A. Ioan-Facsinay (2014). "Fatty acids, lipid mediators, and T-cell function." Front Immunol 5: 483.

de Kant, E., I. Heide, C. Thiede, R. Herrmann and C. F. Rochlitz (1996). "MDR1 expression correlates with mutant p53 expression in colorectal cancer metastases." J Cancer Res Clin Oncol 122(11): 671-675.

De Monte, L., M. Reni, E. Tassi, D. Clavenna, I. Papa, H. Recalde, M. Braga, V. Di Carlo, C. Doglioni and M. P. Protti (2011). "Intratumor T helper type 2 cell infiltrate correlates with cancer-associated fibroblast thymic stromal lymphopoietin production and reduced survival in pancreatic cancer." J Exp Med 208(3): 469-478.

De Palma, M., D. Biziato and T. V. Petrova (2017). "Microenvironmental regulation of tumour angiogenesis." Nat Rev Cancer 17(8): 457-474.

Degenhardt, K., R. Mathew, B. Beaudoin, K. Bray, D. Anderson, G. Chen, C. Mukherjee, Y. Shi, C. Gelinas, Y. Fan, D. A. Nelson, S. Jin and E. White (2006). "Autophagy promotes tumor cell survival and restricts necrosis, inflammation, and tumorigenesis." Cancer Cell 10(1): 51-64.

Dobrzyn, P., A. Dobrzyn, M. Miyazaki, P. Cohen, E. Asilmaz, D. G. Hardie, J. M. Friedman and J. M. Ntambi (2004). "Stearoyl-CoA desaturase 1 deficiency increases fatty acid oxidation by activating

AMP-activated protein kinase in liver." Proc Natl Acad Sci U S A 101(17): 6409-6414.

Dobrzyn, P., H. Sampath, A. Dobrzyn, M. Miyazaki and J. M. Ntambi (2008). "Loss of stearoyl-CoA desaturase 1 inhibits fatty acid oxidation and increases glucose utilization in the heart." Am J Physiol Endocrinol Metab 294(2): e357-364.

Dong, H. and M. J. Czaja (2011). "Regulation of lipid droplets by autophagy." Trends Endocrinol. Metab 22(6): 234-240.

Durham, K. K., K. M. Chathely and B. L. Trigatti (2018). "High-density lipoprotein protects cardiomyocytes against necrosis induced by oxygen and glucose deprivation through SR-B1, PI3K, and AKT1 and 2." Biochem J 475(7): 1253-1265.

Eikawa, S., M. Nishida, S. Mizukami, C. Yamazaki, E. Nakayama and H. Udono (2015). "Immune-mediated antitumor effect by type 2 diabetes drug, metformin." Proc Natl Acad Sci U S A 112(6): 1809-1814.

Elrod, J. W., R. Wong, S. Mishra, R. J. Vagnozzi, B. Sakthievel, S. A. Goonasekera, J. Karch, S. Gabel, J. Farber, T. Force, J. H. Brown, E. Murphy and J. D. Molkentin (2010). "Cyclophilin D controls mitochondrial pore-dependent Ca(2+) exchange, metabolic flexibility, and propensity for heart failure in mice." J Clin Invest 120(10): 3680-3687.

Endo, H., S. Owada, Y. Inagaki, Y. Shida and M. Tatemichi (2018). "Glucose starvation induces LKB1-AMPK-mediated MMP-9 expression in cancer cells." Sci Rep 8(1): 10122.

Erdogan, B. and D. J. Webb (2017). "Cancer-associated fibroblasts modulate growth factor signaling and extracellular matrix remodeling to regulate tumor metastasis." Biochem Soc Trans 45(1): 229-236.

Erez, N., S. Glanz, Y. Raz, C. Avivi and I. Barshack (2013). "Cancer associated fibroblasts express pro-inflammatory factors in human breast and ovarian tumors." Biochem Biophys Res Commun 437(3): 397-402.

Eyden, B., S. S. Banerjee, P. Shenjere and C. Fisher (2009). "The myofibroblast and its tumours." J Clin Pathol 62(3): 236-249.

Facciabene, A., G. T. Motz and G. Coukos (2012). "T-regulatory cells: key players in tumor immune escape and angiogenesis." Cancer Res 72(9): 2162-2171.

Fan, T. J., G. H. Sun, X. D. Sun, L. J. Zhao, R. G. Zhong and Y. Z. Peng (2019). "Tumor energy metabolism and potential of 3-bromopyruvate as an inhibitor of aerobic glycolysis: Implications in tumor treatment." Cancers 11(3): 317.

Feig, C., J. O. Jones, M. Kraman, R. J. Wells, A. Deonarine, D. S. Chan, C. M. Connell, E. W. Roberts, Q. Zhao, O. L. Caballero, S. A. Teichmann, T. Janowitz, D. I. Jodrell, D. A. Tuveson and D. T. Fearon (2013). "Targeting CXCL12 from FAP-expressing carcinoma-associated fibroblasts synergizes with anti-PD-L1 immunotherapy in pancreatic cancer." Proc Natl Acad Sci U S A 110(50): 20212-20217.

Flowers, M. T., M. P. Keller, Y. Choi, H. Lan, C. Kendziorski, J. M. Ntambi and A. D. Attie (2008). "Liver gene expression analysis reveals endoplasmic reticulum stress and metabolic dysfunction in SCD1-deficient mice fed a very low-fat diet." Physiol. Genomics 33(3): 361-372.

Flowers, M. T. and J. M. Ntambi (2008). "Role of stearoyl-coenzyme A desaturase in regulating lipid metabolism." Curr Opin Lipidol 19(3): 248-256.

Forkink, M., G. R. Manjeri, D. C. Liemburg-Apers, E. Nibbeling, M. Blanchard, A. Wojtala, J. A. Smeitink, M. R. Wieckowski, P. H. Willems and W. J. Koopman (2014). "Mitochondrial hyperpolarization during chronic complex I inhibition is sustained by low activity of complex II, III, IV and V." Biochim Biophys Acta (BBA)-Bioenergetics 1837(8): 1247-1256.

Fu, Y., S. Liu, S. Yin, W. Niu, W. Xiong, M. Tan, G. Li and M. Zhou (2017). "The reverse Warburg effect is likely to be an Achilles' heel of cancer that can be exploited for cancer therapy." Oncotarget 8(34): 57813-57825.

Furuta, E., S. K. Pai, R. Zhan, S. Bandyopadhyay, M. Watabe, Y. Y. Mo, S. Hirota, S. Hosobe, T. Tsukada, K. Miura, S. Kamada, K. Saito, M. Iiizumi, W. Liu, J. Ericsson and K. Watabe (2008). "Fatty acid synthase gene is up-regulated by hypoxia via activation of Akt and sterol regulatory element binding protein-1." Cancer Res 68(4): 1003-1011.

Gaggioli, C., S. Hooper, C. Hidalgo-Carcedo, R. Grosse, J. F. Marshall, K. Harrington and E. Sahai (2007). "Fibroblast-led collective invasion of carcinoma cells with differing roles for RhoGTPases in leading and following cells." Nat Cell Biol 9(12): 1392-1400.

Galluzzi, L., O. Kepp, M. G. Vander Heiden and G. Kroemer (2013). "Metabolic targets for cancer therapy." Nature Reviews Drug Discovery 12(11): 829.

Gao, Q., S. Wang, X. Chen, S. Cheng, Z. Zhang, F. Li, L. Huang, Y. Yang, B. Zhou, D. Yue, D. Wang, L. Cao, N. R. Maimela, B. Zhang, J. Yu, L. Wang and Y. Zhang (2019). "Cancer-cell-secreted CXCL11 promoted CD8(+) T cells infiltration through docetaxel-induced-release of HMGB1 in NSCLC." J. Immunother Cancer 7(1): 42.

Garces, R. and M. Mancha (1993). "One-step lipid extraction and fatty-acid methyl-esters preparation from fresh plant-tissues." Anal Biochem 211(1): 139-143.

Giorgi, C., C. Agnoletto, A. Bononi, M. Bonora, E. De Marchi, S. Marchi, S. Missiroli, S. Patergnani, F. Poletti and A. Rimessi (2012). "Mitochondrial calcium homeostasis as potential target for mitochondrial medicine." Mitochondrion 12(1): 77-85.

Giorgi, C., F. Baldassari, A. Bononi, M. Bonora, E. De Marchi, S. Marchi, S. Missiroli, S. Patergnani, A. Rimessi and J. M. Suski (2012). "Mitochondrial Ca2+ and apoptosis." Cell Calcium 52(1): 36-43.

Giorgio, V., S. Von Stockum, M. Antoniel, A. Fabbro, F. Fogolari, M. Forte, G. D. Glick, V. Petronilli, M. Zoratti and I. Szabó (2013). "Dimers of mitochondrial ATP synthase form the permeability transition pore." Proc Natl Acad Sci U S A 110(15): 5887-5892.

Gnant, M., B. Mlineritsch, H. Stoeger, G. Luschin-Ebengreuth, D. Heck, C. Menzel, R. Jakesz, M. Seifert, M. Hubalek, G. Pristauz, T. Bauernhofer, H. Eidtmann, W. Eiermann, G. Steger, W. Kwasny, P. Dubsky, G. Hochreiner, E. P. Forsthuber, C. Fesl, R. Greil, B. Austrian and V. A. Colorectal Cancer Study Group (2011). "Adjuvant endocrine therapy plus zoledronic acid in premenopausal women with early-stage breast cancer: 62-month follow-up from the ABCSG-12 randomised trial." Lancet Oncol 12(7): 631-641.

Gong, J., Y. Lin, H. Zhang, C. Liu, Z. Cheng, X. Yang, J. Zhang, Y. Xiao, N. Sang, X. Qian, L. Wang, X. Cen, X. Du and Y. Zhao (2020). "Reprogramming of lipid metabolism in cancer-associated fibroblasts potentiates migration of colorectal cancer cells." Cell Death Dis 11(4): 267.

Gorjao, R., M. F. Cury-Boaventura, T. M. de Lima and R. Curi (2007). "Regulation of human lymphocyte proliferation by fatty acids." Cell Biochem Funct 25(3): 305-315.

Griffiths, E. J. and G. A. Rutter (2009). "Mitochondrial calcium as a key regulator of mitochondrial ATP production in mammalian cells." Biochim Biophys Acta (BBA)-Bioenergetics 1787(11): 1324-1333.

Groom, J. R. and A. D. Luster (2011). "CXCR3 in T cell function." Exp Cell Res 317(5): 620-631.

Gu, L., J. L. Larson-Casey and A. B. Carter (2017). "Macrophages utilize the mitochondrial calcium uniporter for profibrotic polarization." FASEB J 31(7): 3072-3083.

Guido, C., D. Whitaker-Menezes, C. Capparelli, R. Balliet, Z. Lin, R. G. Pestell, A. Howell, S. Aquila, S. Andò and U. Martinez-Outschoorn (2012). "Metabolic reprogramming of cancer-associated fibroblasts by TGF-β drives tumor growth: connecting TGF-β signaling with "Warburg-like" cancer metabolism and L-lactate production." Cell Cycle 11(16): 3019-3035.

Gupta, S., A. Roy and B. S. Dwarakanath (2017). "Metabolic cooperation and competition in the tumor microenvironment: Implications for therapy." Front Oncol 7: 68.

Győrffy, B., P. Surowiak, J. Budczies and A. Lánczky (2013). "Online survival analysis software to assess the prognostic value of biomarkers using transcriptomic data in non-small-cell lung cancer." PLoS One 8(12).

Haabeth, O. A., K. B. Lorvik, C. Hammarstrom, I. M. Donaldson, G. Haraldsen, B. Bogen and A. Corthay (2011). "Inflammation driven by tumour-specific Th1 cells protects against B-cell cancer." Nat Commun 2(1): 240.

Haghikia, A., S. Jorg, A. Duscha, J. Berg, A. Manzel, A. Waschbisch, A. Hammer, D. H. Lee, C. May, N. Wilck, A. Balogh, A. I. Ostermann, N. H. Schebb, D. A. Akkad, D. A. Grohme, M. Kleinewietfeld, S. Kempa, J. Thone, S. Demir, D. N. Muller, R. Gold and R. A. Linker (2015). "Dietary fatty acids directly impact central nervous system autoimmunity via the small Intestine." Immunity 43(4): 817-829.

Hay, N. (2016). "Reprogramming glucose metabolism in cancer: can it be exploited for cancer therapy?" Nat Rev Cancer 16(10): 635.

Hermans, D., S. Gautam, J. C. Garcia-Canaveras, D. Gromer, S. Mitra, R. Spolski, P. Li, S. Christensen, R. Nguyen, J. X. Lin, J. Oh, N. Du, S. Veenbergen, J. Fioravanti, R. Ebina-Shibuya, C. Bleck, L. M. Neckers, J. D. Rabinowitz, L. Gattinoni and W. J. Leonard (2020). "Lactate dehydrogenase inhibition synergizes with IL-21 to promote CD8(+) T cell stemness and antitumor immunity." Proc Natl Acad Sci U S A 117(11): 6047-6055.

Hirayama, A., K. Kami, M. Sugimoto, M. Sugawara, N. Toki, H. Onozuka, T. Kinoshita, N. Saito, A. Ochiai, M. Tomita, H. Esumi and T. Soga (2009). "Quantitative metabolome profiling of colon and stomach cancer microenvironment by capillary electrophoresis time-of-flight mass spectrometry." Cancer Res 69(11): 4918-4925.

Ho, G. T., R. E. Aird, B. Liu, R. K. Boyapati, N. A. Kennedy, D. A. Dorward, C. L. Noble, T. Shimizu, R. N. Carter, E. T. S. Chew, N. M. Morton, A. G. Rossi, R. B. Sartor, J. P. Iredale and J. Satsangi (2018). "MDR1 deficiency impairs mitochondrial homeostasis and promotes intestinal inflammation." Mucosal Immunol 11(1): 120-130.

Holder, A. M., A. M. Gonzalez-Angulo, H. Q. Chen, A. Akcakanat, K. A. Do, W. F. Symmans, L. Pusztai, G. N. Hortobagyi, G. B. Mills and F. Meric-Bernstam (2013). "High stearoyl-CoA desaturase 1 expression is associated with shorter survival in breast cancer patients." Breast Cancer Res Treat 137(1): 319-327.

Hu, X., M. Chao and H. Wu (2017). "Central role of lactate and proton in cancer cell resistance to glucose deprivation and its clinical translation." Signal Transduct Target Ther 2(1): 16047.

Hu, Y. L., Y. Yin, H. Y. Liu, Y. Y. Feng, Z. H. Bian, L. Y. Zhou, J. W. Zhang, B. J. Fei, Y. G. Wang and Z. H. Huang (2016). "Glucose deprivation induces chemoresistance in colorectal cancer cells by increasing ATF4 expression." World J Gastroenterol 22(27): 6235-6245.

Huang, T. Li, L. Wang, L. Zhang, R. Yan, K. Li, S. Xing, G. Wu, L. Hu, W. Jia, S. C. Lin, C. V. Dang, L. Song, P. Gao and H. Zhang (2016). "Hepatocellular carcinoma redirects to ketolysis for progression under nutrition deprivation stress." Cell Res 26(10): 1112-1130.

Huang, Y., S. Zhou, Y. Huang, D. Zheng, Q. Mao, J. He, Y. Wang, D. Xue, X. Lu, N. Yang and Y. Zhao (2017). "Isolation of fibroblast-activation protein-specific cancer-associated fibroblasts." Biomed Res Int 2017: 4825108.

Hwang, S. H., M. C. Kim, S. Ji, Y. Yang, Y. Jeong and Y. Kim (2019). "Glucose starvation induces resistance to metformin through the elevation of mitochondrial multidrug resistance protein 1." Cancer Sci 110(4): 1256.

Ino, Y., R. Yamazaki-Itoh, S. Oguro, K. Shimada, T. Kosuge, J. Zavada, Y. Kanai and N. Hiraoka (2013). "Arginase II expressed in cancer-associated fibroblasts indicates tissue hypoxia and predicts poor outcome in patients with pancreatic cancer." PLoS One 8(2): e55146.

Inoki, K., T. Zhu and K. L. Guan (2003). "TSC2 mediates cellular energy response to control cell growth and survival." Cell 115(5): 577-590.

Ioan-Facsinay, A., J. C. Kwekkeboom, S. Westhoff, M. Giera, Y. Rombouts, V. van Harmelen, T. W. Huizinga, A. Deelder, M. Kloppenburg and R. E. Toes (2013). "Adipocyte-derived lipids modulate CD4+ T-cell function." Eur J Immunol 43(6): 1578-1587.

Ippolito, L., A. Morandi, M. L. Taddei, M. Parri, G. Comito, A. Iscaro, M. R. Raspollini, F. Magherini, E. Rapizzi and J. Masquelier (2019). "Cancer-associated fibroblasts promote prostate cancer malignancy via metabolic rewiring and mitochondrial transfer." Oncogene 38(27): 5339-5355.

Jaguin, M., N. Houlbert, O. Fardel and V. Lecureur (2013). "Polarization profiles of human M-CSF-generated macrophages and comparison of M1-markers in classically activated macrophages from GM-CSF and M-CSF origin." Cell Immunol 281(1): 51-61.

Janikiewicz, J., K. Hanzelka, A. Dziewulska, K. Kozinski, P. Dobrzyn, T. Bernas and A. Dobrzyn (2015). "Inhibition of SCD1 impairs palmitate-derived autophagy at the step of autophagosome-lysosome fusion in pancreatic β-cells." J. Lipid Res 56(10): 1901-1911.

Jeong, J. and J. O. Deasy (2014). "Modeling the relationship between fluorodeoxyglucose uptake and tumor radioresistance as a function of the tumor microenvironment." Comput Math Methods Med 2014.

Jiang, Y., Y. Li and B. Zhu (2015). "T-cell exhaustion in the tumor microenvironment." Cell Death Dis 6(6): e1792.

Jin, S. M., M. Lazarou, C. Wang, L. A. Kane, D. P. Narendra and R. J. Youle (2010). "Mitochondrial membrane potential regulates PINK1 import and proteolytic destabilization by PARL." J Cell Biol 191(5): 933-942.

Jo, H., J. Lee, J. Jeon, S. Y. Kim, J. I. Chung, H. Y. Ko, M. Lee and M. Yun (2020). "The critical role of glucose deprivation in epithelial-mesenchymal transition in hepatocellular carcinoma under hypoxia." Sci Rep 10(1): 1538.

Jump, D. B. (2011). "Fatty acid regulation of hepatic lipid metabolism." Curr Opin Clin Nutr Metab Care 14(2): 115-120.

Jung, C. H., S. H. Ro, J. Cao, N. M. Otto and D. H. Kim (2010). "mTOR regulation of autophagy." FEBS Lett 584(7): 1287-1295.

Justus, C. R., E. J. Sanderlin and L. V. Yang (2015). "Molecular connections between cancer cell metabolism and the tumor microenvironment." Int J Mol Sci 16(5): 11055-11086.

Karantza-Wadsworth, V., S. Patel, O. Kravchuk, G. Chen, R. Mathew, S. Jin and E. White (2007). "Autophagy mitigates metabolic stress and genome damage in mammary tumorigenesis." Genes Dev 21(13): 1621-1635.

Karch, J., J. Q. Kwong, A. R. Burr, M. A. Sargent, J. W. Elrod, P. M. Peixoto, S. Martinez-Caballero, H. Osinska, E. H. Y. Cheng, J. Robbins, K. W. Kinnally and J. D. Molkentin (2013). "Bax and Bak function as the outer membrane component of the mitochondrial permeability pore in regulating necrotic cell death in mice." Elife 2: e00772.

Kathawala, R. J., P. Gupta, C. R. Ashby Jr and Z.-S. Chen (2015). "The modulation of ABC transporter-mediated multidrug resistance in cancer: a review of the past decade." Drug Resist Updat 18: 1-17.

Kelley, L. C., Q. Chi, R. Cáceres, E. Hastie, A. J. Schindler, Y. Jiang, D. Q. Matus, J. Plastino and D. R. Sherwood (2019). "Adaptive F-actin polymerization and localized ATP production drive basement membrane invasion in the absence of MMPs." Dev. Cell 48(3): 313-328. e318.

Kim, J. H., T. H. Kang, K. H. Noh, H. C. Bae, S. H. Kim, Y. D. Yoo, S. Y. Seong and T. W. Kim (2009). "Enhancement of dendritic cell-based vaccine potency by anti-apoptotic siRNAs targeting key pro-apoptotic proteins in cytotoxic CD8(+) T cell-mediated cell death." Immunol Lett 122(1): 58-67.

Kim, K.-T., H. W. Lee, H.-O. Lee, S. C. Kim, Y. J. Seo, W. Chung, H. H. Eum, D.-H. Nam, J. Kim and K. M. Joo (2015). "Single-cell mRNA sequencing identifies subclonal heterogeneity in anti-cancer drug responses of lung adenocarcinoma cells." Genome Biol 16(1): 127.

Kim, M.-C., S.-H. Hwang, N.-Y. Kim, H.-S. Lee, S. Ji, Y. Yang and Y. Kim (2018). "Hypoxia promotes acquisition of aggressive phenotypes in human malignant mesothelioma." BMC Cancer 18(1): 819.

Kobayashi, T., P. Y. Lam, H. Jiang, K. Bednarska, R. Gloury, V. Murigneux, J. Tay, N. Jacquelot, R. Li, Z. K. Tuong, G. R. Leggatt, M. K. Gandhi, M. M. Hill, G. T. Belz, S. Ngo, A. Kallies and S. R. Mattarollo (2020). "Increased lipid metabolism impairs NK cell function and mediates adaptation to the lymphoma environment." Blood 136(26): 3004-3017.

Kojima, Y., A. Acar, E. N. Eaton, K. T. Mellody, C. Scheel, I. Ben-Porath, T. T. Onder, Z. C. Wang, A. L. Richardson and R. A. Weinberg (2010). "Autocrine TGF-β and stromal cell-derived factor-1 (SDF-1) signaling drives the evolution of tumor-promoting mammary stromal myofibroblasts." Proc Natl Acad Sci U S A 107(46): 20009-20014.

Konkel, J. E., D. Zhang, P. Zanvit, C. Chia, T. Zangarle-Murray, W. Jin, S. Wang and W. Chen (2017). "Transforming growth factor-β signaling in regulatory T cells controls T helper-17 cells and tissue-specific immune responses." Immunity 46(4): 660-674.

Koo, Y. J., T. J. Kim, K. J. Min, K. A. So, U. S. Jung and J. H. Hong (2017). "CXCL11 mediates TWIST1-induced angiogenesis in epithelial ovarian cancer." Tumour Biol 39(5): 1010428317706226.

Kriegova, E., R. Fillerova, T. Tomankova, B. Hutyrova, F. Mrazek, T. Tichy, V. Kolek, R. M. du Bois and M. Petrek (2011). "T-helper cell type-1 transcription factor T-bet is upregulated in pulmonary sarcoidosis." Eur Respir J 38(5): 1136-1144.

Kroemer, G. and B. Levine (2008). "Autophagic cell death: the story of a misnomer." Nat Rev Mol Cell Biol 9(12): 1004.

Kroemer, G. and J. Pouyssegur (2008). "Tumor cell metabolism: cancer's Achilles' heel." Cancer Cell 13(6): 472-482.

Labernadie, A., T. Kato, A. Brugues, X. Serra-Picamal, S. Derzsi, E. Arwert, A. Weston, V. Gonzalez-Tarrago, A. Elosegui-Artola, L.

Albertazzi, J. Alcaraz, P. Roca-Cusachs, E. Sahai and X. Trepat (2017). "A mechanically active heterotypic E-cadherin/N-cadherin adhesion enables fibroblasts to drive cancer cell invasion." Nat Cell Biol 19(3): 224-237.

Lee, A. S. (2014). "Glucose-regulated proteins in cancer: molecular mechanisms and therapeutic potential." Nat Rev Cancer 14(4): 263-276.

Lewis, C. A., C. Brault, B. Peck, K. Bensaad, B. Griffiths, R. Mitter, P. Chakravarty, P. East, B. Dankworth, D. Alibhai, A. L. Harris and A. Schulze (2015). "SREBP maintains lipid biosynthesis and viability of cancer cells under lipid- and oxygen-deprived conditions and defines a gene signature associated with poor survival in glioblastoma multiforme." Oncogene 34(40): 5128-5140.

Li, C., P. Jiang, S. Wei, X. Xu and J. Wang (2020). "Regulatory T cells in tumor microenvironment: new mechanisms, potential therapeutic strategies and future prospects." Mol Cancer 19(1): 116.

Li, J., S. Condello, J. Thomes-Pepin, X. Ma, Y. Xia, T. D. Hurley, D. Matei and J.-X. Cheng (2017). "Lipid desaturation is a metabolic marker and therapeutic target of ovarian cancer stem cells." Cell Stem Cell 20(3): 303-314. e305.

Li, J., Q. Huang, X. Long, X. Guo, X. Sun, X. Jin, Z. Li, T. Ren, P. Yuan and X. Huang (2017). "Mitochondrial elongation-mediated glucose metabolism reprogramming is essential for tumour cell survival during energy stress." Oncogene 36(34): 4901-4912.

Li, Y., W.-X. Zong and W.-X. Ding (2017). "Recycling the danger via lipid droplet biogenesis after autophagy." Autophagy 13(11): 1995-1997.

Liberti, M. V., Locasale, Jason W (2016). "The Warburg effect: how does it benefit cancer cells?" Trends Biochem Sci 41(3): 211-218.

Lim, J.-H., Z. Gerhart-Hines, J. E. Dominy, Y. Lee, S. Kim, M. Tabata, Y. K. Xiang and P. J. J. o. B. C. Puigserver (2013). "Oleic acid stimulates complete oxidation of fatty acids through protein kinase

A-dependent activation of SIRT1-PGC1α complex." J. Biol. Chem 288(10): 7117-7126.

Lin, J., L. Xia, J. Liang, Y. Han, H. Wang, L. Oyang, S. Tan, Y. Tian, S. Rao, X. Chen, Y. Tang, M. Su, X. Luo, Y. Wang, H. Wang, Y. Zhou and Q. Liao (2019). "The roles of glucose metabolic reprogramming in chemo- and radio-resistance." J Exp Clin Cancer Res 38(1): 218.

Lin, X., Z. Xiao, T. Chen, S. H. Liang and H. Guo (2020). "Glucose metabolism on tumor plasticity, diagnosis, and treatment." Front Oncol 10: 317.

Lin, Y., J. Xu and H. Lan (2019). "Tumor-associated macrophages in tumor metastasis: biological roles and clinical therapeutic applications." J Hematol Oncol 12(1): 76.

Ling, X. L., Y. Q. He, G. Q. Zhang, Y. Zhou and B. Yan (2012). "Increased P-glycoprotein expression in mitochondria is related to acquired multidrug resistance in human hepatoma cells depleted of mitochondrial DNA." Int J Oncol 40(1): 109-118.

Ling, X., Y. Zhou, S.-W. Li, B. Yan and L. Wen (2010). "Modulation of mitochondrial permeability transition pore affects multidrug resistance in human hepatocellular carcinoma cells." Int J Biol Sci 6(7): 773.

Liu, T., C. Han, S. Wang, P. Fang, Z. Ma, L. Xu and R. Yin (2019). "Cancer-associated fibroblasts: an emerging target of anti-cancer immunotherapy." J Hematol Oncol 12(1): 86.

Liu, X., M. S. Strable and J. M. Ntambi (2011). "Stearoyl CoA desaturase 1: role in cellular inflammation and stress." Adv Nutr 2(1): 15-22.

Liu, Y., P. T. Nguyen, X. Wang, Y. Zhao, C. E. Meacham, Z. Zou, B. Bordieanu, M. Johanns, D. Vertommen, T. Wijshake, H. May, G. Xiao, S. Shoji-Kawata, M. H. Rider, S. J. Morrison, P. Mishra and B. Levine (2020). "TLR9 and beclin 1 crosstalk regulates muscle AMPK activation in exercise." Nature 578(7796): 605-609.

Liu, Y., X. D. Song, W. Liu, T. Y. Zhang and J. Zuo (2003). "Glucose deprivation induces mitochondrial dysfunction and oxidative stress in PC12 cell line." J Cell Mol Med 7(1): 49-56.

Liu, Z., R. Ravindranathan, J. Li, P. Kalinski, Z. S. Guo and D. L. Bartlett (2016). "CXCL11-Armed oncolytic poxvirus elicits potent antitumor immunity and shows enhanced therapeutic efficacy." Oncoimmunology 5(3): e1091554.

Long, X., W. Xiong, X. Zeng, L. Qi, Y. Cai, M. Mo, H. Jiang, B. Zhu, Z. Chen and Y. Li (2019). "Cancer-associated fibroblasts promote cisplatin resistance in bladder cancer cells by increasing IGF-1/ERβ/Bcl-2 signalling." Cell Death Dis 10(5): 1-16.

Ma, L., Y. Tao, A. Duran, V. Llado, A. Galvez, J. F. Barger, E. A. Castilla, J. Chen, T. Yajima and A. Porollo (2013). "Control of nutrient stress-induced metabolic reprogramming by PKCζ in tumorigenesis." Cell 152(3): 599-611.

Maimela, N. R., S. Liu and Y. Zhang (2019). "Fates of CD8+ T cells in tumor microenvironment." Comput Struct Biotechnol J 17: 1-13.

Mammucari, C. and R. Rizzuto (2010). "Signaling pathways in mitochondrial dysfunction and aging." Mech Ageing Dev 131(7-8): 536-543.

Marchenko, N. D., A. Zaika and U. M. Moll (2000). "Death signal-induced localization of p53 protein to mitochondria a potential role in apoptotic signaling." J. Biol. Chem 275(21): 16202-16212.

Masgras, I., A. Rasola and P. Bernardi (2012). "Induction of the permeability transition pore in cells depleted of mitochondrial DNA." Biochim Biophys Acta (BBA)-Bioenergetics 1817(10): 1860-1866.

Masoud, G. N., Li, Wei (2015). "HIF-1α pathway: role, regulation and intervention for cancer therapy." Acta Pharmaceutica Sinica B 5(5): 378-389.

Mathew, R., V. Karantza-Wadsworth and E. White (2007). "Role of autophagy in cancer." Nat Rev Cancer 7(12): 961-967.

McGowan, T. A., M. Madesh, Y. Zhu, L. Wang, M. Russo, L. Deelman, R. Henning, S. Joseph, G. Hajnoczky and K. Sharma (2002). "TGF-β-induced Ca2+ influx involves the type III IP3 receptor and regulates actin cytoskeleton." Am J Physiol Renal Physiol 282(5): F910-F920.

Menendez, J. A., L. Vellon, I. Mehmi, B. P. Oza, S. Ropero, R. Colomer and R. Lupu (2004). "Inhibition of fatty acid synthase (FAS) suppresses HER2/neu (erbB-2) oncogene overexpression in cancer cells." Proc Natl Acad Sci U S A 101(29): 10715-10720.

Michalek, R. D., V. A. Gerriets, S. R. Jacobs, A. N. Macintyre, N. J. MacIver, E. F. Mason, S. A. Sullivan, A. G. Nichols and J. C. Rathmell (2011). "Cutting edge: distinct glycolytic and lipid oxidative metabolic programs are essential for effector and regulatory CD4+ T cell subsets." J Immunol 186(6): 3299-3303.

Migita, T., K. i. Takayama, T. Urano, D. Obinata, K. Ikeda, T. Soga, S. Takahashi and S. Inoue (2017). "ACSL 3 promotes intratumoral steroidogenesis in prostate cancer cells." Cancer Sci 108(10): 2011-2021.

Miyazaki, M. and J. M. Ntambi (2003). "Role of stearoyl-coenzyme A desaturase in lipid metabolism." Prostaglandins Leukot Essent Fatty Acids 68(2): 113-121.

Mizushima, N. (2007). "Autophagy: process and function." Genes Dev 21(22): 2861-2873.

Mizushima, N., T. Yoshimori and B. Levine (2010). "Methods in mammalian autophagy research." Cell 140(3): 313-326.

Monteith, G. R., N. Prevarskaya and S. J. Roberts-Thomson (2017). "The calcium–cancer signalling nexus." Nat Rev Cancer 17(6): 367.

Morris, J. K. (1965). "A formaldehyde glutaraldehyde fixative of high osmolality for use in electron microscopy." J. cell Biol 27: 1A-149A.

Munir, R., J. Lisec, J. V. Swinnen and N. Zaidi (2019). "Lipid metabolism in cancer cells under metabolic stress." Br J Cancer 120(12): 1090-1098.

Mwaikambo, B. R., C. Yang, S. Chemtob and P. Hardy (2009). "Hypoxia Up-regulates CD36 Expression and Function via Hypoxia-inducible Factor-1-and Phosphatidylinositol 3-Kinase-dependent Mechanisms." J. Biol. Chem 284(39): 26695-26707.

Najafi, S. and A. Mirshafiey (2019). "The role of T helper 17 and regulatory T cells in tumor microenvironment." Immunopharmacol Immunotoxicol 41(1): 16-24.

Nazio, F., M. Bordi, V. Cianfanelli, F. Locatelli and F. Cecconi (2019). "Autophagy and cancer stem cells: molecular mechanisms and therapeutic applications." Cell Death Differ 26(4): 690-702.

Neupert, W. and J. M. Herrmann (2007). "Translocation of proteins into mitochondria." Annu. Rev. Biochem. 76: 723-749.

Nishimoto, A., N. Kugimiya, T. Hosoyama, T. Enoki, T.-S. Li and K. Hamano (2014). "HIF-1α activation under glucose deprivation plays a central role in the acquisition of anti-apoptosis in human colon cancer cells." Int J Oncol 44(6): 2077-2084.

Noto, A., C. De Vitis, M. E. Pisanu, G. Roscilli, G. Ricci, A. Catizone, G. Sorrentino, G. Chianese, O. Taglialatela-Scafati and D. Trisciuoglio (2017). "Stearoyl-CoA-desaturase 1 regulates lung cancer stemness via stabilization and nuclear localization of YAP/TAZ." Oncogene 36(32): 4573-4584.

Nunnari, J. and A. Suomalainen (2012). "Mitochondria: in sickness and in health." Cell 148(6): 1145-1159.

Ogasawara, K., S. Hida, Y. Weng, A. Saiura, K. Sato, H. Takayanagi, S. Sakaguchi, T. Yokochi, T. Kodama and M. Naitoh (2002). "Requirement of the IFN-α/β-induced CXCR3 chemokine signalling for CD8+ T cell activation." Genes to Cells 7(3): 309-320.

Ogasawara, Y., E. Itakura, N. Kono, N. Mizushima, H. Arai, A. Nara, T. Mizukami and A. Yamamoto (2014). "Stearoyl-CoA desaturase 1 activity is required for autophagosome formation." J. Biol. Chem 289(34): 23938-23950.

Östman, A., Augsten, Martin (2009). "Cancer-associated fibroblasts and tumor growth-bystanders turning into key players." Curr. Opin. Genet. Dev 19(1): 67-73.

Pacella, I., C. Procaccini, C. Focaccetti, S. Miacci, E. Timperi, D. Faicchia, M. Severa, F. Rizzo, E. M. Coccia and F. Bonacina (2018). "Fatty acid metabolism complements glycolysis in the selective regulatory T cell expansion during tumor growth." Proc Natl Acad Sci U S A 115(28): E6546-E6555.

Palorini, R., G. Votta, Y. Pirola, H. De Vitto, S. De Palma, C. Airoldi, M. Vasso, F. Ricciardiello, P. P. Lombardi, C. Cirulli, R. Rizzi, F. Nicotra, K. Hiller, C. Gelfi, L. Alberghina and F. Chiaradonna (2016). "Protein kinase A activation promotes cancer cell resistance to glucose starvation and anoikis." PLoS Genet 12(3): e1005931.

Park, J. A., Cheung, Nai-Kong V (2017). "Limitations and opportunities for immune checkpoint inhibitors in pediatric malignancies." Cancer Treat Commun 58: 22-33.

Park, S., J. H. Won, I. Hwang, S. Hong, H. K. Lee and J. W. Yu (2015). "Defective mitochondrial fission augments NLRP3 inflammasome activation." Sci Rep 5(1): 15489.

Pascual, G., A. Avgustinova, S. Mejetta, M. Martin, A. Castellanos, C. S. O. Attolini, A. Berenguer, N. Prats, A. Toll, J. A. Hueto, C. Bescos, L. Di Croce and S. A. Benitah (2017). "Targeting metastasis-initiating cells through the fatty acid receptor CD36." Nature 541(7635): 41-+.

Passos, M. E., H. H. Alves, C. M. Momesso, F. G. Faria, G. Murata, M. F. Cury-Boaventura, E. Hatanaka, S. Massao-Hirabara and R. Gorjao (2016). "Differential effects of palmitoleic acid on human lymphocyte proliferation and function." Lipids Health Dis 15(1): 217.

Paton, C. M. and J. M. Ntambi (2009). "Biochemical and physiological function of stearoyl-CoA desaturase." Am J Physiol Endocrinol Metab 297(1): E28-37.

Patron, M., A. Raffaello, V. Granatiero, A. Tosatto, G. Merli, D. De Stefani, L. Wright, G. Pallafacchina, A. Terrin and C. Mammucari

(2013). "The mitochondrial calcium uniporter (MCU): molecular identity and physiological roles." J. Biol. Chem 288(15): 10750-10758.

Pavlides, S., D. Whitaker-Menezes, R. Castello-Cros, N. Flomenberg, A. K. Witkiewicz, P. G. Frank, M. C. Casimiro, C. Wang, P. Fortina, S. Addya, R. G. Pestell, U. E. Martinez-Outschoorn, F. Sotgia and M. P. Lisanti (2009). "The reverse Warburg effect: aerobic glycolysis in cancer associated fibroblasts and the tumor stroma." Cell Cycle 8(23): 3984-4001.

Pearce, E. L., M. C. Walsh, P. J. Cejas, G. M. Harms, H. Shen, L. S. Wang, R. G. Jones and Y. Choi (2009). "Enhancing CD8 T-cell memory by modulating fatty acid metabolism." Nature 460(7251): 103-107.

Peck, B., Z. T. Schug, Q. F. Zhang, B. Dankworth, D. T. Jones, E. Smethurst, R. Patel, S. Mason, M. Jiang, R. Saunders, M. Howell, R. Mitter, B. Spencer-Dene, G. Stamp, L. McGarry, D. James, E. Shanks, E. O. Aboagye, S. E. Critchlow, H. Y. Leung, A. L. Harris, M. J. O. Wakelam, E. Gottlieb and A. Schulze (2016). "Inhibition of fatty acid desaturation is detrimental to cancer cell survival in metabolically compromised environments." Cancer Metab 4(1): 1-18.

Perez, V. L., L. Van Parijs, A. Biuckians, X. X. Zheng, T. B. Strom and A. K. Abbas (1997). "Induction of peripheral T cell tolerance in vivo requires CTLA-4 engagement." Immunity 6(4): 411-417.

Perucha, E., R. Melchiotti, J. A. Bibby, W. Wu, K. S. Frederiksen, C. A. Roberts, Z. Hall, G. LeFriec, K. A. Robertson, P. Lavender, J. G. Gerwien, L. S. Taams, J. L. Griffin, E. de Rinaldis, L. G. M. van Baarsen, C. Kemper, P. Ghazal and A. P. Cope (2019). "The cholesterol biosynthesis pathway regulates IL-10 expression in human Th1 cells." Nat Commun 10(1): 498.

Piao, C., X. Cui, B. Zhan, J. Li, Z. Li, Z. Li, X. Liu, J. Bi, Z. Zhang and C. Kong (2019). "Inhibition of stearoyl CoA desaturase-1 activity suppresses tumour progression and improves prognosis in human bladder cancer." J Cell Mol Med 23(3): 2064-2076.

Piao, C., X. Cui, B. Zhan, J. Li, Z. Li, Z. Li, X. Liu, J. Bi, Z. Zhang and C. Kong (2019). "Inhibition of stearoyl CoA desaturase-1 activity suppresses tumour progression and improves prognosis in human bladder cancer." J Cell Mol Med 23(3): 2064-2076.

Pinto, M. C., A. H. Kihara, V. A. Goulart, F. M. Tonelli, K. N. Gomes, H. Ulrich and R. R. Resende (2015). "Calcium signaling and cell proliferation." Cell Signal 27(11): 2139-2149.

Pisanu, M. E., A. Noto, C. De Vitis, S. Morrone, G. Scognamiglio, G. Botti, F. Venuta, D. Diso, Z. Jakopin, F. Padula, A. Ricci, S. Mariotta, M. R. Giovagnoli, E. Giarnieri, I. Amelio, M. Agostini, G. Melino, G. Ciliberto and R. Mancini (2017). "Blockade of Stearoyl-CoA-desaturase 1 activity reverts resistance to cisplatin in lung cancer stem cells." Cancer Lett 406: 93-104.

Polo-Hernandez, E., V. Tello, A. A. Arroyo, M. Dominguez-Prieto, F. de Castro, A. Tabernero and J. M. Medina (2014). "Oleic acid synthesized by stearoyl-CoA desaturase (SCD-1) in the lateral periventricular zone of the developing rat brain mediates neuronal growth, migration and the arrangement of prospective synapses." Brain Res 1570: 13-25.

Porporato, P. E., N. Filigheddu, J. M. B. Pedro, G. Kroemer and L. Galluzzi (2018). "Mitochondrial metabolism and cancer." Cell Res 28(3): 265-280.

Prasad, K. and G. K. Prabhu (2012). "Image analysis tools for evaluation of microscopic views of immunohistochemically stained specimen in medical research-a review." J Med Syst 36(4): 2621-2631.

Protti, M. P. and L. De Monte (2012). "Cross-talk within the tumor microenvironment mediates Th2-type inflammation in pancreatic cancer." Oncoimmunology 1(1): 89-91.

Puchert, M., J. Obst, C. Koch, K. Zieger and J. Engele (2020). "CXCL11 promotes tumor progression by the biased use of the chemokine receptors CXCR3 and CXCR7." Cytokine 125: 154809.

Qiao, Y., C. Zhang, A. Li, D. Wang, Z. Luo, Y. Ping, B. Zhou, S. Liu, H. Li, D. Yue, Z. Zhang, X. Chen, Z. Shen, J. Lian, Y. Li, S. Wang, F. Li, L. Huang, L. Wang, B. Zhang, J. Yu, Z. Qin and Y. Zhang (2018). "IL6 derived from cancer-associated fibroblasts promotes chemoresistance via CXCR7 in esophageal squamous cell carcinoma." Oncogene 37(7): 873-883.

Qu, C., W. Zhang, G. Zheng, Z. Zhang, J. Yin and Z. He (2014). "Metformin reverses multidrug resistance and epithelial-mesenchymal transition (EMT) via activating AMP-activated protein kinase (AMPK) in human breast cancer cells." Mol Cell Biochem 386(1-2): 63-71.

Rambold, A. S., S. Cohen and J. Lippincott-Schwartz (2015). "Fatty acid trafficking in starved cells: regulation by lipid droplet lipolysis, autophagy, and mitochondrial fusion dynamics." Dev. Cell 32(6): 678-692.

Ran, H., Y. Zhu, R. Deng, Q. Zhang, X. Liu, M. Feng, J. Zhong, S. Lin, X. Tong and Q. Su (2018). "Stearoyl-CoA desaturase-1 promotes colorectal cancer metastasis in response to glucose by suppressing PTEN." J Exp Clin Cancer Res 37(1): 54.

Rao, X., X. Huang, Z. Zhou and X. Lin (2013). "An improvement of the 2^(-delta delta CT) method for quantitative real-time polymerase chain reaction data analysis." Biostat Bioinforma Biomath 3(3): 71-85.

Rasola, A. and P. Bernardi (2011). "Mitochondrial permeability transition in Ca2+ -dependent apoptosis and necrosis." Cell Calcium 50(3): 222-233.

Raulien, N., K. Friedrich, S. Strobel, S. Rubner, S. Baumann, M. von Bergen, A. Korner, M. Krueger, M. Rossol and U. Wagner (2017). "Fatty acid oxidation compensates for lipopolysaccharide-induced Warburg effect in glucose-deprived monocytes." Front Immunol 8: 609.

Reddy, P. H. (2014). "Inhibitors of mitochondrial fission as a therapeutic strategy for diseases with oxidative stress and mitochondrial dysfunction." J Alzheimers Dis 40(2): 245-256.

Rizzuto, R., D. De Stefani, A. Raffaello and C. Mammucari (2012). "Mitochondria as sensors and regulators of calcium signalling." Nat. Rev. Mol. Cell Biol 13(9): 566-578.

Roa-Mansergas, X., R. Fado, M. Atari, J. F. Mir, H. Muley, D. Serra and N. Casals (2018). "CPT1C promotes human mesenchymal stem cells survival under glucose deprivation through the modulation of autophagy." Sci Rep 8(1): 6997.

Robinson, B. W., A. W. Musk and R. A. Lake (2005). "Malignant mesothelioma." The Lancet 366(9483): 397-408.

Rocha, V. Z., E. J. Folco, G. Sukhova, K. Shimizu, I. Gotsman, A. H. Vernon and P. Libby (2008). "Interferon-ɣ, a Th1 cytokine, regulates fat inflammation: a role for adaptive immunity in obesity." Circ Res 103(5): 467-476.

Rodgers, J. T. and P. Puigserver (2007). "Fasting-dependent glucose and lipid metabolic response through hepatic sirtuin 1." Proc Natl Acad Sci U S A 104(31): 12861-12866.

Roongta, U. V., J. G. Pabalan, X. Wang, R.-P. Ryseck, J. Fargnoli, B. J. Henley, W.-P. Yang, J. Zhu, M. T. Madireddi and R. M. Lawrence (2011). "Cancer cell dependence on unsaturated fatty acids implicates stearoyl-CoA desaturase as a target for cancer therapy." Mol Cancer Res 9(11): 1551-1561.

Rossi, A., P. Pizzo and R. Filadi (2019). "Calcium, mitochondria and cell metabolism: A functional triangle in bioenergetics." Biochim Biophys Acta (BBA) Mol Cell Res 1866(7): 1068-1078.

Sahai, E., I. Astsaturov, E. Cukierman, D. G. DeNardo, M. Egeblad, R. M. Evans, D. Fearon, F. R. Greten, S. R. Hingorani, T. Hunter, R. O. Hynes, R. K. Jain, T. Janowitz, C. Jorgensen, A. C. Kimmelman, M. G. Kolonin, R. G. Maki, R. S. Powers, E. Pure, D. C. Ramirez, R. Scherz-Shouval, M. H. Sherman, S. Stewart, T. D. Tlsty, D. A. Tuveson, F. M. Watt, V. Weaver, A. T. Weeraratna and Z. Werb (2020). "A framework for advancing our understanding of cancer-associated fibroblasts." Nat Rev Cancer 20(3): 174-186.

Saito, T., A. Kuma, Y. Sugiura, Y. Ichimura, M. Obata, H. Kitamura, S. Okuda, H. C. Lee, K. Ikeda, Y. Kanegae, I. Saito, J. Auwerx, H. Motohashi, M. Suematsu, T. Soga, T. Yokomizo, S. Waguri, N. Mizushima and M. Komatsu (2019). "Autophagy regulates lipid metabolism through selective turnover of NCoR1." Nat Commun 10(1): 1567.

Sakaguchi, S., M. Miyara, C. M. Costantino and D. A. Hafler (2010). "FOXP3+ regulatory T cells in the human immune system." Nat Rev Immunol 10(7): 490-500.

Salmond, R. J., A. Filby, I. Qureshi, S. Caserta and R. Zamoyska (2009). "T-cell receptor proximal signaling via the Src-family kinases, Lck and Fyn, influences T-cell activation, differentiation, and tolerance." Immunol Rev 228(1): 9-22.

Sansores-Garcia, L., W. Bossuyt, K. Wada, S. Yonemura, C. Tao, H. Sasaki and G. Halder (2011). "Modulating F-actin organization induces organ growth by affecting the Hippo pathway." EMBO J 30(12): 2325-2335.

Santi, A., A. Caselli, F. Ranaldi, P. Paoli, C. Mugnaioni, E. Michelucci and P. Cirri (2015). "Cancer associated fibroblasts transfer lipids and proteins to cancer cells through cargo vesicles supporting tumor growth." Biochim Biophys Acta (BBA) Mol Cell Res 1853(12): 3211-3223.

Santi, A., F. G. Kugeratski and S. Zanivan (2018). "Cancer associated fibroblasts: The architects of stroma remodeling." Proteomics 18(5-6): e1700167.

Santo-Domingo, J. and N. Demaurex (2010). "Calcium uptake mechanisms of mitochondria." Biochim Biophys Acta (BBA)-Bioenergetics 1797(6-7): 907-912.

Shiga, K., M. Hara, T. Nagasaki, T. Sato, H. Takahashi and H. Takeyama (2015). "Cancer-associated fibroblasts: Their characteristics and their roles in tumor growth." Cancers 7(4): 2443-2458.

Shimazu, K., Y. Tada, T. Morinaga, M. Shingyoji, I. Sekine, H. Shimada, K. Hiroshima, T. Namiki, K. Tatsumi and M. Tagawa (2017). "Metformin produces growth inhibitory effects in combination with nutlin-3a on malignant mesothelioma through a cross-talk between mTOR and p53 pathways." BMC Cancer 17(1): 309.

Shintani, T. and D. J. Klionsky (2004). "Autophagy in health and disease: a double-edged sword." Science 306(5698): 990-995.

Sierra-Filardi, E., C. Nieto, A. Dominguez-Soto, R. Barroso, P. Sanchez-Mateos, A. Puig-Kroger, M. Lopez-Bravo, J. Joven, C. Ardavin, J. L. Rodriguez-Fernandez, C. Sanchez-Torres, M. Mellado and A. L. Corbi (2014). "CCL2 shapes macrophage polarization by GM-CSF and M-CSF: identification of CCL2/CCR2-dependent gene expression profile." J Immunol 192(8): 3858-3867.

Singh, R., S. Kaushik, Y. Wang, Y. Xiang, I. Novak, M. Komatsu, K. Tanaka, A. M. Cuervo and M. J. Czaja (2009). "Autophagy regulates lipid metabolism." Nature 458(7242): 1131-1135.

Snaebjornsson, M. T., S. Janaki-Raman and A. Schulze (2020). "Greasing the wheels of the cancer machine: The role of lipid metabolism in cancer." Cell Metab 31(1): 62-76.

Son, Y. M., I. S. Cheon, N. P. Goplen, A. L. Dent and J. Sun (2020). "Inhibition of stearoyl-CoA desaturases suppresses follicular help T- and germinal center B-cell responses." Eur J Immunol 50(7): 1067–1077, 2020.

Spitz, D. R., J. E. Sim, L. A. Ridnour, S. S. Galoforo and Y. J. Lee (2000). "Glucose deprivation-induced oxidative stress in human tumor cells. A fundamental defect in metabolism?" Ann N Y Acad Sci 899(1): 349-362.

Su, P., Q. Wang, E. Bi, X. Ma, L. Liu, M. Yang, J. Qian and Q. Yi (2020). "Enhanced lipid accumulation and metabolism are required for the differentiation and activation of tumor-associated macrophages." Cancer Res 80(7): 1438-1450.

Suen, D. F., K. L. Norris and R. J. Youle (2008). "Mitochondrial dynamics and apoptosis." Genes Dev 22(12): 1577-1590.

Sullivan, M. R., L. V. Danai, C. A. Lewis, S. H. Chan, D. Y. Gui, T. Kunchok, E. A. Dennstedt, M. G. Vander Heiden and A. Muir (2019). "Quantification of microenvironmental metabolites in murine cancers reveals determinants of tumor nutrient availability." Elife 8: e44235.

Sun, Y., J. Campisi, C. Higano, T. M. Beer, P. Porter, I. Coleman, L. True and P. S. Nelson (2012). "Treatment-induced damage to the tumor microenvironment promotes prostate cancer therapy resistance through WNT16B." Nat Med 18(9): 1359-1368.

Swann, J. B. and M. J. Smyth (2007). "Immune surveillance of tumors." J Clin Invest 117(5): 1137-1146.

Szydlowska, K. and M. Tymianski (2010). "Calcium, ischemia and excitotoxicity." Cell Calcium 47(2): 122-129.

Takahashi, T., Y. Kuniyasu, M. Toda, N. Sakaguchi, M. Itoh, M. Iwata, J. Shimizu and S. Sakaguchi (1998). "Immunologic self-tolerance maintained by CD25(+)CD4(+) naturally anergic and suppressive T cells: induction of autoimmune disease by breaking their anergic/suppressive state." Int. Immunol 10(12): 1969-1980.

Taraboletti, G., L. Perin, B. Bottazzi, A. Mantovani, R. Giavazzi and M. Salmona (1989). "Membrane fluidity affects tumor-cell motility, invasion and lung-colonizing potential." Int J Cancer 44(4): 707-713.

Tarasov, A. I., E. J. Griffiths and G. A. Rutter (2012). "Regulation of ATP production by mitochondrial Ca2+." Cell Calcium 52(1): 28-35.

Tirinato, L., C. Liberale, S. Di Franco, P. Candeloro, A. Benfante, R. La Rocca, L. Potze, R. Marotta, R. Ruffilli, V. P. Rajamanickam, M. Malerba, F. De Angelis, A. Falqui, E. Carbone, M. Todaro, J. P. Medema, G. Stassi and E. Di Fabrizio (2015). "Lipid droplets: a new player in colorectal cancer stem cells unveiled by spectroscopic imaging." Stem Cells 33(1): 35-44.

Togashi, Y., K. Shitara and H. Nishikawa (2019). "Regulatory T cells in cancer immunosuppression—implications for anticancer therapy." Nat Rev Clin Oncol 16(6): 356-371.

Tredan, O., C. M. Galmarini, K. Patel and I. F. Tannock (2007). "Drug resistance and the solid tumor microenvironment." J. Natl. Cancer Inst 99(19): 1441-1454.

Turnis, M. E., D. V. Sawant, A. L. Szymczak-Workman, L. P. Andrews, G. M. Delgoffe, H. Yano, A. J. Beres, P. Vogel, C. J. Workman and D. A. Vignali (2016). "Interleukin-35 limits anti-tumor immunity." Immunity 44(2): 316-329.

Van Cutsem, E. and J. Arends (2005). "The causes and consequences of cancer-associated malnutrition." Eur J Oncol Nurs 9 Suppl 2: S51-63.

van Dijk, A., B. Naaijkens, W. Jurgens, R. Oerlemans, G. Scheffer, J. Kassies, J. Aznou, M. Brouwer, A. van Rossum and G. Schuurhuis (2012). "The multidrug resistance protein breast cancer resistance protein (BCRP) protects adipose-derived stem cells against ischemic damage." Cell Biol Toxicol 28(5): 303-315.

Vander Heiden, M. G., L. C. Cantley and C. B. Thompson (2009). "Understanding the Warburg effect: the metabolic requirements of cell proliferation." Science 324(5930): 1029-1033.

Vasiliou, V., K. Vasiliou and D. W. Nebert (2009). "Human ATP-binding cassette (ABC) transporter family." Hum Genomics 3(3): 281-290.

Visioli, F., Y. Wang, G. N. Alam, Y. Ning, P. V. Rados, J. E. Nor and P. J. Polverini (2014). "Glucose-regulated protein 78 (Grp78) confers chemoresistance to tumor endothelial cells under acidic stress." PLoS One 9(6): e101053.

Von Roemeling, C. A., L. A. Marlow, J. J. Wei, S. J. Cooper, T. R. Caulfield, K. Wu, W. W. Tan, H. W. Tun and J. A. Copland (2013). "Stearoyl-CoA desaturase 1 is a novel molecular therapeutic target for clear cell renal cell carcinoma." Clin Cancer Res 19(9): 2368-2380.

Vultur, A., C. S. Gibhardt, H. Stanisz and I. Bogeski (2018). "The role of the mitochondrial calcium uniporter (MCU) complex in cancer." Pflugers Arch 470(8): 1149-1163.

Wajner, M. and A. U. Amaral (2016). "Mitochondrial dysfunction in fatty acid oxidation disorders: insights from human and animal studies." Biosci Rep 36(1).

Wang, C. and R. J. Youle (2009). "The role of mitochondria in apoptosis." Annu Rev Genet 43: 95-118.

Wang, L., Z. Shang, Y. Zhou, X. Hu, Y. Chen, Y. Fan, X. Wei, L. Wu, Q. Liang, J. Zhang and Z. Gao (2018). "Autophagy mediates glucose starvation-induced glioblastoma cell quiescence and chemoresistance through coordinating cell metabolism, cell cycle, and survival." Cell Death Dis 9(2): 213.

Wang, M., J. Zhao, L. Zhang, F. Wei, Y. Lian, Y. Wu, Z. Gong, S. Zhang, J. Zhou, K. Cao, X. Li, W. Xiong, G. Li, Z. Zeng and C. Guo (2017). "Role of tumor microenvironment in tumorigenesis." J Cancer 8(5): 761-773.

Wang, T., J. F. Fahrmann, H. Lee, Y.-J. Li, S. C. Tripathi, C. Yue, C. Zhang, V. Lifshitz, J. Song and Y. Yuan (2018). "JAK/STAT3-regulated fatty acid β-oxidation is critical for breast cancer stem cell self-renewal and chemoresistance." Cell Metab 27(1): 136-150. e135.

Wappler, E. A., A. Institoris, S. Dutta, P. V. Katakam and D. W. Busija (2013). "Mitochondrial dynamics associated with oxygen-glucose deprivation in rat primary neuronal cultures." PLoS One 8(5): e63206.

Whitaker-Menezes, D., U. E. Martinez-Outschoorn, Z. Lin, A. Ertel, N. Flomenberg, A. K. Witkiewicz, R. Birbe, A. Howell, S. Pavlides and R. Gandara (2011). "Evidence for a stromal-epithelial "lactate shuttle" in human tumors: MCT4 is a marker of oxidative stress in cancer-associated fibroblasts." Cell Cycle 10(11): 1772-1783.

Wilke, C. M., I. Kryczek, S. Wei, E. Zhao, K. Wu, G. Wang and W. Zou (2011). "Th17 cells in cancer: help or hindrance?" Carcinogenesis 32(5): 643-649.

Wing, K., Y. Onishi, P. Prieto-Martin, T. Yamaguchi, M. Miyara, Z. Fehervari, T. Nomura and S. Sakaguchi (2008). "CTLA-4 control

over Foxp3+ regulatory T cell function." Science 322(5899): 271-275.

Winslow, M. M., T. L. Dayton, R. G. Verhaak, C. Kim-Kiselak, E. L. Snyder, D. M. Feldser, D. D. Hubbard, M. J. DuPage, C. A. Whittaker, S. Hoersch, S. Yoon, D. Crowley, R. T. Bronson, D. Y. Chiang, M. Meyerson and T. Jacks (2011). "Suppression of lung adenocarcinoma progression by Nkx2-1." Nature 473(7345): 101-104.

Witkiewicz, A. K., D. Whitaker-Menezes, A. Dasgupta, N. J. Philp, Z. Lin, R. Gandara, S. Sneddon, U. E. Martinez-Outschoorn, F. Sotgia and M. P. Lisanti (2012). "Using the "reverse Warburg effect" to identify high-risk breast cancer patients: stromal MCT4 predicts poor clinical outcome in triple-negative breast cancers." Cell Cycle 11(6): 1108-1117.

Wong, T. L., N. Che and S. Ma (2017). "Reprogramming of central carbon metabolism in cancer stem cells." Biochim Biophys Acta (BBA) Mol Basis Dis 1863(7): 1728-1738.

Wu, D., L. Zhuo and X. Wang (2017). "Metabolic reprogramming of carcinoma-associated fibroblasts and its impact on metabolic heterogeneity of tumors." Semin. Cell Dev. Biol, Elsevier.

Wu, S., K. J. Rhee, E. Albesiano, S. Rabizadeh, X. Wu, H. R. Yen, D. L. Huso, F. L. Brancati, E. Wick, F. McAllister, F. Housseau, D. M. Pardoll and C. L. Sears (2009). "A human colonic commensal promotes colon tumorigenesis via activation of T helper type 17 T cell responses." Nature Medicine 15(9): 1016-1022.

Wu, Y., J. Deng, P. G. Rychahou, S. Qiu, B. M. Evers and B. P. Zhou (2009). "Stabilization of snail by NF-κB is required for inflammation-induced cell migration and invasion." Cancer Cell 15(5): 416-428.

Yang, Z. J., C. E. Chee, S. Huang and F. A. Sinicrope (2011). "The role of autophagy in cancer: therapeutic implications." Mol Cancer Ther 10(9): 1533-1541.

Yeoh, B. S., P. Saha, V. Singh, X. Xiao, Y. Ying, J. K. Vanamala, M. J. Kennett, K. J. Harvatine, B. Joe and M. Vijay-Kumar (2016). "Deficiency of stearoyl-CoA desaturase-1 aggravates colitogenic

potential of adoptively transferred effector T cells." Am. J. Physiol. Gastrointest. Liver Physiol 311(4): G713-G723.

Yeom, C. J., Y. Goto, Y. Zhu, M. Hiraoka and H. Harada (2012). "Microenvironments and cellular characteristics in the micro tumor cords of malignant solid tumors." Int J Mol Sci 13(11): 13949-13965.

Yeung, T.-L., C. S. Leung, K.-K. Wong, G. Samimi, M. S. Thompson, J. Liu, T. M. Zaid, S. Ghosh, M. J. Birrer and S. C. Mok (2013). "TGF-β modulates ovarian cancer invasion by upregulating CAF-derived versican in the tumor microenvironment." Cancer Res 73(16): 5016-5028.

Yi, M., J. Li, S. Chen, J. Cai, Y. Ban, Q. Peng, Y. Zhou, Z. Zeng, S. Peng and X. Li (2018). "Emerging role of lipid metabolism alterations in Cancer stem cells." J Exp Clin Cancer Res 37(1): 118.

Yonesaka, K., K. Haratani, S. Takamura, H. Sakai, R. Kato, N. Takegawa, T. Takahama, K. Tanaka, H. Hayashi, M. Takeda, S. Kato, O. Maenishi, K. Sakai, Y. Chiba, T. Okabe, K. Kudo, Y. Hasegawa, H. Kaneda, M. Yamato, K. Hirotani, M. Miyazawa, K. Nishio and K. Nakagawa (2018). "B7-H3 negatively modulates CTL-mediated cancer immunity." Clin Cancer Res 24(11): 2653-2664.

Zeng, X., M. Zhu, X. Liu, X. Chen, Y. Yuan, L. Li, J. Liu, Y. Lu, J. Cheng and Y. Chen (2020). "Oleic acid ameliorates palmitic acid induced hepatocellular lipotoxicity by inhibition of ER stress and pyroptosis." Nutrition Meta 17(1): 1-14.

Zhang, J. P., J. Yan, J. Xu, X. H. Pang, M. S. Chen, L. Li, C. Wu, S. P. Li and L. Zheng (2009). "Increased intratumoral IL-17-producing cells correlate with poor survival in hepatocellular carcinoma patients." J Hepatol 50(5): 980-989.

Zhang, Q., H. Wang, C. Mao, M. Sun, G. Dominah, L. Chen and Z. Zhuang (2018). "Fatty acid oxidation contributes to IL-1β secretion in M2 macrophages and promotes macrophage-mediated tumor cell migration." Mol Immunol 94: 27-35.

Zhang, R., F. Qi, F. Zhao, G. Li, S. Shao, X. Zhang, L. Yuan and Y. Feng (2019). "Cancer-associated fibroblasts enhance tumor-

associated macrophages enrichment and suppress NK cells function in colorectal cancer." Cell Death Dis 10(4): 273.

Zhang, Y., R. Kurupati, L. Liu, X. Y. Zhou, G. Zhang, A. Hudaihed, F. Filisio, W. Giles-Davis, X. W. Xu, G. C. Karakousis, L. M. Schuchter, W. Xu, R. Amaravadi, M. Xiao, N. Sadek, C. Krepler, M. Herlyn, G. J. Freeman, J. D. Rabinowitz and H. C. J. Ertl (2017). "Enhancing CD8(+) T cell fatty acid catabolism within a metabolically challenging tumor microenvironment increases the efficacy of melanoma immunotherapy." Cancer Cell 32(3): 377.

Zheng, J. (2012). "Energy metabolism of cancer: Glycolysis versus oxidative phosphorylation." Oncol. Lett 4(6): 1151-1157.

Ziani, L., S. Chouaib and J. Thiery (2018). "Alteration of the antitumor immune response by cancer-associated fibroblasts." Front Immunol 9: 414.

Zohar, Y., G. Wildbaum, R. Novak, A. L. Salzman, M. Thelen, R. Alon, Y. Barsheshet, C. L. Karp and N. Karin (2014). "CXCL11-dependent induction of FOXP3-negative regulatory T cells suppresses autoimmune encephalomyelitis." J Clin Invest 124(5): 2009-2022.

국문초록

포도당 결핍에 따른 종양조직 구성세포들의 표현형 및 분자생물학적 특성 변화

황 성 현

지도 교수: 김 용 백

서울대학교 대학원 수의학과
수의병인생물학 및 예방수의학 전공

종양 미세 환경에서 종양 세포의 호기성 해당작용 및 신생 혈관 형성증은 포도당 결핍 환경을 유도한다. 종양 조직 내 종양 섬유아 세포 및 면역세포는 정상 조직 내 동일 세포와 대사 표현형이 다르며, 종양세포와 상호작용을 통해 종양 악성도를 향상시킨다. 그러나, 포도당 결핍 환경이 종양세포, 종양 섬유아 세포 및 종양 면역세포에 미치는 역할은 거의 연구가 되어있지 않다. 본 연구는 포도당 결핍에 의해 변화된 종양세포, 종양 섬유아 세포 및 종양 면역세포의 대사 작용이 종양 악성도에 미치는 역할에 대해 연구하였다.

포도당 결핍 환경에 적응한 악성 중피종 세포에 Metformin 을 처치 시 약물 저항성 관련 인자인 multidrug resistance protein 1 (MDR1)의 발현이 세포막, 핵보다 미토콘드리아에서 증가하였다. 또한,

미토콘드리아의 기능 및 형태적 변형이 관찰되었다. 특히, 심각한 mitochondrial membrane potential (MMP) 과분극이 관찰되었다. 하지만, MMP 탈분극 유도제인 Carbonyl cyanide m-chlorophenyl hydrazone 처치 시, 미토콘드리아 내 MDR1 발현이 감소되었으며, metformin 저항성이 감소하였다. 포도당 결핍 환경에서 생존한 MDR1 의 유전자적 발현이 제거된 중피종 세포는 정상 세포와 비교하여 metformin 저항성이 유의적으로 감소하였다. 본 연구는 포도당 결핍에 적응한 악성 중피종 세포의 미토콘드리아 대사 변형에 의해 증가되는 MDR1 이 metformin 저항성을 유도함을 확인하였다.

정상 섬유아 세포와 달리 종양 섬유아 세포는 종양 세포의 이동능, 증식, 전이능 등을 향상시켜 악성도를 증가시킨다. 또한, 종양 조직의 비정상적인 신생혈관 형성증은 동일한 종양 조직 내에서 이질적인 반응을 유도한다. 하지만, 포도당 결핍 환경에서 정상 섬유아 세포와 차별적인 종양 섬유아 세포의 이질적인 표현형 및 대사적 특징에 관한 연구는 수행되지 않았다. 본 연구에서 동일한 종양 조직을 6 개로 절제한 후 각각의 종양 조직에서 섬유아 세포를 분리 배양한 뒤, 포도당 결핍 환경에서 배양하였다. 그리고 정상 섬유아 세포는 동일 연령의 마우스의 피부 및 폐 조직에서 분리 배양하였다. 포도당 결핍 환경에서 종양 섬유아 세포는 정상 섬유아 세포와 달리, 세포 증식 및 에너지 합성이 증가되었으며, 각 조직 유래 종양 섬유아 세포에서 동일한 패턴이 관찰되었다. 하지만, 정도는 이질적이였다. 정상 섬유아 세포와 비교하여, transforming growth factor-β (TGF-β) signaling 와 mitochondrial calcium uniporter (MCU)의 발현은 종양 섬유아 세포에서 증가되며, 포도당 결핍 환경에서 더욱 향상된다. 하지만 TGF-β signaling 을 억제할 경우, 세포 증식, 에너지 합성 및 미토콘드리아 내 칼슘양이 유의적으로 감소되었다. 또한, 종양 섬유아 세포에서 TGF-β signaling 억제는 MCU 의 발현을 감소시켜 미토콘드리아 내 칼슘 함량을

감소시켰다. 하지만 정상 섬유아 세포에서는 큰 차이를 보이지 않았다. 포도당 결핍 환경에서 증가된 칼슘은 미토콘드리아 내 ATP 합성을 촉진시켜 종양 섬유아 세포의 증식을 향상시켰다. 하지만, 미토콘드리아 내 ATP 합성 효소를 억제할 경우, 칼슘은 배출되지 못해 계속 축적되며, 이는 심각한 세포 사멸을 유도하였다.

종양 섬유아 세포는 직접적 또는 매개인자를 통한 간접적으로 종양 세포의 악성도를 향상시킨다. 정상 섬유아 세포와 비교하여 종양 섬유아 세포에서 증가된 stearoyl-CoA desaturase (SCD) 발현은 oleic acid (OA) 합성을 증가시킴을 확인하였다. 또한, 종양 섬유아 세포 유래 OA 는 세포 외로 배출되어 지방 수송 통로를 통해 폐암 세포로 이동되어 포도당 결핍 환경에서 자가 포식 작용에 의해 분해되어 지방 대사를 활성화시킨다. 이 결과, 폐암 세포 내 증가된 SCD 발현은 β-oxidation 과 액틴 중합체를 향상시켜 yes-associated protein 를 핵 내로 이동시켜 폐암 줄기 세포 형성을 촉진한다. 그리고, SCD 과발현 폐암 세포를 면역 결핍 마우스에 접종 시 종양의 크기는 정상 및 SCD knock out 세포 접종 군과 비교하여 유의적으로 증가된다. 그리고 비소세포폐암 환자의 조직에서 SCD 염색 결과, 폐암의 진행 및 등급이 높을수록 발현이 증가됨을 확인하였다.

종양 섬유아 세포 유래 OA 은 종양 세포뿐만 아니라 $CD4^+$ 종양 침윤 림프구로도 이동하여 SCD 의 발현을 증가시킨다. 포도당 결핍 환경에서 SCD 의 발현은 더욱 증가되며 Th1 세포 표현형 마커인 T-bet, interleukin-2, interferon-ɣ의 발현을 증가시킨다. 하지만, SCD 억제제를 처치할 경우, 포화 지방산인 palmitic acid 의 함량이 증가되어 mitochondrial superoxide 를 합성하여 regulatory T cell 표현형 마커인 Foxp3, TGF-β, CD25 의 발현이 증가된다. 그리고 SCD 의 발현이 증가된 $CD4^+$ T cell 는 CXCL11 를 과량 분비하며, 이는 $CD8^+$ T cell 의 C-X-C chemokine receptor type 3 (CXCR3)와 결합하여 암세포 사멸

효과를 유의적으로 향상시킨다. 실제로 마우스 종양 모델에서 CXCR3-$CD8^+$ T cell 의 접종은 뛰어난 종양 억제 효과를 보였다.

본 연구들의 결과는 포도당 결핍에 의해 종양 세포, 종양 섬유아 세포와 종양 면역세포의 변화된 대사 표현형이 단독 또는 세포들 간의 상호관계에 미치는 분자생물학적 기전을 연구하였다. 이러한 결과는, 적대적 종양 미세환경인 포도당 결핍이 종양 세포, 비 종양 세포에 미치는 대사 및 분자생물학적 기전 이해에 지대한 역할을 할 수 있다고 사료된다. 또한, 포도당 결핍에 의해 조절되는 종양 악성도를 향상시키는 주요 인자를 대상으로 한 연구는 항암 치료를 향상시킬 수 있다.

핵심어: 종양 미세환경, 포도당 결핍 환경, 종양 섬유아 세포, 종양 침윤 림프구, 종양 줄기 세포, 지방 대사, 항암.

학 번: 2016-21772